

**Structural / magnetic phase transitions and superconductivity in  
 $\text{Ba}(\text{Fe}_{1-x}\text{TM}_x)_2\text{As}_2$  (TM=Co, Ni, Cu, Co / Cu, Rh and Pd) single crystals**

by

Ni Ni

A dissertation submitted to the graduate faculty  
in partial fulfillment of the requirements for the degree of  
**DOCTOR OF PHILOSOPHY**

Major: Condensed Matter Physics

Program of Study Committee:  
Paul C. Canfield, Co-major Professor  
Sergey L. bud'ko, Co-major Professor  
Bruce N. Harmon  
Steve W. Martin  
James Cochran

Iowa State University

Ames, Iowa

2009

## DEDICATION

I would like to dedicate this thesis to my husband Zhongbo Kang and my parents.

## TABLE OF CONTENTS

<b>LIST OF FIGURES</b> . . . . .	vi
<b>ACKNOWLEDGEMENTS</b> . . . . .	xvi
<b>CHAPTER 1. Introduction</b> . . . . .	1
<b>CHAPTER 2. Overview of superconductivity</b> . . . . .	10
2.1 Zero resistivity and Meissner effect . . . . .	11
2.2 Ginzburg-Landau theory and type II superconductor . . . . .	13
2.2.1 Coherence length and penetration depth . . . . .	14
2.2.2 Type II superconductor . . . . .	15
2.3 BCS theory . . . . .	16
2.3.1 Superconducting state . . . . .	16
2.3.2 Excitation spectrum, gap function and gap symmetry . . . . .	18
2.3.3 Thermodynamic properties . . . . .	22
2.4 Eliashberg theory: the extension of BCS theory . . . . .	22
2.4.1 Electron-phonon spectrum and pseudopotential . . . . .	22
2.4.2 Thermodynamic properties . . . . .	23
2.5 Impurity effects on the superconducting temperature . . . . .	25
2.5.1 Nonmagnetic impurities . . . . .	26
2.5.2 Upper critical field: WHH theory . . . . .	32
<b>CHAPTER 3. Experimental methods</b> . . . . .	36
3.1 Crystal growth . . . . .	36
3.1.1 High temperature solution growth method . . . . .	37

3.1.2	Single crystal growth of $\text{Ba}(\text{Fe}_{1-x}\text{TM}_x)_2\text{As}_2$ (TM = Co, Ni, Cu, Cu / Co, Rh and Pd)	38
3.2	Measurement methods	46
3.2.1	X-ray diffraction measurements	46
3.2.2	Wave-length dispersive spectroscopy	48
3.2.3	Resistivity measurement	49
3.2.4	Magnetization measurement	50
3.2.5	Specific heat measurement	51
3.2.6	Signatures of structural, antiferromagnetic and superconducting phase transitions in transport and thermodynamic measurements	51
<b>CHAPTER 4. Physical properties of <math>\text{BaFe}_2\text{As}_2</math> single crystals</b>		<b>54</b>
4.1	Introduction	54
4.2	Results and discussion	54
4.2.1	Single crystalline $\text{BaFe}_2\text{As}_2$ grown from FeAs flux	54
4.2.2	Single crystalline $\text{BaFe}_2\text{As}_2$ grown from Sn flux	57
4.3	Summary	60
<b>CHAPTER 5. Transport, thermodynamic properties and anisotropic <math>H_{c2}</math> of <math>\text{Ba}(\text{Fe}_{1-x}\text{Co}_x)_2\text{As}_2</math> single crystals</b>		<b>61</b>
5.1	Introduction	61
5.2	Experimental results	62
5.2.1	Structural, transport and thermodynamic properties	62
5.2.2	Anisotropic $H_{c2}(T)$ curves	67
5.3	Discussion	71
5.4	Summary and conclusions	76
<b>CHAPTER 6. Transport and thermodynamic properties of <math>\text{Ba}(\text{Fe}_{1-x}\text{TM}_x)_2\text{As}_2</math> (TM=Ni, Cu, Co / Cu, Rh and Pd) single crystals</b>		<b>78</b>
6.1	Introduction and overview	78
6.2	Experimental results	80



6.2.1	Ba(Fe <sub>1-x</sub> Ni <sub>x</sub> ) <sub>2</sub> As <sub>2</sub> . . . . .	80
6.2.2	Ba(Fe <sub>1-x</sub> Cu <sub>x</sub> ) <sub>2</sub> As <sub>2</sub> . . . . .	86
6.2.3	Ba(Fe <sub>1-x-y</sub> Co <sub>x</sub> Cu <sub>y</sub> ) <sub>2</sub> As <sub>2</sub> ( $x \sim 0.022$ ) . . . . .	92
6.2.4	Ba(Fe <sub>1-x-y</sub> Co <sub>x</sub> Cu <sub>y</sub> ) <sub>2</sub> As <sub>2</sub> ( $x \sim 0.047$ ) . . . . .	98
6.2.5	Ba(Fe <sub>1-x</sub> Rh <sub>x</sub> ) <sub>2</sub> As <sub>2</sub> . . . . .	103
6.2.6	Ba(Fe <sub>1-x</sub> Pd <sub>x</sub> ) <sub>2</sub> As <sub>2</sub> . . . . .	107
6.3	Discussion . . . . .	111
6.3.1	Comparison of the phase diagrams of Ba(Fe <sub>1-x</sub> TM <sub>x</sub> ) <sub>2</sub> As <sub>2</sub> (TM=Co, Ni, Cu, Co / Cu, Rh and Pd) series . . . . .	111
6.3.2	Anisotropic upper critical field $H_{c2}$ . . . . .	121
6.3.3	Universal scaling of $\Delta C_p/T$ at $T_c$ [54] . . . . .	124
<b>CHAPTER 7. Summary and conclusions . . . . .</b>		<b>126</b>
<b>BIBLIOGRAPHY . . . . .</b>		<b>130</b>

## LIST OF FIGURES

Figure 1.1	History of the discovery of superconductors with exceptional $T_c$ values [3, 4, 6, 7, 8, 11, 19, 23, 30]. . . . .	1
Figure 1.2	The crystal structure of a) $\text{BaFe}_2\text{As}_2$ [40] and b) $\text{LaFeAsO}$ [43]. . . .	4
Figure 1.3	$\rho$ vs. $T$ and $\chi_{mol}$ vs. $T$ (inset) for (a) Polycrystalline $\text{BaFe}_2\text{As}_2$ [40] and (b) Polycrystalline $\text{LaFeAsO}$ [42]. $C_p$ vs. $T$ for (c) Polycrystalline $\text{BaFe}_2\text{As}_2$ [40] and (d) Polycrystalline $\text{LaFeAsO}$ [42]. . . . .	6
Figure 1.4	Polycrystalline $\text{BaFe}_2\text{As}_2$ : (a) Left panel: powder X-ray diffraction patterns. Right panel: lattice parameters in tetragonal and orthorhombic phases. For clarity, $a$ in the tetragonal phase are multiplied by $\sqrt{2}$ [40]. (b) $^{57}\text{Fe}$ Mössbauer spectra with transmission integral fits [40]. (c) Magnetic structure of $\text{BaFe}_2\text{As}_2$ ( $a$ is the longer in-plane axis) [46]. . . . .	9
Figure 2.1	Schematic diagram of the magnetic induction $\mathbf{B}$ in field-cooled sequence (a) Perfect conductor, (b) Superconductor. . . . .	13
Figure 2.2	Schematic diagram of Fermi surface at (a) Normal ground state, (b) Superconducting state. . . . .	17
Figure 2.3	(a) Momentum dependent occupation probability $\nu_k^2$ . (b) Quasiparticle excitation spectrum. . . . .	19
Figure 2.4	Solid line: the evolution of the gap function with temperature. Hollow square: experiment data of Nb. Hollow circle: experiment data of Ta. Solid circle: experiment data of Sn [81]. . . . .	20
Figure 2.5	Superconducting gap with different gap in $k$ space. . . . .	21

Figure 2.6	(a) The $T_c/\omega_{ln}$ dependent $2\Delta(0)/k_B T_c$ . The solid dots are theoretical results from the full numerical Eliashberg calculation, which agrees with the experiment data within 10%. (b) The $T_c/\omega_{ln}$ dependent $\Delta C(T_c)/\gamma T_c$ . The solid dots are theoretical results from the full numerical Eliashberg calculation, which agrees with the experiment data within 10% [66]. .	25
Figure 2.7	(a) $T_c/T_{c0}$ vs. nonmagnetic impurity concentration for $s$ -wave superconductor, In [102, 103] and $\text{LuNi}_2\text{B}_2\text{C}$ [105]; non- $s$ -wave superconductor $\text{CeCoIn}_5$ [101], YBCO [104] and LSCO [104]. Inset: Enlarged $T_c/T_{c0}$ vs. nonmagnetic impurity concentration for $s$ -wave superconductor, In [102, 103]. (b) Relative change of $T_c$ with dopant concentration vs. number of valence electrons of $\text{Y}(\text{Ni}_{1-x}\text{TM}_x)_2\text{B}_2\text{C}$ [108]. . . . .	28
Figure 2.8	$T_c$ and $T_N$ vs. the de Gennes factor for pure $\text{RNi}_2\text{B}_2\text{C}$ [109]. . . . .	30
Figure 2.9	(a) $T/T_{c0}$ vs. $n/n_c$ . Solid line: from the AG theory. Dots: experiment data for $\text{La}_{1-x}\text{Gd}_x\text{Al}_2$ . (b) Solid line: de Gennes factor $(g_J - 1)^2 J(J+1)$ normalized to the value of Gd vs. different rear earth elements. Dots: $-(dT_c/dn) _{n=0}$ normalized to the value of Gd impurity vs. different rare earth impurities in $\text{La}_{1-x}\text{Gd}_x\text{Al}_2$ and $\text{La}_{0.99}\text{R}_{0.01}$ . (c) $\Delta_c/\Delta_{c0}$ vs. $T_c/T_{c0}$ . Solid line: numerical result of from AG theory. Broken line: theoretical curve from BCS theory. Dots: experiment data for $\text{La}_{1-x}\text{Gd}_x\text{Al}_2$ and $\text{La}_{0.99}\text{R}_{0.01}$ [95]. . . . .	31
Figure 2.10	The schematic plot of the free energies of superconducting and normal states [72] . . . . .	34
Figure 2.11	(a) Normalized upper critical field $h^*$ vs. the normalized superconducting temperature $t$ without spin effects [71]. (b) Normalized upper critical field $h^*$ vs. the normalized superconducting temperature $t$ with spin effects [72]. . . . .	35
Figure 3.1	Binary phase diagram (a) As-Sn [131]. (b) Ba-Sn [132]. (c) Fe-Sn [133]. (d) As-Fe [134]. . . . .	39

Figure 3.2	Diagram of the ampoule used for crystal growth (see text) . . . . .	40
Figure 3.3	(a) Single crystal of $\text{BaFe}_2\text{As}_2$ grown from Sn flux against $1\text{mm}$ scale. (b) Single crystal of $\text{Ba}(\text{Fe}_{0.926}\text{Co}_{0.074})_2\text{As}_2$ grown from self flux against $1\text{mm}$ scale. . . . .	41
Figure 3.4	The graphic summary of the results from the elemental analysis for the $\text{Ba}(\text{Fe}_{1-x}\text{TM}_x)_2\text{As}_2$ (TM = Co, Ni, Rh, Pd, Cu, Cu / Co) series. . . .	46
Figure 3.5	Powder X-ray patterns for pure and doped $\text{BaFe}_2\text{As}_2$ . Si is added as an internal standard. . . . .	47
Figure 3.6	(a) Temperature-dependent electrical resistivity of three samples of $\text{Ba}(\text{Fe}_{0.962}\text{Co}_{0.038})_2\text{As}_2$ . (b) Temperature-dependent electrical resistivity of three samples of $\text{Ba}(\text{Fe}_{0.962}\text{Co}_{0.038})_2\text{As}_2$ normalized to their room temperature respective slopes: $\rho(T)/(d\rho/dT) _{300\text{K}}$ . (c) The same data as (b) with upper curve shifted down by 85.7 K and intermediate curve shifted down by 28 K to account for differences in temperature independent, residual resistivity. . . . .	49
Figure 3.7	Characteristic signatures in resistivity, magnetization and heat capacity measurements near the transition temperature of a (a) antiferromagnetic phase transition. (b) structural phase transition. (c) superconducting phase transition. . . . .	52
Figure 4.1	Single crystalline $\text{BaFe}_2\text{As}_2$ grown from FeAs flux: (a) Normalized in-plane resistivity $\rho_a(T)/\rho_a(300\text{K})$ vs. T. Inset: $d(\rho_a(T)/\rho_a(300\text{K}))/dT$ vs. T near the phase transition (upper left); anisotropic parameter $\gamma_p = \rho_c/\rho_a$ [53] (lower right). (b) $M$ vs. H taken at 5 K and 300 K with $H \perp c$ . (c) $M/H$ vs. T taken at 1 T with $H \parallel c$ and $H \perp c$ . (d) $C_p$ vs. T. Inset: enlarged $C_p$ vs. T near the phase transition. . . . .	55

Figure 4.2	Single crystalline $\text{BaFe}_2\text{As}_2$ grown from Sn flux: (a) Temperature dependent in-plane electrical resistivity taken at 0 and 7 T with $H \perp c$ . (b) $M(T)/H$ taken at 0.1 T with $H \parallel c$ and $H \perp c$ . (c) $C_p$ vs. $T$ . (d) Lattice parameters and unit-cell volume for the tetragonal and orthorhombic phases. For clarity, the lattice parameter $a$ in the high-temperature tetragonal phase has been multiplied by a factor of $\sqrt{2}$ so as to allow for comparison to the low temperature orthorhombic phase data [25]. .	58
Figure 5.1	Lattice parameters, $a$ and $c$ as well as unit cell volume, $V$ , normalized to the values of pure $\text{BaFe}_2\text{As}_2$ as a function of measured Co concentration, $x_{WDS}$ [34]. . . . .	62
Figure 5.2	(a) Electrical resistivities normalized to their room temperature values for $\text{Ba}(\text{Fe}_{1-x}\text{Co}_x)_2\text{As}_2$ single crystals ( $0.00 \leq x_{WDS} \leq 0.166$ ). Each subsequent data set is shifted downward by 0.3 for clarity. (b) Low temperature data showing superconducting transition [34]. . . . .	63
Figure 5.3	$M/H$ vs. $T$ of $\text{Ba}(\text{Fe}_{1-x}\text{Co}_x)_2\text{As}_2$ single crystals taken at 2.5 mT with $H \perp c$ . Zero-field-cooled warming data as well as field-cooled warming data are shown [34]. . . . .	64
Figure 5.4	$M/H$ vs. $T$ of $\text{Ba}(\text{Fe}_{1-x}\text{Co}_x)_2\text{As}_2$ single crystals taken at 1 T with $H \perp c$ . Insets: $M(H)$ data of selected Co concentrations [34]. . . . .	65
Figure 5.5	$C_p$ vs. $T$ of $\text{Ba}(\text{Fe}_{1-x}\text{Co}_x)_2\text{As}_2$ with $x = 0.038$ (upper panel) and 0.047 (lower panel). Lower insets: $dC_p/dT$ . Upper insets: low temperature $C_p(T)$ data taken at 0 (solid line) and 9 T (dashed line) with $H \parallel c$ [34].	66
Figure 5.6	$C_p$ vs. $T$ of the superconducting $\text{Ba}(\text{Fe}_{1-x}\text{Co}_x)_2\text{As}_2$ . Data are shifted by a multiple of 50 mJ/mol $\text{K}^2$ along the $y$ - axis for clarity. Inset: enlarged $C_p/T$ vs. $T$ plot near $T_c$ for $\text{Ba}(\text{Fe}_{0.926}\text{Co}_{0.074})_2\text{As}_2$ , lines show the "isoentropic" construction to infer $T_c$ and $\Delta C$ [54]. . . . .	67

Figure 5.7	Isothermal $R(H)$ data of $\text{Ba}(\text{Fe}_{1-x}\text{Co}_x)_2\text{As}_2$ ( $x = 0.038$ ) with $H \parallel c$ (upper panel) and $H \perp c$ (lower panel). Dotted lines show onset and offset criteria used to determine $H_{c2}(T)$ values [34]. . . . .	68
Figure 5.8	Anisotropic $H_{c2}(T)$ curves determined for Co-doping level of $x = 0.038$ (left panel) and $x = 0.114$ (right panel) using onset criterion and offset criteria. . . . .	69
Figure 5.9	Anisotropic $H_{c2}(T)$ curves determined for Co-doping level of (a) $x = 0.047$ (b) $x = 0.10$ (c) $x = 0.058$ (d) $x = 0.074$ using onset criterion and offset criteria. . . . .	70
Figure 5.10	(a) Criteria used to determine transition temperatures for upper phase transition. Upper panel: $dC_p/dT$ emphasizes breaks in slope of $C_p(T)$ data. Middle panel: $(dR(T)/dT)/R(300K)$ and $R(T)/R(300K)$ . Bottom panel: $d(M(T)/H)/dT$ and $M(T)/H$ . (b) Neutron scattering measurement [152]. . . . .	71
Figure 5.11	$T - x$ phase diagram of $\text{Ba}(\text{Fe}_{1-x}\text{Co}_x)_2\text{As}_2$ single crystals for $x \leq 0.166$ . . . . .	73
Figure 5.12	Anisotropy of the upper critical field, $\gamma = H_{c2}^{\perp c}(T)/H_{c2}^{\parallel c}(T)$ , as a function of effective temperature, $T/T_c$ , for $\text{Ba}(\text{Fe}_{1-x}\text{Co}_x)_2\text{As}_2$ single crystals. Upper panel: offset criterion; lower panel: onset criterion. . . . .	74
Figure 5.13	(a) $H_{c2}$ curves of $(\text{Ba}_{0.55}\text{K}_{0.45})\text{Fe}_2\text{As}_2$ [144] as a function of $T$ . (b) $H_{c2}$ curves of $\text{Ba}(\text{Fe}_{0.926}\text{Co}_{0.074})_2\text{As}_2$ [34] as a function of $T$ . . . . .	76
Figure 6.1	Lattice parameters of $\text{Ba}(\text{Fe}_{1-x}\text{Ni}_x)_2\text{As}_2$ series, $a$ and $c$ as well as unit cell volume, $V$ , normalized to the values of pure $\text{BaFe}_2\text{As}_2$ as a function of measured Ni concentration, $x_{WDS}$ . . . . .	81
Figure 6.2	$\text{Ba}(\text{Fe}_{1-x}\text{Ni}_x)_2\text{As}_2$ series: (a) The temperature dependent resistivity, normalized to the room temperature value. Each subsequent data set is shifted downward by 0.3 for clarity. (b) $d(\rho(T)/\rho_{300K})/dT$ for $y \leq 0.032$ . (c) Enlarged low temperature $\rho(T)/\rho_{300K}$ . . . . .	82

Figure 6.3	Ba(Fe <sub>1-x</sub> Ni <sub>x</sub> ) <sub>2</sub> As <sub>2</sub> series: (a) Field-cooled (FC) and zero-field-cooled (ZFC) low field $M(T)/H$ data taken at 2.5 mT with $H \perp c$ . (b) $M(T)/H$ data taken at 1 T with $H \perp c$ . . . . .	83
Figure 6.4	$C_p$ vs. $T$ of the superconducting Ba(Fe <sub>1-x</sub> Ni <sub>x</sub> ) <sub>2</sub> As <sub>2</sub> compounds. Data are shifted by a multiple of 50 mJ/mol K <sup>2</sup> along the $y$ -axis for clarity. Inset: enlarged $C_p/T$ vs. $T$ plot near $T_c$ for Ba(Fe <sub>0.954</sub> Ni <sub>0.046</sub> ) <sub>2</sub> As <sub>2</sub> , lines show the "isoentropic" construction to infer $T_c$ and $\Delta C$ [54]. . . .	84
Figure 6.5	$T - x$ phase diagram of Ba(Fe <sub>1-x</sub> Ni <sub>x</sub> ) <sub>2</sub> As <sub>2</sub> single crystals for $x \leq 0.072$ .	85
Figure 6.6	Lattice parameters of Ba(Fe <sub>1-x</sub> Cu <sub>x</sub> ) <sub>2</sub> As <sub>2</sub> series, $a$ and $c$ as well as unit cell volume, $V$ , normalized to the values of pure BaFe <sub>2</sub> As <sub>2</sub> as a function of measured Cu concentration, $x_{WDS}$ . . . . .	86
Figure 6.7	The temperature dependent resistivity, normalized to the room temperature value, for Ba(Fe <sub>1-x</sub> Cu <sub>x</sub> ) <sub>2</sub> As <sub>2</sub> . Each subsequent data set is shifted downward by 0.3 for clarity respectively for (a) and (b). . . . .	87
Figure 6.8	(a) $d(\rho(T)/\rho_{300K})/dT$ of Ba(Fe <sub>1-x</sub> Cu <sub>x</sub> ) <sub>2</sub> As <sub>2</sub> for $0.05 \geq x$ . (b) Enlarged low temperature $\rho(T)/\rho_{300K}$ data of Ba(Fe <sub>0.956</sub> Cu <sub>0.044</sub> ) <sub>2</sub> As <sub>2</sub> . . . . .	88
Figure 6.9	$M(T)/H$ taken at 1 T with $H \perp c$ for Ba(Fe <sub>1-x</sub> Cu <sub>x</sub> ) <sub>2</sub> As <sub>2</sub> series. . . . .	89
Figure 6.10	(a) Enlarged temperature dependent heat capacity of Ba(Fe <sub>1-x</sub> Cu <sub>x</sub> ) <sub>2</sub> As <sub>2</sub> ( $x = 0, 0.0077, 0.02$ and $0.026$ ). Inset: $C_p$ vs. $T^2$ for Ba(Fe <sub>0.956</sub> Cu <sub>0.044</sub> ) <sub>2</sub> As <sub>2</sub> . (b) Enlarged $dC_p/dT$ vs. $T$ for Ba(Fe <sub>1-x</sub> Cu <sub>x</sub> ) <sub>2</sub> As <sub>2</sub> ( $x = 0.02$ and $0.026$ ). . . . .	90
Figure 6.11	$T - x$ phase diagram of Ba(Fe <sub>1-x</sub> Cu <sub>x</sub> ) <sub>2</sub> As <sub>2</sub> single crystals for $x \leq 0.061$ .	91
Figure 6.12	Lattice parameters of Ba(Fe <sub>1-x-y</sub> Co <sub>x</sub> Cu <sub>y</sub> ) <sub>2</sub> As <sub>2</sub> ( $x \sim 0.022$ ) series, $a$ and $c$ as well as unit cell volume, $V$ , normalized to the values of Ba(Fe <sub>0.976</sub> Co <sub>0.024</sub> ) <sub>2</sub> As <sub>2</sub> ( $a_0=3.9598(6)\text{\AA}$ , $c_0=13.0039(30)\text{\AA}$ ) as a function of measured Cu concentration, $y_{WDS}$ . . . . .	93

Figure 6.13	Ba(Fe <sub>1-x-y</sub> Co <sub>x</sub> Cu <sub>y</sub> ) <sub>2</sub> As <sub>2</sub> ( $x \sim 0.022$ ) series. (a) The temperature dependent resistivity, normalized to the room temperature values. Each subsequent data set is shifted downward by 0.3 for clarity. (b) $d(\rho(T)/\rho_{300K})/dT$ for $y \leq 0.019$ . (c) Enlarged low temperature $\rho(T)/\rho_{300K}$ . . . . .	94
Figure 6.14	Ba(Fe <sub>1-x-y</sub> Co <sub>x</sub> Cu <sub>y</sub> ) <sub>2</sub> As <sub>2</sub> ( $x \sim 0.022$ ) series: (a) Field-cooled (FC) and zero-field-cooled (ZFC) low field $M(T)/H$ data taken at 2.5 mT with $H \perp c$ . (b) $M(T)/H$ data taken at 1 T with $H \perp c$ . . . . .	95
Figure 6.15	Temperature dependent heat capacity of Ba(Fe <sub>0.953</sub> Co <sub>0.021</sub> Cu <sub>0.026</sub> ) <sub>2</sub> As <sub>2</sub> . Inset: $C_p/T$ vs. T. . . . .	96
Figure 6.16	$T - y$ phase diagram of Ba(Fe <sub>1-x-y</sub> Co <sub>x</sub> Cu <sub>y</sub> ) <sub>2</sub> As <sub>2</sub> ( $x \sim 0.022$ ) single crystals. . . . .	97
Figure 6.17	Lattice parameters of Ba(Fe <sub>1-x-y</sub> Co <sub>x</sub> Cu <sub>y</sub> ) <sub>2</sub> As <sub>2</sub> ( $x \sim 0.047$ ) series, $a$ and $c$ as well as unit cell volume, $V$ , normalized to the values of Ba(Fe <sub>0.935</sub> Co <sub>0.047</sub> ) <sub>2</sub> As <sub>2</sub> ( $a_0=3.9605(6)\text{\AA}$ , $c_0=12.9916(38)\text{\AA}$ ) as a function of measured Cu concentration, $y_{WDS}$ . . . . .	98
Figure 6.18	Ba(Fe <sub>1-x-y</sub> Co <sub>x</sub> Cu <sub>y</sub> ) <sub>2</sub> As <sub>2</sub> ( $x \sim 0.047$ ) series: (a) The temperature dependent resistivity, normalized to the room temperature value. Each subsequent data set is shifted downward by 0.3 for clarity. (b) $d(\rho(T)/\rho_{300K})/dT$ for $y=0$ and 0.0045. (c) Enlarged low temperature $\rho(T)/\rho_{300K}$ . . . . .	99
Figure 6.19	Ba(Fe <sub>1-x-y</sub> Co <sub>x</sub> Cu <sub>y</sub> ) <sub>2</sub> As <sub>2</sub> ( $x \sim 0.047$ ) series: (a) Field-cooled (FC) and zero-field-cooled (ZFC) low field $M(T)/H$ data taken at 2.5 mT with $H \perp c$ . (b) $M(T)/H$ data taken at 1 T with $H \perp c$ for $0 \leq y \leq 0.034$ . . . . .	100
Figure 6.20	Temperature dependent heat capacity of Ba(Fe <sub>0.934</sub> Co <sub>0.047</sub> Cu <sub>0.019</sub> ) <sub>2</sub> As <sub>2</sub> . Inset: $C_p/T$ vs. T near the superconducting transition with the estimated $\Delta C_p$ shown. . . . .	101
Figure 6.21	$T - y$ phase diagram of Ba(Fe <sub>1-x-y</sub> Co <sub>x</sub> Cu <sub>y</sub> ) <sub>2</sub> As <sub>2</sub> ( $x \sim 0.047$ ) single crystals. . . . .	102



Figure 6.22	Lattice parameters of $\text{Ba}(\text{Fe}_{1-x}\text{Rh}_x)_2\text{As}_2$ series, $a$ and $c$ as well as unit cell volume, $V$ , normalized to the values of pure $\text{BaFe}_2\text{As}_2$ as a function of measured Rh concentration, $x_{WDS}$ . . . . .	103
Figure 6.23	$\text{Ba}(\text{Fe}_{1-x}\text{Rh}_x)_2\text{As}_2$ series: (a) The temperature dependent resistivity, normalized to the room temperature value. Each subsequent data set is shifted downward by 0.3 for clarity. (b) $d(\rho(T)/\rho_{300K})/dT$ for $x \leq 0.039$ . (c) Enlarged low temperature $\rho(T)/\rho_{300K}$ . . . . .	104
Figure 6.24	(a) Low magnetic field $M(T)/H$ of $\text{Ba}(\text{Fe}_{1-x}\text{Rh}_x)_2\text{As}_2$ series. Inset: the criterion used to infer $T_c$ is shown for $\text{Ba}(\text{Fe}_{0.961}\text{Rh}_{0.039})_2\text{As}_2$ . (b) Temperature dependent heat capacity of $\text{Ba}(\text{Fe}_{0.943}\text{Rh}_{0.057})_2\text{As}_2$ . Inset: $C_p$ vs. $T$ near the superconducting transition with the estimated $\Delta C_p$ shown. . . . .	105
Figure 6.25	$T - x$ phase diagram of $\text{Ba}(\text{Fe}_{1-x}\text{Rh}_x)_2\text{As}_2$ single crystals. . . . .	106
Figure 6.26	Lattice parameters of $\text{Ba}(\text{Fe}_{1-x}\text{Pd}_x)_2\text{As}_2$ series, $a$ and $c$ as well as unit cell volume, $V$ , normalized to the values of pure $\text{BaFe}_2\text{As}_2$ as a function of measured Pd concentration, $x_{WDS}$ . . . . .	107
Figure 6.27	$\text{Ba}(\text{Fe}_{1-x}\text{Pd}_x)_2\text{As}_2$ series: (a) The temperature dependent resistivity, normalized to the room temperature value. Each subsequent data set is shifted downward by 0.3 for clarity. (b) $d(\rho(T)/\rho_{300K})/dT$ for $x \leq 0.027$ . (c) Enlarged low temperature $\rho(T)/\rho_{300K}$ . . . . .	108
Figure 6.28	(a) Low magnetic field $M(T)/H$ of $\text{Ba}(\text{Fe}_{1-x}\text{Pd}_x)_2\text{As}_2$ series. (b) Temperature dependent heat capacity of $\text{Ba}(\text{Fe}_{0.957}\text{Pd}_{0.043})_2\text{As}_2$ . Inset: $C_p$ vs. $T$ near the superconducting transition with the estimated $\Delta C_p$ shown. . . . .	109
Figure 6.29	$T - x$ phase diagram of $\text{Ba}(\text{Fe}_{1-x}\text{Pd}_x)_2\text{As}_2$ single crystals. . . . .	110
Figure 6.30	(a) $T - x$ phase diagrams of $\text{Ba}(\text{Fe}_{1-x}\text{Rh}_x)_2\text{As}_2$ and $\text{Ba}(\text{Fe}_{1-x}\text{Co}_x)_2\text{As}_2$ series. (b) $T - x$ phase diagrams of $\text{Ba}(\text{Fe}_{1-x}\text{Pd}_x)_2\text{As}_2$ and $\text{Ba}(\text{Fe}_{1-x}\text{Ni}_x)_2\text{As}_2$ series. . . . .	113

Figure 6.31	(a) $T - x$ phase diagrams of $\text{Ba}(\text{Fe}_{1-x}\text{TM}_x)_2\text{As}_2$ (TM=Co, Ni, Cu, Co / Cu). (Note: for Co / Cu doping, $x_{WDS} = x + y$ ). (a) $T - e$ phase diagrams of $\text{Ba}(\text{Fe}_{1-x}\text{TM}_x)_2\text{As}_2$ (TM=Co, Ni, Cu, Co / Cu). . . . .	114
Figure 6.32	$T_c$ as a function of extra electrons, $e$ , per Fe/TM site for all the series we grew. . . . .	115
Figure 6.33	Comparison of the lattice parameters ( $T \sim 300$ K), normalized to the values of pure $\text{BaFe}_2\text{As}_2$ , for all the $3d$ electron doped series: (a) $a/a_0$ , (b) $c/c_0$ , (c) $V/V_0$ , (d) $(a/c)/(a_0/c_0)$ as a function of transition metal doping, $x$ ; and (e) $(a/c)/(a_0/c_0)$ as a function of extra conduction electrons added, $e$ . . . . .	116
Figure 6.34	Comparison of the lattice parameters ( $T \sim 300$ K), normalized to the values of pure $\text{BaFe}_2\text{As}_2$ , for Co-doped, Ni-doped, Rh-doped and Pd-doped $\text{BaFe}_2\text{As}_2$ series: (a) $a/a_0$ as a function of transition metal doping concentration $x$ , (b) $(a/c)/(a_0/c_0)$ as a function of extra electrons added, $e$ . . . . .	117
Figure 6.35	$T_s - T_m$ as a function of $T_s$ . The data points from the samples indexed by "*" and "**" are not included. . . . .	119
Figure 6.36	(a) $T_c$ as a function of $T_s$ . (b) $T_c$ as a function of $T_m$ . The data points from the samples indexed by "*" and "**" are not included. (c) Transition temperature as a function of adjusted $x$ . $x$ is normalized so as to bring the interpolated values of $T_s$ onto the transition associated with $\text{Ba}(\text{Fe}_{0.953}\text{Co}_{0.047})_2\text{As}_2$ : for Co doped $\text{BaFe}_2\text{As}_2$ , $x = x_{WDS}$ ; for Rh doped $\text{BaFe}_2\text{As}_2$ , $x = x_{WDS} \times 0.047/0.039$ ; for Pd doped $\text{BaFe}_2\text{As}_2$ , $x = x_{WDS} \times 0.047/0.028$ ; for Ni doped $\text{BaFe}_2\text{As}_2$ , $x = x_{WDS} \times 0.047/0.03$ . . . . .	120
Figure 6.37	$R(H)$ data of $\text{Ba}(\text{Fe}_{0.954}\text{Ni}_{0.046})_2\text{As}_2$ with $H \perp c$ (upper panel) and $H \parallel c$ (lower panel). . . . .	122

- Figure 6.38 (a)  $H_{c2}$  vs.  $T$  from offset criterion (upper panel) and onset criterion (lower panel) of  $\text{Ba}(\text{Fe}_{0.954}\text{Ni}_{0.046})_2\text{As}_2$  and  $\text{Ba}(\text{Fe}_{0.953}\text{Co}_{0.047})_2\text{As}_2$ . (b)  $H_{c2}$  vs.  $T/T_c$  from offset criterion (upper panel) and onset criterion (lower panel) of  $\text{Ba}(\text{Fe}_{0.954}\text{Ni}_{0.046})_2\text{As}_2$  and  $\text{Ba}(\text{Fe}_{0.926}\text{Co}_{0.074})_2\text{As}_2$  (c)  $\gamma = H_{c2}^{\perp c}/H_{c2}^{\parallel c}$  vs.  $T/T_c$  for  $\text{Ba}(\text{Fe}_{0.954}\text{Ni}_{0.046})_2\text{As}_2$ . . . . . 123
- Figure 6.39 (a)  $\Delta C_p/T_c$  and  $T_c$  as functions of the doping level  $x$ . (b)  $\Delta C_p$  as a function of  $T_c$ . The solid line is the curve according to  $\Delta C_p = 0.055 T_c^3$ . (c) log-log plot of  $\Delta C_p/T_c$  vs.  $T_c$  [24, 25, 34, 35, 36, 54, 159, 160]. . . . 125

## ACKNOWLEDGEMENTS

I would like to take this opportunity to express my sincere thanks to those who have helped and supported me in the past several years.

First and foremost, I would like to thank my Ph.D. advisor, Dr. Paul. C. Canfield, for his guidance, trust and encouragement throughout the process in doing my research and writing this thesis. He is the best advisor I could imagine and I thank him for spending a lot of time and effort to guide me, teach me, discuss with me and make jokes with me.

I would also like to thank my co-advisor Dr. S. L. Bud'ko for the guidance and valuable discussions on various physics problems.

Special thanks to Dr. M. A. Tanatar, Dr. V. G. Kogan for the nice discussions, suggestions and encouragement.

I would like to thank my collaborators A. Thaler, Dr. J. Q. Yan and N. H. Sung for the sample growth, A. Kracher for the elemental analysis, M. E. Tillman and Dr. S. T. Hannahs for the upper critical field  $H_{c2}$  measurements.

Thanks must also go to Dr. S. Jia, Dr. A. Kreyssig, Dr. C. Martin, E. D. Mun, Dr. E. Colombier, R. Gorden, Dr. S. Nandi, D. Pratt, Dr. R. Prozorov, Dr. R. J. McQueeney, Dr. A. I. Goldman, Dr. R. W. McCallum, Dr. R. W. Hu, X. Lin, S. Kim, H. Kim, H. Hodovanets and S. Ran for the nice help and discussion.

Finally, I want to thank my beloved husband Zhongbo Kang, my parents and parents in law, who have always been patient and supportive to me. Without their love, I would not have been able to complete this work.

Work at the Ames Laboratory was supported by the Department of Energy, Basic Energy Sciences under Contract No. DE-AC02-07CH11358.

## CHAPTER 1. Introduction

Since its discovery in 1911 [1], superconductivity has been one of the most actively studied fields in condensed matter physics and has attracted immense experimental and theoretical effort. At this point in time, with more and more superconductors discovered in elements, alloys, intermetallic compounds and oxides, it is becoming clear that superconductivity is actually not so rare in nature.

Almost half of the elements in the periodic table and hundreds of compounds have been found to be superconducting. Fig. 1.1 shows the milestones in discovering higher  $T_c$  superconductors. Among the elemental superconductors, Niobium has the highest superconducting transition temperature,  $T_c$ , of 9.5 K. This record held for more than ten years, until the discovery of niobium nitride which superconducts below 16 K. It took another thirty years for  $T_c$  to increase from 16 K in niobium nitride to 23 K in niobium germanium.

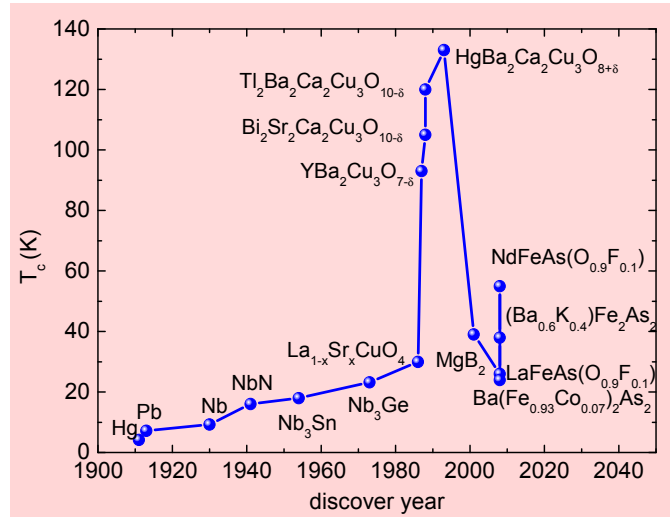


Figure 1.1 History of the discovery of superconductors with exceptional  $T_c$  values [3, 4, 6, 7, 8, 11, 19, 23, 30].

Even though the critical temperatures stayed below 25 K for almost half a century, researchers remained optimistic. In 1977, when V. L. Ginzburg and D. A. Kirzhnits wrote in their book "High-temperature superconductivity":

*"Specially we have in mind the possibility of producing "high-temperature" superconductors with  $T_c \geq 90K$ , which can be cooled by liquid air (nitrogen) or even superconductors with critical temperatures of the order of room temperature, i.e., with  $T_c \approx 300K$ " [2]*

they could not have expected that only 9 years later the first of these goals would actually come true.

In April 1986, a big breakthrough was made by Karl Müller and Johannes Bednorz [3]. Their discovery of  $(La_{1-x}Ba_x)CuO_4$ , with a transition temperature of 30 K range, started the new episode of high  $T_c$  superconductors. Nine months later,  $T_c$  rose to 93 K in  $YBa_2Cu_3O_{7-\delta}$  discovered by M. K. Wu, C. W. Chu and the collaborators [4] (and later confirmed by R. J. Cava, et al. [5]);  $T_c$  now exceeded the boiling point of liquid nitrogen.  $T_c$  continued to dramatically increase over the next several years. In 1988, the bismuth strontium calcium copper oxide,  $Bi_2Sr_2Ca_nCu_{n+1}O_{2n+6-\delta}$  was discovered superconducting at 95 K when  $n = 1$  [6], 105 K when  $n=2$  [6], and thallium based cuprates  $Tl_2Ba_2Ca_nCu_{n+1}O_{2n+6-\delta}$  ( $n=2$ ) was discovered with  $T_c$  of 120 K [7]. In 1993, mercury barium calcium copper oxide  $HgBa_2Ca_{n-1}Cu_nO_{2n+2+\delta}$  ( $n=3$ ) was found with  $T_c$  as high as 133 K [8] and with Tl substitution on Hg sites,  $T_c$  rose to 138 K which is the current record of highest  $T_c$  at ambient pressure [9]. The highest  $T_c$  under pressure is currently 164 K in  $HgBa_2Ca_2Cu_3O_{8+\delta}$  at 31 GPa applied pressure [10].

For a long time the cuprates were thought to be the only "high temperature" superconductors. This situation was changed in February 2008 when Fe-pnictides were added to the ranks of high temperature superconductors [11]. Their discovery traces back to 2006 when H. Hosono put the research efforts of his group in the layered  $LaTPnO$  ( $T = Fe, Co$ , and  $Ni$ ,  $Pn=P$  and  $As$ ) compounds. At that time, there is no doping trial or physical property measurements being made on these compounds although  $LaTPO$  ( $T = Fe, Co$ , and  $Ni$ ) com-

pounds were first synthesized by B. I. Zimmer, et al. in 1995 [12] and LaTAsO ( $T = \text{Fe, Co, and Ni}$ ) compounds were first synthesized by P. Quebe et al. in 1999 [13]. This work led to the discovery of superconductivity at 5 K and 3 K in LaTPO ( $T=\text{Fe, Ni}$ ) in 2006 and 2007 respectively [14, 15]. In 2008, layered  $\text{LaFeAsO}_{0.9}\text{F}_{0.1}$  was reported superconducting around 26 K at ambient pressure by Hosono's group [11] and later at 43 K, under applied pressures up to 4 GPa [16].  $T_c$  soon rose to 55 K at ambient pressure in  $\text{RFeAsO}_{0.9}\text{F}_{0.1}$  one month later ( $\text{R}=\text{Ce, Pr, Nd, Sm}$ ) [17, 18, 19, 20]. But single crystal sizes of these 1111 superconductors, grown by either high temperature, high pressure technique [21] or flux method [22], were small and limit the research on the 1111 system. In addition, problems associated with the stoichiometry of O and F made reproducibility hard to maintain in these compounds.

In June 2008, another high  $T_c$ , Fe-pnictide family with  $T_c$  up to 38 K,  $(\text{Ba}_{1-x}\text{K}_x)\text{Fe}_2\text{As}_2$ , was discovered [23, 24]. Following the discovery of this oxygen-free, K doped,  $\text{BaFe}_2\text{As}_2$  compound, sizable single crystals of  $(\text{Ba}_{1-x}\text{K}_x)\text{Fe}_2\text{As}_2$  were grown, using solution growth methods, up to  $3 \times 3 \times 0.2 \text{ mm}^3$  scale [25, 26, 27]. Unfortunately these  $K$ -doped samples were found to be rather inhomogeneous and there is a significant layer to layer concentration variation even in one piece [25, 28]. On the other hand, it was soon found that the transition metal doping on the Fe site in these families can induce superconductivity up to 24 K [29, 30, 31, 32, 33]. This discovery was important not only because it made Fe pnictides different from cuprates in the sense that superconductivity is destroyed by doping in the CuO plane, but also because large, high quality, homogeneous single crystals can be easily grown and reproduced [26, 30, 33, 34, 35, 36, 37, 38, 39]. The crystal size can be as big as  $0.2 \text{ cm}^3$  and the samples are the most homogeneous ones among all the Fe pnictide superconductors, which is critical for advanced studies.

The parent compound in 122 system,  $\text{BaFe}_2\text{As}_2$  [40, 41], has very similar structural and physical properties to the parent compound in 1111 system,  $\text{LaFeAsO}$  [42, 43]. A comparison of the structures of  $\text{BaFe}_2\text{As}_2$  with  $\text{LaFeAsO}$  is shown in Fig. 1.2. We can see clear similarities in the structures of these compounds: both of them possess FeAs sheets of edge-sharing  $\text{FeAs}_4$  tetrahedra. For  $\text{BaFe}_2\text{As}_2$ , the FeAs sheets are separated by barium atoms whereas for

LaFeAsO, FeAs sheets alternate with LaO layers of edge-sharing  $\text{OLa}_4$  tetrahedra along the  $c$  axis.

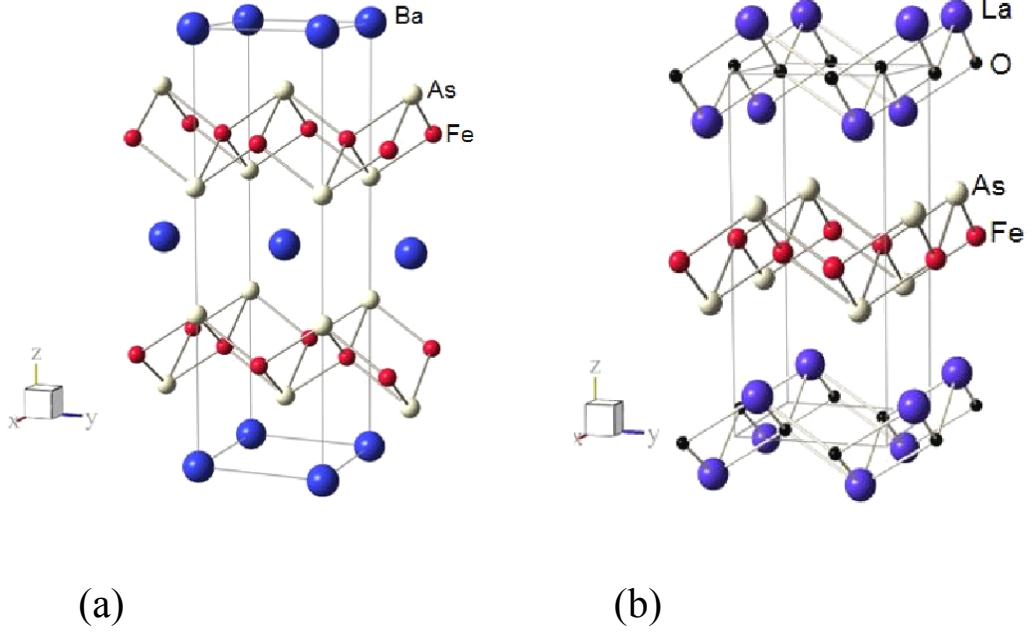


Figure 1.2 The crystal structure of a)  $\text{BaFe}_2\text{As}_2$  [40] and b)  $\text{LaFeAsO}$  [43].

	$\text{BaFe}_2\text{As}_2$ [40]		$\text{LaFeAsO}$ [43]	
T(K)	297	20	300	120
space group	$I4/mmm$	$Fmmm$	$P4/nmm, Z=2$	$cmma, Z=4$
$a\text{\AA}$	3.9625(1)	5.6146(1)	4.03268(1)	5.68262(3)
$b\text{\AA}$	$=a$	5.5742(1)	$=a$	5.71043(3)
$c\text{\AA}$	1.30168(3)	1.29453(2)	8.74111(4)	8.71964(4)
$V\text{\AA}^3$	204.38(1)	405.14(2)	142.1524(8)	282.954(2)
$Z$	2	4	2	4

Table 1.1 Detailed crystal structural information of  $\text{BaFe}_2\text{As}_2$  [40] and  $\text{LaFeAsO}$  [43].

The temperature dependent resistivity and magnetization of polycrystalline  $\text{BaFe}_2\text{As}_2$  studied by Rotter et al. [40] are presented in Fig. 1.3 (a). The high temperature resistivity is roughly temperature independent. Below about 140 K, the resistivity decreases dramatically, giving rise to a value of RRR,  $\rho(300K)/\rho(4K)$ , of  $\sim 6$ . The resistivity in the measured temper-



ature range varies from  $0.2 \text{ m}\Omega \text{ cm}$  at low temperature, to  $1.2 \text{ m}\Omega \text{ cm}$  at room temperature. The inset of Fig. 1.3 (a) shows the magnetic susceptibility taken at 0.5 T, which varies from  $\sim 9 \times 10^{-4} \text{ emu/mole}$  to  $\sim 11 \times 10^{-4} \text{ emu/mole}$ . A drop in the susceptibility occurs around 140 K, which is consistent with the feature seen in the resistivity data. The increase of the susceptibility below 100 K may be attributed to traces of moment bearing impurities.

As a comparison, temperature dependent resistivity and magnetization of polycrystalline LaFeAsO [42] are shown in Fig. 1.3 (b). It manifests very similar features in transport and thermodynamic properties to the ones in BaFe<sub>2</sub>As<sub>2</sub>: a large drop of both resistivity and magnetization around 160 K is observed in LaFeAsO; LaFeAsO is also a poor metal with the resistivity ranging from 2.5 to 4  $\text{m}\Omega \text{ cm}$  in the temperature range from 2 K to 300 K. But for LaFeAsO, the magnetic susceptibility measured at 1 T spans from 1 to  $3 \times 10^{-4} \text{ emu/mole}$ , which is roughly one order smaller than the one for polycrystalline BaFe<sub>2</sub>As<sub>2</sub>; the low temperature Curie tail in the LaFeAsO as shown in Fig. 1.3 (b) [42] is also smaller than the one that is seen in the BaFe<sub>2</sub>As<sub>2</sub> as shown in Fig. 1.3 (a) [40].

Temperature dependent  $C_p$  data of polycrystalline BaFe<sub>2</sub>As<sub>2</sub> are presented in Fig. 1.3 (c). A sharp peak can be seen around 140 K which indicates a phase transition at this temperature and is in agreement with the anomalies in resistivity and susceptibility measurements. From the inflection point of the  $\lambda$ -anomaly, a transition temperature of  $139.9 \pm 0.5 \text{ K}$  [40] was inferred. As a comparison,  $C_p$  vs.  $T$  data for polycrystalline LaFeAsO are shown in Fig. 1.3(d). Instead of a similar sharp heat capacity peak observed for BaFe<sub>2</sub>As<sub>2</sub>, a broad feature with two kinks is seen at the temperature where the resistivity and magnetization drop significantly for LaFeAsO. These features in LaFeAsO were reported to be associated with a tetragonal to orthorhombic phase transition around 160 K and a paramagnetic to antiferromagnetic phase transition around 145 K [42, 43, 44, 45].

The similarities between BaFe<sub>2</sub>As<sub>2</sub> and LaFeAsO are further seen in temperature dependent powder X-ray measurements of BaFe<sub>2</sub>As<sub>2</sub> [40]. Fig. 1.4 (a) presents X-ray powder diffraction data from BaFe<sub>2</sub>As<sub>2</sub> between 150 and 40 K. Below 140 K, several peaks broaden and as temperature decreases, these peaks clearly get split, indicating the occurrence of a structural

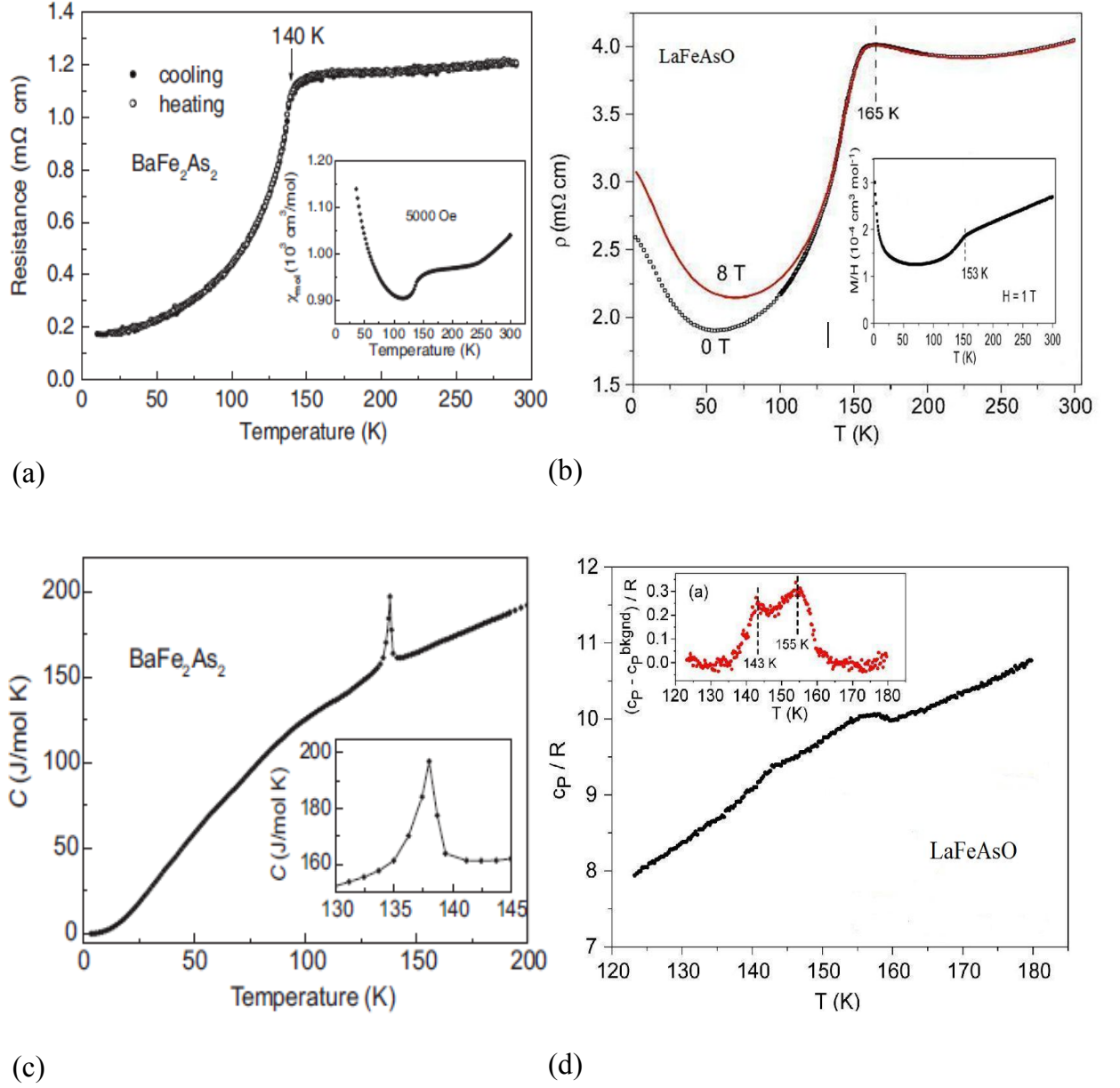


Figure 1.3  $\rho$  vs.  $T$  and  $\chi_{mol}$  vs.  $T$  (inset) for (a) Polycrystalline BaFe<sub>2</sub>As<sub>2</sub> [40] and (b) Polycrystalline LaFeAsO [42].  $C_p$  vs.  $T$  for (c) Polycrystalline BaFe<sub>2</sub>As<sub>2</sub> [40] and (d) Polycrystalline LaFeAsO [42].

phase transition. The refinement of the low temperature patterns shows the low temperature phase belongs to the orthorhombic  $Fmmm$  space group. The evolution of the lattice parameters with temperature from 180 to 100 K is shown in the right panel of Fig. 1.4 (a). The refined lattice constant data are shown and compared with LaFeAsO in Table 1.1.

$^{57}\text{Fe}$  Mössbauer spectroscopy investigation of  $\text{BaFe}_2\text{As}_2$  [40] with transmission integral fits at 298, 77, and 4.2 K is presented in Fig. 1.4 (b). At room temperature, a single signal is observed, indicating a paramagnetic state exists at this temperature. At 77 K, well below the anomaly temperature shown in Fig. 1.3 (a), a clear hyperfine field splitting at the iron nuclei is observed, which clearly shows the existence of the long range magnetic ordering. At 4.2 K, the magnetic moment was estimated to be  $0.4\mu_B / \text{Fe}$  for  $\text{BaFe}_2\text{As}_2$  whereas this number is  $0.25(5) \mu_B / \text{Fe}$  inferred from  $^{57}\text{Fe}$  Mössbauer spectra of LaFeAsO [44].

The detailed magnetic structure of  $\text{BaFe}_2\text{As}_2$  was later studied by neutron scattering [46]. It was found that the structural and magnetic phase transitions occur at the same temperature in  $\text{BaFe}_2\text{As}_2$ . This is different from LaFeAsO, in which the structural phase transition occurs around 160 K whereas the antiferromagnetic transition occurs around 145 K [42, 44, 45]. Fig.1.4 (c) shows the magnetic structure of  $\text{BaFe}_2\text{As}_2$ . The magnetic wavevector is (101), the same as the one in LaFeAsO. Fe magnetic moments are aligned antiferromagnetically along the  $a$  (longer in-plane axis) and  $c$ -axis, but ferromagnetically along the  $b$  axis (shorter in-plane axis). The ordered magnetic moment is  $0.87(3) \mu_B / \text{Fe}$  at 5 K whereas this number is  $0.36(5) \mu_B$  per Fe in LaFeAsO [45] (both values are substantially larger than those inferred from Mössbauer data).

Given the similarities in the structural and magnetic phase transitions among these two Fe arsenides and the fact that they can be tuned superconducting under doping, the systematic study of the doping effects on these compounds is vital to establish an understanding of this superconducting state. In this work, I focus on transition metal (TM) doped  $\text{BaFe}_2\text{As}_2$  single crystals, since they are the most homogeneous ones in Fe pnictides, can be easily reproduced and quantified [30, 33, 34, 36, 37, 39], and offer a wide range of doping. Seven series of

$\text{Ba}(\text{Fe}_{1-x}\text{TM}_x)_2\text{As}_2$  (TM=Co, Ni, Cu, Co / Cu mixture, Rh and Pd) were grown and studied. All the microscopic, structural, transport and thermodynamic measurements on these seven series allow us to provide the first indications of the interplay between the structural, magnetic and superconducting transitions and have led to an explosion of experimental and theoretical work [33, 34, 35, 47, 48, 49, 50, 51, 52, 53, 54, 55].

This thesis will be organized as following. In Chapter 3, details about the growth method and a brief review of the measurement techniques with the elemental analysis data of these series will be given. In Chapter 4, the structural, transport and thermodynamic properties of the parent compound  $\text{BaFe}_2\text{As}_2$  are summarized for single crystals grown from FeAs flux and Sn flux. In chapter 5, the  $\text{Ba}(\text{Fe}_{1-x}\text{Co}_x)_2\text{As}_2$  series is presented as the archetypical TM-doped series. The effects of Co doping in  $\text{BaFe}_2\text{As}_2$  compound are extracted from the transport and thermodynamic measurements, the upper critical field  $H_{c2}$  measurements up to 35 T are presented, and a detailed temperature-doping ( $T - x$ ) phase diagram is mapped out. In chapter 6, the transport and thermodynamic properties in  $\text{Ba}(\text{Fe}_{1-x}\text{Ni}_x)_2\text{As}_2$ ,  $\text{Ba}(\text{Fe}_{1-x}\text{Cu}_x)_2\text{As}_2$ ,  $\text{Ba}(\text{Fe}_{1-x-y}\text{Co}_x\text{Cu}_y)_2\text{As}_2$  ( $x \sim 0.022$ ) and  $\text{Ba}(\text{Fe}_{1-x-y}\text{Co}_x\text{Cu}_y)_2\text{As}_2$  ( $x \sim 0.047$ ) series as well as  $\text{Ba}(\text{Fe}_{1-x}\text{Rh}_x)_2\text{As}_2$  and  $\text{Ba}(\text{Fe}_{1-x}\text{Pd}_x)_2\text{As}_2$  series are presented. Detailed temperature-doping concentration ( $T - x$ ) and temperature-extra electrons ( $T - e$ ) phase diagrams are plotted out and compared. Chapter 7 is a summary of the work in this thesis and some of the conclusions drawn from it.

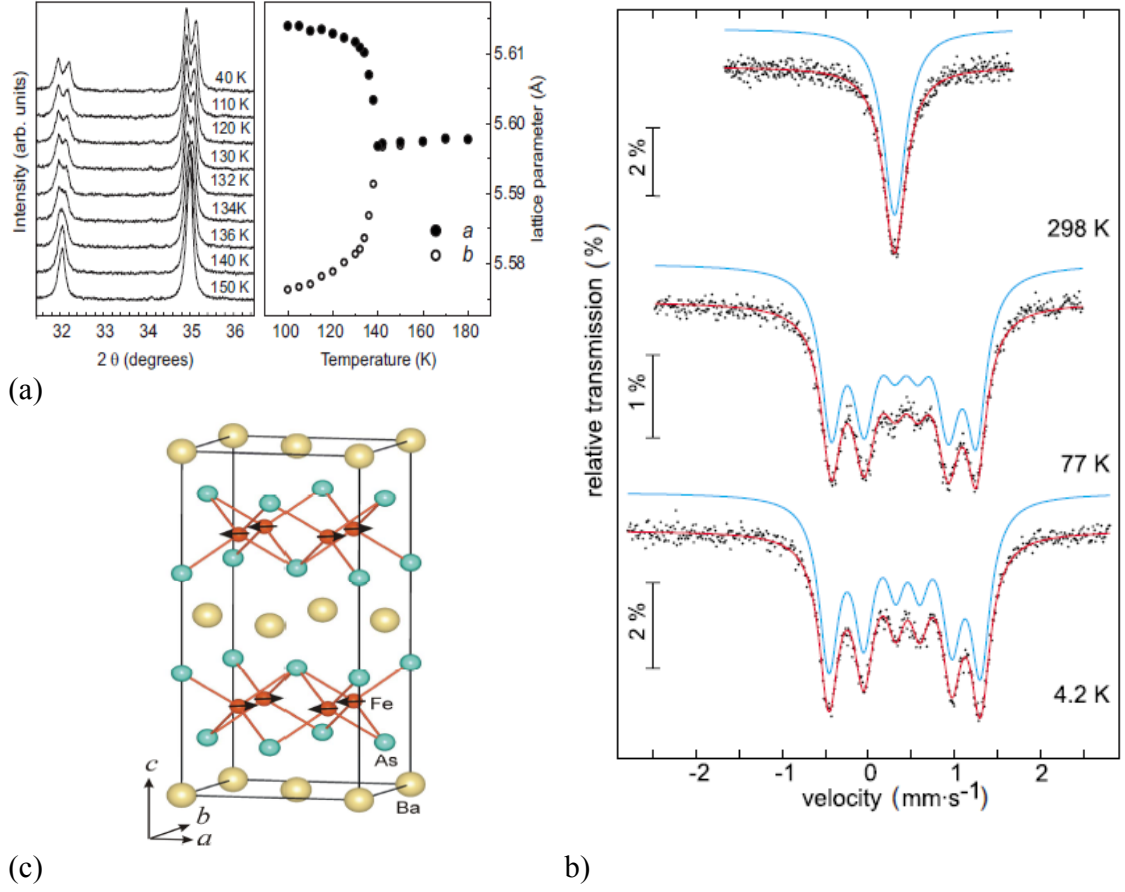


Figure 1.4 Polycrystalline  $\text{BaFe}_2\text{As}_2$ : (a) Left panel: powder X-ray diffraction patterns. Right panel: lattice parameters in tetragonal and orthorhombic phases. For clarity,  $a$  in the tetragonal phase are multiplied by  $\sqrt{2}$  [40]. (b)  $^{57}\text{Fe}$  Mössbauer spectra with transmission integral fits [40]. (c) Magnetic structure of  $\text{BaFe}_2\text{As}_2$  ( $a$  is the longer in-plane axis) [46].

## CHAPTER 2. Overview of superconductivity

The first theory satisfactorily providing a classical phenomenological description of superconductivity was London theory [56], proposed in 1935 shortly after the discovery of Meissner effect [57]. However, since superconductivity is a quantum phenomenon, the London theory only provided a good qualitative agreement with experiment rather than a quantitative one. The most successful phenomenological theory describing superconductivity is Ginzburg-Landau (GL) theory, proposed in 1950 [58], which was based on Landau's second-order phase transition theory and also took account of quantum effects. The wavefunction of superconducting electrons,  $\psi(\mathbf{r})$  was employed as the order parameter. It predicted the type II superconductor [59] and achieved good quantitative agreement in the vicinity of  $T_c$ . However, both London and GL theory only answered "how a superconductor behaves" rather than "what is superconductivity". This question was addressed by J. Bardeen, L. N. Cooper and J. R. Schriffer in 1957. Three papers [60, 61, 62], "Bound Electron Pairs in a Degenerate Fermi Gas", "Microscopic Theory of Superconductivity" and "Theory of Superconductivity", lead to the microscopic understanding of superconductivity. In the first paper, Cooper constructed a wave function and showed that two electrons in the vicinity of Fermi surface, under an arbitrarily small attractive interaction, can form a bound state. In the second paper, they dealt with the many body system represented by noninteracting electron pairs; they demonstrated that if a net attraction existed in an electron pair, no matter how weak it is, a condensed state of electron pairs ( $k, -k$ ) with antiparallel spins exists. By assuming the attractive interaction is mediated by phonons and simplifying the electron-phonon interaction as a constant, a proper energy gap between the ground state and the elementary excitation state can be naturally achieved, which had been proposed as being responsible for the superconductivity in 1955 [63]. In the third paper, de-

tailed calculations of the thermodynamic properties were presented which quantitatively agree with the experimental data. The bridge between the successful microscopic BCS theory and macroscopic GL theory was built by L. P. Gor'kov who found the quantitative relation between the order parameter and the superconducting gap [64]. Using the BCS theoretic frame work, a lot of theoretical work has been developed. A more realistic and sophisticated description of the electron-phonon interaction was later introduced and used by G. M. Eliashberg [65], and excellent agreement was achieved for a large number of superconductors [66].

The interplay between magnetism and superconductivity was also of interest. The theory for the superconducting alloys with nonmagnetic [67, 68] and magnetic impurities [69] was developed by A. A. Abrikosov, L. P. Gor'kov and P. W. Anderson. The upper critical field theory of the type II superconductors was systematically studied by N. R. Werthamer, at co-workers [70, 71, 72, 73, 74]. For the conventional superconductors, BCS theory works very well, however it was unable to interpret many properties in the high  $T_c$  superconductors assuming electron-phonon interaction as the pairing mechanism. Although other pairing mechanisms, such as spin fluctuations, polarons, etc. have been proposed to lead to the formation of Cooper pairs, the mechanism for the high superconducting temperature is still far from being answered.

In this chapter, I will give a brief introduction of superconductivity in both experimental and theoretical aspects. Basic experimental facts including the featured transport and magnetic behavior of superconductor will be discussed in section 2.1. Microscopic BCS theory, Eliashberg theory as well as the effect of nonmagnetic and magnetic impurities will be presented in section 2.2.

## 2.1 Zero resistivity and Meissner effect

Superconductors have two basic characteristics which are zero resistivity and flux exclusion, the Meissner effect. In 1911, H. Kamerlingh Onnes, in University of Leiden, found DC resistivity of mercury abruptly dropped to zero as temperature was cooled below 4.15 K [1]. This phenomenon was later named superconductivity. Above the transition temperature  $T_c$ , the superconductor has finite resistivity and is in its normal state; below the transition temper-

ature, the resistivity quickly decreases to zero and the superconductor is in its superconducting state. This transition is a second order phase transition.

In 1933, Meissner and Ochsenfeld discovered the other characteristic of superconductivity: the perfect diamagnetism [57]. Assume superconductors are only perfect conductors and the magnetic properties of the superconducting state are completely determined by their zero resistivity and obey Maxwell's equation. Two different sequences can be used to measure the magnetization below  $T_c$ : zero-field-cooled sequence (ZFC) and field-cooled sequence (FC). For ZFC sequence, the superconductor is cooled down below  $T_c$  in zero external magnetic field, then the magnetic field  $\mathbf{H}$  is switched on. According to the Maxwell's equation

$$\nabla \times (\mathbf{j}\rho) = -\frac{\partial \mathbf{B}}{c\partial t} \quad (2.1)$$

the zero resistivity below  $T_c$  leads to a constant  $\mathbf{B}$ . Since  $\mathbf{B}$  is zero before switching on the magnetic field,  $\mathbf{B}$  should be still zero in the field. For the FC sequence: the magnetic field  $\mathbf{H}$  is switched on above  $T_c$  at which the superconductor is in its normal state, since the resistivity is not zero in the normal state,  $\mathbf{B}$  inside the superconductor is not zero, then the superconductor is cooled down below  $T_c$ , the resulted  $\mathbf{B}$  will not change in the superconducting state due to eq. 2.1 and should be nonzero, as shown in Fig. 2.1 (a). However, this is not what Meissner and Ochsenfeld observed. Instead, they found  $\mathbf{B}$  is always zero no matter which sequence was employed, as shown in Fig. 2.1 (b). The perfect diamagnetism in the superconductor can not be explained by the zero resistivity and it is the intrinsic property of the superconductor.

Since  $\mathbf{B} = 4\pi\mathbf{M} + \mathbf{H}_0 = 0$  due to the Meissner effect, the work done by the external magnetic field can be written as

$$-\int_0^{H_0} \mathbf{M} d\mathbf{H} = \frac{1}{4\pi} \mathbf{H} d\mathbf{H}_0 = \frac{H^2}{8\pi} \quad (2.2)$$

Therefore, the Helmholtz free energy is

$$F_s(H) = F_s(0) + \frac{H^2}{8\pi} \quad (2.3)$$

where  $F_s(0)$  is the free energy of a superconductor in zero magnetic field. When

$$F_s(H_c) = F_n = F_s(0) + \frac{H_c^2}{8\pi} \quad (2.4)$$



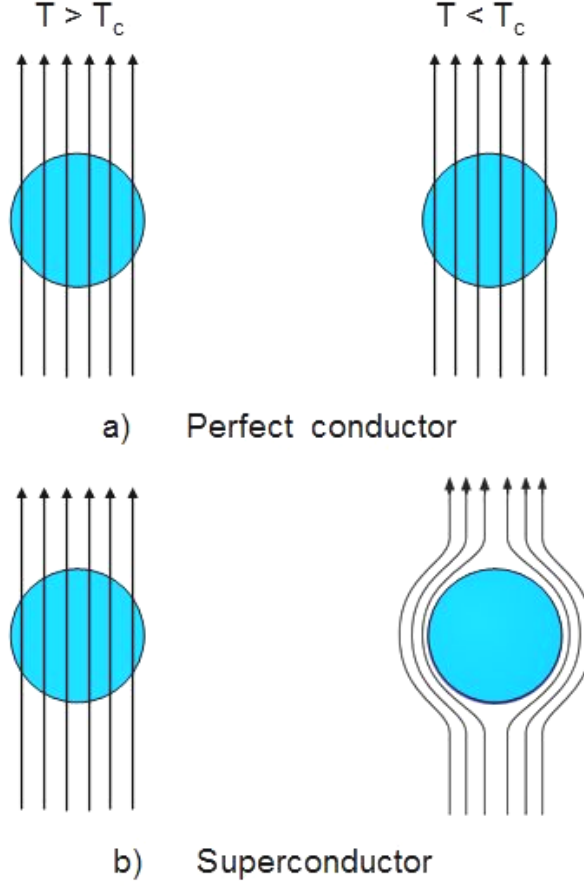


Figure 2.1 Schematic diagram of the magnetic induction  $\mathbf{B}$  in field-cooled sequence (a) Perfect conductor, (b) Superconductor.

the superconducting state can be destroyed by an external magnetic field, the field  $H_c$  is called thermodynamic critical field. The critical field will be discussed further below.

## 2.2 Ginzburg-Landau theory and type II superconductor

Ginzburg-Landau theory is the most successful macroscopic theory to describe superconductivity [58, 75, 76]. Without knowing the microscopic mechanism, Ginzburg and Landau amazingly predicted the behavior of superconductors based on excellent physics intuition. Three assumptions were made. First, Landau's second-order phase transition theory is applicable for superconductors since the phase transition from superconducting state to normal

state is a second-order one when the external magnetic field is zero. Second, quantum mechanics should be reasonably combined into Landau's theory since superconductivity is a quantum phenomenon rather than a classical one. It assumed all superconducting electrons behaved coherently and superconducting electrons could be described by a single phased wavefunction  $\psi(\mathbf{r}) = |\psi(\mathbf{r})|e^{i\phi}$ . Third,  $\psi(\mathbf{r})$  can be used as the order parameter.

For an inhomogeneous superconductor in a magnetic field, the Gibbs free energy can be written as :

$$G_s(H) = G_n + \int \left( \frac{\hbar^2}{2m^*} |\nabla\psi - i\frac{e^*}{\hbar c} \mathbf{A}\psi|^2 + a|\psi|^2 + \frac{b}{2}|\psi|^4 + \frac{B^2}{8\pi} - \frac{\mathbf{B} \cdot \mathbf{H}}{4\pi} \right) dV \quad (2.5)$$

where  $\mathbf{A}$  is the magnetic vector potential, the magnetic induction  $\mathbf{B} = \nabla \times \mathbf{A}$ ,  $H$  is the external magnetic field,  $\frac{B^2}{8\pi}$  is the magnetic energy,  $\psi(\mathbf{r}) = |\psi(\mathbf{r})|e^{i\phi}$  is the order parameter which can be normalized so that  $|\psi(\mathbf{r})|^2$  is equal to the superfluid density,  $|\psi(\mathbf{r})|^2 = n_s^*$ . Over a small range near  $T_c$ ,

$$a(T) \approx a_0(T/T_c - 1), b(T) \approx b_0 \quad (2.6)$$

By minimizing the Gibbs free energy by  $\partial G_s / \partial \psi = 0$  and  $\partial G_s / \partial \mathbf{A} = \mathbf{0}$ , two coupled Ginzburg-Landau equations can be obtained. These two equations together with eq. 2.5 set up the basis of GL theory.

### 2.2.1 Coherence length and penetration depth

Two characteristic lengths for superconductors can be defined qualitatively. One is  $\xi$  named as coherence length over which the order parameter  $\psi$  varies significantly and we will see later that the coherence length is the size of the Cooper pair in the microscopic theory.

$$\xi = \sqrt{\frac{\hbar^2}{2m^*|a|}} \quad (2.7)$$

The other one is penetration depth,  $\lambda$ , over which the magnetic field can penetrate into the surface appreciably,

$$\lambda = \sqrt{\frac{m^*c^2b}{4\pi e^{*2}|a|}} \quad (2.8)$$

It can be seen that the superfluid density  $n_s^* \propto \lambda^{-2}$ .

### 2.2.2 Type II superconductor

For  $\lambda \gg \xi$ , the magnetic field penetrates into the superconductor much larger than the variation range of the order parameter, therefore, the order parameter is significantly affected by the magnetic field. A mixture of superconducting and normal states can exist under this condition.

Assuming there is a mixture of superconducting and normal domains in the external field  $H$ , the sign of the interface energy  $\sigma_{ns}$  is determined by the Ginzburg-Landau parameter  $\kappa \equiv \frac{\lambda}{\xi}$ ,

$$\kappa < \frac{1}{\sqrt{2}} \implies \sigma_{ns} > 0 \quad \text{type I superconductor} \quad (2.9)$$

$$\kappa > \frac{1}{\sqrt{2}} \implies \sigma_{ns} < 0 \quad \text{type II superconductor} \quad (2.10)$$

If  $\sigma_{ns}$  is larger than zero, the formation of the interface is not energy favorable, the superconducting phase and the normal state will only exist at  $H < H_c$  or  $H > H_c$  respectively. This type of superconductor is called type I superconductor. Most element superconductors are type I superconductor, for many the coherence length  $\xi_0$  is about  $10^{-4}cm$  which is almost 100 times larger than the penetration depth. If  $\sigma_{ns} < 0$ , the formation of the interface becomes energetically favorable under certain circumstances. These type of superconductors are type II superconductors. When  $H < H_{c1}$ , the average field  $B$  inside the specimen is zero which shows the pure Meissner effect. When  $H_{c1} < H < H_{c2}$ , the magnetic field penetrates inside the specimen, the superconductor is divided into normal and superconducting domains which are parallel to the external field. The normal domains are vortices, each with radius of the order  $\xi$ . The density of the vortices increases with increasing external field until  $H_{c2}$ , at which the distance between two vortices is about  $\xi$  and the specimen changes to the normal state. High  $T_c$  cuprates are type II superconductors with  $\xi_0$  around  $10^{-7}cm$  and  $\lambda_0$  around  $10^{-5}cm$ .

In a tetragonal type II superconductor,

$$H_{c1}^{\perp c} = \frac{\Phi_0}{4\pi\lambda_{ab}\lambda_c}(\ln \kappa_{ab} + 0.08) \quad H_{c2}^{\perp c} = \frac{\Phi_0}{2\pi\xi_{ab}\xi_c} \quad (2.11)$$

$$H_{c1}^{\parallel c} = \frac{\Phi_0}{4\pi\lambda_{ab}^2}(\ln \kappa_c + 0.08) \quad H_{c2}^{\parallel c} = \frac{\Phi_0}{2\pi\xi_{ab}^2} \quad (2.12)$$

where  $\Phi_0$  is the elementary flux quantum,  $2.07 \times 10^{-7} \text{Oecm}^2$ . The anisotropic  $H_{c2}$  parameter defined as  $H_{c2}^{\perp c}/H_{c2}^{\parallel c}$ , is equal to  $\xi_{ab}/\xi_c$ . In many cases, the lower critical field,  $H_{c1}$ , is a small field, on the order of a  $mT$  while the upper critical field,  $H_{c2}$ , can be as high as several tens of T. The coherence length is usually estimated from this equation with the data from upper critical field measurements.

## 2.3 BCS theory

In 1950, two groups independently found that different isotopes of mercury have different  $T_c$  [77, 78] which were later found to obey the relation  $T_c M^\beta = \text{constant}$ , where  $M$  is the mass of the isotope. Inspired by this isotope effect, Bardeen, Cooper and Schrieffer (BCS) assumed an electron-phonon interaction as the pairing mechanism. Although other pairing mechanisms, like spin fluctuation, etc, were hypothesized for nonconventional superconductors, the idea of the formation of Cooper pairs, the key ingredient of superconductivity remains the same. Eliashberg theory [65] is an extension of BCS theory. In BCS theory, to simplify the calculation, a lot of assumptions were made, such as constant electron-phonon interaction, Fermi sphere assumption, etc, on the other hand, Eliashberg theory considered a more realistic situation and took care of electron-phonon spectral function, band structure, etc. I will briefly review BCS theory and list the important outcomes from this theory [75, 76]. Then I will list the important results from Eliashberg theory.

### 2.3.1 Superconducting state

In 1950, Frolich [79] demonstrated that electrons can indirectly interact with each other in a crystal by emitting and absorbing phonons. Electron 1 with wave vector  $k_1$  emits a phonon and goes to state  $k'_1$ , electron 2 with wave vector  $k_2$  absorbs this phonon and goes to state  $k'_2$ . This process can be understood as  $(k_1, k_2)$  state is scattered to  $(k'_1, k'_2)$  state by phonon. By this interaction, electrons within a thin shell of  $\hbar\omega_D$  in the vicinity of the Fermi surface are attractive to each other.

In 1956, Cooper considered two electrons which are attractive to each other above the

Fermi surface, he solved the two body Schrödinger equation and calculate the binding energy of these two electrons. He found the binding energy is always negative and a bound pair with negative potential can always be formed no matter how small the interaction is [60].

Combining the two facts above, Bardeen, Cooper and Schrieffer developed the microscopic theory of superconductivity. In a crystal, electron pairs in the  $\hbar\omega_D$  shell near Fermi surface are formed due to the electron-phonon interaction and scattered from below the Fermi surface to above the Fermi surface, the potential energy is lowered while the kinetic energy is increased in this process. If the decrease of potential energy is larger than the increase of the kinetic energy, the ground state of the system is no longer the one for the normal state that all the electrons occupy the states inside the Fermi surface, as shown in Fig. 2.2 (a), but rather the one in

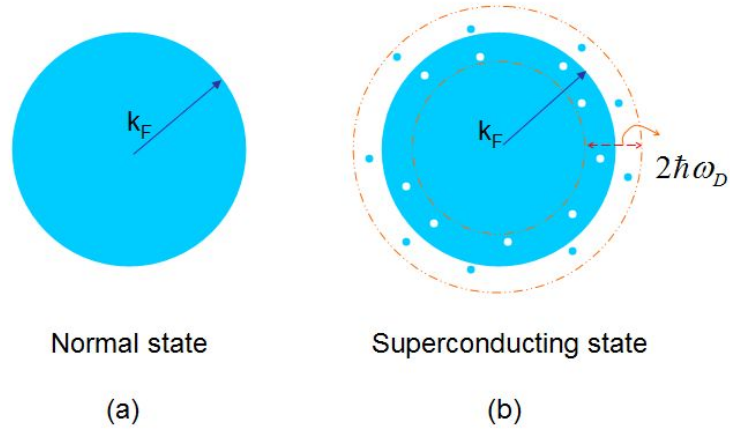


Figure 2.2 Schematic diagram of Fermi surface at (a) Normal ground state, (b) Superconducting state.

which some states above Fermi surface were occupied and some states below Fermi surface were empty, as shown in Fig. 2.2 (b). To form as many pairs as possible, so that the lowest energy can be achieved, the two electrons in one pair will be favored with opposite momentum, which mean  $k_1 = -k_2 = k$ , and if we also consider the electron spins, antiparallel configuration often lowers the energy even more. The electron pair with momentum  $(k, -k)$  and antiparallel spin is called Cooper pair. Due to the Pauli exclusion principle, the wavefunction of the pair state should be antisymmetrical under the particle exchange. If the spin of these two electrons form a spin singlet state ( $S=0$ ), the spacial wavefunction should be with one even parity, which

means the angular momentum should be  $L=0, 2, 4, \dots$ , etc. If the spins form a spin triplet state ( $S=1$ ), the spacial wavefunction should have odd parity and the angular momentum should be  $L=1, 3, \dots$ , etc. In very rare situations, such as ferromagnetic superconductor  $\text{Sr}_2\text{RuO}_4$  [80], Cooper pairs are thought to be formed with parallel spins.

In BCS theory, to simplify the calculation, several assumptions are made. First, the Fermi surface is assumed to be a sphere. Second, the pair state is assumed to be with  $L=0$  and  $S=0$ . Third, the electron-phonon interaction,  $V_{kk'}$ , is simplified as a constant:

$$V_{kk'} = \begin{cases} -V & \text{if } |\varepsilon_k| \leq \hbar\omega_D, |\varepsilon_{k'}| \leq \hbar\omega_D \\ 0 & \text{if } |\varepsilon_k| > \hbar\omega_D, |\varepsilon_{k'}| > \hbar\omega_D \end{cases} \quad (2.13)$$

where  $\varepsilon_k$  is the relative kinetic energy of the electron defined as

$$\varepsilon_k = \frac{\hbar^2 k^2}{2m} - \frac{\hbar^2 k_f^2}{2m} \quad (2.14)$$

Assuming  $\nu_k^2$  is the probability that pair state  $(k, -k)$  is occupied, the energy can be written as

$$E_s = \sum 2\varepsilon_k \nu_k^2 + \sum V_{kk'} \nu_{k'} \mu_k \nu_k \mu_{k'} \quad (2.15)$$

Since the system will not be in equilibrium until the Gibbs free energy  $G_s$  is minimum, by setting  $\partial G_s / \partial \nu_k^2 = 0$ ,  $\nu_k^2$  can be obtained as:

$$\nu_k^2 = \frac{1}{2} (1 - \varepsilon_k / E_k) \quad (2.16)$$

where  $E_k = \sqrt{\varepsilon_k^2 + \Delta_0^2}$

Fig.2.3 (a) plots the momentum dependent  $\nu_k^2$ . It quantitatively shows that the Fermi surface becomes "smeared out" in the superconducting state.

### 2.3.2 Excitation spectrum, gap function and gap symmetry

The elementary excitation energy can be expressed as

$$E_k = \sqrt{\varepsilon_k^2 + \Delta^2} \quad (2.17)$$

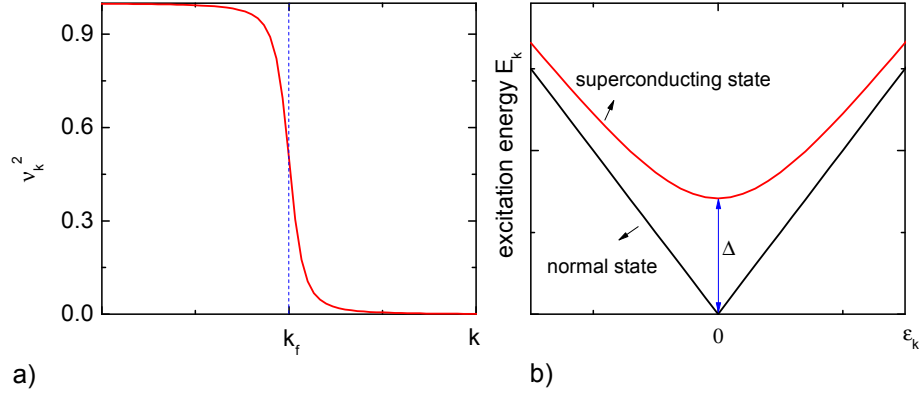


Figure 2.3 (a) Momentum dependent occupation probability  $\nu_k^2$ . (b) Quasiparticle excitation spectrum.

Where  $\Delta$  has the physics meaning as "energy gap" since the excitation energy are not constant as in the normal metal, but have the smallest value as  $\Delta$ , as shown in Fig.2.3 (b). To break one Cooper pair, at least  $2\Delta$  energy is needed. As temperature increases, more and more pairs break and the gap becomes smaller and smaller. At the critical temperature  $T_c$ , the gap decreases to zero. An implicit expression of this gap can be obtained,

$$1 = VD(0) \int_0^{\varepsilon_0} \frac{\tanh \sqrt{\varepsilon_k^2 + \Delta^2}/2k_B T_c}{\sqrt{\varepsilon_k^2 + \Delta^2}} d\varepsilon \quad (2.18)$$

In most simple cases,  $\varepsilon_0 \gg k_B T_c$ .  $\Delta(T)$  is plotted in Fig. 2.4 and compared with experimental data of Nb, Sn and Ta [81]. A good agreement is achieved.

The features of  $\Delta(T)$  are summarized below:

(1) At  $T = 0K$ ,

$$\Delta(0) = \frac{\hbar\omega_D}{\sinh(\frac{1}{D(E_f)V})} \quad (2.19)$$

in the weak coupling limit,  $D(E_f)V \ll 1$ ,  $k_B T_c \ll \hbar\omega_D$

$$\Delta(0) \approx 2\hbar\omega_D \exp(-\frac{1}{D(E_f)V}) \quad (2.20)$$

in the strong coupling limit,

$$\Delta(0) \approx \hbar\omega_D D(E_f)V \quad (2.21)$$

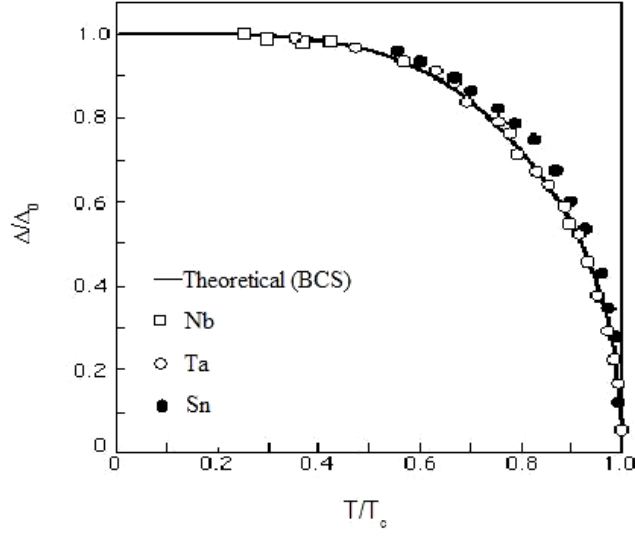


Figure 2.4 Solid line: the evolution of the gap function with temperature. Hollow square: experiment data of Nb. Hollow circle: experiment data of Ta. Solid circle: experiment data of Sn [81].

(2) Near  $T_c$ , in the weak coupling limit,

$$\Delta(T) \approx 3.06T_c(1 - T/T_c)^{1/2} \quad (2.22)$$

(3) At low temperature, in weak coupling limit,  $k_B T \ll \Delta(0)$ ,  $\Delta(T)$  acts like

$$\Delta(T) \approx \Delta(0)[1 - \sqrt{2\pi k_B T / \Delta_0} \exp(-\Delta_0 / k_B T)] \quad (2.23)$$

The superconducting gap is a very important quantity in superconductors not only because it determines the thermodynamic properties of superconductor, which we will discuss in the next section, but also because it is closely related to the Cooper pair state and superconducting order parameter. It was proved [64] that the order parameter  $\psi(\mathbf{r})$  in Ginzburg-Landau theory is actually the pair wavefunction in microscopic theory and is proportional to the superconducting energy gap. Therefore, by measuring the superconducting gap, information about the pairing symmetry, which is critical in determine the pairing mechanism, can be provided. Fig. 2.5 shows the schematic representation of  $\Delta$  in  $k$  space. Fig. 2.5 (a) shows the isotropic  $s$ -wave superconducting gap with  $L = 0$  and  $S = 0$ , the superconductor is fully gapped, which is the



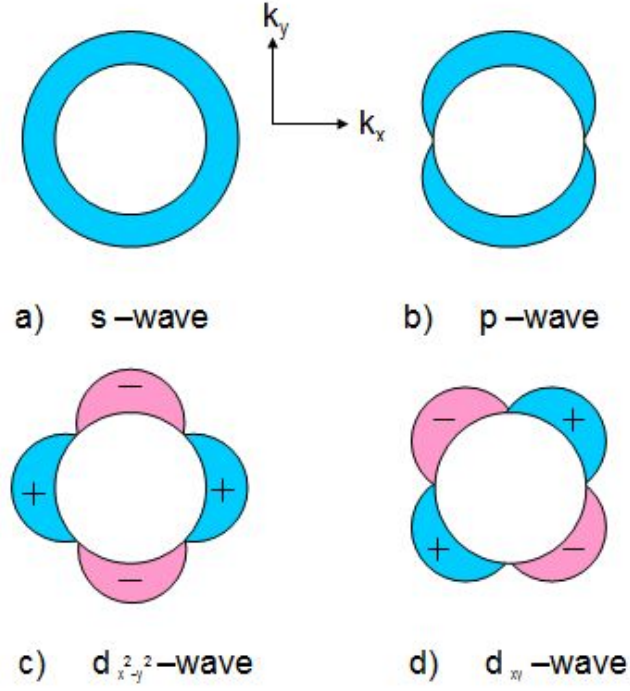


Figure 2.5 Superconducting gap with different gap in  $k$  space.

situation discussed in the original BCS theory. For the so called  $s_{\pm}$ -wave pairing symmetry, which was proposed to be favored in FeAs based superconductors, the superconductor is fully gapped on both the electron and the hole Fermi sheets but with opposite signs between them [82, 83, 84, 85, 86] Fig. 2.5 (b) shows the anisotropic  $p$ -wave gap with  $L = 1$  and  $S = 1$ . Fig. 2.5 (c) and (d) show the anisotropic  $d$ -wave gap with  $L = 2$  and  $S = 0$ . For different gap symmetry, the angular dependent superconducting gap,  $\Delta(\mathbf{k})$ , can be written as [87]

$$g(\mathbf{k}) = \begin{cases} 1 & \text{isotropic } s - \text{wave} \\ \cos(2\varphi) & d_{x^2-y^2} - \text{wave} \\ \sin(2\varphi) & d_{xy} - \text{wave} \end{cases} \quad (2.24)$$

The gap anisotropy is defined as

$$\Omega \equiv 1 - \frac{\langle \Delta(\mathbf{k}) \rangle^2}{\langle \Delta(\mathbf{k})^2 \rangle} \quad (2.25)$$

which is 0 for isotropic  $s$ -wave superconductors and 1 for  $d$ -wave superconductors.

### 2.3.3 Thermodynamic properties

(1) The ratio of  $2\Delta(0)/k_B T_c$ , in the weak coupling limit, is

$$k_B T_c \approx 1.14 \hbar \omega_D \exp\left(-\frac{1}{D(E_f)V}\right), \quad \frac{2\Delta(0)}{k_B T_c} = 3.53 \quad . \quad (2.26)$$

In the strong coupling limit, it is

$$k_B T_c \approx \hbar \omega_D D(E_f)V/2, \quad \frac{2\Delta(0)}{k_B T_c} = 4 \quad . \quad (2.27)$$

(2) In the weak coupling limit, the specific heat jump can be expressed as the universal relation,

$$\frac{C_s - C_n}{\gamma T}|_{T_c} = 1.43 \quad (2.28)$$

where  $\gamma = \frac{2}{3}\pi^2 k_B^2 D(E_f)$ ,

(3) In the weak coupling limit, the thermodynamic critical field can be expressed as

$$H_c(0) = -0.55 T_c \frac{dH_c}{dT}|_{T_c} \quad (2.29)$$

where  $(\frac{dH_c}{dT})|_{T_c} = 4.4\sqrt{\gamma}$

(4) In the weak coupling limit, at very low temperature,

$$C \propto \frac{\Delta(0)^{2.5}}{T^{1.5}} \exp\left(-\frac{\Delta(0)}{k_B T}\right) \quad (2.30)$$

## 2.4 Eliashberg theory: the extension of BCS theory

Eliashberg theory can be considered as an extension of BCS theory [65, 88]. Since Eliashberg theory employed a lot of mathematical techniques beyond the scope of this thesis, I will just summarize the main improvements in Eliashberg theory comparing to BCS theory.

### 2.4.1 Electron-phonon spectrum and pseudopotential

In BCS theory, the electron-phonon interaction is taken as a constant  $-V$ , as we showed in the last section. In Eliashberg theory, the electron-phonon mass enhancement factor,  $\lambda$ , which is equal to  $D(E_f)V$  in BCS theory can be expressed as

$$\lambda \equiv 2 \int_0^\infty \frac{\alpha^2 F(\nu)}{\nu} d\nu \quad (2.31)$$

where  $\alpha^2 F(\nu)$  is the electron-phonon spectral function (Eliashberg function). It is defined as

$$\alpha^2 F(\varepsilon, \varepsilon', \nu) = \sum_{kk'} \frac{\alpha_{kk'}^2 F(\nu) \delta(\varepsilon - \varepsilon_k) \delta(\varepsilon - \varepsilon'_k)}{D(\varepsilon) D(\varepsilon')} \quad (2.32)$$

where  $\alpha$  is the electron-phonon coupling strength,  $F(\nu)$  is the phonon density of states,  $\alpha_{kk'}^2 F(\nu)$  is related to the phonon spectral function, which can be calculated from the band structure calculation or obtained from fitting to the phonon dispersion curves from the inelastic neutron scattering.

Therefore, in Eliashberg theory, information about the band structure and the phonon spectrum of a specific compound is included.

The cut off frequency is no longer  $\omega_D$ , but the characteristic phonon frequency,

$$\omega_{ln} \equiv \exp\left[\frac{2}{\lambda} \int_0^\infty \ln \nu \frac{\alpha^2 F(\nu)}{\nu} d\nu\right] \quad (2.33)$$

which contains the detailed information of  $\alpha^2 F(\nu)$ .

The electron-electron Coulomb interaction is also taken care of. A phenomenological Coulomb pseudopotential  $\mu^*$  is introduced to describe this effect.

Practically, the determination of the electron-phonon spectral function is an iterative process between experiment and theory. First, the electron-phonon spectrum is calculated and the Coulomb pseudopotential is guessed, then corrections are made with an iterated fitting process between theoretical calculation and experimentally measured functions [88, 89]. The corrected electron-phonon spectrum  $\alpha^2 F(\nu)$  and Coulomb pseudopotential  $\mu^*$  are then used in the Eliashberg equations to calculate  $T_c$ , the superconducting density of state, gap, etc. Good agreements are generally achieved. More discussion about this procedure can be found in reference [88].

#### 2.4.2 Thermodynamic properties

Although there is still no analytic solution for the Eliashberg theory, numerical ones are available.

In the BCS limit in which the electron-phonon mass enhancement factor  $\lambda$  is assumed to be a constant in the vicinity of the Fermi surface, the transition temperature can be written as the McMillan equation [88, 90],

$$k_B T_c = \frac{\hbar \omega_{ln}}{1.2} \exp \left[ -\frac{1.04(1 + \lambda)}{\lambda - \mu^*(1 + 0.62\lambda)} \right] \quad (2.34)$$

The isotope effect in the BCS limit can be presented as [88]

$$T_c = A M^\beta \quad (2.35)$$

$$\beta = \frac{1}{2} \left( 1 - \frac{1.04(1 + \lambda)(1 + 0.62\lambda)}{[\lambda - \mu^*(1 + 0.62\lambda)]^2} \mu^{*2} \right) \quad (2.36)$$

whereas in BCS theory  $\beta$  is equal to 0.5. The isotope effect can be used to check if the pairing mechanism is electron-phonon interaction. Combining eq. 2.34 with 2.36, one can actually get a qualitative estimation of  $\lambda$  and  $\mu^*$  for that superconductor, if they are unrealistic numbers, electron-phonon interaction mechanism should be excluded. The isotope effect has been studied in a lot of systems, such as MgB<sub>2</sub> and cuprates [91, 92]. It demonstrated that phonon mechanism is responsible for the superconductivity in MgB<sub>2</sub>, but not in cuprates.

Accurate numerical solutions of Eliashberg equations for a lot of superconductors based on the experimental information of electron-phonon spectral function from tunnelling data have been obtained [93]. The difference between the calculated  $2\Delta_0$  and experimental  $2\Delta_0$  is within several percentages. The resulting ratios of  $2\Delta_0/k_B T_c$  are summarized in Fig. 2.6 (a) as the "dot" symbols. An empirical function of  $2\Delta_0/k_B T_c$  could be obtained by fitting the numerical data, which is expressed as [93]

$$\frac{2\Delta(0)}{k_B T_c} = 3.53 \left[ 1 + a \left( \frac{T_c}{\omega_{ln}} \right)^2 \ln \left( \frac{\omega_{ln}}{b T_c} \right) \right] \quad (2.37)$$

where  $a$  and  $b$  are the fitting parameters with the converged values of 12.5 and 2 respectively. This empirical equation was plotted in Fig. 2.6 (a) as the solid line. It follows the numerical data very well.

Similar procedure was made for the ratio of  $\Delta C(T_c)/\gamma T_c$  [94], where  $\gamma$  is the Sommerfield ratio. The empirical function of this ratio can be expressed as

$$\frac{\Delta C(T_c)}{\gamma T_c} = 1.43 \left[ 1 + a \left( \frac{T_c}{\omega_{ln}} \right)^2 \ln \left( \frac{\omega_{ln}}{b T_c} \right) \right] \quad (2.38)$$

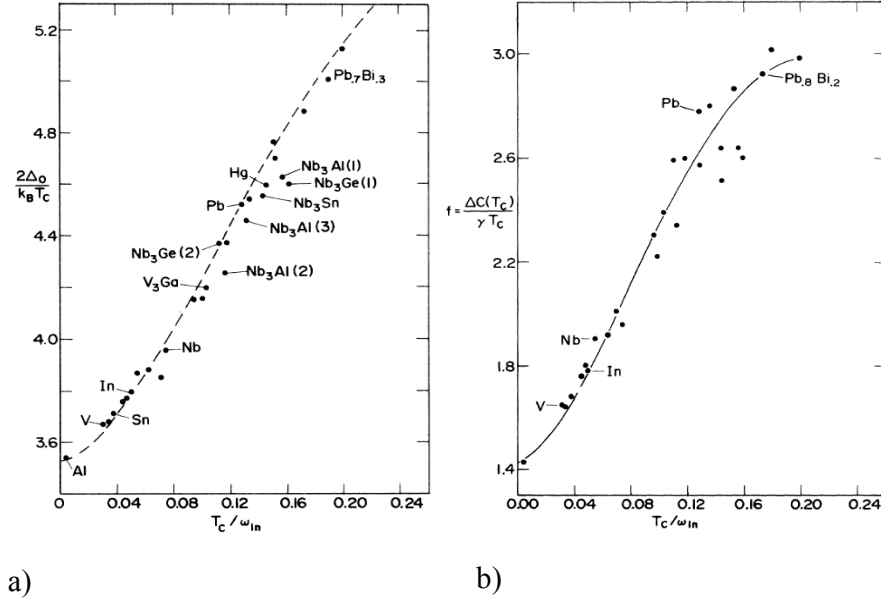


Figure 2.6 (a) The  $T_c/\omega_{ln}$  dependent  $2\Delta(0)/k_B T_c$ . The solid dots are the theoretical results from the full numerical Eliashberg calculation, which agrees with the experiment data within 10%. (b) The  $T_c/\omega_{ln}$  dependent  $\Delta C(T_c)/\gamma T_c$ . The solid dots are theoretical results from the full numerical Eliashberg calculation, which agrees with the experiment data within 10% [66].

The fitting between the numerical results and this equation led to  $a = 53$  and  $b = 3$ . The numerical data and the curve are presented in Fig. 2.6 (b).

## 2.5 Impurity effects on the superconducting temperature

The Hamiltonian of the interaction between the impurities and conduction electrons can be written as three terms [69, 95, 96]:

$$H_{int} = \sum_a \int U_0(\mathbf{r} - \mathbf{r}_a) + U_{so}(\mathbf{r} - \mathbf{r}_a) + U_{ex}(\mathbf{r} - \mathbf{r}_a) \psi^\dagger(\mathbf{r}) \psi(\mathbf{r}) d^3\mathbf{r} \quad (2.39)$$

where  $\mathbf{r}_a$  is the position of the impurity atom and the summation runs over all the impurities.

$U_0$  is the interaction energy of an electron and impurity without considering the effects of the impurity spin. For nonmagnetic impurities, only this term will exist.

$U_{so}$  is the spin-orbit interactions between the vector potential associated with the spin of the

impurities and the momentum of the conduction electrons, this term is a time-reversal invariant energy contribution. It does not change the self-consistent equation of the superconducting transition temperature and gap function, therefore it does not affect the superconducting temperature and thermodynamic properties. Spin-orbit interaction only leads to the substitution from  $\frac{1}{\tau}$  to  $\frac{1}{\tau} + \frac{1}{\tau_{so}}$  and affects the magnetic properties.

$U_{ex}$  is the exchange energy between the total angular momentum of the impurity and the spin of the conduction electrons. It is this term which breaks the time-reversal invariance and gives non-trivial contributions to the superconducting temperature and thermodynamic properties in superconducting alloys. For transition metal impurities, the orbital angular momentum is quenched, the exchange interaction can be written as

$$U_{ex} = -2I\mathbf{S} \cdot \sigma \quad (2.40)$$

where  $I$  is the coupling between the spin of impurity atoms and the spin of conduction electrons giving rise to the superconductivity,  $\mathbf{S}$  is the spin of impurity atoms and  $\sigma$  is the spin of conduction electrons. For rare earth element impurities, since the total angular momentum is  $\mathbf{J} = \mathbf{L} + \mathbf{S}$ , the exchange interaction is

$$U_{ex} = -2I(g_J - 1)\mathbf{J} \cdot \sigma \quad (2.41)$$

$U_{so}$  and  $U_{ex}$  are related to the contributions from the impurity spin and will be present in the magnetic impurity case.

The discussion in the rest of this section is based on the assumption that the impurity scattering is not momentum dependent (isotropic scattering).

### 2.5.1 Nonmagnetic impurities

The presence of isoelectronic, nonmagnetic, impurities will suppress  $T_c$  according to [97, 98, 99, 100, 101]:

$$\ln \frac{T_{c0}}{T_c} = \Omega \left[ \varphi\left(\frac{1}{2} + \frac{\mu}{2}\right) - \varphi\left(\frac{1}{2}\right) \right] \quad (2.42)$$

where  $\varphi(x)$  is the digamma function,  $\mu = \hbar/2\pi k_B T_c \tau$  and  $\Omega$  is the gap anisotropy which is defined in eq. 2.25.

As we can see from eq. 2.42, for isotropic  $s$ -wave superconductors, since  $\Omega=0$ , the introduction of isoelectronic nonmagnetic impurities does not change the gap size and thus does not change the transition temperature or thermodynamic properties. This result is named as "Anderson's theorem" [68]. However, since in BCS theory (section 2.3.2), we know  $T_c$  is also related to the Debye frequency and density of states according to  $k_B T_c \approx 1.14 \hbar \omega_D \exp(-\frac{1}{D(E_f)V})$ , the change of density of states due to the non-isoelectronic impurities and the change in Debye frequency can also lead to changes in  $T_c$  in an isotropic  $s$ -wave superconductor. For anisotropic superconductors, since  $\Omega \neq 0$ ,  $T_c$  can be suppressed by the nonmagnetic impurities.

At low concentrations when  $\mu \ll 1$ ,

$$\frac{T_c}{T_{c0}} = 1 - \Omega \frac{\pi \hbar}{8 k_B \tau} \quad (2.43)$$

As we can see, the suppression of  $T_c$  is linearly proportional to the impurity concentration.

At high concentration when  $\mu \gg 1$ ,

$$\frac{T_c}{T_{c0}} = [\Delta(0) \frac{k_B \tau}{\hbar}]^{\frac{\Omega}{1-\Omega}} \quad (2.44)$$

As we can see,  $T_c$  will not be suppressed to zero unless  $\Omega=1$  ( $d$ -wave).

Fig. 2.7 shows the experiment data of the  $T_c$  suppression due to the nonmagnetic impurities for some  $s$ -wave and non- $s$ -wave superconductors. As we can see from Fig. 2.7 (a), the suppression of  $T_c$  due to the non-magnetic impurities Cd, in  $s$ -wave superconductor, In [102, 103], is much slower than the suppression of  $T_c$  of non- $s$ -wave superconductors, such as heavy fermion superconductor CeCoIn<sub>5</sub> [101] and high  $T_c$  cuprates YBCO and LSCO [104], which agrees with eq. 2.42. From Fig. 2.7 (b), it can be clearly seen the suppression of  $T_c$  caused by nonmagnetic impurities, Cd, in the low concentration range ( $T_c \ll T_{c0}$ ) for  $s$ -wave superconductor, In, is linearly proportional to the impurity concentration, which is consistent with eq. 2.43.

In Fig. 2.7 (a),  $T_c/T_{c0}$  with respect to the impurity concentration for two series of doped LuNi<sub>2</sub>B<sub>2</sub>C (a nonmagnetic superconductor with  $T_c$  of 16 K [105]), were also presented. The first series is (Lu<sub>1-x</sub>Y<sub>x</sub>)Ni<sub>2</sub>B<sub>2</sub>C, where Lu atoms are substituted by the isoelectronic Y atoms; the second series is Lu(Ni<sub>1-x</sub>Co<sub>x</sub>)<sub>2</sub>B<sub>2</sub>C, where the nonmagnetic Ni atoms are substituted by

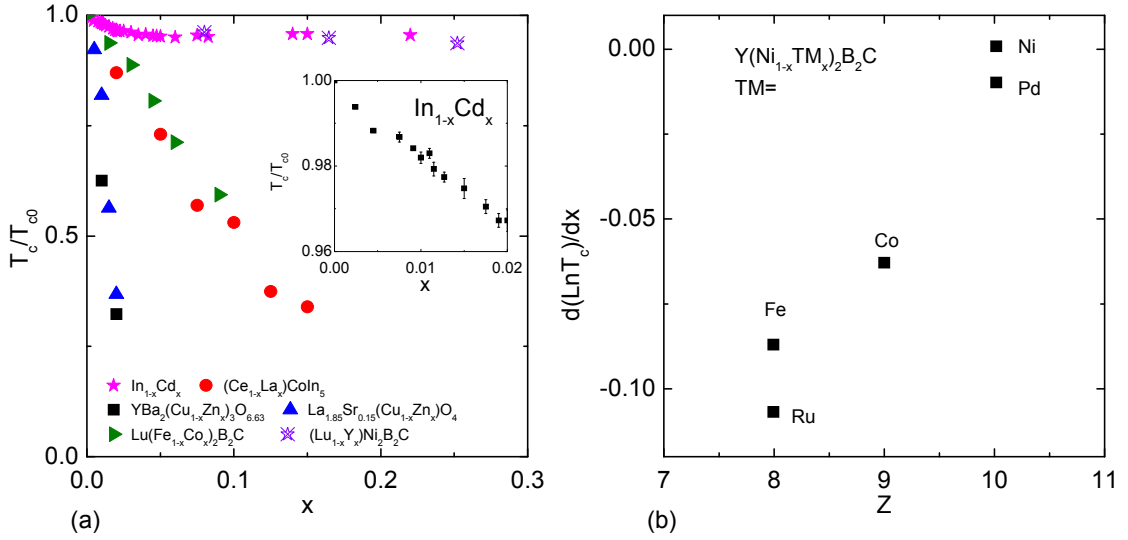


Figure 2.7 (a)  $T_c/T_{c0}$  vs. nonmagnetic impurity concentration for  $s$ -wave superconductor, In [102, 103] and  $\text{LuNi}_2\text{B}_2\text{C}$  [105]; non- $s$ -wave superconductor  $\text{CeCoIn}_5$  [101], YBCO [104] and LSCO [104]. Inset: Enlarged  $T_c/T_{c0}$  vs. nonmagnetic impurity concentration for  $s$ -wave superconductor, In [102, 103]. (b) Relative change of  $T_c$  with dopant concentration vs. number of valence electrons of  $\text{Y}(\text{Ni}_{1-x}\text{TM}_x)_2\text{B}_2\text{C}$  [108].

nonmagnetic Co atoms. For  $(\text{Lu}_{1-x}\text{Y}_x)\text{Ni}_2\text{B}_2\text{C}$  series, with rigid-band approximation,  $D(E_f)$  is invariant with doping and does not contribute to the variation of  $T_c$ . In this series, the suppression of  $T_c$  mainly comes from the scattering effect and the fact that the small  $T_c$  suppression is comparable to the one in  $\text{In}_{1-x}\text{Cd}_x$  is consistent with the  $s$ -wave gap symmetry of  $\text{LuNi}_2\text{B}_2\text{C}$ . For  $\text{Lu}(\text{Ni}_{1-x}\text{Co}_x)_2\text{B}_2\text{C}$  series, since the density of states of  $\text{LuNi}_2\text{B}_2\text{C}$  mainly comes from Ni  $3d$  bands and manifests a peak at the Fermi level [106, 107], the holes introduced by Co atoms lead to the decrease of  $D(E_f)$  and thus result in a substantial decrease of  $T_c$ . Indeed, a much faster suppression of  $T_c$  than the one in  $(\text{Lu}_{1-x}\text{Y}_x)\text{Ni}_2\text{B}_2\text{C}$  was observed in  $\text{Lu}(\text{Ni}_{1-x}\text{Co}_x)_2\text{B}_2\text{C}$ , as shown in Fig. 2.7 (a). The effect of the  $D(E_f)$  change on affecting  $T_c$  can be better seen in Fig. 2.7 (b), which presents the  $d\text{Ln}T_c/dx$  data vs.  $Z$ , the valence electron, for  $\text{Lu}(\text{Ni}_{1-x}\text{TM}_x)_2\text{B}_2\text{C}$  ( $\text{TM} = \text{Fe}, \text{Ru}, \text{Co}, \text{Ni}$  and  $\text{Pd}$ ) series [108]. As we can see  $d\text{Ln}T_c/dx$  roughly scales with  $Z$ , indicating the dominant effect of the  $D(E_f)$  decrease on the  $T_c$  suppression in  $\text{Lu}(\text{Ni}_{1-x}\text{TM}_x)_2\text{B}_2\text{C}$  series.



### 2.5.1.1 Magnetic impurities [95]

The presence of magnetic impurities will suppress  $T_c$  even in isotropic  $s$ -wave superconductors [69]:

$$\ln \frac{T_{c0}}{T_c} = \varphi\left(\frac{1}{2} + \frac{\mu_m}{2}\right) - \varphi\left(\frac{1}{2}\right) \quad (2.45)$$

which has the same form as  $T_c$  suppression in  $d$ -wave superconductors due to nonmagnetic impurities, except  $\mu_m = \hbar/\pi k_B T_c \tau$  which is two times larger than the one in eq. 2.42. It can also be written as [95]:

$$\ln \frac{T_{c0}}{T_c} = \varphi\left(\frac{1}{2} + 0.14 \frac{\alpha T_{c0}}{\alpha_c T_c}\right) - \varphi\left(\frac{1}{2}\right) \quad (2.46)$$

where  $\alpha$  is the pair breaking parameter which is defined as  $\frac{1}{\tau}$ . and has the expression below for rare earth impurities,

$$\alpha \equiv \frac{1}{\tau} = \frac{n_i}{\hbar} \left[ \frac{D(E_f)}{2k_B} \right] I^2 (g_J - 1) J(J + 1) \quad (2.47)$$

where  $(g_J - 1)^2 J(J + 1)$  is the de Gennes factor. By substituting it into eq. 2.46, the relation between  $T_c$  and the impurity concentration  $n_i$  can be obtained,

$$\ln \frac{T_{c0}}{T_c} = \varphi\left(\frac{1}{2} + 0.14 \frac{n_i T_{c0}}{n_{ic} T_c}\right) - \varphi\left(\frac{1}{2}\right) \quad (2.48)$$

where  $n_{ic}$  is the critical impurity concentration when  $T_c$  is completely suppressed. It can be seen that this equation leads to a universal relation of  $\frac{T_c}{T_{c0}}$  with the normalized impurity concentration  $\frac{n_i}{n_{ic}}$ .

At low concentration,  $\frac{T_c}{T_{c0}}$  is suppressed linearly with  $\frac{n_i}{n_{ic}}$ ,

$$\frac{T_c}{T_{c0}} = 1 - \frac{\pi \hbar}{4k_B \tau} = 1 - 0.691 \frac{n_i}{n_{ic}} \quad (2.49)$$

As we can see this suppression rate is two time larger than the one in  $d$ -wave superconductors caused by the nonmagnetic impurities as shown in eq. 2.43.

The suppression rate of  $T_c$  with  $n_i$  is given by [95]

$$\left. \frac{dT_c}{dn_i} \right|_{n_i \rightarrow 0} = - \left[ \frac{\pi^2 D(E_f)}{2k_B} \right] I^2 (g_J - 1)^2 J(J + 1) \quad (2.50)$$

This equation indicates for the dilute magnetic impurity limit,

$$T_c/T_{c0} = 1 - \left[ \frac{\pi^2 D(E_f)}{2k_B} \right] I^2 (g_J - 1)^2 J(J+1) \quad (2.51)$$

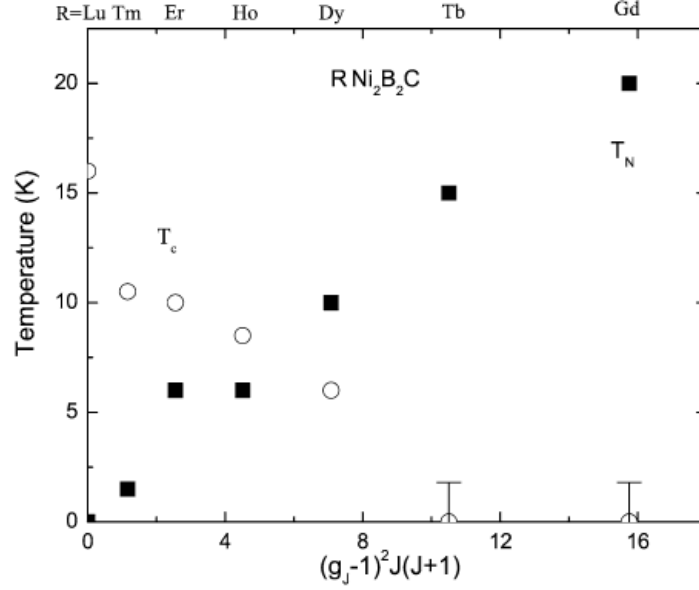


Figure 2.8  $T_c$  and  $T_N$  vs. the de Gennes factor for pure  $\text{RNi}_2\text{B}_2\text{C}$  [109].

Fig. 2.8 shows the data of  $T_c$  and  $T_N$  with respect to the de Gennes factor,  $(g_J - 1)^2 J(J+1)$ , for pure  $\text{RNi}_2\text{B}_2\text{C}$  compounds [109, 110]. As we can see, the de Gennes factor can work as a scaling parameter for both  $T_N$  and  $T_c$  in these compounds. The fact that  $T_c$  roughly scales with the de Gennes factor is consistent with eq. 2.51 although more subtle interactions are revealed with more careful analysis [109, 110]. And the fact that  $T_N$  scales well with the de Gennes factor is consistent with the RKKY interaction which gives rise to the long range ordering in these compounds.

In Fig. 2.9 (a), the solid line represents the theoretical universal curve of  $\frac{T_c}{T_{c0}}$  vs.  $\frac{n_i}{n_{ic}}$  from AG theory [95]. The experimental data are collected for  $\text{La}_{1-x}\text{Gd}_x\text{Al}_2$  series [95] and shown as the "dot" symbols, a good agreement was achieved. In Fig. 2.9 (b), the normalized suppression rate of  $T_c$  in different rare earth element doped  $\text{La}_{1-x}\text{Gd}_x\text{Al}_2$  and  $\text{La}_{0.99}\text{R}_{0.01}$  series were presented as the "dot" symbols, the solid line is the theoretical curve of de Gennes factor  $(g_J - 1)^2 J(J+1)$ . Good agreements were also achieved.

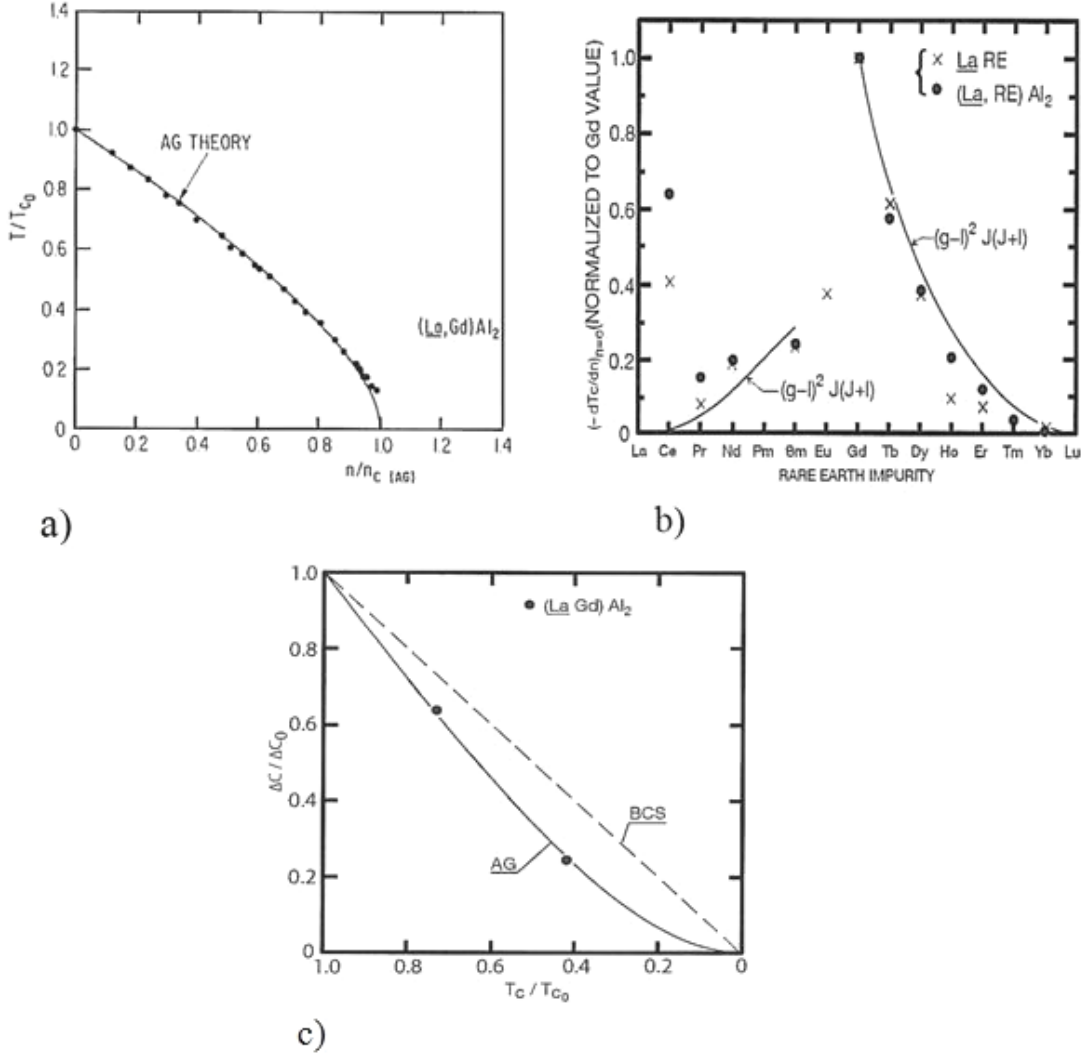


Figure 2.9 (a)  $T/T_{c0}$  vs.  $n/n_c$ . Solid line: from the AG theory. Dots: experiment data for  $\text{La}_{1-x}\text{Gd}_x\text{Al}_2$ . (b) Solid line: de Gennes factor  $(g_J - 1)^2 J(J + 1)$  normalized to the value of Gd vs. different rare earth elements. Dots:  $-(dT_c/dn)|_{n=0}$  normalized to the value of Gd impurity vs. different rare earth impurities in  $\text{La}_{1-x}\text{Gd}_x\text{Al}_2$  and  $\text{La}_{0.99}\text{R}_{0.01}$ . (c)  $\Delta_c/\Delta_{c0}$  vs.  $T_c/T_{c0}$ . Solid line: numerical result of from AG theory. Broken line: theoretical curve from BCS theory. Dots: experiment data for  $\text{La}_{1-x}\text{Gd}_x\text{Al}_2$  and  $\text{La}_{0.99}\text{R}_{0.01}$  [95].

One of two other important outcomes from AG theory is the universal specific heat jump  $\Delta C/\Delta C_0$  [111] with respect to  $T_c/T_{c0}$ . Fig. 2.9 (c) shows the comparison between the experiment data of  $\text{La}_{1-x}\text{Gd}_x\text{Al}_2$  series and the theoretical calculation from AG and BCS theory. We can see the AG theory clearly shows deviation from BCS theory and much better fits the experiment data. The other one is the so called gapless superconductor. It was approved that when  $n_i > 0.91n_{ic}$ , the superconducting gap size becomes zero although  $T_c$  is not completely suppressed. This property leads to the linear temperature dependence of  $C_s(T)$  at low temperatures.

It was shown that if the order parameter, impurity scattering and pairing interaction in a superconductor with arbitrary anisotropy can be expanded into a series of Fermi surface harmonics, the superconductor can be mathematically treated as a multiband superconductor [112, 113]. According to this formalism, A. A. Golubov and I. I. Mazin found if the parts of the Fermi surface with positive order parameter were labelled as band 1 and those with negative order parameter were labelled as band 2, only nonmagnetic interband impurities and magnetic intraband scattering are pairing breaking [113]. They proved analytically that when the average order parameter is zero (e.g., in  $d$ -wave superconductors), the suppression of  $T_c$  due to the magnetic or nonmagnetic impurity scattering is the same [113]. This suppression rate is twice slower in  $d$ -wave superconductor than that of  $s$ -wave superconductors due to the magnetic scattering, according to what we have seen from eq. 2.42 and 2.45.

The nonmagnetic and magnetic impurities were found to have practically indistinguishable effects on suppressing  $T_c$  in a  $s^\pm$ -wave superconductors from the standard  $d$ -wave superconductors [113, 114, 115, 116]. Considering the robust superconductivity in K, Co doped  $\text{BaFe}_2\text{As}_2$  [23, 34], more investigation along this line is needed.

### 2.5.2 Upper critical field: WHH theory

The first theoretical description of the upper critical field  $H_{c2}$  was presented by A. A. Abrikosov, based on the Ginzburg-Landau theory, which restricted the application to the temperature range near  $T_c$  and demonstrated that the superconductor with negative surface energy

undergoes a second order phase transition to normal metal at  $H_{c2}$  which is larger than the thermodynamic critical field  $H_c$  [59]. The first microscopic theory of the upper critical field was presented by L. P. Gor'kov for the clean superconductors with mean free path  $l = \infty$  based on the linearized Gor'kov equation [117]. The subsequent, substantial contribution to this subject was from N. R. Werthamer and co-authors, who systematically studied this problem and provided a description over the whole temperature range for all  $l$  [70, 71, 72, 73, 74]. They solved the linear Gor'kov equations for superconducting alloys, taking care of the effects of the impurity scattering, Zeeman splitting (effect of Pauli spin paramagnetism) and the spin-orbit interaction [70, 71, 72]. Later on they also considered the Fermi surface anisotropy effect [73] and strong electron-phonon coupling [74].

The external magnetic field  $H$  interacts with electron spins via two process. The first one is Zeeman effect. An electron spin in a magnetic field has energy

$$E = g\mu_B H \cdot S = 2\mu_B H \cdot S \quad (2.52)$$

Since a Cooper pair contains an electron with spin  $1/2$  and the other one with spin  $-1/2$ , between these two electrons, the external magnetic field will lead to an energy difference as  $2\mu_B H$ . If we consider this Zeeman effect as the only interaction between external field and the Cooper pairs, since the energy of  $2\Delta = 3.53k_B T_c$  is needed to break one Cooper pair, we get the relation [118]:

$$H_{pauli} = 1.84T_c(Tesla) \quad (2.53)$$

where  $H_{pauli}$  is called Pauli limiting field. It was pointed out that the Zeeman interaction can affect  $H_{c2}$  significantly when the field is larger than 5 Tesla [71, 118].

Since the Zeeman energy can be significantly increased by the spin-orbit interaction, this interaction is the other effect caused by electron spin which can not be ignored [119, 120]. The calculation in [72] showed that the spin-orbit interaction can reduce the effect of Zeeman interaction in limiting  $H_{c2}$ .

Fig. 2.10 [72] shows the schematic plot of the magnetic field dependent free energy in the superconducting and normal state. The red curves are the free energy of the normal state

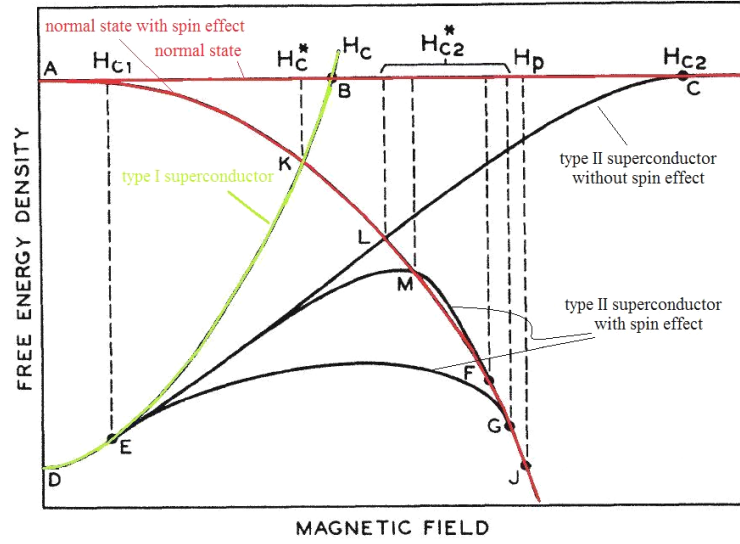


Figure 2.10 The schematic plot of the free energies of superconducting and normal states [72]

without counting Zeeman effect (AC curve) and with Zeeman effect (ALJ curve). Zeeman effect reduces the free energy of the normal state. The green curve (DEB curve) represents the type I superconductor. The intersection "B" of the green curve with the red curve AC gives the traditional thermodynamic critical field  $H_c$ . The black curves are the free energy of type II superconductor. The DEC curve is the free energy without spin effect, DMJ and DGJ are the two situations with spin effect. Points F, G, J and C indicate a second phase transition there while points M, L, B, K indicate first order phase transition.

In WHH theory, it is assumed the transition is a second order phase transition. Fig. 2.11 shows the normalized upper critical field  $h^*$  vs. the normalized superconducting temperature  $t = T/T_c$ , where  $h^*$  is expressed as

$$h^*(t) = -H_{c2} \frac{dH_{c2}}{dt} \Big|_{t=1}, \quad H_{c2} = -h^* T_c \frac{dH_{c2}}{dT} \Big|_{T_c} \quad (2.54)$$

The calculation shown in Fig. 2.11 (a) does not include spin effects and thus is applicable for materials with  $H_{c2}$  smaller than 5 Tesla.  $\lambda$  is defined as

$$\lambda = \frac{1}{2\pi T_c \tau} = 0.882 \xi_0 / l \quad (2.55)$$

Therefore, the  $\lambda = 0$  curve is the  $H_{c2}$  curve in the clean limit,  $h^*(0) = 0.727$ ;  $\lambda = \infty$  curve is the  $H_{c2}$  curve in the dirty limit,  $h^*(0) = 0.693$ . Bringing these numbers into eq. 2.54, we get the WHH formula,

$$H_{c2} = -0.693T_c \frac{dH_{c2}}{dT} \Big|_{T_c}, \quad \text{dirty limit} \quad (2.56)$$

$$H_{c2} = -0.727T_c \frac{dH_{c2}}{dT} \Big|_{T_c}, \quad \text{clean limit} \quad (2.57)$$

Fig. 2.11 (b) shows the experimental  $H_{c2}$  data for  $\text{Ti}_{0.56}\text{Nb}_{0.44}$  and the theoretical calculation including the spin effects in dirty limit.  $\alpha = 0$  where there is no Zeeman effect included.  $\lambda = 0$  when there is no spin-orbit interaction. It can be seen that the  $H_{c2}$  is the highest without considering any spin effects, it becomes smaller with accounting both Zeeman effect and spin-orbit effect, it is reduced to the smallest when only Zeeman effect is included. The curve which includes both spin effects fits the experimental data the best.

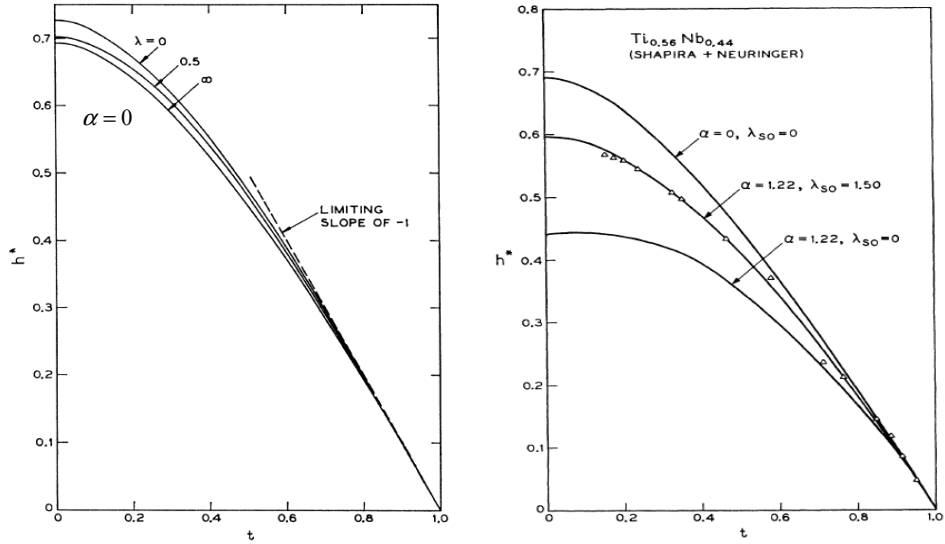


Figure 2.11 (a) Normalized upper critical field  $h^*$  vs. the normalized superconducting temperature  $t$  without spin effects [71]. (b) Normalized upper critical field  $h^*$  vs. the normalized superconducting temperature  $t$  with spin effects [72].

## CHAPTER 3. Experimental methods

### 3.1 Crystal growth

Although novel materials are often discovered and preliminarily characterized in polycrystalline form, high quality single crystals are essential for advanced scientific research due to their special advantages. First, since a single crystal has only one boundary and the impurity phases often exist between the grain boundaries, a single crystal often has substantially lower impurities and, in addition, often suffers less strain compared to a polycrystal. Secondly, for many measurement techniques, high purity single crystalline samples are critical. For example, de Haas - van Alphen (dHvA) measurements, which can provide information about Fermi surface topology and effective mass of the electrons, require single crystalline samples with high purity and low residual resistance. A single crystal also has sizable, atomically ordered surfaces, which are vital for surface sensitive measurements. For example, angle resolved photoemission spectroscopy (ARPES), which provides direct information about Fermi surface, gap size and symmetry, can only be made on a perfectly cleaved surface, which can only exist in a single crystalline sample. Third, but not the least, a single crystal has a well-defined orientation. This is important for all anisotropic measurements.

Many techniques have been developed to grow single crystalline samples. These techniques can be classified into melt growth methods, vapor growth methods and solution growth methods [121, 122, 123]. Melt growth processes such as Bridgman, Czochralski and floating zone methods are widely used in the semiconductor industry to produce large single crystalline Si and Ge semiconductors. However, melt growth methods require the composition of the melt to be the same, or very similar, to that of the expected product. This limits the application of these methods to congruently or near-congruently melting compounds. Vapor transport



growth methods often result in very high purity, small single crystals, but require the existence of volatile phases of all the components as well as a transport agent (if self transport is not possible). The high temperature solution growth method is widely used and recognized as a powerful technique for obtaining single crystals of complex materials. It is a viable technique for both congruently and incongruently melting materials and can be used to control high vapor pressures of constituent elements. The samples presented in this thesis were all grown using a high temperature solution growth method.

### 3.1.1 High temperature solution growth method

In high temperature solution growth, several factors should be considered carefully: solvent, initial concentrations, cooling rate and decanting temperature [124, 125, 126].

A solvent that has a relatively low melting temperature and offers good solubility for the other components in the growth is vital for successful single crystal synthesis via solution growth. The solvent used in high-temperature solution growth is also called "flux". Flux can be classified into two types: one is self flux, the excess of one or more constituent elements of the desired compound is used as the solvent; the other one is non-self-flux which introduces elements other than the ones in the desired compound to act as a solvent. It is often preferable to use a self flux since it does not introduce any other elements into the melt, and thus no other element can enter into the desired single crystal, and the number of possible undesired phases can also be reduced. However, it is not always practical to use self flux because the self flux may have too high of a melting temperature, one that exceeds the working temperatures of ampules or furnaces, or too high of a vapor pressure which will lead to loss of stoichiometry in the resulted single crystals or even possible explosion. For example, from the Ce-Sb binary phase diagrams, it can be seen if we want to grow CeSb single crystal, we need at least 1500° C to access a liquidus line for CeSb [127]. This temperature is higher than the softening temperature of silica tube and may exceed the maximum furnace temperature. Even if we try to manage it with tantalum tube and use a high temperature furnace, the resulting crystals can have a lot of defects due to entropic effects enhanced by the high growth temperature [124]. Therefore, in

many situations, a non-self-flux is used [124, 128]. There are some empirical rules for selecting flux : low vapor pressure, high solubility for the constituent elements, compatibility with the crucibles, cheap and non-toxic, etc. For intermetallic compounds, Zn, Al, Ga, In, Ge, Sn, Pb, Sb and Bi are often used as flux (Sn was used for CeSb single crystal growth).

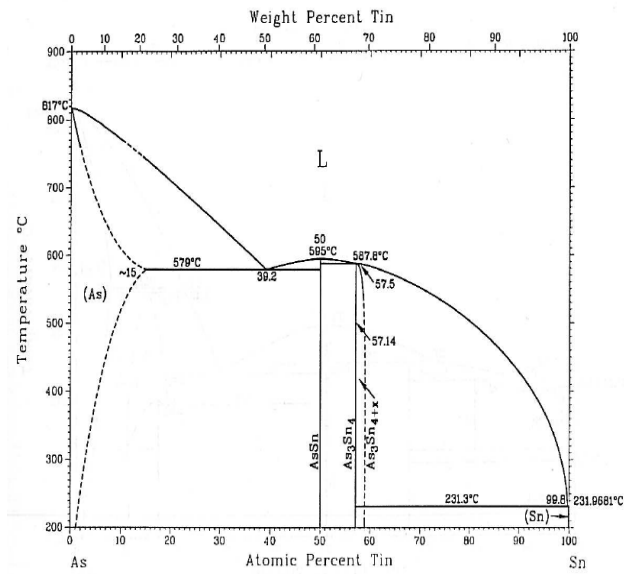
At high temperatures, all the constituent elements are dissolved in the flux and form a uniform solution. As the temperature decreases, the solubility of the target compound decreases, the desired compound starts to precipitate out of the solution (ideally in single crystal form) below a critical temperature. As the temperature continuously decreases at a constant and slow rate, crystals grow. The sample size depends on the number of the nucleation sites and the cooling rate; often, the slower the cooling, the larger the crystal. Another advantage of a slow cooling rate is that crystals relatively free of strains can be grown [124, 125, 126]. Once the crystals are grown, they can be separated from the remaining liquid flux by decanting the liquid using a centrifuge. It is important to carefully choose the decanting temperature. It should be high enough so that no impurity phases exist and the flux is still liquid; on the other hand, it should be low enough so that the desired crystal has as large of a temperature window to grow in as possible. If there is a little flux left on the sample surface, it can either be etched by an appropriate acid / base or mechanically polished / cleaved.

### **3.1.2 Single crystal growth of $\text{Ba}(\text{Fe}_{1-x}\text{TM}_x)_2\text{As}_2$ (TM = Co, Ni, Cu, Cu / Co, Rh and Pd)**

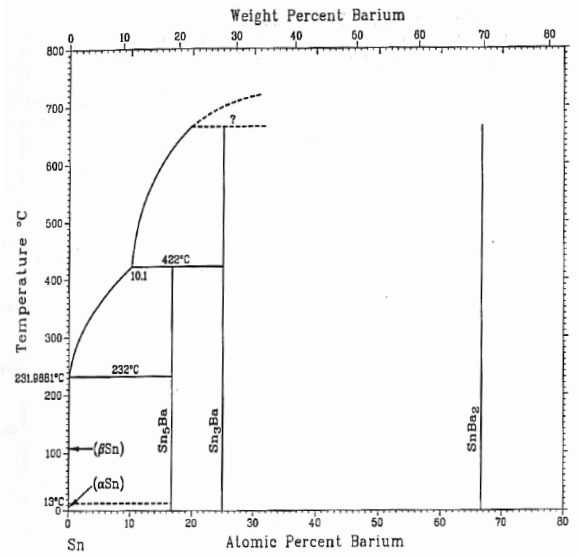
Single crystals of pure and doped  $\text{BaFe}_2\text{As}_2$  can be grown using a conventional, high temperature solution technique. Both Sn-flux and FeAs-self-flux can be used.

#### **3.1.2.1 Single crystals grown from Sn flux**

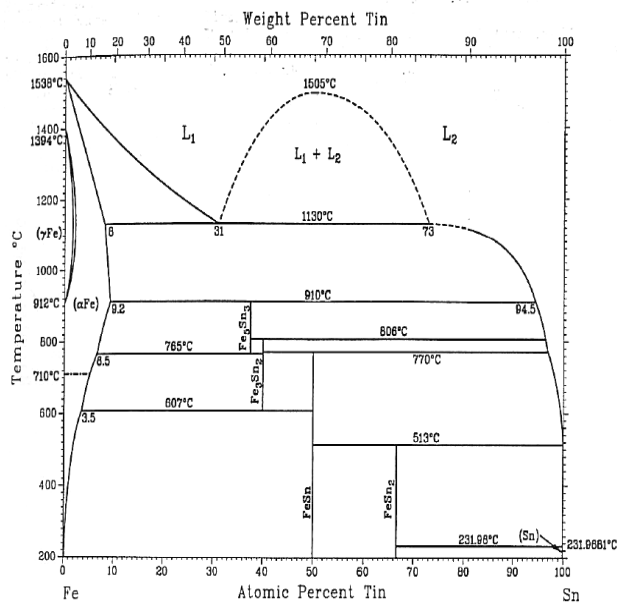
The first sizable single crystals of FeAs-based compounds were  $\text{Ba}_{1-x}\text{K}_x\text{Fe}_2\text{As}_2$  ( $x=0, 0.45$ ) grown in our group using Sn as flux [25]. Later on  $\text{SrFe}_2\text{As}_2$  [129] and  $\text{CaFe}_2\text{As}_2$  [130], were also successfully grown from Sn flux.



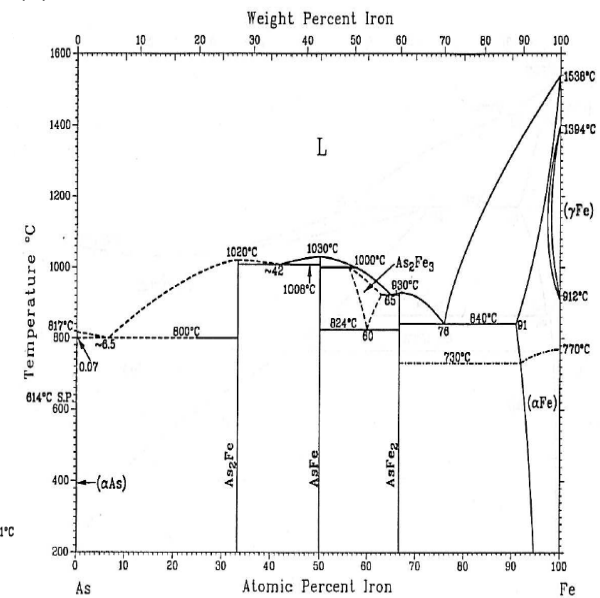
(a)



(b)



(c)



(d)

Figure 3.1 Binary phase diagram (a) As-Sn [131]. (b) Ba-Sn [132]. (c) Fe-Sn [133]. (d) As-Fe [134].

Fig. 3.1 (a), (b) and (c) show the binary phase diagrams of As-Sn, Ba-Sn and Fe-Sn respectively [131, 132, 133]. They indicate that there is fair solubility of dilute Ba and Fe in Sn solvent as well as essentially full solubility of As in Sn solvent. In addition, given Sn's low melting point, we do not need to heat the system to a very high temperature; the decanting temperature can be chosen to be relatively low because the binary impurities only exist at low temperatures, therefore a large temperature window for the single crystals to form in exists. We grew single crystals of  $\text{BaFe}_2\text{As}_2$  during our first trial. After several further trials, the optimal procedure to grow  $\text{BaFe}_2\text{As}_2$  was fixed.

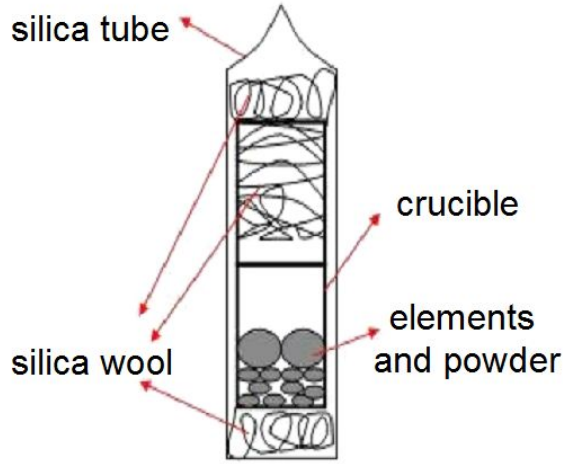


Figure 3.2 Diagram of the ampoule used for crystal growth (see text)

Elemental Ba, Fe and As and Sn were loaded in a 2 ml MgO crucible according to the ratio of  $(\text{Ba}:2\text{Fe}:2\text{As}) : \text{Sn} = 1 : 48$ . Sn was placed on the top of the other elements since it will melt first with increasing temperature. A second, catch, crucible containing silica wool was placed on top of the growth crucible and both were sealed in a silica ampoule under approximately  $1/3$  atmosphere of Ar gas. The assembled ampoule is shown schematically in Fig. 3.2. It should be noted that the packing and assembly of the growth ampoule were performed in a glove box with one atmosphere of  $\text{N}_2$  gas since barium is highly air sensitive. The sealed ampoule was placed in a programmable furnace and heated from room temperature to  $600^\circ\text{C}$  at a rate of  $100^\circ\text{C}/\text{hour}$ , dwelled for 1 hour so that the As could be completely incorporated into the

melt. Then the ampoule was continuously heated up to  $1000^{\circ}\text{C}$  at a rate of  $100^{\circ}\text{C}/\text{hour}$ , stayed at  $1000^{\circ}\text{C}$  for 2 hours so that the liquid mixed completely, and then cooled over 36 hours to  $500^{\circ}\text{C}$ . Once the furnace reached  $500^{\circ}\text{C}$  the liquid was decanted from the resulted  $\text{BaFe}_2\text{As}_2$  crystals. The little Sn flux left on the surface of the single crystals can be quickly etched by concentrated HCl acid for one minute and then rinsed with water and then ethanol. The resulted single crystal can be as big as  $3 \times 3 \times 0.2\text{mm}^3$ . Fig. 3.3 (a) shows a picture of a single crystal of  $\text{BaFe}_2\text{As}_2$  grown from Sn flux against a  $1\text{mm}$  scale. The as-grown flat surface is the  $ab$  plane. The sample also has clear  $[100]$  edges.

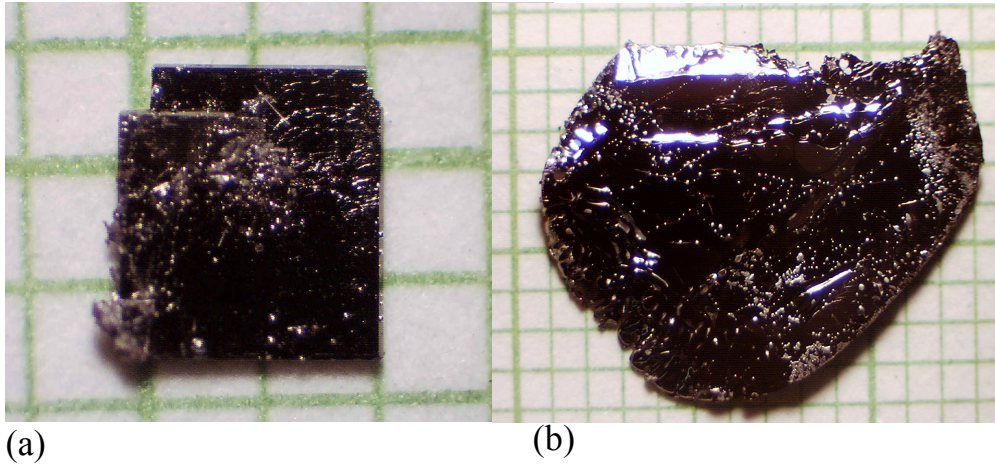


Figure 3.3 (a) Single crystal of  $\text{BaFe}_2\text{As}_2$  grown from Sn flux against  $1\text{mm}$  scale. (b) Single crystal of  $\text{Ba}(\text{Fe}_{0.926}\text{Co}_{0.074})_2\text{As}_2$  grown from self flux against  $1\text{mm}$  scale.

### 3.1.2.2 Single crystals of $\text{Ba}(\text{Fe}_{1-x}\text{TM}_x)_2\text{As}_2$ grown from self flux

After the development of Sn-flux growth, it was found that single crystals of  $\text{BaFe}_2\text{As}_2$  (and other 122 compounds) can be grown from a self flux of FeAs [26]. Although this is a more difficult process, it leads to larger crystals and allows for homogenous TM doping. Fig. 3.1 (d) shows the binary Fe-As phase diagram [134]; FeAs melts above  $1030^{\circ}\text{C}$ . In this paper, all the doped  $\text{Ba}(\text{Fe}_{1-x}\text{TM}_x)_2\text{As}_2$  ( $\text{TM} = \text{Co}, \text{Ni}, \text{Cu}, \text{Co} / \text{Cu}, \text{Rh}$  and  $\text{Pd}$ ) were grown from a FeAs self flux.

TMA<sub>s</sub> was used as flux (and dopant). It was synthesized by a conventional solid state reaction method. Commercial transition metal powders and As were weighed according to the atomic ratio TM : As = 1.05 : 1 and mixed thoroughly in a mortar and pestle. Pellets, about 10 mm in diameter and 3 to 5 mm thick, were pressed under a pressure of 5 tons. All of the above operations were performed in a glove box with one atmosphere of N<sub>2</sub> gas to ensure safety. The pellets were then sealed in an evacuated silica tube and back filled with  $\sim 1/3$  atmosphere of Ar gas. The ampoule was heated to 580°C and dwelled for 15 hours. Sometimes further heat treatment at 900°C for 15 hours was necessary in order to obtain single phase TMA<sub>s</sub>. Since As sublimates at  $\sim 600^\circ\text{C}$ , it is necessary to ensure that there is a secondary safeguard in place which can accommodate the reactants in the event of a failure (explosion) of the silica ampoule. Since the alloy Haynes 230 can work in air in the temperature range of 500°C to 1000°, a Haynes 230 tube with 1 inch diameter and 0.060 inch thick walls is used as the double ended retort. The retort passes through the tube furnace and gets water cooled at both ends. Due to the fact that the volume of this retort is only about 0.25 liter, an expansion volume of approximately 2 liters is also placed on one end. N<sub>2</sub> is flowing through the retort and up to the exhaust system during operation. The flowing N<sub>2</sub> carries any poisonous vapor to the exhaust system and also prevents possible oxidization of starting elements.

For Ba(Fe<sub>1-x</sub>TM<sub>x</sub>)<sub>2</sub>As<sub>2</sub> (TM = Co, Ni), small Ba chunks and FeAs/TMA<sub>s</sub> powders were mixed together according to the ratio Ba : FeAs : TMA<sub>s</sub> = 1 : (4 - x) : x. The mixture was placed into an alumina crucible with a second "catch" crucible containing silica wool placed on top. Both crucibles were sealed in a silica tube under a 1/3, partial atmosphere, of Ar gas. To minimize attack on the crucible, a 50° C/hour heating rate was used. The sealed silica tube was heated up to 1180 °C, held at 1180 °C for 5 to 8 hours, and then cooled to 1000 °C over 35 to 50 hours. Once the furnace reached 1000 °C, the excess liquid was decanted from the plate-like single crystals shown in Fig. 3.3 (b). The plate-like single crystals can be very easily cut or exfoliated. Although the plate itself is perpendicular to the crystallographic *c*-axis, it does not have clear [100] edges. This is different from the crystals grown out of Sn flux which has clear edges [25, 129, 130]. The dimension of the single crystals grown out of FeAs flux can

exceed to  $12 \times 8 \times 0.8 \text{ mm}^3$ . For  $\text{Ba}(\text{Fe}_{1-x}\text{TM}_x)_2\text{As}_2$  (TM = Rh, Pd), the procedure described above was used except the decanting temperature was 1050 °C instead of 1000 °C.

For  $\text{Ba}(\text{Fe}_{1-x}\text{TM}_x)_2\text{As}_2$  (TM = Cu, Co / Cu), small pieces of Cu shot were used to introduce the dopant because no CuAs compound is known to exist. For Cu doped  $\text{BaFe}_2\text{As}_2$ , small Ba chunks, FeAs powder and Cu shot were mixed together according to the ratio Ba : FeAs : Cu = 1 : 4 :  $m$ . The nominal concentration  $x_{\text{nominal}}$  can be calculated as  $\text{Cu}/(\text{Cu}+\text{Fe})=m/(4+m)$ . For  $\text{Ba}(\text{Fe}_{1-x-y}\text{Co}_x\text{Cu}_y)_2\text{As}_2$  ( $x \sim 0.022$ ), small Ba chunks, FeAs, CoAs powder and Cu shot were mixed together according to the ratio Ba : FeAs : CoAs : Cu = 1 : 3.88 : 0.12 :  $m$ . For  $\text{Ba}(\text{Fe}_{1-x-y}\text{Co}_x\text{Cu}_y)_2\text{As}_2$  ( $x \sim 0.047$ ), Ba : FeAs : CoAs : Cu = 1 : 3.75 : 0.25 :  $m$ . The packing and the temperature program are the same as what we used for  $\text{Ba}(\text{Fe}_{1-x}\text{TM}_x)_2\text{As}_2$  (TM = Co, Ni).

The nominal  $x$ ,  $y$  values as well as the measured (via wavelength dispersive spectroscopy, see section 3.2.2 below)  $x$ ,  $y$  values of the  $\text{Ba}(\text{Fe}_{1-x}\text{TM}_x)_2\text{As}_2$  (TM = Co, Ni, Cu, Cu / Co, Rh and Pd) series, are summarized in Tables 3.1 and 3.2. The samples were carefully cleaved and cut into several pieces. Elemental analysis was performed on up to 5 pieces of samples in each batch. N is the total number of spots measured in one batch. Although we did not make enormous WDS measurements on all the batches, we do have more than 20 spots measured for some batches so that we can have a better statistics.  $x_{\text{nominal}}$  and  $y_{\text{nominal}}$  are the nominal doping concentrations.  $x_{\text{WDS}}$  and  $y_{\text{WDS}}$  are the average values of the N measurements for a given batch.  $2\sigma$  is twice the standard deviation of the N values measured in one batch, which is taken as the compositional error bar for this thesis. The  $2\sigma$  error bars, for all the spots measured in one batch over multiple layers are  $\lesssim 10\%$  of the average  $x$  values. These results further demonstrate the relative homogeneity of the  $\text{Ba}(\text{Fe}_{1-x}\text{TM}_x)_2\text{As}_2$  series.

In contrast, in reference [25], we have shown that  $(\text{Ba}_{1-x}\text{K}_x)\text{Fe}_2\text{As}_2$  grown out of Sn flux had a distribution of K concentration from 0.36 to 0.53 in one sample, which is roughly  $\pm 30\%$  of the average concentration. In addition in reference [28],  $(\text{Ba}_{1-x}\text{K}_x)\text{Fe}_2\text{As}_2$  grown out of FeAs flux has a  $T_c$  of 25 K for the outer layer of one piece and 32.7 K for the inner layer of

Ba(Fe <sub>1-x</sub> Co <sub>x</sub> ) <sub>2</sub> As <sub>2</sub>										
N	8	8	7	9	7	6	10	5	5	9
$x_{nominal}$	0.0125	0.025	0.05	0.0625	0.075	0.1	0.125	0.15	0.17	0.20
$x_{WDS}$	0.013	0.02	0.038	0.047	0.058	0.074	0.10	0.114	0.135	0.166
$2\sigma$	0.001	0.001	0.002	0.002	0.002	0.003	0.002	0.004	0.002	0.003

Ba(Fe <sub>1-x</sub> Ni <sub>x</sub> ) <sub>2</sub> As <sub>2</sub>							
N	18	10	44	18	11	12	28
$x_{nominal}$	0.01	0.02	0.03	0.04	0.05	0.07	0.09
$x_{WDS}$	0.0067	0.016	0.024	0.032	0.046	0.054	0.072
$2\sigma$	0.001	0.002	0.002	0.003	0.002	0.002	0.004

Ba(Fe <sub>1-x</sub> Rh <sub>x</sub> ) <sub>2</sub> As <sub>2</sub>								
N	16	16	18	15	20	34	33	20
$x_{nominal}$	0.025	0.05	0.07	0.1	0.125	0.15	0.18	0.22
$x_{WDS}$	0.012	0.026	0.039	0.057	0.076	0.096	0.131	0.171
$2\sigma$	0.001	0.001	0.002	0.003	0.004	0.006	0.005	0.002

Ba(Fe <sub>1-x</sub> Pd <sub>x</sub> ) <sub>2</sub> As <sub>2</sub>								
N	18	8	52	6	6	12	14	52
$x_{nominal}$	0.0125	0.025	0.0325	0.04	0.05	0.0625	0.085	0.1
$x_{WDS}$	0.012	0.021	0.027	0.030	0.043	0.053	0.067	0.077
$2\sigma$	0.001	0.002	0.003	0.002	0.001	0.002	0.002	0.005

Table 3.1 The elemental analysis data for Ba(Fe<sub>1-x</sub>TM<sub>x</sub>)<sub>2</sub>As<sub>2</sub> (TM = Co, Ni, Rh, Pd) series.

the same piece, indicating a large inhomogeneity in this growth.

Fig. 3.4 shows a graphic summary of the measured doping concentration vs. nominal doping concentration for all doped series. From Fig. 3.4 (a) to Fig. 3.4 (d), it can be clearly seen that  $x_{WDS}$  roughly linearly increases with the nominal doping concentration for the Co, Ni, Rh, Pd doped Ba122 samples we grew. The data can be fit by a line; the ratio of the measured Co concentration over the nominal Co concentration is roughly 0.74. This ratio



Ba(Fe <sub>1-x</sub> Cu <sub>x</sub> ) <sub>2</sub> As <sub>2</sub>						
N	16	11	17	26	12	16
$x_{nominal}$	0.005	0.012	0.022	0.024	0.027	0.029
$x_{WDS}$	0.0077	0.02	0.026	0.035	0.044	0.05
$2\sigma$	0.002	0.002	0.002	0.004	0.002	0.002
N	43	12	10	8	17	23
$x_{nominal}$	0.034	0.038	0.061	0.101	0.20	0.429
$x_{WDS}$	0.061	0.068	0.092	0.165	0.288	0.356
$2\sigma$	0.002	0.002	0.008	0.02	0.02	0.02

Ba(Fe <sub>1-x-y</sub> Co <sub>x</sub> Cu <sub>y</sub> ) <sub>2</sub> As <sub>2</sub> ( $x \sim 0.022$ )							
N	18	12	20	30	20	20	28
$x_{WDS}$	0.024	0.024	0.022	0.022	0.021	0.021	0.021
$2\sigma$	0.001	0.001	0.001	0.001	0.001	0.001	0.001
$y_{nominal}$	0	0.0035	0.0074	0.012	0.017	0.022	0.034
$y_{WDS}$	0	0.005	0.01	0.019	0.026	0.032	0.043
$2\sigma$	0	0.002	0.002	0.003	0.004	0.003	0.004

Ba(Fe <sub>1-x-y</sub> Co <sub>x</sub> Cu <sub>y</sub> ) <sub>2</sub> As <sub>2</sub> ( $x \sim 0.047$ )						
N	7	8	37	36	7	41
$x_{WDS}$	0.047	0.047	0.051	0.047	0.045	0.045
$2\sigma$	0.002	0.002	0.003	0.002	0.002	0.002
$y_{nominal}$	0	0.0025	0.012	0.022	0.029	0.036
$y_{WDS}$	0	0.0045	0.019	0.034	0.046	0.058
$2\sigma$	0	0.001	0.002	0.004	0.004	0.006

Table 3.2 The elemental analysis data for Ba(Fe<sub>1-x</sub>TM<sub>x</sub>)<sub>2</sub>As<sub>2</sub> (TM=Cu, Co / Cu mixture) series.

is 0.80 for Ni doping, 0.67 for Rh doping and 0.77 for Pd doping. Fig. 3.4 (e) summarizes the measured Cu concentration vs. nominal Cu concentration in all Ba(Fe<sub>1-x</sub>Cu<sub>x</sub>)<sub>2</sub>As<sub>2</sub> and Ba(Fe<sub>1-x-y</sub>Co<sub>x</sub>Cu<sub>y</sub>)<sub>2</sub>As<sub>2</sub> ( $x \sim 0.022$  and  $x \sim 0.047$ ) growths. Even though these are different series, all the data points collapse on the same curve. The measured Cu concentration is roughly 1.6 times the nominal Cu concentration in the low doping range.

For large Cu doping values, the ratio of WDS measured Cu concentration over nominal Cu concentration decreases and the  $x_{WDS}$  value saturates around 0.35 in Ba(Fe<sub>1-x</sub>Cu<sub>x</sub>)<sub>2</sub>As<sub>2</sub> as shown in Fig. 3.4 (f). This could be due to the increase of TM:As ratio as  $x_{Cu}^{nominal}$  increases.

It is 1.4 : 1 when  $x_{Cu}^{nominal}=0.4$  and 1.6 : 1 when  $x_{Cu}^{nominal}=0.6$ , which are much larger than the value of 1: 1. For a comparison, we can see in Fig. 3.4 (f) that  $Ba(Fe_{1-x}Co_x)_2As_2$  series does not saturate in all  $Ba(Fe_{1-x}Co_x)_2As_2$  growths.

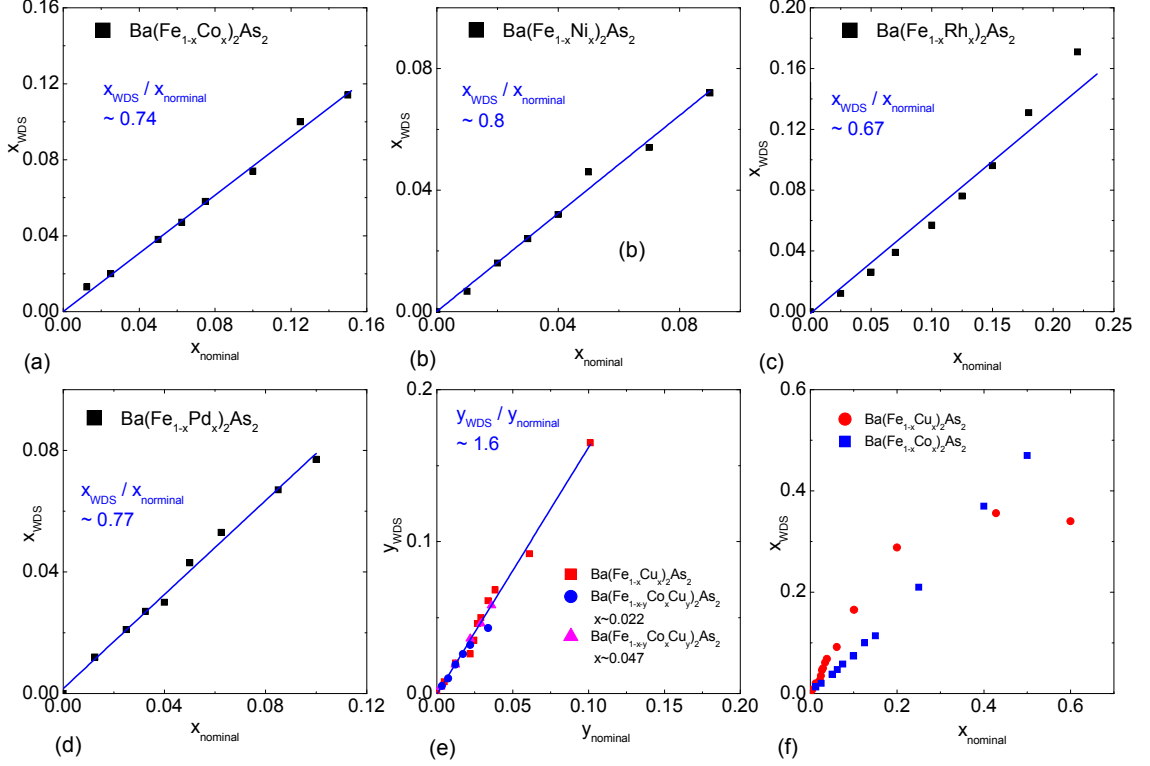


Figure 3.4 The graphic summary of the results from the elemental analysis for the  $Ba(Fe_{1-x}TM_x)_2As_2$  (TM = Co, Ni, Rh, Pd, Cu, Cu / Co) series.

## 3.2 Measurement methods

### 3.2.1 X-ray diffraction measurements

To check whether impurity phases are present in the samples and determine the lattice parameters, powder X-ray diffraction measurements were performed at room temperature using a Rigaku Miniflex diffractometer with Cu  $K_\alpha$  radiation. Si powder, with lattice parameter  $a=5.4301 \text{ \AA}$  was used as an internal standard. Diffraction patterns were taken on the mixture of Si powder and ground single crystals from each batch. The average difference between the

expected and experimental Si peak positions were used to estimate the slight, instrumental zero shift for each run. From powder X-ray measurements, no detectable impurities were found in any of the compounds grown from self flux. There are small impurity peaks from excess Sn for the compounds grown from Sn flux. The unit cell parameters were refined by "UnitCell" software. Error bars were taken as twice the standard deviation,  $\sigma$ , which was obtained from the refinements by the "Unitcell" software.

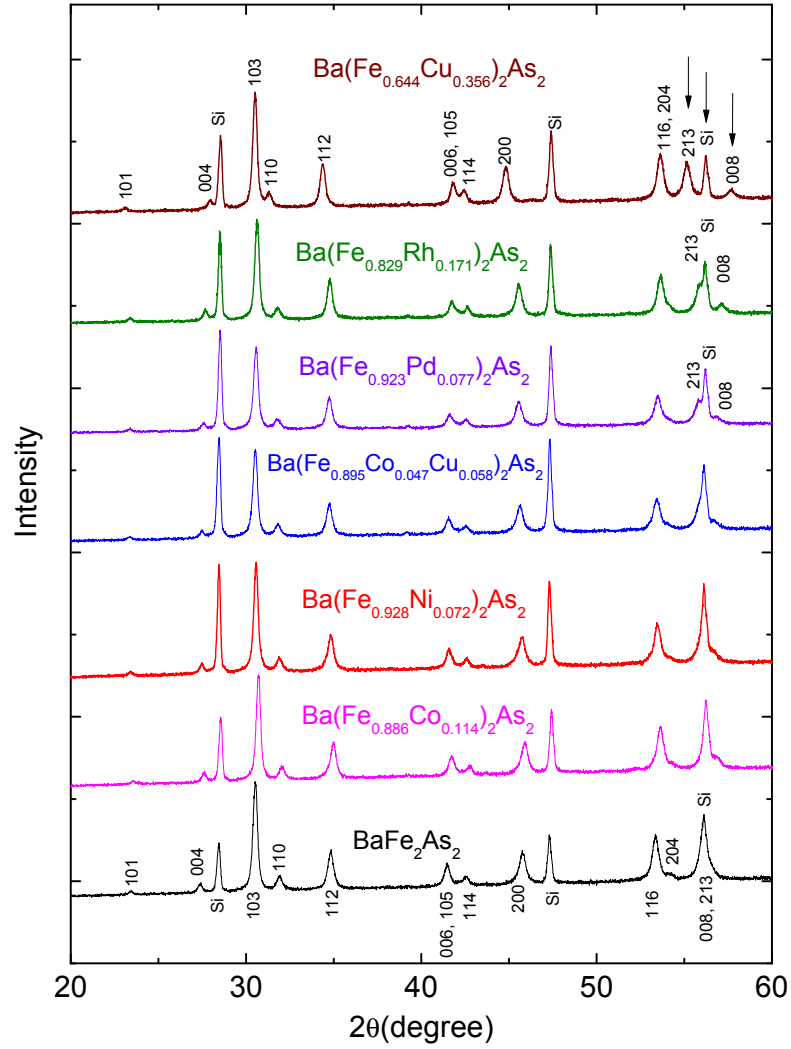


Figure 3.5 Powder X-ray patterns for pure and doped  $\text{BaFe}_2\text{As}_2$ . Si is added as an internal standard.

Fig. 3.5 shows the powder X-ray diffraction patterns for  $\text{BaFe}_2\text{As}_2$ ,  $\text{Ba}(\text{Fe}_{0.644}\text{Cu}_{0.356})_2\text{As}_2$ ,

$\text{Ba}(\text{Fe}_{0.829}\text{Rh}_{0.171})_2\text{As}_2$ ,  $\text{Ba}(\text{Fe}_{0.923}\text{Pd}_{0.077})_2\text{As}_2$ ,  $\text{Ba}(\text{Fe}_{0.928}\text{Ni}_{0.072})_2\text{As}_2$ ,  $\text{Ba}(\text{Fe}_{0.886}\text{Co}_{0.114})_2\text{As}_2$  and  $\text{Ba}(\text{Fe}_{0.936}\text{Co}_{0.047}\text{Cu}_{0.058})_2\text{As}_2$  respectively. No impurity phases can be detected in any of these batches. Since  $\text{Ba}(\text{Fe}_{0.644}\text{Cu}_{0.356})_2\text{As}_2$  has the highest doping concentration among all series, and Rh and Pd have much larger atomic radii than Fe, the lattice parameters for these three dopings have the largest changes. We do see the combined Si, 213 and 008 peaks around  $56^\circ$  in pure  $\text{BaFe}_2\text{As}_2$  splits into three peaks which are indicated by arrows in  $\text{Ba}(\text{Fe}_{0.644}\text{Cu}_{0.356})_2\text{As}_2$ ,  $\text{Ba}(\text{Fe}_{0.829}\text{Rh}_{0.171})_2\text{As}_2$  and  $\text{Ba}(\text{Fe}_{0.923}\text{Pd}_{0.077})_2\text{As}_2$ . This is a clear evidence that the transition metals are incorporated into the crystallographic lattice.

### 3.2.2 Wave-length dispersive spectroscopy

Given the nature of solution growth, the nominal concentration of a dopant does not have to be the actual concentration in a grown crystal. In addition, given the difficulties associated with K homogeneity [25, 28], determining how homogeneous the TM doped samples are is important. Elemental analysis of the  $\text{Ba}(\text{Fe}_{1-x}\text{TM}_x)_2\text{As}_2$  samples was performed to directly get the doping concentration of the samples using wavelength dispersive X-ray spectroscopy (WDS) in the electron probe microanalyzer of a JEOL JXA-8200 electron-microprobe. In the WDS measurement, an electron beam with sufficient energy (20 kV is used in our measurements) is incident on the sample surface and interacts with the atoms in the sample. Characteristic X-ray can be produced in this process. Since the characteristic X-ray is unique for each element, its energy can be used to identify the elements present in the sample and its intensity can be used for quantitative elemental analysis. WDS measurements were performed for all the batches, especially on the pieces which were used to make the resistivity, magnetization and heat capacity measurements. For those pieces, the samples were carefully exfoliated and cut into several pieces. WDS measurements were made on each piece and up to five pieces of samples were measured in each batch. The average doping values measured at several locations on the sample from wavelength dispersive X-ray spectroscopy (WDS) measurement,  $x_{WDS}$  and  $y_{WDS}$ , were used in this thesis as  $x$  and  $y$  rather than  $x_{nominal}$  and  $y_{nominal}$ .

### 3.2.3 Resistivity measurement

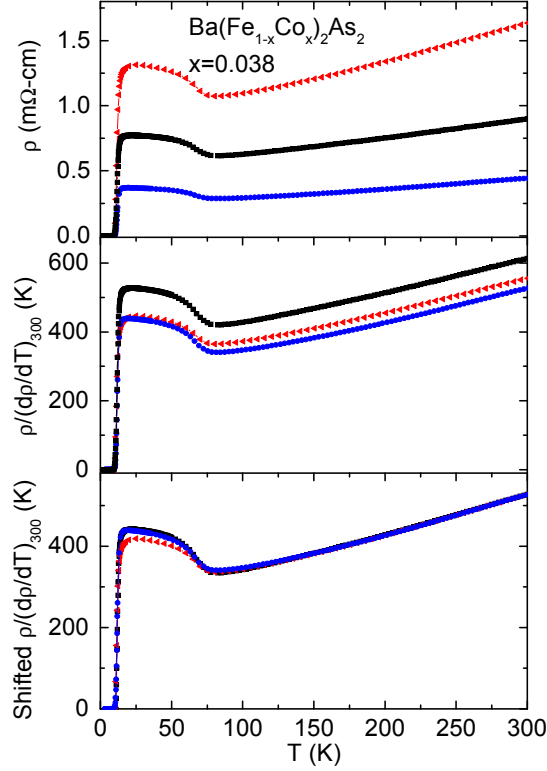


Figure 3.6 (a) Temperature-dependent electrical resistivity of three samples of  $\text{Ba}(\text{Fe}_{0.962}\text{Co}_{0.038})_2\text{As}_2$ . (b) Temperature-dependent electrical resistivity of three samples of  $\text{Ba}(\text{Fe}_{0.962}\text{Co}_{0.038})_2\text{As}_2$  normalized to their room temperature respective slopes:  $\rho(T)/(d\rho/dT)|_{300\text{K}}$ . (c) The same data as (b) with upper curve shifted down by 85.7 K and intermediate curve shifted down by 28 K to account for differences in temperature independent, residual resistivity.

The temperature dependent AC resistivity measurements in zero magnetic field were performed in either Quantum Design (QD) Magnetic Properties Measurement System (MPMS) using a Linear Research LR-700 AC resistance bridge (  $f = 16 \text{ Hz}$ ,  $I = 3 \text{ mA}$  ) or in the QD Physical Properties Measurement System (PPMS) using the AC transport (ACT) option (  $f = 16 \text{ Hz}$ ,  $I = 3 \text{ mA}$  ). In some cases, the He-3 option in the QD-PPMS was employed to measure down to 0.4 K, but for most of the measurements the temperature range used was from 2 K to 300 K. The outer layers of plate-like samples were cleaved and the inner layers of

the samples were cut into rectangular resistivity bars with typical cross section  $0.1 \times 0.5 \text{ mm}^2$  with the distance between the voltage contacts being roughly  $1.5 \text{ mm}$ . Pt wires were attached to the resistivity bar by Epotek H20E silver epoxy in a standard AC four-probe configuration. They were cured at  $100^\circ \text{ C}$  for 30 minutes. Typical contact resistance was between  $1 \, \Omega$  and  $3 \, \Omega$ . The current flow was in  $ab$  plane, i. e., perpendicular to the  $c$  axis. The temperature dependent AC electrical transport measurements in magnetic field up to 7 T were collected in a 7 T - MPMS using a Linear Research LR-700 AC resistance bridge ( $f = 16 \text{ Hz}$ ,  $I = 3 \text{ mA}$ ).

The field-dependent DC resistivity measurements in 35 T or 33 T resistive magnets down to 2 K were performed in the National High Magnetic Field Laboratory in Tallahassee, FL. Two samples with the same doping concentration were run for both  $H||c$  with  $H$  perpendicular to the basal plane and  $H \perp c$  with  $H$  parallel to the basal plane. The zero field  $T_c$  values measured inside MPMS or PPMS were used as a correction for slight temperature offsets associated with the resistive probe used at the NHMFL. These shifts were at most 10% of  $T_c$  and significantly smaller than 10% of  $T_c$  for most runs.

The pure and doped  $\text{BaFe}_2\text{As}_2$  single crystals are very easy to be exfoliated or crack and this leads to the potential for uncertainty of the geometric factors when we infer the value of resistivity. Fig. 3.6 (a) shows the resistivity data obtained from three pieces of  $\text{Ba}(\text{Fe}_{0.926}\text{Co}_{0.074})_2\text{As}_2$ . As it can be seen these plots vary significantly. If, on the other hand, we plot resistivity normalized to the room-temperature slopes,  $(d\rho/dT)|_{300\text{K}}$ , which can compensate for the uncertainty of the geometric factors, the resistivity plots of these three samples become parallel to each other as shown in Fig. 3.6 (b), indicating the same transport behavior in these samples except the slight different residue resistances, which is further confirmed in Fig. 3.6 (c). These data (and analysis) are consistent with the hypothesis that cracks / splits give rise to a poorly controlled, internal geometry. Therefore, in this thesis,  $\rho(T)/\rho_{300}$ , instead of  $\rho(T)$  is used.

### 3.2.4 Magnetization measurement

Magnetization measurements from 2 K to 300 K were made using either a 5.5 T QD-MPMS or 7 T QD-MPMS. Due to the weak magnetic signal at the normal state (normally

$M/H \sim 10^{-4} \text{ emu/mole}$ ) for these samples, 10 *mg* to 30 *mg* of samples were used. For superconducting samples, to diminish the remanent field, a demagnetization sequence,  $0T \rightarrow 4T \rightarrow -4T \rightarrow 2T \rightarrow -2T \rightarrow 1mT \rightarrow -1mT \rightarrow 0T$ , was used before the low field measurement. Zero-field-cooled (ZFC) and field-cooled (FC) magnetization data were then taken at 2.5 mT with  $H \perp c$  near and below the superconducting temperature, so that rough estimation of the superconducting volume fraction could be made.

### 3.2.5 Specific heat measurement

Temperature dependent heat capacity data ( $H = 0$  T and 9 T) were collected using the heat capacity option in a 9 T QD-PPMS system down to 2 K; the He-3 option in the QD-PPMS system allowed us to measure down to 0.4 K when necessary. The outer layers of the samples were cleaved and the remaining sample was cut to typical  $2 \times 2 \text{ mm}^2$  with mass between 5 *mg* to 15 *mg*. The samples were attached to the heat capacity platform with a thin layer Apiezon N grease. The sample chamber was pumped down to 0.01 *mTorr* to minimize the thermal contact with the environment.

The heat capacity option in QD-PPMS uses a relaxation technique. During each measurement, a known amount of heat is applied at a constant power for a fixed time (heating process); this is followed by a cooling time of the same duration. After each measurement cycle (a heating process and a cooling process), the heat capacity values can be obtained by fitting the entire temperature response of the sample platform to a model which includes both thermal relaxation of the sample platform to the bath temperature and the thermal relaxation between the platform and sample itself.

### 3.2.6 Signatures of structural, antiferromagnetic and superconducting phase transitions in transport and thermodynamic measurements

Characteristic signatures of structural, antiferromagnetic and superconducting phase transitions manifesting in resistivity, magnetization and heat capacity measurements near the transition temperatures are shown in Fig. 3.7.

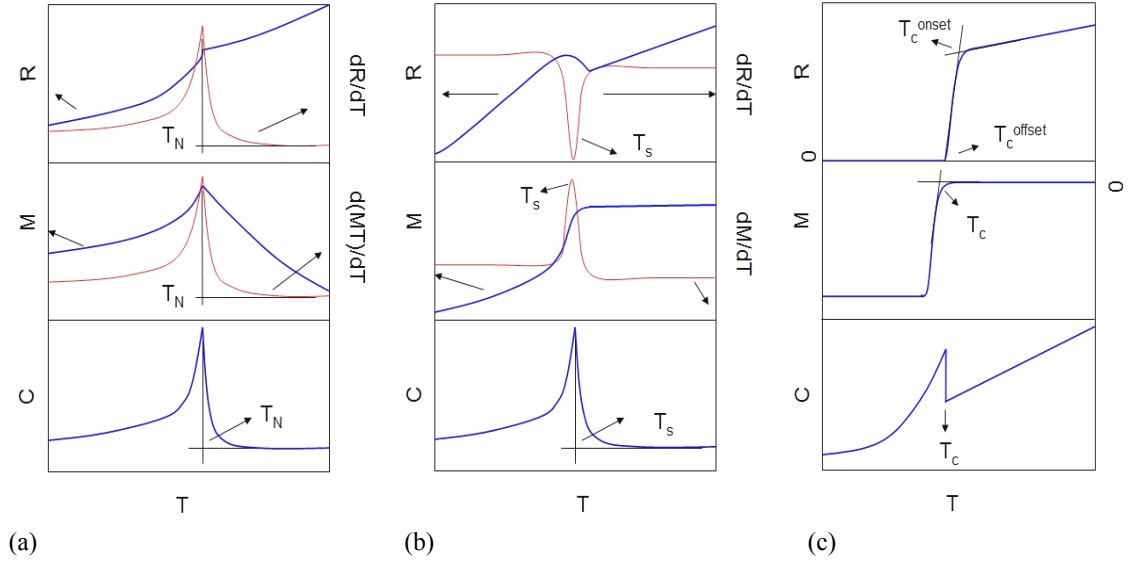


Figure 3.7 Characteristic signatures in resistivity, magnetization and heat capacity measurements near the transition temperature of a (a) antiferromagnetic phase transition. (b) structural phase transition. (c) superconducting phase transition.

Typical signatures of a second order antiferromagnetic phase transition are presented in Fig. 3.7 (a). Due to the loss of spin disorder scattering, a drop in resistivity can be observed. A decrease in the temperature dependent susceptibility caused by the long range antiferromagnetic ordering leads to a relatively sharp feature in the magnetization. A "λ" peak indicating a second order phase transition can be detected in the heat capacity measurement. The antiferromagnetic transition temperature,  $T_N$ , can be directly inferred from the peak in  $C_p$  as shown in Fig. 3.7 (a), or from the peaks in  $d(MT)/dT$  and  $d(\rho)/dT$ , which have been proved to be proportional to the heat capacity singularity near  $T_N$  by M. E. Fisher [135, 136].

A structural phase transition often leads to a decrease of density of states at Fermi level,  $D(E_f)$ , a particularly clear example of this is a charge density wave, which can partially gap part of the Fermi surface. A compound undergoing such a structural phase transition will manifest: an abrupt upturn in resistivity due to the decrease in the conduction electrons, a decrease in the Pauli susceptibility associated with the decrease of  $D(E_f)$ , and a peak in specific heat indicating the occurrence of a phase transition, as shown in Fig. 3.7 (b). The



structural phase transition temperature,  $T_s$ , can be inferred from the peaks of  $d\rho/dT$ ,  $dM/dT$  and  $C_p$ .

Fig. 3.7 (c) presents the features associated with the superconducting phase transition. Due to the characteristics of a superconductor which we have discussed in Chapter 2, a compound undergoing a superconducting transition will manifest zero resistivity, large diamagnetism in the field-cooled measurement and a specific heat jump, which is  $1.43\gamma T_c$  for a BCS superconductor. The general criteria to infer superconducting temperature,  $T_c$ , are shown in Fig. 3.7 (c) as well.

## CHAPTER 4. Physical properties of $\text{BaFe}_2\text{As}_2$ single crystals

### 4.1 Introduction

Since the focus of this thesis is the effects of transition metal doping (TM=Co, Ni, Cu, Co /Cu mixture, Rh and Pd) on  $\text{BaFe}_2\text{As}_2$  single crystals, before outlining the results of our doping studies, I will first focus on the physical properties of  $\text{BaFe}_2\text{As}_2$  single crystals grown from both FeAs flux and Sn flux.

### 4.2 Results and discussion

#### 4.2.1 Single crystalline $\text{BaFe}_2\text{As}_2$ grown from FeAs flux

Single crystals of  $\text{BaFe}_2\text{As}_2$  can be grown from excess FeAs solution (see chapter 3). Fig. 4.1 (a) shows the normalized, temperature dependent, in-plane resistivity,  $\rho_a(T)/\rho_a(300\text{K})$ , where the current flows through  $ab$  plane. As the temperature decreases, the resistivity decreases with a smaller slope above  $T_{s/m}$  and a larger slope below  $T_{s/m}$ . Comparing with polycrystalline samples (see Fig. 1.3 (a)) [40], there is a clear, gradual drop in resistance upon cooling from room-temperature to  $\sim 140$  K and there is a much sharper resistivity drop at  $T_{s/m}$ . The upper left inset in Fig. 4.1 (a) shows the temperature derivative of the normalized resistivity, a clear kink associated with a sudden slope change in resistivity can be observed at 134 K, the criterion to determine  $T_{s/m}$  is shown. RRR,  $\rho(300\text{K})/\rho(2\text{K})$ , of this single crystal is around 2.5, which is comparable to the values of  $\text{BaFe}_2\text{As}_2$  single crystals grown from FeAs flux in other groups [26, 30], but is smaller than 6, the one in polycrystalline  $\text{BaFe}_2\text{As}_2$  (see Fig. 1.3 (a)) [40].

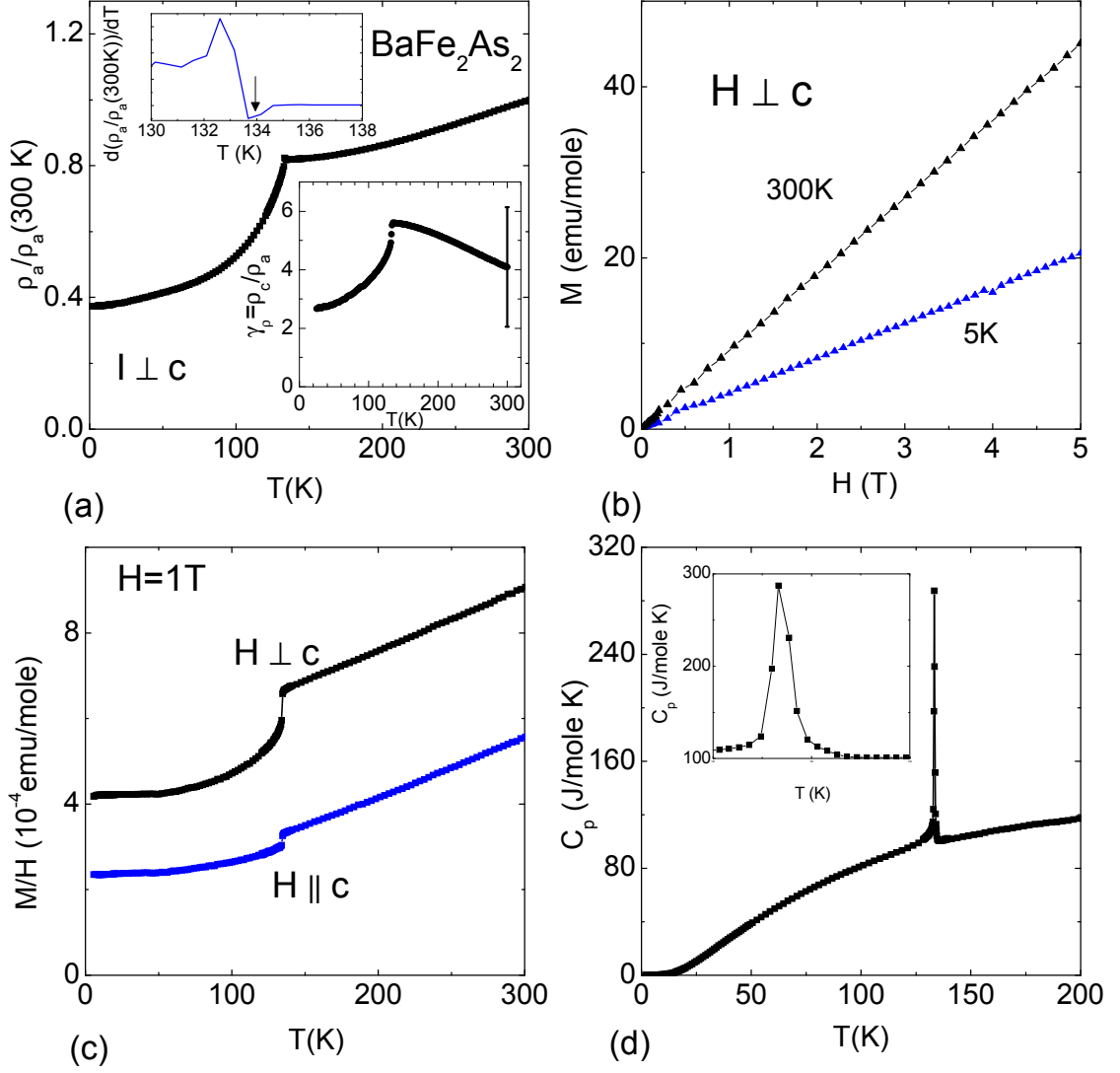


Figure 4.1 Single crystalline  $\text{BaFe}_2\text{As}_2$  grown from FeAs flux: (a) Normalized in-plane resistivity  $\rho_a(T)/\rho_a(300K)$  vs.  $T$ . Inset:  $d(\rho_a(T)/\rho_a(300K))/dT$  vs.  $T$  near the phase transition (upper left); anisotropic parameter  $\gamma_p = \rho_c/\rho_a$  [53] (lower right). (b)  $M$  vs.  $H$  taken at 5 K and 300 K with  $H \perp c$ . (c)  $M/H$  vs.  $T$  taken at 1 T with  $H \parallel c$  and  $H \perp c$ . (d)  $C_p$  vs.  $T$ . Inset: enlarged  $C_p$  vs.  $T$  near the phase transition.

The anisotropic parameter [53] defined as the ratio of the out-of-plane resistivity over the in-plane resistivity,  $\gamma_p = \rho_c / \rho_a$ , is shown in the lower right inset of Fig. 4.1 (a). With increasing temperature,  $\gamma_p$  manifests a slow increase below  $T_{s/m}$ , a sharp upturn near  $T_{s/m}$  and a slow decrease above  $T_{s/m}$ . Considering the error bars,  $\gamma_p$  of  $\text{BaFe}_2\text{As}_2$  at room temperature ranges from 2 to 6. Resistivity measurements for 5 pieces of  $\text{BaFe}_2\text{As}_2$  single crystals presented in reference [53] give the value of  $260 \pm 55 \mu\Omega \text{ cm}$  for the in-plane  $\rho_a(300\text{K})$  and  $1760 \pm 1310 \mu\Omega \text{ cm}$  for the out-of-plane  $\rho_c(300\text{K})$ , which are comparable to  $1200 \mu\Omega \text{ cm}$  inferred from the polycrystalline samples.

The field dependent magnetization measurement up to 5 T taken at 5 K and 300 K with  $H$  perpendicular to  $c$  axis is shown in Fig. 4.1 (b). The temperature dependent  $M/H$  at  $H = 1$  T with the magnetic field applying along  $c$  axis and perpendicular to  $c$  axis is presented in Fig. 4.1 (c). No Curie-tail type feature, which was seen in polycrystalline  $\text{BaFe}_2\text{As}_2$  at low temperatures (see Fig. 1.3 (a)) [40], can be observed in single crystalline  $\text{BaFe}_2\text{As}_2$  grown from FeAs flux. The data from 4.1 (b) and (c) demonstrate the non-existence of moment bearing and ferromagnetic impurities. Comparing to polycrystalline samples, the susceptibility manifests a clear and sudden drop in susceptibility at  $T_{s/m}$ . An almost T-linear behavior of the susceptibility can be observed for both directions with the same slope above the structural / magnetic phase transition temperature. At room temperature,  $M/H$  is around  $5 \times 10^{-4} \text{ emu/mole}$  when  $H$  is along  $c$  axis whereas it is about  $9 \times 10^{-4} \text{ emu/mole}$  when  $H$  is perpendicular to  $c$  axis. This fact leads to the magnetic anisotropy,  $M^{\perp c} / M^{\parallel c}$  around 1.8, which is comparable to the value of 1.5 with  $(M/H)^{\perp c}$  around  $12 \times 10^{-4} \text{ emu/mole}$  and  $(M/H)^{\parallel c}$  around  $8 \times 10^{-4} \text{ emu/mole}$  in reference [26].

The temperature dependent heat capacity data are presented in Fig. 4.1 (d). Comparing with polycrystalline samples (see Fig. 1.3 (c)) [40], a much sharper and narrower peak associated with the structural / magnetic phase transition is observed as shown in the inset.

FeAs-self flux grown single crystals manifest clearer features of the structural / magnetic phase transitions at  $T_{s/m} = 134$  K than the ones shown in polycrystalline samples. In addition the resistive and magnetic anisotropies are measured. These data will serve as a base line for

our doping studies.

#### 4.2.2 Single crystalline $\text{BaFe}_2\text{As}_2$ grown from Sn flux

The first single crystals of  $\text{BaFe}_2\text{As}_2$  were grown out of Sn flux in our group using conventional high temperature solution growth method [25]. Although Sn was a particularly simple flux to use, it resulted in slight Sn doping. Elemental analysis gave a Ba : Fe : As ratio of 1:2:2 with approximately 1% Sn, which is not surface Sn simply associated with small amounts of residual flux, but rather Sn that has been incorporated into the  $\text{BaFe}_2\text{As}_2$  lattice. In reference [25], it was suggested from WDS measurement that Sn likely was substituted for As sites, however, it was latter found from single crystal X-ray measurements that Sn was substituted for Ba sites [137, 138].

The temperature dependent resistivity data for single crystalline  $\text{BaFe}_2\text{As}_2$  grown from Sn flux with current flowing through  $ab$  plane is shown in Fig. 4.2(a). It shows a different shape of resistivity compared to the ones of polycrystalline samples and single crystals grown from FeAs flux. For  $90 \text{ K} < T < 300 \text{ K}$ , the resistivity is weakly temperature dependent.  $\rho(300\text{K})$  is around  $1000 \mu\Omega \text{ cm}$  which is almost 4 times larger than the in-plane resistivity of  $\text{BaFe}_2\text{As}_2$  grown from FeAs flux; as the sample is cooled below  $\sim 85 \text{ K}$  the resistivity increases rapidly rather than decreasing, and at  $4 \text{ K}$  the resistivity reaches  $1200 \mu\Omega \text{ cm}$ , which is approximately 50% larger than it is at  $90 \text{ K}$ . The application of a  $7 \text{ T}$  magnetic field perpendicular to the  $c$ -axis has no effect on the  $T \sim 85 \text{ K}$  phase transition and only the smallest effect on the  $T < 10 \text{ K}$  resistivity.

Temperature dependent  $M/H$  data taken at  $0.1 \text{ T}$  with  $H$  applying along  $c$  axis and perpendicular to  $c$  axis are presented in Fig. 4.2(b). A Curie-Weiss like behavior can be observed in the whole temperature range, which is quite different from those of the polycrystalline samples and single crystals grown from FeAs flux. The magnitude of the  $M(T)/H$  data from the Sn-grown sample is almost one order larger than the ones measured in polycrystalline samples and single crystals grown from FeAs flux. Near room temperature the sample is close to isotropic, but below  $\sim 85 \text{ K}$  there is a larger anisotropy with  $\chi_{\parallel c} < \chi_{\perp c}$ . A small kink around

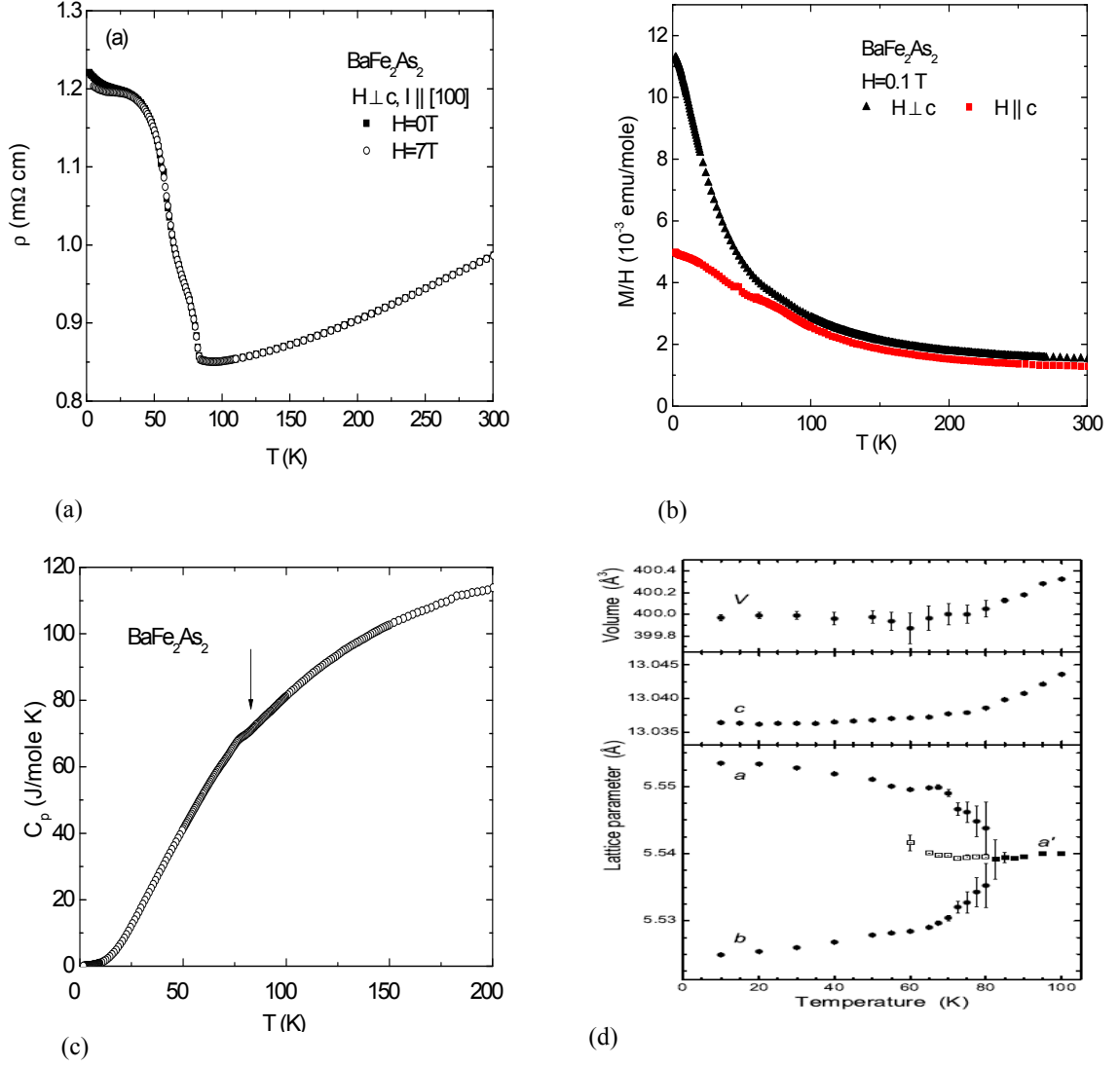


Figure 4.2 Single crystalline  $\text{BaFe}_2\text{As}_2$  grown from Sn flux: (a) Temperature dependent in-plane electrical resistivity taken at 0 and 7 T with  $H \perp c$ . (b)  $M(T)/H$  taken at 0.1 T with  $H \parallel c$  and  $H \perp c$ . (c)  $C_p$  vs.  $T$ . (d) Lattice parameters and unit-cell volume for the tetragonal and orthorhombic phases. For clarity, the lattice parameter  $a$  in the high-temperature tetragonal phase has been multiplied by a factor of  $\sqrt{2}$  so as to allow for comparison to the low temperature orthorhombic phase data [25].

85 K can be better seen in the  $\chi_{\parallel c}$  data, there is a clear break in slope in the  $\chi_{\perp c}$  data near this temperature as well.

The temperature dependent  $C_p$  data for Sn-grown  $\text{BaFe}_2\text{As}_2$  are shown in Fig. 4.2(c). There is a broad feature near 85 K which is consistent with the resistivity and magnetization measurements. This feature in heat capacity is different from the very sharp peak around 134 K observed in the polycrystal as well as single crystals from FeAs flux.

The resistivity, magnetization and specific heat data shown in Fig. 4.2(a), (b) and (c) manifest a feature near 85 K which is quite different from the feature associated with the 140 K transition reported for the polycrystalline samples of  $\text{BaFe}_2\text{As}_2$  [23]. Given that these single crystals have been grown out of excess Sn, appear to have a small, but detectable amount of Sn incorporated into their bulk, and show a slightly expanded  $c$ -axis at room temperature, it is plausible that the changes that we have found are another manifestation of the fact that this transition is very sensitive to small changes in stoichiometry, band filling and / or lattice parameter. To answer the question whether the nature of the 85 K transition in these crystals is similar to the structural phase transition that was found in pure  $\text{BaFe}_2\text{As}_2$  samples, temperature dependent single crystal X-ray diffraction data were collected on  $\text{BaFe}_2\text{As}_2$ . Fig. 4.2(d) plots the temperature dependence of the lattice parameters between 10 and 100 K. In addition to the splitting of the tetragonal  $a$ -lattice parameter below 85 K, the  $c$ -lattice parameter and the unit cell volume change their temperature dependencies below 85 K as well, becoming essentially temperature independent at lower temperatures. The relative splitting of the lattice parameter in the orthorhombic phase is approximately 70% of the splitting found in the polycrystalline material [40], due presumably to the Sn incorporation in the lattice.

Neutron scattering measurement on  $\text{BaFe}_2\text{As}_2$  single crystals grown out of Sn have been made [139]. A simultaneous tetragonal to orthorhombic and paramagnetic to antiferromagnetic phase transitions  $\sim 90\text{K}$  were found. The ordered magnetic moment is  $\sim 0.99 \mu_B / \text{Fe}$ , which is larger than  $0.87 \mu_B / \text{Fe}$ , the one for polycrystalline sample [46].

Compared with pure  $\text{BaFe}_2\text{As}_2$ , Sn doped  $\text{BaFe}_2\text{As}_2$  manifests different transport and ther-

modynamic behavior. The changes in shape of the resistivity, magnetization and heat capacity have been reproduced and reported by several other groups [139, 140]. On the other hand, the intrinsic physics, the structural / magnetic phase transition, still exist and shift to a lower temperature similar to the effects of transition metal doping on  $\text{BaFe}_2\text{As}_2$ , as will be shown in chapter 5 and 6. In this sense, Sn was our first, unintentional dopant.

### 4.3 Summary

$\text{BaFe}_2\text{As}_2$  single crystal grown out of FeAs flux, shows a rapid resistivity decrease, an abrupt susceptibility drop and a sharp heat capacity peak associated with the structural / magnetic phase transition at 134 K, which resemble the features of these measurements in polycrystalline  $\text{BaFe}_2\text{As}_2$  with even sharper and narrower signatures.

$\text{BaFe}_2\text{As}_2$  single crystals grown out of Sn flux manifest different transport and thermodynamic behaviors from both polycrystals and single crystals grown from FeAs flux. A rapid resistivity rise, a small kink embedded in the Curie-Weiss like susceptibility and a broad peak in heat capacity occur near 85 K. The single crystal X-ray diffraction and neutron scattering measurements reveal that the nature of these different features in  $\text{BaFe}_2\text{As}_2$  single crystal grown out of Sn flux is the same as the other two: simultaneous tetragonal to orthorhombic and paramagnetic to antiferromagnetic phase transitions [25, 139]. The suppression of these transition from 134 K to  $\sim 85$  K is due to around 1% of Sn incorporation into the lattice. It implies  $\text{BaFe}_2\text{As}_2$  could be tuned by small changes in stoichiometry, however, the amount of Sn incorporated into the sample could not be readily controlled. Systematic and controlled doping studies of  $\text{BaFe}_2\text{As}_2$  by other means are required.



## CHAPTER 5. Transport, thermodynamic properties and anisotropic $H_{c2}$ of $\text{Ba}(\text{Fe}_{1-x}\text{Co}_x)_2\text{As}_2$ single crystals

### 5.1 Introduction

The discovery of superconductivity in K-doped  $\text{BaFe}_2\text{As}_2$  [23] compounds at 38 K attracted a lot of attention due to the availability of sizable single crystalline samples [25, 27, 141, 142, 143, 144, 145]. However, single crystals of K-doped  $\text{BaFe}_2\text{As}_2$  have large K concentration variations, as mentioned in chapter 3.1.2.2. This inhomogeneity of the  $(\text{Ba}_{1-x}\text{K}_x)\text{Fe}_2\text{As}_2$  samples has hindered the systematic study across the whole superconducting range. On the other hand, the realization of superconductivity in Co doped  $\text{BaFe}_2\text{As}_2$  [30] provides another opportunity to study the interplay of structure, magnetism, and the superconductivity in Fe pnictides. Although the transition temperature  $T_c$  is 24 K or less, the Co doped  $\text{BaFe}_2\text{As}_2$  series has become an archetypical system, and extensive experimental efforts [33, 34, 36, 37, 39, 146, 147] have been made to characterize and delineate the nature of superconductivity.

In this chapter, detailed structural, transport and thermodynamic measurements of single crystalline  $\text{Ba}(\text{Fe}_{1-x}\text{Co}_x)_2\text{As}_2$ , including measurements of the anisotropic upper critical field,  $H_{c2}(T)$ , up to 35 T, are presented. The analysis of these data allows us to create a detailed temperature-doping phase diagram that indicates: i) the structural and magnetic phase transitions, that are coincident for  $x = 0$ , separate as they are suppressed with Co doping. ii) superconductivity occurs in both orthorhombic / antiferromagnetic and tetragonal / paramagnetic phases, an observation that is clearly reflected by significant differences in the anisotropy of  $H_{c2}$  in these two regions.

## 5.2 Experimental results

### 5.2.1 Structural, transport and thermodynamic properties

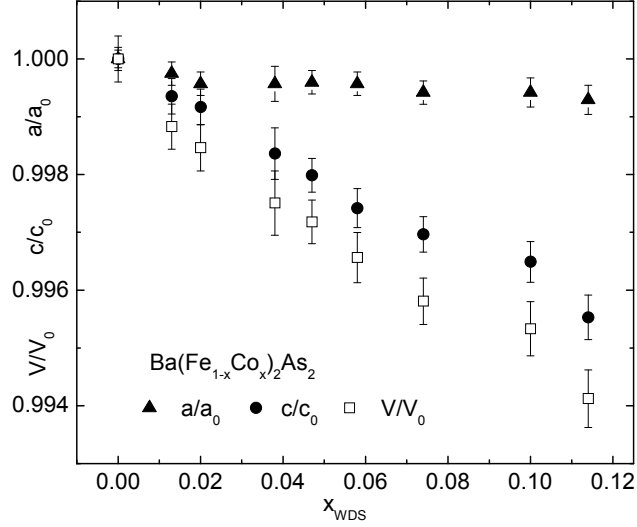


Figure 5.1 Lattice parameters,  $a$  and  $c$  as well as unit cell volume,  $V$ , normalized to the values of pure  $\text{BaFe}_2\text{As}_2$  as a function of measured Co concentration,  $x_{WDS}$  [34].

Fig. 5.1 presents the unit cell parameter data as a function of the WDS measured Co concentration,  $x_{WDS}$ . The lattice parameters are normalized to the parameters of  $\text{BaFe}_2\text{As}_2$ ,  $a_0 = 3.9621(8)\text{\AA}$ ,  $c_0 = 13.0178(20)\text{\AA}$  and  $V = 204.3565(814)\text{\AA}^3$ , so that the relative change in lattice constants can be seen. A monotonic, and essentially linear, decrease in the  $a$ - and  $c$ -lattice parameters, as well as the unit cell volume was observed. The Co substitution for the Fe site mainly affected the lattice parameter  $c$  in the sense that at  $x=0.114$  the decrease in the lattice parameter  $c$  is roughly 0.5% whereas the decrease in  $a$  is only 0.07%.

The temperature dependent electrical resistivity curves of  $\text{Ba}(\text{Fe}_{1-x}\text{Co}_x)_2\text{As}_2$  series, normalized to their room temperature values, are shown in Fig. 5.2. As outlined in chapter 4, for  $\text{BaFe}_2\text{As}_2$ ,  $x = 0.00$ , the sharp decrease in resistivity at 134 K is associated with the combined structural and antiferromagnetic transition [23, 46]. With Co doping, the temperature of the resistive anomaly is suppressed monotonically, no longer being detectable for  $x > 0.058$ . For  $x \geq 0.038$ , superconductivity is readily detected by a sharp, and complete, decrease of the

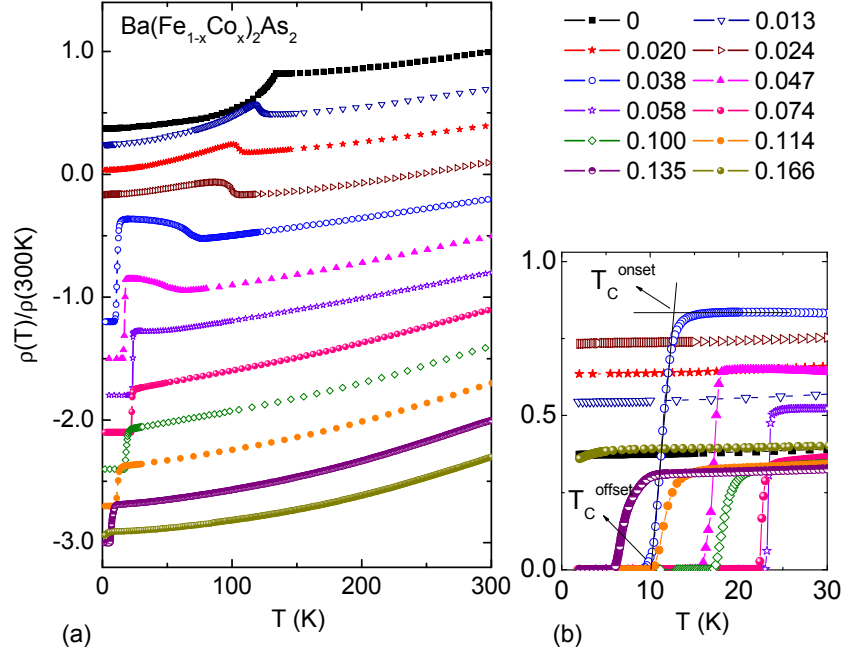


Figure 5.2 (a) Electrical resistivities normalized to their room temperature values for  $\text{Ba}(\text{Fe}_{1-x}\text{Co}_x)_2\text{As}_2$  single crystals ( $0.00 \leq x_{WDS} \leq 0.166$ ). Each subsequent data set is shifted downward by 0.3 for clarity. (b) Low temperature data showing superconducting transition [34].

resistivity to zero. This is shown more clearly in the inset of Fig. 5.2. The zero resistivity temperature starts to show up around 10 K at  $x = 0.038$ . This temperature rises to 23 K at  $x = 0.058$  and 0.074. With even more Co doping, this temperature is lowered to 10 K at  $x=0.114$ , 6 K at  $x=0.135$  and completely suppressed at  $x=0.166$ . For  $x = 0.038, 0.047$  and even 0.058, both the higher temperature resistive anomaly and superconductivity are detected.

It is worth noting that for the lowest three Co substitution levels,  $x = 0.013, 0.020$  and 0.024, the resistive anomaly is very reminiscent of that seen for pure  $\text{CaFe}_2\text{As}_2$  [130, 148, 149]: the resistivity abruptly increases below the high temperature transition and then decreases again. But for  $x = 0.038$  and 0.047, the resistive anomaly shows a broad upturn with decreasing temperature, which is very similar to that originally found for  $\text{BaFe}_2\text{As}_2$  grown out of Sn flux [25] inside which  $\sim 1 - 2\%$  Sn was found to be substituted for the Ba sites [137, 138]. A similar evolution of the shape of resistive anomaly can be seen by comparing the resistivity of single

crystal  $\text{SrFe}_2\text{As}_2$  [129] to those of polycrystalline  $\text{Sr}(\text{Fe}_{1-x}\text{Co}_x)_2\text{As}_2$  [150]. For the Co doping level  $x = 0.075$  in polycrystalline  $\text{Sr}(\text{Fe}_{1-x}\text{Co}_x)_2\text{As}_2$ , an increase similar to what we observe for  $x = 0.038$  and  $0.047$  in  $\text{Ba}(\text{Fe}_{1-x}\text{Co}_x)_2\text{As}_2$  can be found.

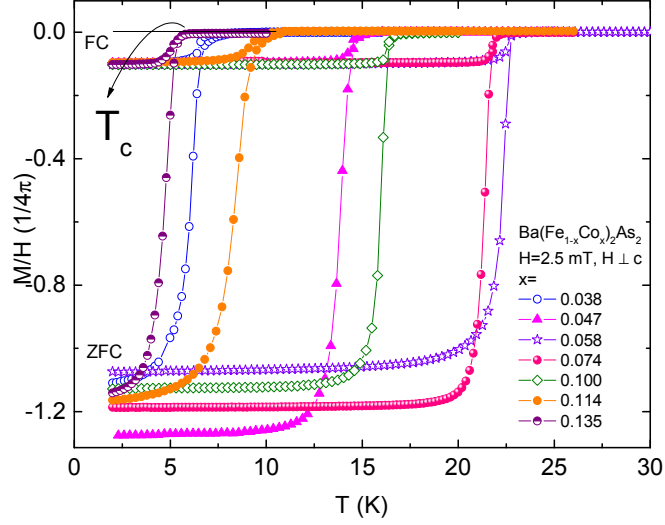


Figure 5.3  $M/H$  vs.  $T$  of  $\text{Ba}(\text{Fe}_{1-x}\text{Co}_x)_2\text{As}_2$  single crystals taken at 2.5 mT with  $H \perp c$ . Zero-field-cooled warming data as well as field-cooled warming data are shown [34].

Both the antiferromagnetic / structural phase transition as well as superconductivity can also be detected in temperature dependent magnetization measurements. Fig. 5.3 presents the  $M(T)/H$  data in 2.5 mT with applied field perpendicular to the crystallographic  $c$ -axis of the samples. Each data set is compared to  $1/4\pi$  (by using the unit cell volume). The upper curves are field-cooled data whereas the lower curves are zero-field-cooled data. The field-cooled magnetization data manifest clear Meissner effect. Fig. 5.4 shows the  $M(T)/H$  data taken at 1 T with the field perpendicular to  $c$ -axis. For  $0.00 \leq x \leq 0.047$  (upper panel) there is a clear drop in the susceptibility at the temperature associated with the higher resistive anomaly and a lower temperature feature associated with superconductivity for  $x = 0.038$  and  $0.047$ . For  $0.047 \leq x \leq 0.135$  (lower panel) superconductivity feature can be observed, but there is no longer any signature of the higher temperature structural / magnetic transition. At  $x=0.166$ , neither structural / magnetic phase transition nor superconductivity can be detected, which

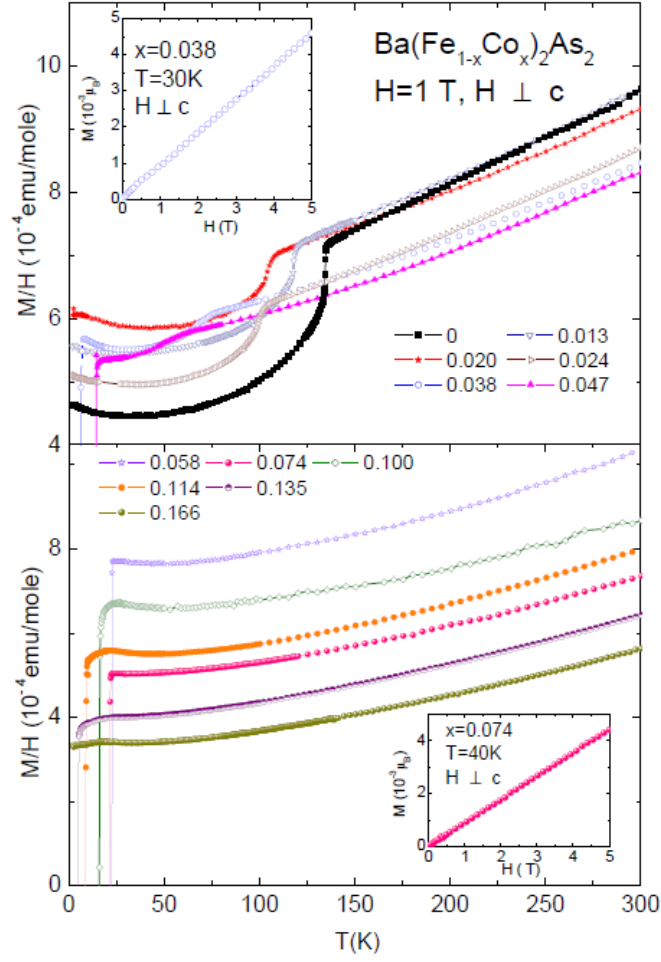


Figure 5.4  $M/H$  vs.  $T$  of  $\text{Ba}(\text{Fe}_{1-x}\text{Co}_x)_2\text{As}_2$  single crystals taken at 1 T with  $H \perp c$ . Insets:  $M(H)$  data of selected Co concentrations [34].

is consistent with the resistivity measurement shown in Fig. 5.2. It is worth noting that the high field magnetization data show an almost linear behavior at high temperatures [38].

Specific heat data ( $H = 0$  and 9 T applied along the crystallographic  $c$ -axis) were measured for Co-doping levels of  $x = 0.038$  and  $0.047$ , which are shown in Fig. 5.5 up to 90 K. For  $x = 0.038$  two breaks in slope quite similar to the data in specific heat measurement of  $\text{LaFeAsO}$  (see Fig. 1.3 (d)) [42] can be seen near the temperature where the resistive anomaly and susceptibility drop occur. These features can be more clearly identified by examining the  $dC_p/dT$  plot in the lower inset. A similar pair of features can also be observed in the  $x = 0.047$

data (these high temperature features will be discussed in section 5.3). A lower temperature feature near the  $T_c$  values identified from the resistivity and susceptibility data shown in Figs. 5.2, 5.3 and 5.4 can also be observed in the specific heat. This feature is even more clearly resolved by comparison with the 9 T data shown in the upper insets of Fig. 5.5.

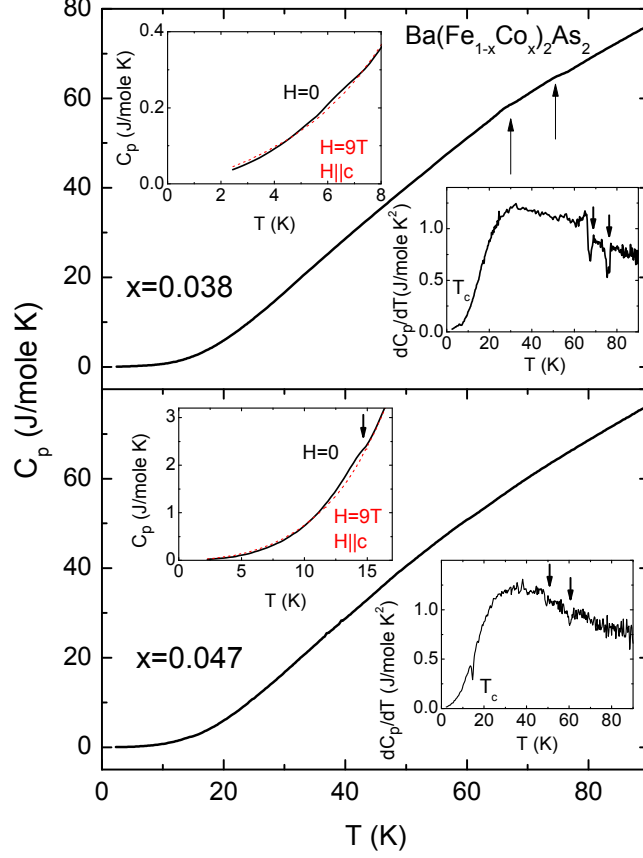


Figure 5.5  $C_p$  vs.  $T$  of  $\text{Ba}(\text{Fe}_{1-x}\text{Co}_x)_2\text{As}_2$  with  $x = 0.038$  (upper panel) and  $0.047$  (lower panel). Lower insets:  $dC_p/dT$ . Upper insets: low temperature  $C_p(T)$  data taken at 0 (solid line) and 9 T (dashed line) with  $H||c$  [34].

Specific heat measurements taken at  $H=0$  also have been performed on compounds with  $x = 0.058, 0.074, 0.10$  and  $0.114$  up to 25 K as presented in Fig. 5.6 [54]. The heat capacity jumps associated with the superconducting transitions are observed in all these concentrations. This feature is relatively sharp for Co-doping levels of  $x = 0.058$  and  $0.074$ , which have the highest  $T_c$ s, and is readily associated with a classical second order phase transition to a low

temperature, superconducting state. For the other  $x$  values, the low temperature anomalies associated with the superconducting phase transition are broader.

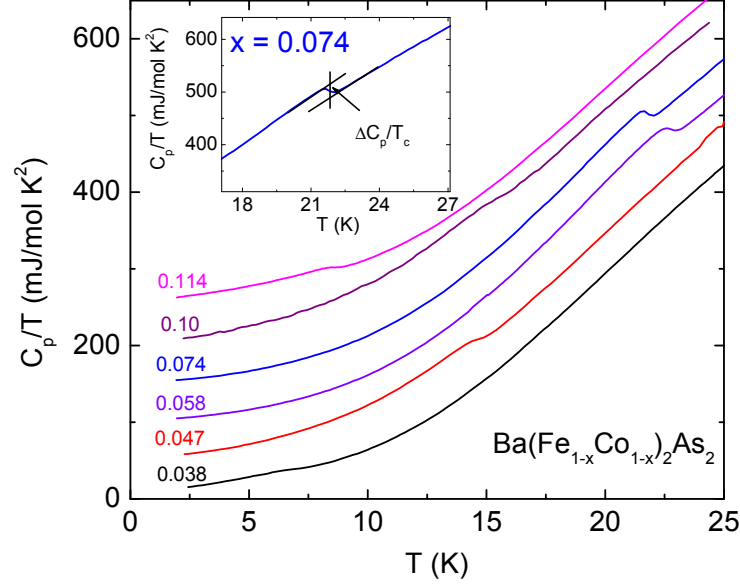


Figure 5.6  $C_p$  vs.  $T$  of the superconducting  $\text{Ba}(\text{Fe}_{1-x}\text{Co}_x)_2\text{As}_2$ . Data are shifted by a multiple of  $50 \text{ mJ/mol K}^2$  along the  $y$  - axis for clarity. Inset: enlarged  $C_p/T$  vs.  $T$  plot near  $T_c$  for  $\text{Ba}(\text{Fe}_{0.926}\text{Co}_{0.074})_2\text{As}_2$ , lines show the "isoentropic" construction to infer  $T_c$  and  $\Delta C$  [54].

### 5.2.2 Anisotropic $H_{c2}(T)$ curves

In order to study the effects of doping on the superconducting state in greater details, anisotropic  $H_{c2}(T)$  data were collected for  $x = 0.038, 0.047, 0.058, 0.10$  and  $0.114$  doping levels that manifest superconductivity. A representative data set of  $R(H)$  data for  $H \parallel c$  and  $H \perp c$  for  $x = 0.038$  compound is shown in Fig. 5.7. The onset and offset criteria that were used to infer  $H_{c2}$  from a given  $R(H)$  curve are shown in Fig. 5.7. These two criteria help define the width of the transition seen in the  $R(H)$  data and will give a sense of the range of possible  $H_{c2}(T)$  values. Figs. 5.8 and 5.9 present the anisotropic  $H_{c2}(T)$  plots inferred from the  $R(H)$  data for each criterion (using two samples for each field direction). In the  $\text{Ba}(\text{Fe}_{1-x}\text{Co}_x)_2\text{As}_2$  series, grossly speaking, the  $H_{c2}(T)$  is higher for larger  $T_c$  values, with  $H_{c2}^{\perp c}(T) > H_{c2}^{\parallel c}(T)$ .

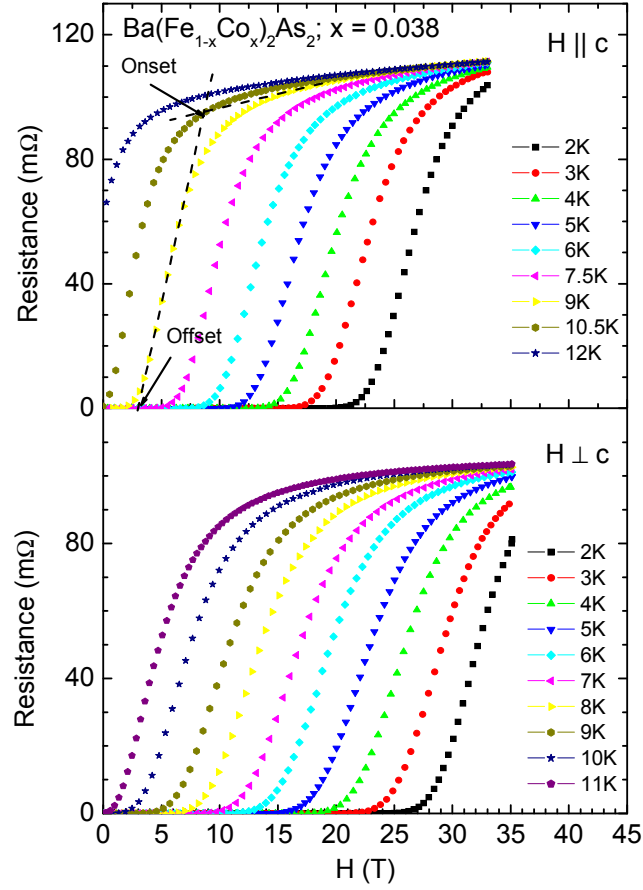


Figure 5.7 Isothermal  $R(H)$  data of  $\text{Ba}(\text{Fe}_{1-x}\text{Co}_x)_2\text{As}_2$  ( $x = 0.038$ ) with  $H \parallel c$  (upper panel) and  $H \perp c$  (lower panel). Dotted lines show onset and offset criteria used to determine  $H_{c2}(T)$  values [34].

Whereas, for the samples with lower  $T_c$  values the 35 T maximum field was almost enough to fully determine the  $H_{c2}(T)$  curves, the samples with  $T_c$  values above 20 K have  $H_{c2}(T = 0)$  values that are significantly larger.

In Fig. 5.8, the left panel shows the  $H_{c2}(T)$  data for  $x = 0.038$  and the right panel shows the data for  $x = 0.114$  sample, both of them have  $T_c$  around 10 K. It can be clearly seen that the  $x = 0.038$  compound has smaller  $H_{c2}$  anisotropy comparing to  $x = 0.114$  sample. For both compounds, the application of 35 T magnetic field almost suppressed the  $T_c$  to 0 K. For  $x = 0.038$  sample,  $H_{c2}^{\perp c}(0)$  can be estimated to be around 40 T from the onset criterion and 35 T from the offset criterion. For  $x = 0.114$  compound,  $H_{c2}^{\perp c}(0)$  is about 35 T from onset



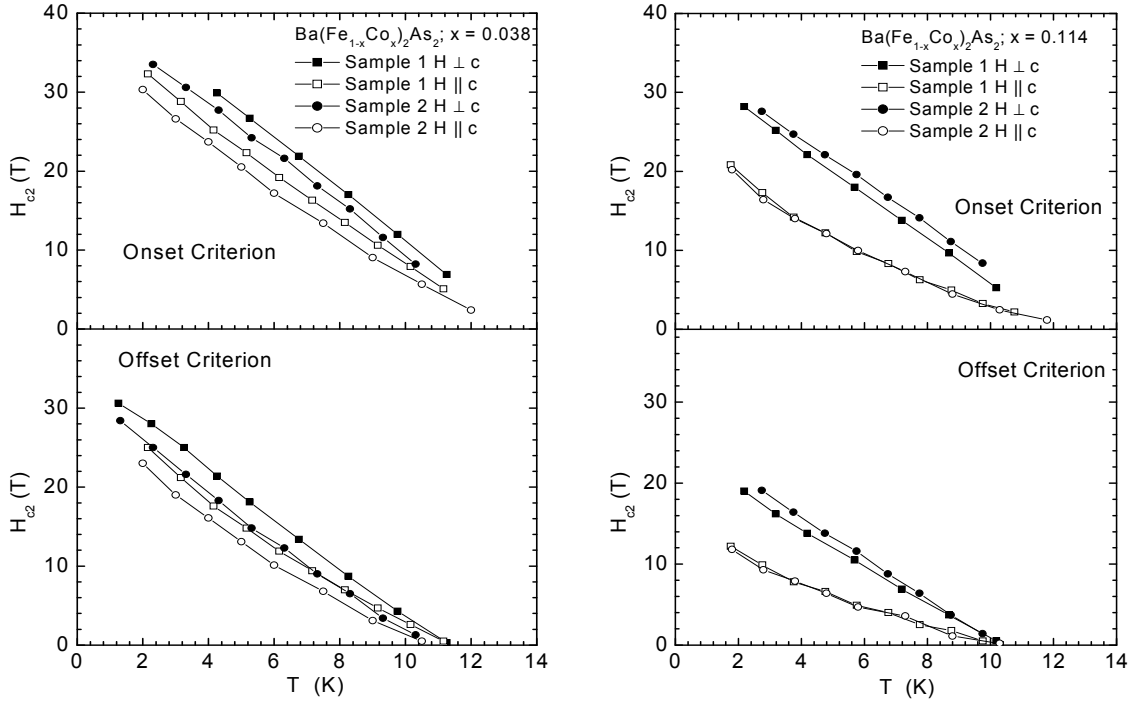


Figure 5.8 Anisotropic  $H_{c2}(T)$  curves determined for Co-doping level of  $x = 0.038$  (left panel) and  $x = 0.114$  (right panel) using onset criterion and offset criteria.

criterion or 25 T from offset criterion.

Fig. 5.9 (a) and (b) present the  $H_{c2}$  data for  $x = 0.047$  and 0.10 compounds, which have  $T_c$  around 17 K. The  $x = 0.047$  compound clearly shows smaller  $H_{c2}$  anisotropy than  $x = 0.10$  compound. The application of 35 T magnetic field only suppresses  $T_c$  by approximately half, as inferred from the onset criterion. Fig. 5.9 (c) and (d) show the  $H_{c2}$  data for  $x = 0.058$  and 0.074 compounds, which have  $T_c$  around 23 K. Since the application of 35 T, which only suppress  $T_c$  by less than 1/3, is not high enough to infer  $H_{c2}(0)$ , the WHH formula for dirty superconductors,  $H_{c2}(0) = -0.693T_c(\frac{dH_{c2}}{dT})|_{T_c}$ , is used to estimate the upper critical field at 0 K. For  $x = 0.058$ , the estimated  $H_{c2}^{\perp c}(0)$  is around 70 T inferred from the onset criterion or 55 T from the offset criterion;  $H_{c2}^{\parallel c}(0)$  is around 40 T. For  $x = 0.074$ , the estimated  $H_{c2}^{\perp c}(0)$  is around 80 T and  $H_{c2}^{\parallel c}(0)$  is around 40 T.

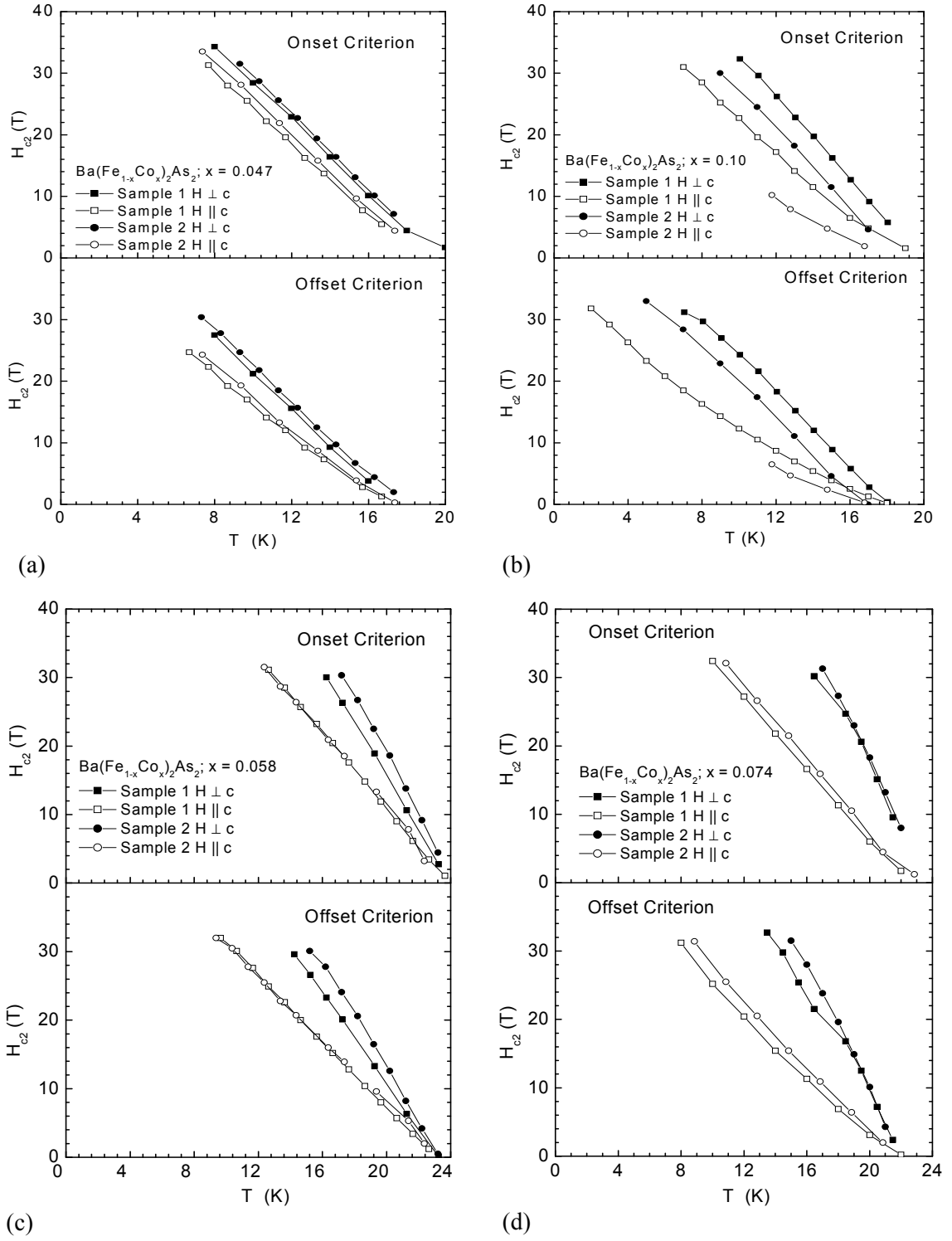


Figure 5.9 Anisotropic  $H_{c2}(T)$  curves determined for Co-doping level of (a)  $x = 0.047$  (b)  $x = 0.10$  (c)  $x = 0.058$  (d)  $x = 0.074$  using onset criterion and offset criteria.

### 5.3 Discussion

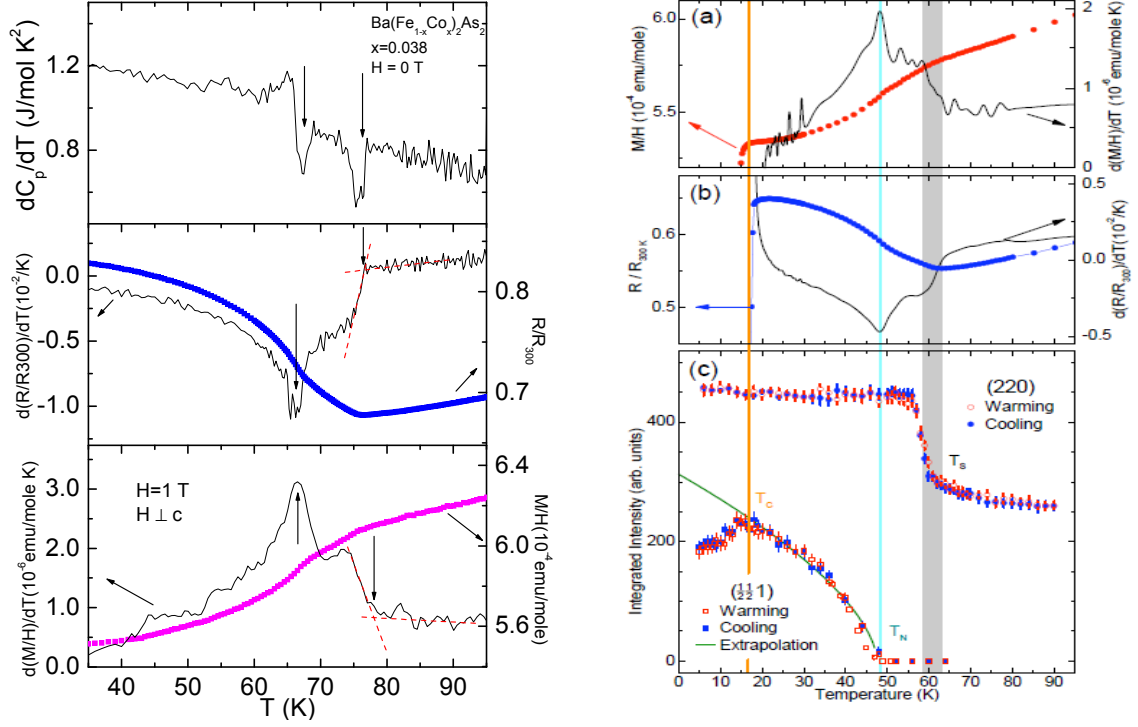


Figure 5.10 (a) Criteria used to determine transition temperatures for upper phase transition. Upper panel:  $dC_p/dT$  emphasizes breaks in slope of  $C_p(T)$  data. Middle panel:  $(dR(T)/dT)/R(300K)$  and  $R(T)/R(300K)$ . Bottom panel:  $d(M(T)/H)/dT$  and  $M(T)/H$ . (b) Neutron scattering measurement [152].

The resistivity, magnetization and specific heat data all clearly show the suppression of the higher temperature structural / magnetic phase transition with increasing Co substitution for Fe. In order to quantify these transitions in details, the criteria to determine the salient temperatures are chosen based on the temperature derivatives of the specific heat, resistivity and susceptibility as shown in Fig. 5.10 (a) [34, 151]. Two features in the resistivity and susceptibility data occur at the similar temperatures as the breaks in slope in the specific heat. There were two possibilities for the observation of these two clear features for intermediate Co concentrations: i) a separation of the structural and magnetic phase transitions that are so strongly coupled for pure  $\text{BaFe}_2\text{As}_2$ . ii) a distribution of transition temperatures associated

with a distribution of Co doping throughout the sample.

dopant	$x$	$\rho$				$M$			$C$		
		$T_s$	$T_m$	$T_c^{onset}$	$T_c^{offset}$	$T_s$	$T_m$	$T_c$	$T_s$	$T_m$	$T_c$
Co	0	134	134			134	134		134	134	
	0.013		119				118				
	0.020	110	104			111	104				
	0.024	105	99			105	99				
	0.038	77	66	12.3	10.5	78	67	8.8	76	68	7
	0.047	64	48	17.8	16.5	64	48	16.1	60	49	14.7
	0.058	$30 \pm 3^*$		23.7	23.1			23.2			22.8
	0.074			22.9	22.3			22.7			21.8
	0.10			19.3	17.4			17.4			15.6
	0.114			12.8	10.4			11.1			8.6
	0.135			8	6			4.5			
	0.166			0	0						

Table 5.1 Summary of  $T_s$ ,  $T_m$  and  $T_c$  from resistivity, magnetization and specific heat measurements for  $\text{Ba}(\text{Fe}_{1-x}\text{Co}_x)_2\text{As}_2$  series. \*: see text.

Neutron scattering measurements shown in Fig. 5.10 (b) demonstrate that these features are associated with the separated structural / magnetic phase transitions [152, 153]. The higher temperature feature corresponds to the structural phase transition whereas the lower temperature feature corresponds to the magnetic phase transition. These measurements support the criteria employed in this thesis to extract the structural / magnetic phase transition temperatures from the thermodynamic and transport data (as shown in Fig. 5.10 (a)).

The criteria to infer the superconducting temperature  $T_c$  also have to be established. For this thesis we use the offset and onset criteria from resistivity data as shown in the inset of Fig. 5.2. In addition an onset criterion for susceptibility shown in Fig. 5.3 is also used. The "isoentropic" construction shown in the inset of Fig. 5.6 is used to determine  $T_c$  from specific heat measurements because of the finite widths of the superconducting transitions.

Using the criteria described above,  $T_s$ ,  $T_m$  and  $T_c$  can be inferred from the transport and thermodynamic measurements. Table 5.1 presents the summary of this information. For the temperature indexed by a "\*", due to the very low structural / magnetic phase transition temperatures, the features associated with them become very broad and weak (e. g. see

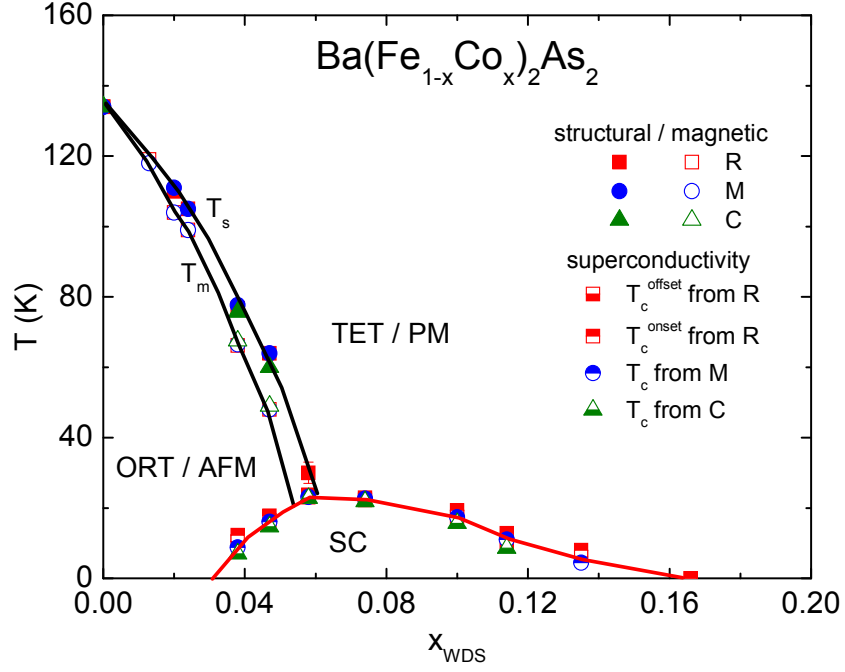


Figure 5.11  $T - x$  phase diagram of  $\text{Ba}(\text{Fe}_{1-x}\text{Co}_x)_2\text{As}_2$  single crystals for  $x \leq 0.166$ .

$x = 0.058$ ) and no detectable kinks can be seen in the derivatives, but we can estimate  $T_s$  by taking the temperature of resistivity minimum as the upper limit of  $T_s$  and the temperature of the inflection point as the lower limit of  $T_s$ . The structural phase transition in  $x = 0.058$  sample has been confirmed by X-ray scattering measurement [154]. Fig. 5.11 shows the temperature - doping concentration ( $T - x$ ) phase diagram which graphically summarizes this information. Filled symbols represent the structural phase transition temperature,  $T_s$ , whereas hollow symbols represent the magnetic phase transition temperature,  $T_m$ . As it can be seen, the structural / magnetic phase transitions are monotonically suppressed and increasingly separate as the Co doping level increases. They are no longer detected in either resistivity or magnetization data for  $x > 0.058$ . A dome-like superconducting region can be observed in this phase diagram: superconductivity is stabilized around 10 K for  $x = 0.038$ , rises to a maximum value of  $\sim 23$  K for  $0.058 \leq x \leq 0.074$ , then drops to  $\sim 10$  K at  $x = 0.114$  again and finally gets completely suppressed at  $x = 0.166$ . It is worth noting that the transition temperatures

inferred from resistivity data (squares), magnetization data (circles) and specific heat data (triangles) are in excellent agreement with each other.

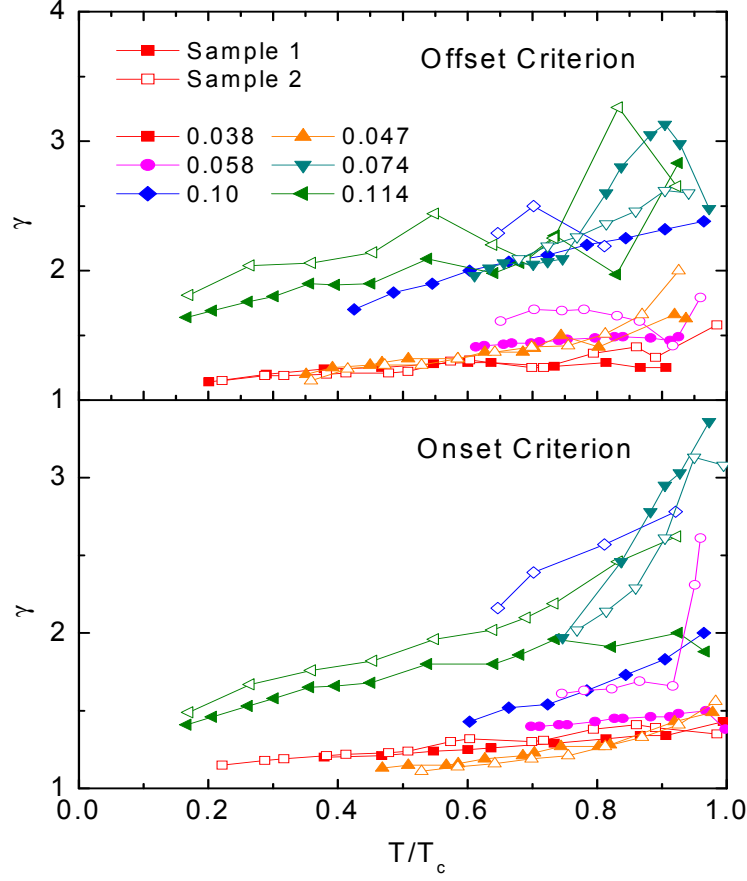


Figure 5.12 Anisotropy of the upper critical field,  $\gamma = H_{c2}^{\perp c}(T)/H_{c2}^{\parallel c}(T)$ , as a function of effective temperature,  $T/T_c$ , for  $\text{Ba}(\text{Fe}_{1-x}\text{Co}_x)_2\text{As}_2$  single crystals. Upper panel: offset criterion; lower panel: onset criterion.

One of the clearest features in Fig. 5.11, as well as the resistivity and magnetization data shown in Figs. 5.2 and 5.4, is the apparent coexistence of the higher temperature, structural / antiferromagnetic phase transitions with lower temperature superconductivity for the lower Co-doping levels. This could imply that superconductivity does exist in the low temperature, orthorhombic / antiferromagnetic state with the assumption that the same parts of the sample are simultaneously superconducting and orthorhombic. Another possibility would be that the sample separates into tetragonal / paramagnetic, superconducting, and orthorhombic / anti-

ferromagnetic, but normal, phases. Some light can be shed on this issue by examining how the properties of the superconducting state vary from one side of the dome to the other. If the superconductivity is associated solely with a tetragonal / paramagnetic phase, there should not be a dramatic change in the anisotropy of the superconductivity across the superconducting dome. On the other hand, if there is a clear difference in the superconducting anisotropy between the samples that are in the orthorhombic part of the phase diagram and the samples that are in the tetragonal part of the phase diagram, this would be the evidence of the superconductivity being affected by the higher temperature phase transition. Fig. 5.12 presents the anisotropy of  $H_{c2}(T)$ ,  $\gamma = H_{c2}^{\perp c}(T)/H_{c2}^{\parallel c}(T)$ , as a function of  $T/T_c$  (extracted from Figs. 5.8 and 5.9). The data inferred from the onset and offset criteria for both samples from each batch are shown. There is a clear bifurcation of data, the three  $\text{Ba}(\text{Fe}_{1-x}\text{Co}_x)_2\text{As}_2$  compounds that are clearly in the tetragonal / paramagnetic phase have an anisotropy varying from 1.5 (low temperature) to 3 (near  $T_c$ ), that is 40 – 60% larger than the samples that manifest superconductivity as well as anomalies associated with the orthorhombic / antiferromagnetic phase transitions. Although this is not proof that superconductivity can arise from the orthorhombic / antiferromagnetic phase, it strongly supports this hypothesis since superconductivity is affected by a different crystallographic / magnetic environment.

We can take a closer look at the anisotropic  $H_{c2}$  measurements. As shown in Fig. 5.12,  $\gamma$  of each  $\text{Ba}(\text{Fe}_{1-x}\text{Co}_x)_2\text{As}_2$  sample, monotonically decreases with decreasing temperature.  $\gamma$  of  $\text{Ba}(\text{Fe}_{1-x}\text{Co}_x)_2\text{As}_2$  samples varies from 1 (low temperature) to 3 (near  $T_c$ ), which is significantly smaller than the values ranging from 5 (low temperature) to 9 (near  $T_c$ ) for superconducting oxypnictides [155, 156, 157, 158]. This fact implies a more 3D character of Fermi surface in  $\text{Ba}(\text{Fe}_{1-x}\text{Co}_x)_2\text{As}_2$  than that of oxypnictides.

To compare the effects of hole doping and electron doping on the superconducting state in Ba122 system,  $H_{c2}$  curves of  $(\text{Ba}_{0.55}\text{K}_{0.45})\text{Fe}_2\text{As}_2$  [144] sample and near-optimally Co doped sample,  $\text{Ba}(\text{Fe}_{0.926}\text{Co}_{0.074})_2\text{As}_2$  [34], are presented in Fig. 5.13. Very similar behaviors can be observed in these two compounds: i)  $(\text{Ba}_{0.55}\text{K}_{0.45})\text{Fe}_2\text{As}_2$  also has a small  $H_{c2}$  anisotropy, monotonically increasing from 1.4 (low temperature) to 3.5 (near  $T_c$ ). ii) for both compounds,

$H_{c2}^{\parallel c}$  curve is roughly linear whereas  $H_{c2}^{\perp c}$  curve has a negative slope and a tendency to saturate.

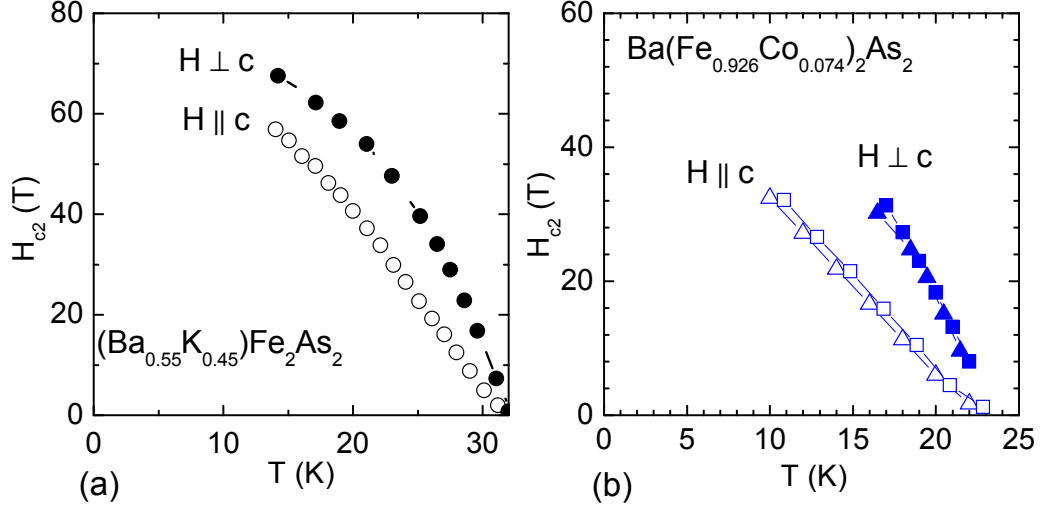


Figure 5.13 (a)  $H_{c2}$  curves of  $(\text{Ba}_{0.55}\text{K}_{0.45})\text{Fe}_2\text{As}_2$  [144] as a function of  $T$ .  
(b)  $H_{c2}$  curves of  $\text{Ba}(\text{Fe}_{0.926}\text{Co}_{0.074})_2\text{As}_2$  [34] as a function of  $T$

## 5.4 Summary and conclusions

The effects of Co substitution for Fe have been studied for  $\text{Ba}(\text{Fe}_{1-x}\text{Co}_x)_2\text{As}_2$  ( $x \leq 0.166$ ) single crystals. The addition of Co monotonically suppresses the higher temperature structural / antiferromagnetic phase transitions at an initial rate of roughly 15 K per atomic percent Co. In addition, superconductivity is stabilized at low temperature for  $x \geq 0.038$  and completely suppressed at our highest doping level of  $x = 0.166$ . The superconducting region has a dome-like appearance with the maximum  $T_c$  values ( $\sim 23$  K) found near  $x \sim 0.07$ . The intermediate values of Co doping lead to a separation of the structural and magnetic phase transitions as indicated by the observation of two features in the temperature derivatives of the thermodynamic and transport data, and supported by neutron scattering measurements. The higher-temperature transition is a tetragonal to orthorhombic, structural phase transition and the lower-temperature transition is associated with the onset of long range order antiferromagnetism.



The  $T - x$  phase diagram inferred for  $\text{Ba}(\text{Fe}_{1-x}\text{Co}_x)_2\text{As}_2$  series suggests the existence of superconductivity in the orthorhombic (antiferromagnetic) phase as well as in the tetragonal (paramagnetic) phase. Analysis of the  $H_{c2}$  anisotropy clearly shows that the superconductivity that occurs in samples that show features associated with the transition to the low temperature orthorhombic / antiferromagnetic state has an  $\sim 50\%$  smaller anisotropy than that is found in samples with higher Co-levels that remain in the tetragonal / paramagnetic phase. This observation strongly supports the hypothesis that superconductivity occurs in both orthorhombic / antiferromagnetic and tetragonal / paramagnetic phases.

On a broader level, for all Co-doping level  $x$ , the higher  $T_c$ , the higher  $H_{c2}(0)$  values. The samples with  $T_c$  values above 20 K have  $H_{c2}(0)$  values that are significantly larger than 35 T whereas for the samples with lower  $T_c$  values the 35 T maximum field was almost enough to fully determine the  $H_{c2}(T)$  plots. The anisotropic  $H_{c2}$  parameter monotonically increases with increasing temperature.

## CHAPTER 6. Transport and thermodynamic properties of Ba(Fe<sub>1-x</sub>TM<sub>x</sub>)<sub>2</sub>As<sub>2</sub> (TM=Ni, Cu, Co / Cu, Rh and Pd) single crystals

### 6.1 Introduction and overview

In chapter 5, the effects of Co substitution in BaFe<sub>2</sub>As<sub>2</sub> single crystals for  $x \leq 0.166$  were presented. A comprehensive temperature-doping concentration ( $T - x$ ) phase diagram was determined [34], one that has been confirmed and reproduced by several other groups [36, 37, 38, 39]. With Co doping, the structural phase transition at 134 K in pure BaFe<sub>2</sub>As<sub>2</sub> is suppressed monotonically and increasingly separates from the lower temperature magnetic phase transition. In addition, superconductivity can be stabilized with Co doping and has a dome-like appearance in the  $T - x$  phase diagram. For the superconducting compounds with lower doping levels, superconductivity coexists with antiferromagnetism in the orthorhombic state [152, 153]. For higher Co doping levels both the structural and antiferromagnetic phase transitions are completely suppressed and superconductivity occurs in the tetragonal (paramagnetic) phase. These data are all consistent with the idea that superconductivity can be stabilized when the structural / magnetic phase transitions are suppressed to "low enough" temperature.

The natural questions following this study were: what will happen if the other transition metals are doped on the Fe site of BaFe<sub>2</sub>As<sub>2</sub>? Will these dopants have effects similar to Co-doping? Will they suppress the structural / magnetic phase transitions and stabilize superconductivity in the same manner as Co-doping? Can the similarities and differences among these dopings be understood and shed some light on the correlation between the structural / antiferromagnetic phase transitions and superconductivity, as well as the conditions for the appearance of superconductivity in the BaFe<sub>2</sub>As<sub>2</sub> system? To answer these questions,

extensive experimental efforts focusing on electron doped  $\text{BaFe}_2\text{As}_2$  series, have been made.  $3d$  transition metal, Ni, Cu, Co / Cu doped and  $4d$  transition metal, Rh and Pd, doped  $\text{BaFe}_2\text{As}_2$  single crystals were grown and characterized by microscopic, structural, transport and thermodynamic measurements.

In all these series, the structural and magnetic phase transitions at 134 K in pure  $\text{BaFe}_2\text{As}_2$  were suppressed monotonically and separated by these dopants. For the  $3d$  electron doped  $\text{Ba}(\text{Fe}_{1-x}\text{Ni}_x)_2\text{As}_2$  series, superconductivity can be stabilized over a smaller doping range compared to the  $\text{Ba}(\text{Fe}_{1-x}\text{Co}_x)_2\text{As}_2$  series. In  $\text{Ba}(\text{Fe}_{1-x}\text{Cu}_x)_2\text{As}_2$  ( $x \leq 0.356$ ) series, the structural and magnetic transitions are suppressed, but superconductivity is not stabilized for  $T > 3$  K. For one concentration,  $x = 0.044$ , a sharp drop of the resistivity to zero shows up near 2 K, this feature of resistivity might be a sign of very limited superconductivity near this Cu doping level. In  $\text{Ba}(\text{Fe}_{1-x-y}\text{Co}_x\text{Cu}_y)_2\text{As}_2$  ( $x \sim 0.021$ ) series, although  $\text{Ba}(\text{Fe}_{0.976}\text{Co}_{0.024})_2\text{As}_2$  is not superconducting, the introduction of extra Cu atoms further suppresses the structural / magnetic phase transitions and a  $T_c$  dome shows up with a maximum value of 12 K. In  $\text{Ba}(\text{Fe}_{1-x-y}\text{Co}_x\text{Cu}_y)_2\text{As}_2$  ( $x \sim 0.047$ ) series, Cu is doped into  $\text{Ba}(\text{Fe}_{0.979}\text{Co}_{0.047})_2\text{As}_2$ , an underdoped compound with  $T_c \sim 16$  K. As Cu is added, the structural and magnetic phase transitions are suppressed further, and  $T_c$  rises to  $\sim 20$  K.

The detailed analysis of all the data collecting from nearly 40 separate batches of  $3d$  electron doped  $\text{BaFe}_2\text{As}_2$ , allows for the determination of the temperature-doping concentration ( $T - x$ ) and temperature-extra electron ( $T - e$ ) phase diagrams of  $3d$  electron doped  $\text{BaFe}_2\text{As}_2$ . The comparison of these systems indicates that the suppression of the upper structural / magnetic phase transitions is a *necessary* but not sufficient condition for the occurrence of superconductivity. Comparisons of the  $T - x$  and  $T - e$  phase diagrams for TM=Co, Ni, Cu, Cu / Co series reveal that, although the suppression of the upper transitions better scales with the doping level  $x$  (or the change in the crystallographic  $c$ -axis), the location and extent of the superconducting dome scales better with the number of extra conduction electrons added (or the change in the ratio of  $a$  over  $c$ ), which are one for each Co, two for each Ni and three for each Cu atom.

The study of 4d electron doped  $\text{BaFe}_2\text{As}_2$  systems shows although  $T-x$  phase diagrams for Co- and Rh-doping are virtually identical, as are the phase diagrams for Ni- and Pd-doping, by analyzing the relative changes in the lattice parameters, whereas  $x$  and  $e$  can still successfully be used to parameterize the structural / magnetic and superconducting phase transitions in the  $\text{Ba}(\text{Fe}_{1-x}\text{TM}_x)_2\text{As}_2$  systems, changes in the lattice parameters, or their ratios, no longer can. This allows for the clear identification of  $x$  and  $e$  as relevant variables (rather than  $c$  and  $a/c$ ) and helped refine further the idea that superconductivity in the  $\text{Ba}(\text{Fe}_{1-x}\text{TM}_x)_2\text{As}_2$  systems requires both the adequate suppression of the upper transitions and an appropriate electron count.

Therefore, by choosing which combination of dopants are used to control the structural / magnetic phase suppression rate and the extra electrons added, we can adjust the relative positions of the upper phase line and the superconducting dome, even to the extreme limit of suppressing the upper structural and magnetic phase transitions without the stabilization of low temperature superconducting domey.

## 6.2 Experimental results

### 6.2.1 $\text{Ba}(\text{Fe}_{1-x}\text{Ni}_x)_2\text{As}_2$

$\text{Ba}(\text{Fe}_{1-x}\text{Ni}_x)_2\text{As}_2$  compounds were first found to superconduct by Xu. et al [31]. However, no detailed presentation of transport and thermodynamic data or determination of a phase diagram of the structural, magnetic and superconducting phases was made. In order to map the phase diagram of  $\text{Ba}(\text{Fe}_{1-x}\text{Ni}_x)_2\text{As}_2$ , single crystals were grown and characterized.

The evolution of the lattice parameters with the doping level is shown in Fig. 6.1. They are normalized to  $a_0 = 3.9621(8) \text{ \AA}$ ,  $c_0 = 13.0178 (20) \text{ \AA}$ ,  $V_0 = 204.357 \text{ \AA}^3$ , which are the lattice parameters of pure  $\text{BaFe}_2\text{As}_2$ . For Ni dopings up to  $x = 0.072$ , the lattice parameter  $a$  increases slightly by 0.04%, while the lattice parameter  $c$  decreases almost ten times faster, by 0.35%, and thus the unit cell volume decreases monotonically by 0.26%. This is different from Co-doped  $\text{BaFe}_2\text{As}_2$ , in which, up to  $x = 0.114$  doping level,  $a$  and  $c$  lattice parameters decrease by 0.07% and 0.5% respectively and the unit cell volume decreases by 0.6%.

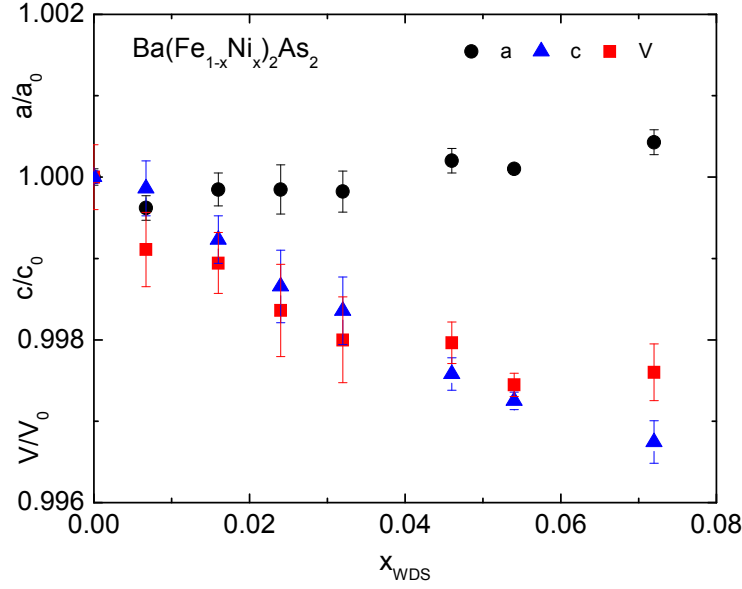


Figure 6.1 Lattice parameters of  $\text{Ba}(\text{Fe}_{1-x}\text{Ni}_x)_2\text{As}_2$  series,  $a$  and  $c$  as well as unit cell volume,  $V$ , normalized to the values of pure  $\text{BaFe}_2\text{As}_2$  as a function of measured Ni concentration,  $x_{WDS}$

Fig. 6.2 (a) shows the normalized resistivity data taken from 2 K to 300 K for  $\text{Ba}(\text{Fe}_{1-x}\text{Ni}_x)_2\text{As}_2$ . Each subsequent data set is shifted downward by 0.3 for clarity. It shows very similar behavior to  $\text{Ba}(\text{Fe}_{1-x}\text{Co}_x)_2\text{As}_2$  [34, 36]. With Ni doping, the resistive anomaly associated with the structural and magnetic phase transitions is suppressed from 134 K, for pure  $\text{BaFe}_2\text{As}_2$ , to lower temperatures. For the lowest doping level,  $x = 0.0067$ , the resistive anomaly is very similar to that seen in pure  $\text{CaFe}_2\text{As}_2$  as well as very lightly Co doped  $\text{BaFe}_2\text{As}_2$  [34, 130]. With higher Ni doping, the resistive anomaly becomes a broad upturn. The evolution of the resistive anomaly can also be seen in Fig. 6.2 (b), which shows the enlarged  $d(\rho(T)/\rho_{300K})/dT$  below 130 K for  $\text{Ba}(\text{Fe}_{1-x}\text{Ni}_x)_2\text{As}_2$ ; two kinks similar to those in  $\text{Ba}(\text{Fe}_{1-x}\text{Co}_x)_2\text{As}_2$  [34] can be observed. Based on the Co-doping work, reviewed in the previous chapter, and considering the similarities between Co-doping and Ni-doping, it is natural to believe that the higher-temperature kink in  $d(\rho(T)/\rho_{300K})/dT$ ,  $d(M/H)/dT$  and  $dC/dT$  is associated with the structural phase transition and the lower-temperature kink is associated with the magnetic phase transition. This assumption has been confirmed by recent neutron scattering work [154] on several different

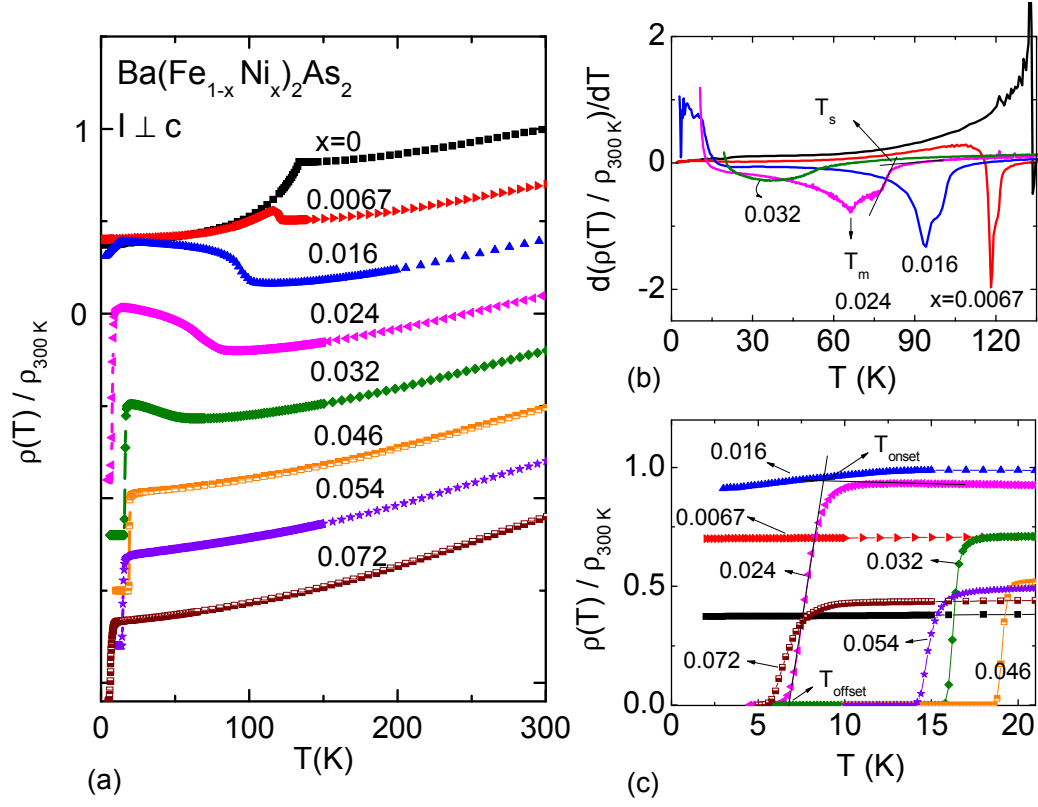


Figure 6.2  $\text{Ba}(\text{Fe}_{1-x}\text{Ni}_x)_2\text{As}_2$  series: (a) The temperature dependent resistivity, normalized to the room temperature value. Each subsequent data set is shifted downward by 0.3 for clarity. (b)  $d(\rho(T)/\rho_{300K})/dT$  for  $y \leq 0.032$ . (c) Enlarged low temperature  $\rho(T)/\rho_{300K}$ .

TM dopants.

For  $x = 0.024$ , the structural phase transition temperature,  $T_s$ , is suppressed to 82.1 K, the magnetic phase transition temperature,  $T_m$ , is suppressed to 66.3 K, and zero resistivity is detected below 6.8 K. At  $x = 0.046$ , the resistive anomaly associated with structural and magnetic phase transitions disappears and the superconducting temperature increases to the maximum value around 19 K. For larger  $x$ ,  $T_c$  decreases and is suppressed to  $\sim 5.7$  K for  $x = 0.072$ . The superconducting feature can be seen more clearly in Fig. 6.2 (c), which shows the low temperature resistivity data for  $\text{Ba}(\text{Fe}_{1-x}\text{Ni}_x)_2\text{As}_2$ . The superconducting transition width of  $\text{Ba}(\text{Fe}_{1-x}\text{Ni}_x)_2\text{As}_2$  is smaller than 2 K.

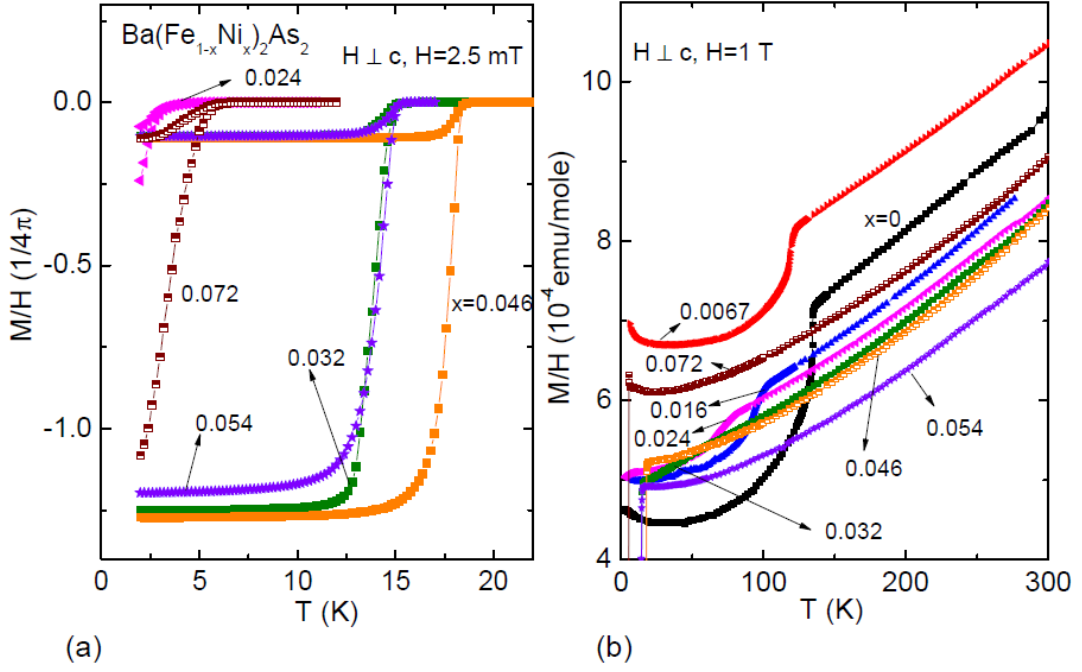


Figure 6.3  $\text{Ba}(\text{Fe}_{1-x}\text{Ni}_x)_2\text{As}_2$  series: (a) Field-cooled (FC) and zero-field-cooled (ZFC) low field  $M(T)/H$  data taken at 2.5 mT with  $H \perp c$ . (b)  $M(T)/H$  data taken at 1 T with  $H \perp c$ .

Fig. 6.3 (a) shows the  $M(T)/H$  data taken at 2.5 mT with  $H$  perpendicular to the crystallographic  $c$ -axis of the  $\text{Ba}(\text{Fe}_{1-x}\text{Ni}_x)_2\text{As}_2$  samples. The Meissner effect can be clearly seen in the field-cooled (FC) data, the zero-field-cooled (ZFC) data highlight the transition even more dramatically. The superconducting fractions are similar to the superconducting fractions of  $\text{Ba}(\text{Fe}_{1-x}\text{Co}_x)_2\text{As}_2$  [34]. Fig. 6.3 (b) shows the  $M(T)/H$  data taken at 1 T with  $H \perp c$ . For pure  $\text{BaFe}_2\text{As}_2$ , a susceptibility drop associated with the structural / magnetic phase transitions around 134 K can be clearly seen. With Ni doping, this feature is suppressed to lower temperature and splits, consistent with the resistivity data shown in Fig. 6.2 (a).  $M(T)/H$  data show a linear temperature dependence above the structural and magnetic phase transition temperatures. This linear behavior is similar to that seen in  $\text{Ba}(\text{Fe}_{1-x}\text{Co}_x)_2\text{As}_2$  [34, 38]. The magnitude of the susceptibility in normal state is between  $4.5 \times 10^{-4}$  emu/mole to  $10 \times 10^{-4}$  emu/mole, which is again similar to that of  $\text{Ba}(\text{Fe}_{1-x}\text{Co}_x)_2\text{As}_2$ .

Fig. 6.4 presents the heat capacity data up to 25 K taken at zero magnetic field for all the

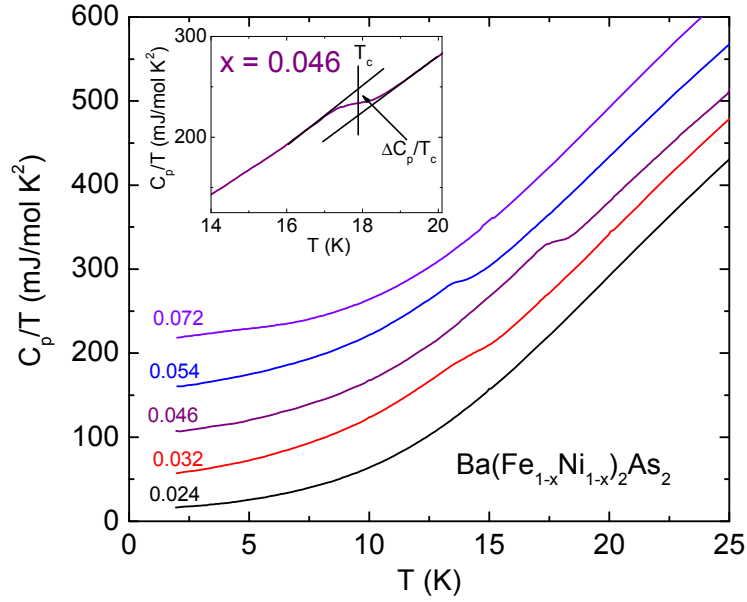


Figure 6.4  $C_p$  vs.  $T$  of the superconducting  $\text{Ba}(\text{Fe}_{1-x}\text{Ni}_x)_2\text{As}_2$  compounds. Data are shifted by a multiple of 50 mJ/mol  $\text{K}^2$  along the  $y$ -axis for clarity. Inset: enlarged  $C_p/T$  vs.  $T$  plot near  $T_c$  for  $\text{Ba}(\text{Fe}_{0.954}\text{Ni}_{0.046})_2\text{As}_2$ , lines show the "isoentropic" construction to infer  $T_c$  and  $\Delta C$  [54].

superconducting Ni doped compounds [54]. The feature associated with the superconducting transition can be clearly observed for  $x=0.032$ , 0.046 and 0.054 whose  $T_c$ s are higher than 10 K whereas a  $C_p$  feature can hardly be detected for the  $x=0.024$  and 0.072 compounds, each with  $T_c$  lower than 5 K. In addition, the heat capacity jump is relatively sharp for the near optimal Ni-doping level of  $x = 0.046$  while it is broad for the other samples. This feature is similar to what we have seen in  $\text{Ba}(\text{Fe}_{1-x}\text{Co}_x)_2\text{As}_2$  and will be discussed at the end of this chapter in detail.

The structural / magnetic and superconducting transition temperatures inferred from Figs. 6.2, 6.3 and 6.4 are summarized in Table 6.1. For  $x = 0.0067$ , due to the small temperature splitting between  $T_s$  and  $T_m$ , although we can still observe two kinks from  $d(\rho/\rho_{300})/dT$  (resistivity measurement is the most sensitive one to detect structural / magnetic phase transitions among these measurements), we can only observe the kink associated with magnetic phase transition in  $d(M/H)/dT$  whereas less obvious shoulder-like feature associated with structural



dopant	$x$	$\rho$				$M$			$C$
		$T_s$	$T_m$	$T_c^{onset}$	$T_c^{offset}$	$T_s$	$T_m$	$T_c$	$T_c$
Ni	0	134	134			134	134		
	0.0067	123	118				119		
	0.016	94	104			103	94		
	0.024	82	66	8.6	6.8	84	68	3.9	2.5
	0.032	56	37**	16.6	15.9	53		15.1	14.6
	0.046			19.4	18.8			18.4	17.8
	0.054			15.5	14.3			14.4	13.9
	0.072			7.5	5.7			6	5.2

Table 6.1 Summary of  $T_s$ ,  $T_m$  and  $T_c$  from resistivity, magnetization and specific heat measurements for  $\text{Ba}(\text{Fe}_{1-x}\text{Ni}_x)_2\text{As}_2$  series. \*\*: see text.

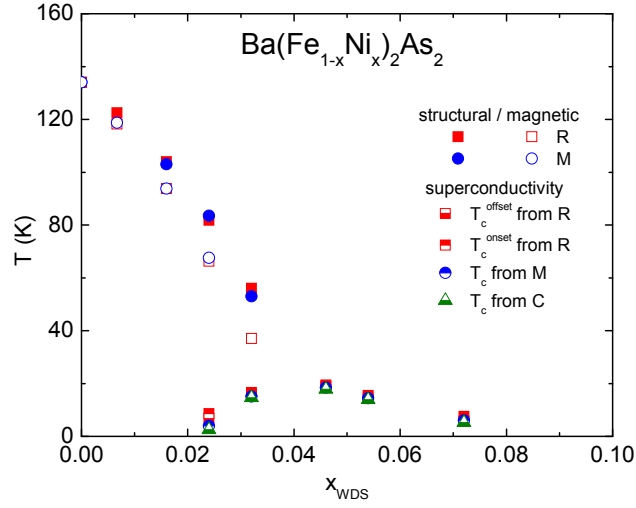


Figure 6.5  $T - x$  phase diagram of  $\text{Ba}(\text{Fe}_{1-x}\text{Ni}_x)_2\text{As}_2$  single crystals for  $x \leq 0.072$ .

phase transition as shown in Fig. 5.11 can not be detected. For  $x = 0.032$ , due to the nearness between magnetic phase transition and the superconducting phase transition, the feature as shown in Fig. 6.2, used to infer  $T_m$  is blurred, therefore  $T_m$  is determined from the minimum of  $d(\rho/\rho_{300})/dT$  below  $T_s$ . No detectable feature of magnetization measurement for  $x = 0.032$  sample can be employed to infer  $T_m$ . All of these data can be used to assemble a temperature-

doping concentration ( $T-x$ ) phase diagram for  $\text{Ba}(\text{Fe}_{1-x}\text{Ni}_x)_2\text{As}_2$  as shown in Fig. 6.5. It has very similar appearance as the one for  $\text{Ba}(\text{Fe}_{1-x}\text{Co}_x)_2\text{As}_2$  except the superconducting dome occurs at a lower  $x$  and is much narrower.

### 6.2.2 $\text{Ba}(\text{Fe}_{1-x}\text{Cu}_x)_2\text{As}_2$

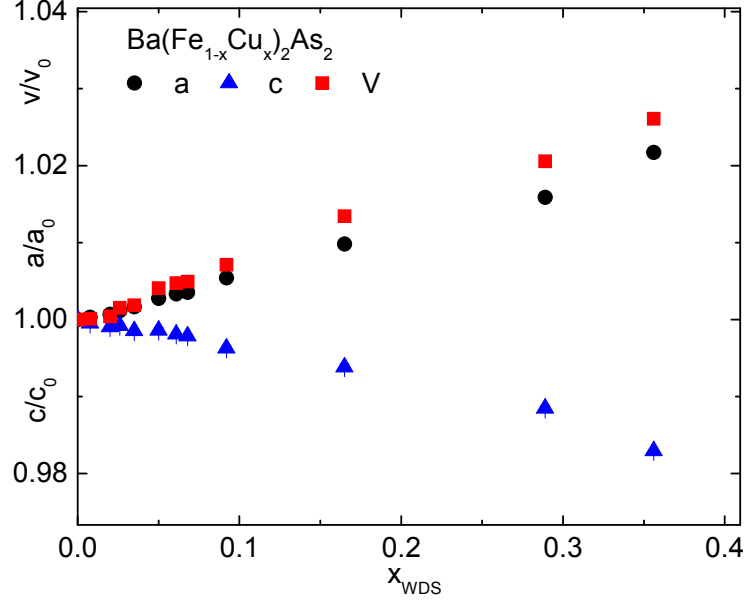


Figure 6.6 Lattice parameters of  $\text{Ba}(\text{Fe}_{1-x}\text{Cu}_x)_2\text{As}_2$  series,  $a$  and  $c$  as well as unit cell volume,  $V$ , normalized to the values of pure  $\text{BaFe}_2\text{As}_2$  as a function of measured Cu concentration,  $x_{\text{WDS}}$

Since superconductivity was found in both  $\text{Ba}(\text{Fe}_{1-x}\text{Co}_x)_2\text{As}_2$  and  $\text{Ba}(\text{Fe}_{1-x}\text{Ni}_x)_2\text{As}_2$ , straightforward questions will be, what will happen if Cu, the next  $3d$  period element, is doped into  $\text{BaFe}_2\text{As}_2$ ? Will the structural / magnetic phase transitions be suppressed in a similar way? Will the superconducting dome shrink further? To answer these questions,  $\text{Ba}(\text{Fe}_{1-x}\text{Cu}_x)_2\text{As}_2$  single crystals were grown and characterized. In Table 3.2, we showed the results of the elemental analysis of  $\text{Ba}(\text{Fe}_{1-x}\text{Cu}_x)_2\text{As}_2$  series. We found Cu-doping has a somewhat larger variation of  $x$  values than the other TM dopings (but still much less variation than K-doping). This may come from the fact that small Cu shot rather than CuAs powder was used in the growth procedure, but considering the fact that Co powder rather than

CoAs powder was used in reference [36] for the growth of  $\text{Ba}(\text{Fe}_{1-x}\text{Cu}_x)_2\text{As}_2$  crystals and very sharp low field  $M(T)/H$  features were observed, it is more likely that this somewhat larger Cu concentration variation is intrinsic in nature.

The evolution of the lattice parameters of  $\text{Ba}(\text{Fe}_{1-x}\text{Cu}_x)_2\text{As}_2$  with  $x$  is shown in Fig. 6.6. Comparing to pure  $\text{BaFe}_2\text{As}_2$ , with Cu doping up to  $x=0.356$ , the lattice parameter  $a$  increases linearly by 2.2%, lattice parameter  $c$  decreases monotonically by 1.7% and the unit cell volume increases by roughly 2.6%.

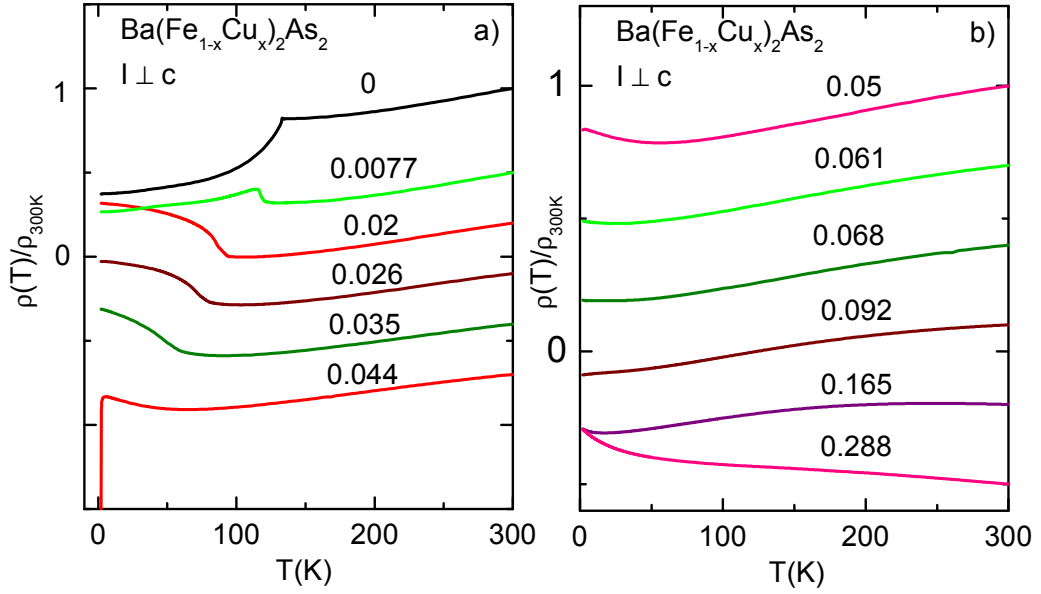


Figure 6.7 The temperature dependent resistivity, normalized to the room temperature value, for  $\text{Ba}(\text{Fe}_{1-x}\text{Cu}_x)_2\text{As}_2$ . Each subsequent data set is shifted downward by 0.3 for clarity respectively for (a) and (b).

The electrical transport data for the  $\text{Ba}(\text{Fe}_{1-x}\text{Cu}_x)_2\text{As}_2$  series from base temperature, 2 K, to 300 K (for  $x = 0.044$ , the base temperature was 0.4 K) are shown in Fig. 6.7. The effects of Cu substitution can be clearly seen in Fig. 6.7. As  $x$  is increased, the resistive anomaly associated with the structural and magnetic phase transitions is suppressed monotonically. For the lowest doping level  $x = 0.0077$ , the resistive anomaly manifests as an abrupt increase in resistivity followed by a decrease as temperature is lowered further. It is very similar to

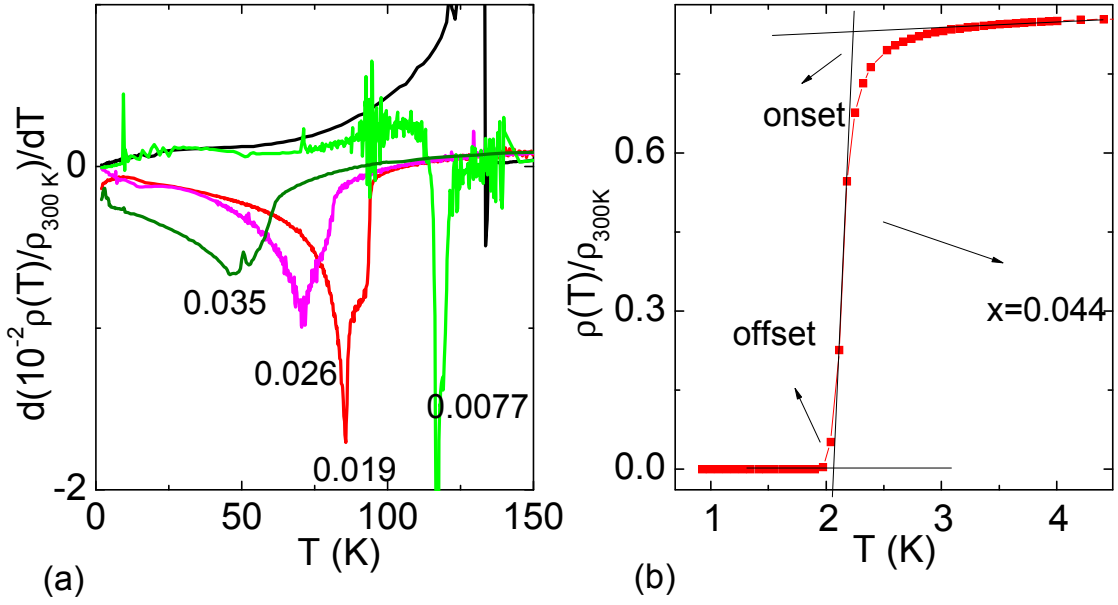


Figure 6.8 (a)  $d(\rho(T)/\rho_{300K})/dT$  of  $\text{Ba}(\text{Fe}_{1-x}\text{Cu}_x)_2\text{As}_2$  for  $0.05 \geq x$ .  
 (b) Enlarged low temperature  $\rho(T)/\rho_{300K}$  data of  $\text{Ba}(\text{Fe}_{0.956}\text{Cu}_{0.044})_2\text{As}_2$

what we have seen in  $\text{Ba}(\text{Fe}_{0.9933}\text{Ni}_{0.0067})_2\text{As}_2$ . With higher Cu doping, the resistive anomalies associated with the structural and magnetic phase transitions show a broad upturn. No clearly defined resistive anomaly can be seen for  $x > 0.035$ , but for  $0.061 \geq x > 0.035$ , a minimum in the resistivity can be observed, which can be used to identify an upper limit for the structural and magnetic phase transitions. No sign of structural and magnetic phase transitions is detected for  $x \geq 0.068$ . The suppression of the structural and magnetic phase transitions is further demonstrated in Fig. 6.8(a). Two kinks, like what we have seen in Co and Ni doped  $\text{BaFe}_2\text{As}_2$  [33], can be observed. These features are suppressed to lower temperatures with increasing Cu doping.

Zero resistivity was found for a single doping:  $x = 0.044$ , below 2.1 K. Fig. 6.8(b) shows the enlarged, low temperature, electric transport data of  $\text{Ba}(\text{Fe}_{0.956}\text{Cu}_{0.044})_2\text{As}_2$ . A very sharp transition to zero resistivity is observed.  $T_c^{\text{offset}}$  is 2.1 K and  $T_c^{\text{onset}}$  is 2.2 K.

Fig. 6.9 shows the temperature dependent  $M(T)/H$  data taken at 1 T from 2 K to 300 K with  $H$  perpendicular to the crystallographic  $c$ -axis of the samples. Due to slight ferromagnetic

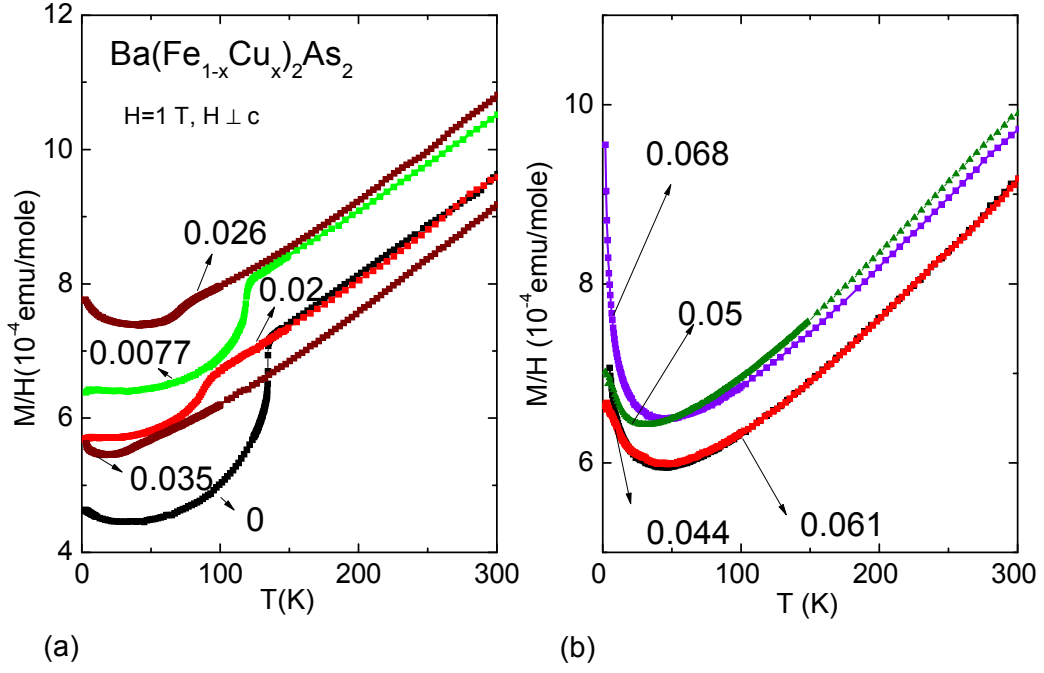


Figure 6.9  $M(T)/H$  taken at 1 T with  $H \perp c$  for  $\text{Ba}(\text{Fe}_{1-x}\text{Cu}_x)_2\text{As}_2$  series.

impurities in the higher Cu concentration  $\text{BaFe}_2\text{As}_2$  samples ( $x > 0.068$ ), we only show the susceptibility for  $x \leq 0.068$ . To make the graph easier to read, the data are grouped into two panels. Fig. 6.9 (a) shows  $M(T)/H$  of  $\text{Ba}(\text{Fe}_{1-x}\text{Cu}_x)_2\text{As}_2$  samples that manifest a clear resistive anomaly in Fig. 6.7. A clear drop at the temperature associated with the resistive anomalies can be seen. Higher temperature susceptibility data show almost linear temperature dependence which is similar to the ones in  $\text{Ba}(\text{Fe}_{1-x}\text{Ni}_x)_2\text{As}_2$  discussed above [34]. Fig. 6.9 (b) shows  $M(T)/H$  of  $\text{Ba}(\text{Fe}_{1-x}\text{Cu}_x)_2\text{As}_2$  samples ( $0.068 \geq x > 0.035$ ). Although a resistivity minimum is present in  $x = 0.05, 0.061$  and  $0.068$  samples, no feature of structural and magnetic phase transitions similar to the ones in Fig. 6.9 (a) can be detected in the susceptibility data. On the other hand, the low temperature susceptibility increases with decreasing temperature whereas the high temperature susceptibility continues to show T-linear behavior. Low field  $M(T)/H$  data, down to 1.8 K, for the  $x=0.044$  sample with zero resistivity around 2 K do not show a diamagnetic signal, but since this is at the edge of range where diamagnetic signal would just be starting, it is hard to conclude if there is bulk superconductivity in  $x=0.044$ .

sample.

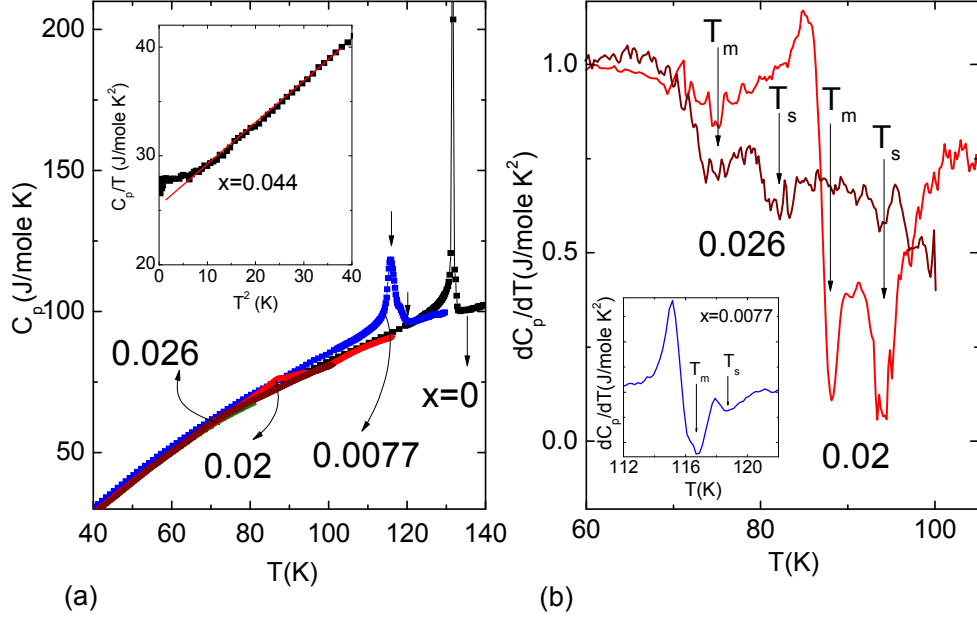


Figure 6.10 (a) Enlarged temperature dependent heat capacity of  $\text{Ba}(\text{Fe}_{1-x}\text{Cu}_x)_2\text{As}_2$  ( $x = 0, 0.0077, 0.02$  and  $0.026$ ). Inset:  $C_p$  vs.  $T^2$  for  $\text{Ba}(\text{Fe}_{0.956}\text{Cu}_{0.044})_2\text{As}_2$ . (b) Enlarged  $dC_p/dT$  vs.  $T$  for  $\text{Ba}(\text{Fe}_{1-x}\text{Cu}_x)_2\text{As}_2$  ( $x = 0.02$  and  $0.026$ ).

Fig. 6.10 (a) shows an enlarged region of specific heat data  $C_p(T)$  vs.  $T$  for the Cu concentrations  $x = 0, 0.077, 0.02$  and  $0.026$ . The very sharp peak around 134 K associated with the structural / magnetic phase transition can be seen in heat capacity measurement for pure  $\text{BaFe}_2\text{As}_2$ . For  $x = 0.077$  Cu doping, the single sharp peak in pure  $\text{BaFe}_2\text{As}_2$  splits into two. With even higher Cu doping, the sharp peaks become broad. To identify these features more clearly,  $dC_p/dT$  for  $x = 0.02$  and  $0.026$  are plotted in Fig. 6.10 (b). We can see two kinks in the  $dC_p/dT$  plot which correspond to the two kinks observed in  $d(\rho/\rho_{300})/dT$ . These features are no longer detectable in either  $C_p$  or  $dC_p/dT$  for  $x \geq 0.035$ , although we still can see features of structural and magnetic phase transitions for  $x = 0.035$  in resistivity and susceptibility measurements. The inset of Fig. 6.10 (a) shows the  $C_p$  vs.  $T^2$  measured down to 0.4 K for  $\text{Ba}(\text{Fe}_{0.956}\text{Cu}_{0.044})_2\text{As}_2$ . No clear superconductivity jump can be observed around 4 K<sup>2</sup>. This is not surprising since the heat capacity jump decreases with decreasing  $T_c$ : for

dopant	$x$	$\rho$				$M$	$C$	
		$T_s$	$T_m$	$T_c^{onset}$	$T_c^{offset}$	$T_m$	$T_s$	$T_m$
Cu	0.0077	121	117			119	119	117
	0.02	94	86			88	94	88
	0.026	83	71			72	82	75
	0.035	63	48					
	0.044	$40 \pm 20^*$		2.2	2.1			
	0.05	$30 \pm 25^*$						
	0.061	$10 \pm 10^*$						

Table 6.2 Summary of  $T_s$ ,  $T_m$  and  $T_c$  from resistivity, magnetization and specific heat measurements for  $\text{Ba}(\text{Fe}_{1-x}\text{Cu}_x)_2\text{As}_2$  series. \*: see text.

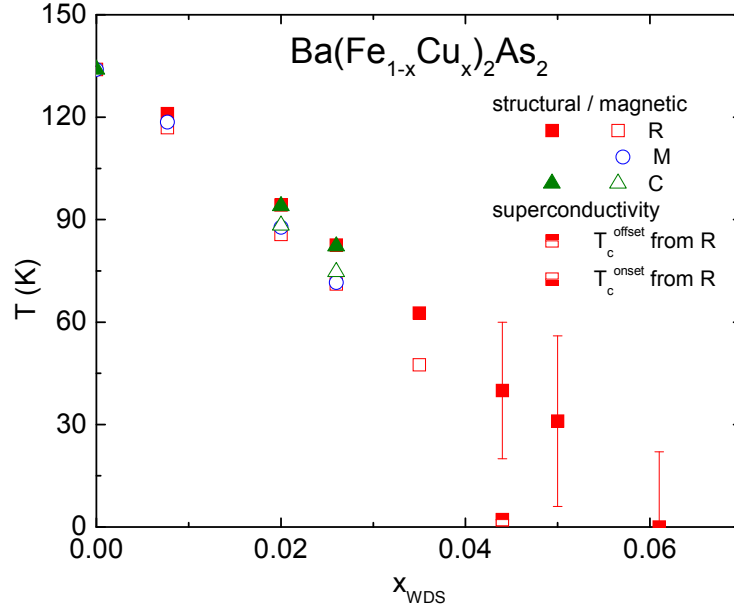


Figure 6.11  $T - x$  phase diagram of  $\text{Ba}(\text{Fe}_{1-x}\text{Cu}_x)_2\text{As}_2$  single crystals for  $x \leq 0.061$ .

Co-doped and Ni-doped  $\text{BaFe}_2\text{As}_2$ , the heat capacity jump is rather subtle for superconductors with very low  $T_c$  due to the broadness, such as Ni doped  $\text{BaFe}_2\text{As}_2$  samples with  $T_c$  around 2.5 K and 4 K which did not show clear specific heat jump either.

The structural / magnetic and superconducting transition temperatures are determined from Figs. 6.7, 6.9 and 6.10 and summarized in Table 6.2. For the concentrations indexed by \*, the resistive features become so broad that the error bars associated with the determination of the upper (only detectable) transition are defined by the temperature of the resistance minima on the high side and the temperature of the inflection point on the low side. The  $T-x$  phase diagram of  $\text{Ba}(\text{Fe}_{1-x}\text{Cu}_x)_2\text{As}_2$  series is plotted Fig. 6.11. The structural and magnetic phase transitions are suppressed and increasingly split with Cu doping in a similar manner as Co, Ni dopings, but the superconductivity possibly occurs only at  $x = 0.044$  with a very low  $T_c \sim 2$  K in this series and current data do not allow to evaluate the volume fraction of the superconducting phase.

### 6.2.3 $\text{Ba}(\text{Fe}_{1-x-y}\text{Co}_x\text{Cu}_y)_2\text{As}_2$ ( $x \sim 0.022$ )

Whereas doping  $\text{BaFe}_2\text{As}_2$  with Co, Ni and Cu suppresses the upper structural / magnetic phase transitions in similar ways, only Co and Ni appear to induce a superconducting dome over substantial ranges of  $x$  values. Cu, while suppressing the structural and magnetic phase transitions, does not lead to any significant superconducting region; possibly only one compound with  $x \sim 0.044$  has  $T_c \sim 2$  K. In order to better understand the effects of Cu on the superconducting state, two mixed ( Cu and Co) doping series ,  $\text{Ba}(\text{Fe}_{1-x-y}\text{Co}_x\text{Cu}_y)_2\text{As}_2$  ( $x \sim 0.022$  and  $x \sim 0.047$ ) were grown and studied.

For the  $\text{Ba}(\text{Fe}_{1-x-y}\text{Co}_x\text{Cu}_y)_2\text{As}_2$  ( $x \sim 0.022$ ) series, the lattice parameters are normalized to the ones of closely related  $\text{Ba}(\text{Fe}_{0.976}\text{Co}_{0.024})_2\text{As}_2$  ( $a/a_0$ ,  $c/c_0$  and  $V/V_0$  are plotted against  $y_{WDS}$  in Fig. 6.12. With Cu doped into  $\text{Ba}(\text{Fe}_{0.978}\text{Co}_{0.022})_2\text{As}_2$ , the lattice parameter  $a$  increases, lattice parameter  $c$  decreases and the unit cell volume increases.

Fig. 6.13 (a) shows the electric transport data of  $\text{Ba}(\text{Fe}_{1-x-y}\text{Co}_x\text{Cu}_y)_2\text{As}_2$  ( $x \sim 0.022$ )



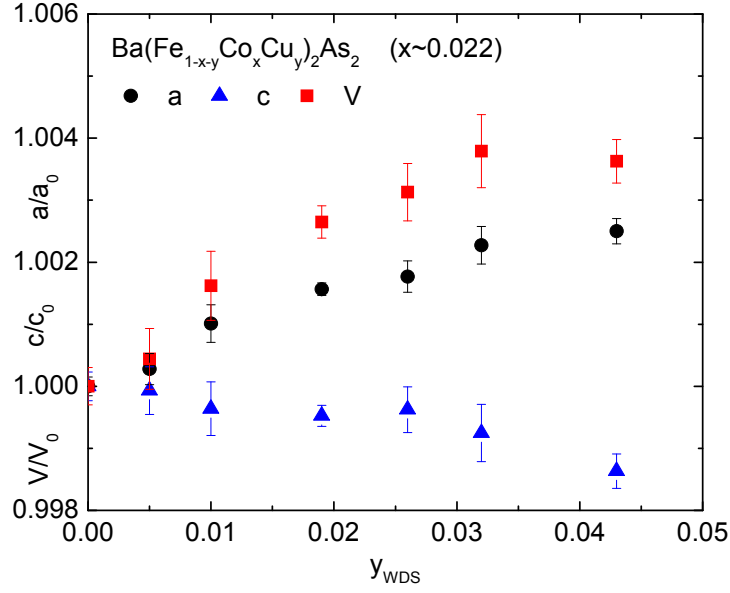


Figure 6.12 Lattice parameters of  $\text{Ba}(\text{Fe}_{1-x-y}\text{Co}_x\text{Cu}_y)_2\text{As}_2$  ( $x \sim 0.022$ ) series,  $a$  and  $c$  as well as unit cell volume,  $V$ , normalized to the values of  $\text{Ba}(\text{Fe}_{0.976}\text{Co}_{0.024})_2\text{As}_2$  ( $a_0=3.9598(6)\text{\AA}$ ,  $c_0=13.0039(30)\text{\AA}$ ) as a function of measured Cu concentration,  $y_{WDS}$

series from 2 K to 300 K. For  $\text{Ba}(\text{Fe}_{0.976}\text{Co}_{0.024})_2\text{As}_2$ , no sign of superconductivity can be detected; as the temperature goes down, the resistivity exhibits an upturn around 110 K and then decreases with further cooling. When Cu is doped into  $\text{Ba}(\text{Fe}_{0.978}\text{Co}_{0.022})_2\text{As}_2$ , the structural / magnetic phase transitions are suppressed to lower temperature and evolve in a manner that is qualitatively similar to what is found for other *TM* dopings. Fig. 6.13 (b) shows the derivative of  $\rho(T)/\rho_{300K}$ . Similar to Co, Ni and Cu doped  $\text{BaFe}_2\text{As}_2$ , two kinks can be seen to separate and drop as more Cu is added. For intermediate  $y$  values, superconductivity can be stabilized. Fig. 6.13 (c) shows an enlarged plot of the low temperature,  $\rho(T)/\rho_{300K}$  data. When  $y = 0.019$ , zero resistivity is detected below 9 K.  $T_c$  reaches a maximum of 12 K for  $y = 0.026$  and drops to 8.3 K for  $y = 0.032$  and 2 K for  $y = 0.043$ .

Fig. 6.14 (a) shows the  $M(T)/H$  data taken at 2.5 mT with H perpendicular to the crystallographic  $c$ -axis of the  $\text{Ba}(\text{Fe}_{1-x-y}\text{Co}_x\text{Cu}_y)_2\text{As}_2$  ( $x \sim 0.022$ ) series. Superconductivity can be clearly seen in the field-cooled (FC) and zero-field-cooled (ZFC) data. Comparing the low field

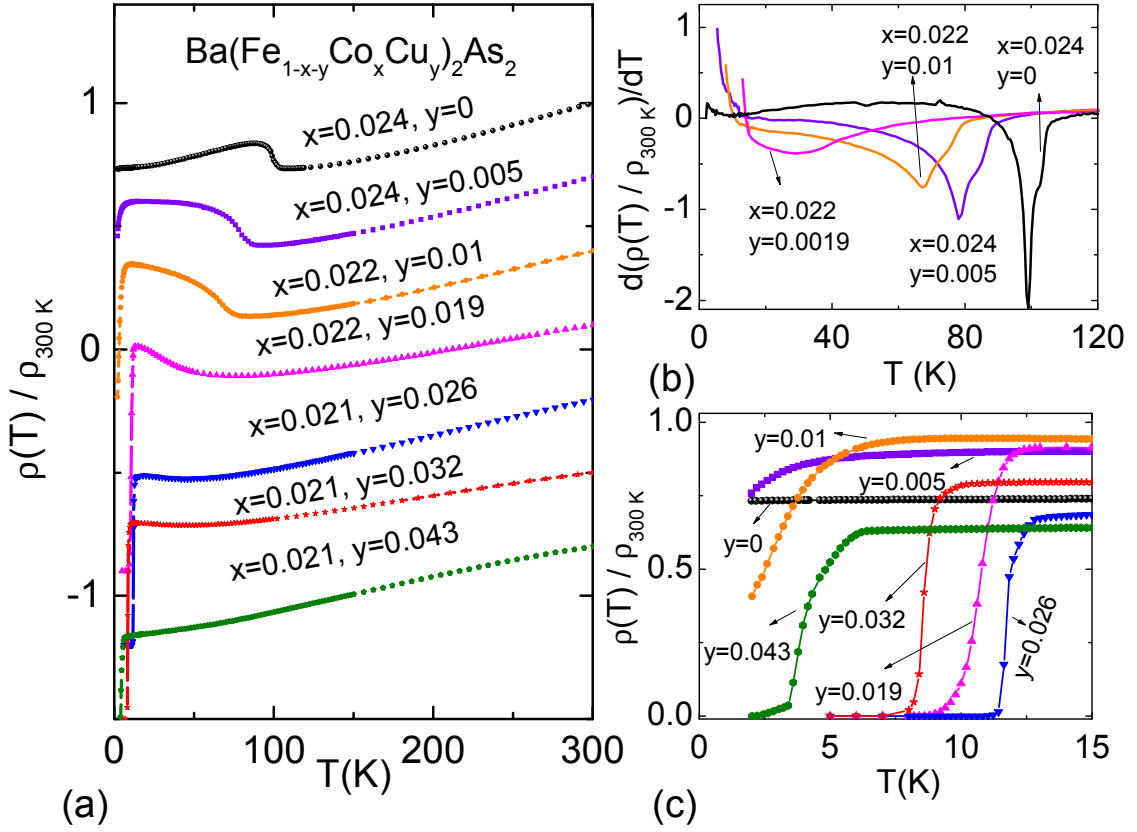


Figure 6.13  $\text{Ba}(\text{Fe}_{1-x-y}\text{Co}_x\text{Cu}_y)_2\text{As}_2$  ( $x \sim 0.022$ ) series. (a) The temperature dependent resistivity, normalized to the room temperature values. Each subsequent data set is shifted downward by 0.3 for clarity. (b)  $d(\rho(T)/\rho_{300K})/dT$  for  $y \leq 0.019$ . (c) Enlarged low temperature  $\rho(T)/\rho_{300K}$ .

$M(T)/H$  data with the ones in  $\text{Ba}(\text{Fe}_{1-x}\text{Co}_x)_2\text{As}_2$  [34], we can see that these two series have very similar superconducting volume fractions / pinning. It is worth noting that, as a "reality check", since the superconductivity in  $\text{Ba}(\text{Fe}_{1-x-y}\text{Co}_x\text{Cu}_y)_2\text{As}_2$  series has a superconducting volume that is comparable to that of the  $\text{Ba}(\text{Fe}_{1-x}\text{Co}_x)_2\text{As}_2$  phase, superconductivity must come from a bulk phase. The width of the superconducting transition shown in Fig. 6.14 (a) is not as sharp as that found for  $\text{Ba}(\text{Fe}_{1-x}\text{Co}_x)_2\text{As}_2$  samples, this could imply that the  $\text{Ba}(\text{Fe}_{1-x-y}\text{Co}_x\text{Cu}_y)_2\text{As}_2$  samples are not as homogeneous as  $\text{Ba}(\text{Fe}_{1-x}\text{Co}_x)_2\text{As}_2$  ones. This is consistent with the WDS measurements, summarized in Table 3.2, which, although showing a homogeneous Co concentration for the  $\text{Ba}(\text{Fe}_{1-x}\text{Co}_x)_2\text{As}_2$  and  $\text{Ba}(\text{Fe}_{1-x-y}\text{Co}_x\text{Cu}_y)_2\text{As}_2$  series,

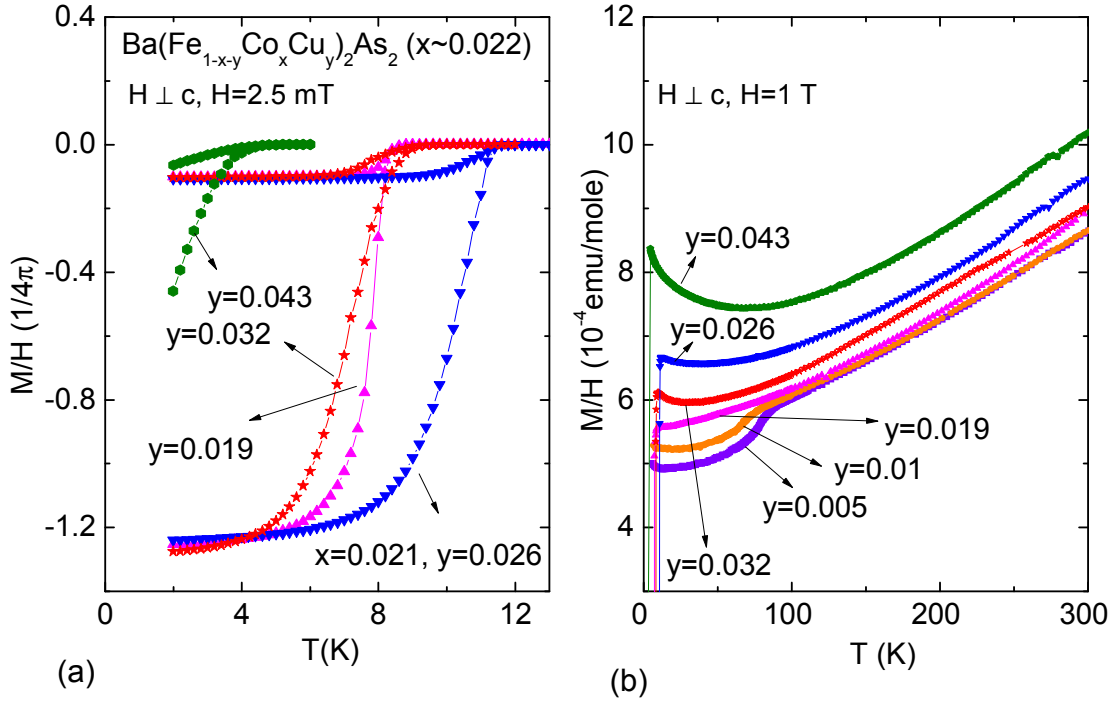


Figure 6.14  $\text{Ba}(\text{Fe}_{1-x-y}\text{Co}_x\text{Cu}_y)_2\text{As}_2$  ( $x \sim 0.022$ ) series: (a) Field-cooled (FC) and zero-field-cooled (ZFC) low field  $M(T)/H$  data taken at 2.5 mT with  $H \perp c$ . (b)  $M(T)/H$  data taken at 1 T with  $H \perp c$ .

indicates that the Cu concentration has a variation of up to 10% of the real Cu concentration in both the  $\text{Ba}(\text{Fe}_{1-x}\text{Cu}_x)_2\text{As}_2$  and  $\text{Ba}(\text{Fe}_{1-x-y}\text{Co}_x\text{Cu}_y)_2\text{As}_2$  series.

Fig. 6.14 (b) shows the  $M(T)/H$  data taken at 1 T with  $H$  perpendicular to the crystallographic  $c$ -axis of the  $\text{Ba}(\text{Fe}_{1-x-y}\text{Co}_x\text{Cu}_y)_2\text{As}_2$  series. The high temperature drop in the susceptibility data is associated with the structural / magnetic phase transitions, and consistent with the resistivity measurements. The high temperature linear susceptibility can also be seen in this series. The magnitude of the susceptibility is comparable to those of  $\text{Ba}(\text{Fe}_{1-x}\text{Co}_x)_2\text{As}_2$  and  $\text{Ba}(\text{Fe}_{1-x}\text{Ni}_x)_2\text{As}_2$ .

Heat capacity data was collected for  $\text{Ba}(\text{Fe}_{0.946}\text{Co}_{0.021}\text{Cu}_{0.032})_2\text{As}_2$ , the composition that manifests the highest  $T_c$  in this series. A clear heat capacity jump can be seen in Fig. 6.15 around 11 K. The inset shows temperature dependent  $C_p/T$  data near  $T_c$ .  $T_c$  and  $\Delta C_p/T_c$  were inferred using an "isoentropic" construction [54] so that the two areas shown in Fig. 6.15

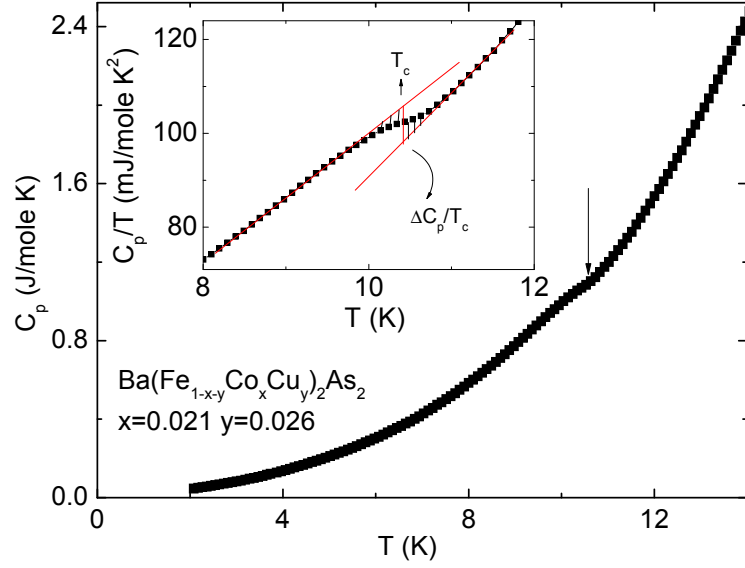


Figure 6.15 Temperature dependent heat capacity of  $Ba(Fe_{0.953}Co_{0.021}Cu_{0.026})_2As_2$ . Inset:  $C_p/T$  vs.  $T$ .

have equal area;  $\Delta C_p/T_c$  is 7.6 mJ/mole  $K^2$  with  $T_c$  equal to 10.4 K.

From Figs. 6.13, 6.14 and 6.15, we can determine the structural / magnetic and superconducting transition temperatures for  $Ba(Fe_{1-x-y}Co_xCu_y)_2As_2$  ( $x \sim 0.022$ ) series. These results are summarized in Table 6.3 and graphically presented as a  $T - y$  phase diagram in Fig. 6.16. For the temperature indexed by \*,  $T_s$  was inferred via the same way as we infer  $T_s$  for the temperatures indexed by \* in  $Ba(Fe_{1-x}Cu_x)_2As_2$  series. For the temperature indexed by \*\*, due to the nearness of  $T_m$  and  $T_c$ , the feature of the derivatives associated with  $T_m$  is not very clear,  $T_m$  is determined by the minimum of  $d(\rho/\rho_{300})/dT$  below  $T_s$ . Fig. 6.16 shows that the structural and magnetic phase transitions are suppressed and increasingly split with doping, in addition, superconductivity is stabilized in a dome-like rangion. The phase diagram shows a very similar appearance as the ones for Co-doped and Ni-doped series. The heat capacity data and  $T - y$  phase diagram make it clear that bulk superconductivity can be stabilized when Cu is present in the lattice. On the other hand, it is worth noting that the maximum  $T_c$  value is around 12 K which is somewhat low. To study this further, a second Co / Cu doping series was examined.

dopant	$x$	$y$	$\rho$				$M$			$C$
			$T_s$	$T_m$	$T_c^{onset}$	$T_c^{offset}$	$T_s$	$T_m$	$T_c$	$T_c$
Cu / Co	0.024	0	105	99						
	0.024	0.005	88	78			90	79		
	0.022	0.01	80	68	4.7	0	81	68		
	0.022	0.019	42	29**	11	9			8.7	
	0.021	0.026	$25 \pm 15^*$		12.1	11			11.6	10.4
	0.021	0.032			8.9	8.3			10.2	
	0.021	0.043			4.6	2			4.3	

Table 6.3 Summary of  $T_s$ ,  $T_m$  and  $T_c$  from resistivity, magnetization and specific heat measurements for  $\text{Ba}(\text{Fe}_{1-x-y}\text{Co}_x\text{Cu}_y)_2\text{As}_2$  ( $x \sim 0.022$ ) series. \* and \*\*: see text.

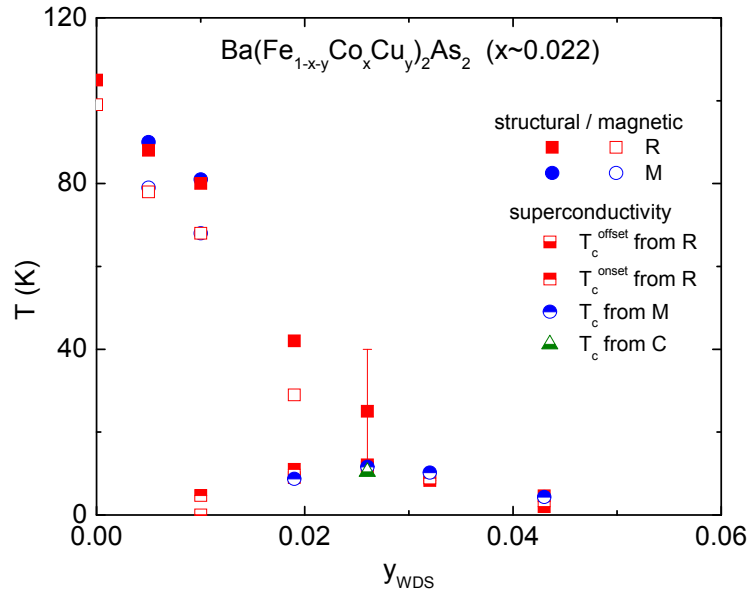


Figure 6.16  $T - y$  phase diagram of  $\text{Ba}(\text{Fe}_{1-x-y}\text{Co}_x\text{Cu}_y)_2\text{As}_2$  ( $x \sim 0.022$ ) single crystals.

#### 6.2.4 Ba(Fe<sub>1-x-y</sub>Co<sub>x</sub>Cu<sub>y</sub>)<sub>2</sub>As<sub>2</sub> ( $x \sim 0.047$ )

So as to further examine the effects of Cu doping on the superconducting dome, a Ba(Fe<sub>1-x-y</sub>Co<sub>x</sub>Cu<sub>y</sub>)<sub>2</sub>As<sub>2</sub> ( $x \sim 0.047$ ) series was also grown. For  $y = 0$ , this is an underdoped, but superconducting, member of the Ba(Fe<sub>1-x</sub>Co<sub>x</sub>)<sub>2</sub>As<sub>2</sub> series. The elemental analysis shown in Table 3.2 indicates that within a single batch the variation of Cu concentration is roughly  $\pm 10\%$  of the average concentration, similar to the variation range in Ba(Fe<sub>1-x</sub>Cu<sub>x</sub>)<sub>2</sub>As<sub>2</sub> and Ba(Fe<sub>1-x-y</sub>Co<sub>x</sub>Cu<sub>y</sub>)<sub>2</sub>As<sub>2</sub> ( $x \sim 0.022$ ) series.

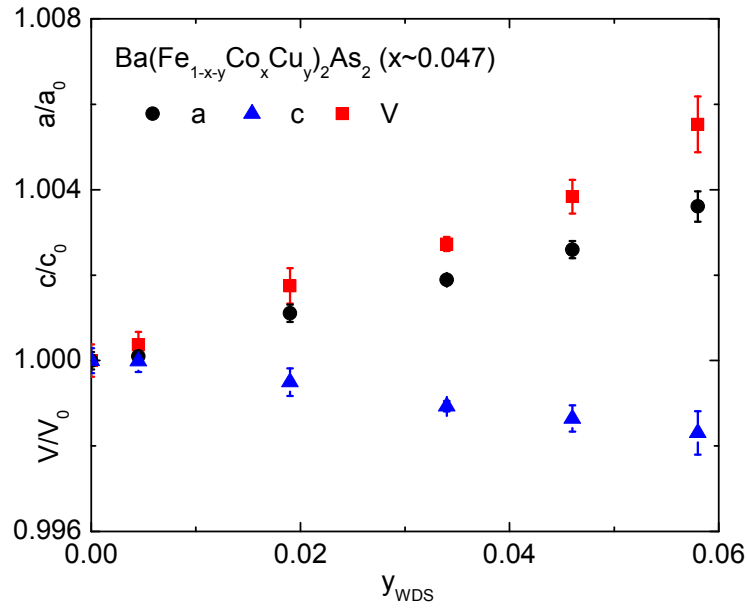


Figure 6.17 Lattice parameters of Ba(Fe<sub>1-x-y</sub>Co<sub>x</sub>Cu<sub>y</sub>)<sub>2</sub>As<sub>2</sub> ( $x \sim 0.047$ ) series,  $a$  and  $c$  as well as unit cell volume,  $V$ , normalized to the values of Ba(Fe<sub>0.935</sub>Co<sub>0.047</sub>)<sub>2</sub>As<sub>2</sub> ( $a_0=3.9605(6)\text{\AA}$ ,  $c_0=12.9916(38)\text{\AA}$ ) as a function of measured Cu concentration,  $y_{WDS}$

Fig. 6.17 presents the normalized lattice parameters  $a/a_0$ ,  $c/c_0$  and  $V/V_0$  for this series, where  $a_0$ ,  $c_0$  and  $V_0$  are the ones of Ba(Fe<sub>0.935</sub>Co<sub>0.047</sub>)<sub>2</sub>As<sub>2</sub>. As Cu is doped into Ba(Fe<sub>0.935</sub>Co<sub>0.047</sub>)<sub>2</sub>As<sub>2</sub>, the lattice parameter  $a$  and unit cell volume increase while the lattice parameter  $c$  decreases. Comparing with Ba(Fe<sub>1-x</sub>Cu<sub>x</sub>)<sub>2</sub>As<sub>2</sub> and Ba(Fe<sub>1-x-y</sub>Co<sub>x</sub>Cu<sub>y</sub>)<sub>2</sub>As<sub>2</sub> ( $x \sim 0.022$ ) series, the effects of Cu doping in these series on changing the lattice parameters are quantitatively similar

to each other.

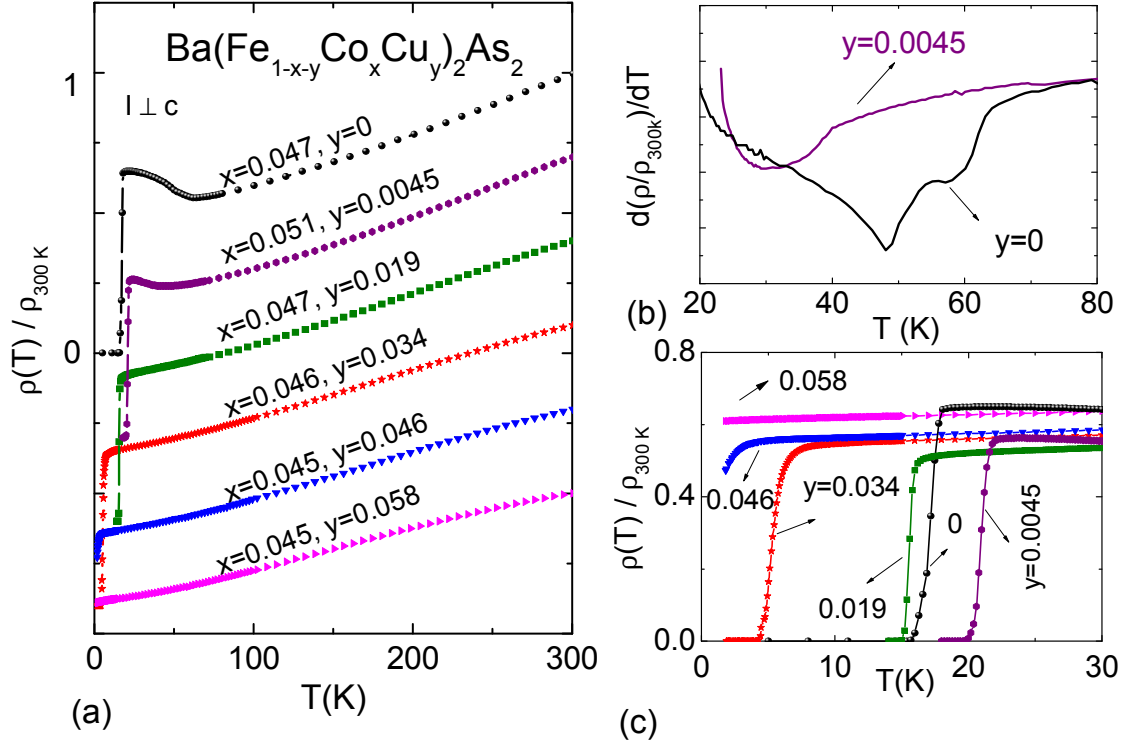


Figure 6.18  $\text{Ba}(\text{Fe}_{1-x-y}\text{Co}_x\text{Cu}_y)_2\text{As}_2$  ( $x \sim 0.047$ ) series: (a) The temperature dependent resistivity, normalized to the room temperature value. Each subsequent data set is shifted downward by 0.3 for clarity. (b)  $d(\rho(T)/\rho_{300K})/dT$  for  $y=0$  and 0.0045. (c) Enlarged low temperature  $\rho(T)/\rho_{300K}$ .

Fig. 6.18 (a) shows the normalized resistivity of this series and Fig. 6.18 (b) shows the enlarged, low temperature resistivity data that emphasize the superconducting transition. From the resistivity data, we can see that  $\text{Ba}(\text{Fe}_{0.953}\text{Co}_{0.047})_2\text{As}_2$  is an underdoped compound with  $T_s = 64K$ ,  $T_m = 48K$  and  $T_c \sim 17K$ . With  $y=0.0045$  of Cu doping,  $T_c$  increases to 20 K and the structural / magnetic phase transitions are suppressed to such an extent that only a resistance minima is detected before superconductivity truncates the rest of the low temperature resistivity data. The superconductivity feature can be more clearly seen in Fig. 6.18 (c).  $y=0.019$  of Cu doping decreases  $T_c$  to 15 K, there is no longer any sign of structural and magnetic phase transitions, and the resistivity has a roughly linear temperature

dependence above  $T_c$ . With even higher Cu doping,  $T_c$  is suppressed to about 5 K for  $y=0.036$  Cu doping. For  $y=0.046$  of Cu doping, no zero resistivity in our measured temperature range can be observed, only some resistivity decrease around 2 K can be seen, which might suggest the onset of the superconducting state. For  $y=0.058$  of Cu doping, there is no sign of a superconducting state.

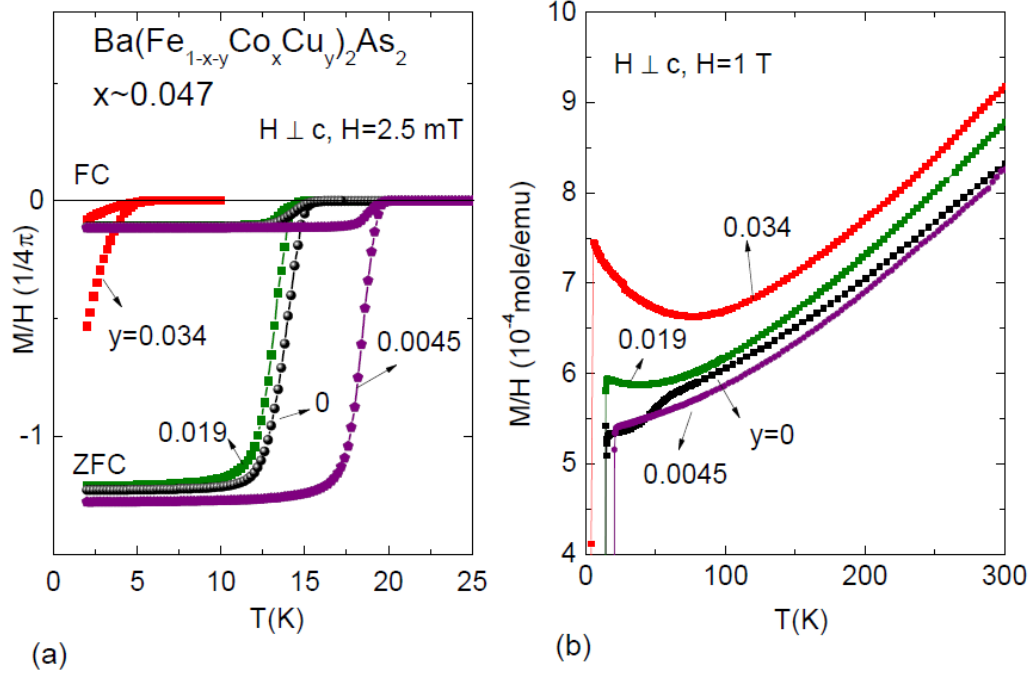


Figure 6.19  $\text{Ba}(\text{Fe}_{1-x-y}\text{Co}_x\text{Cu}_y)_2\text{As}_2$  ( $x \sim 0.047$ ) series: (a) Field-cooled (FC) and zero-field-cooled (ZFC) low field  $M(T)/H$  data taken at 2.5 mT with  $H \perp c$ . (b)  $M(T)/H$  data taken at 1 T with  $H \perp c$  for  $0 \leq y \leq 0.034$ .

Fig. 6.19 (a) shows the low field  $M(T)/H$  data for this series taken at 2.5 mT with  $H$  perpendicular to the  $c$  axis. In FC measurement, the diamagnetic signal of the same magnitude found for  $\text{Ba}(\text{Fe}_{1-x}\text{Co}_x)_2\text{As}_2$ , suggests the same degree of the bulk superconductivity in these samples as is found for the Co or Ni doped series. The  $T_c$  values inferred from the susceptibility data are consistent with the resistivity data. Fig. 6.19 (b) shows the temperature dependent  $M(T)/H$  data taken at 1 T with  $H$  perpendicular to  $c$  axis for  $0.034 \geq y \geq 0$ . For  $y = 0$ , a clear drop around 60 K can be seen in the susceptibility which is consistent with the structural



/ magnetic phase transitions seen in the resistivity data. The second, lower temperature drop, around 20 K, is associated the superconductivity. With Cu doping  $y \geq 0.045$ , no structural

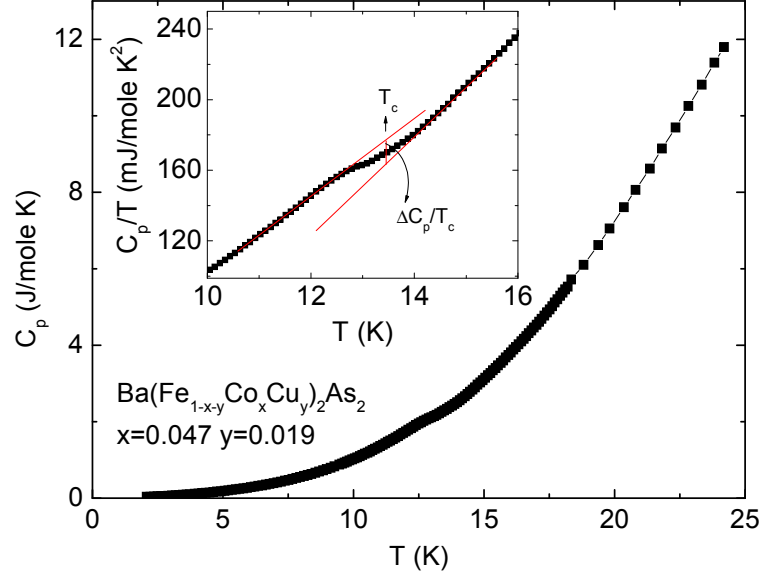


Figure 6.20 Temperature dependent heat capacity of Ba(Fe<sub>0.934</sub>Co<sub>0.047</sub>Cu<sub>0.019</sub>)<sub>2</sub>As<sub>2</sub>. Inset:  $C_p/T$  vs.  $T$  near the superconducting transition with the estimated  $\Delta C_p$  shown.

/ magnetic phase transitions feature can be seen although there is a resistive minima for  $y = 0.0045$  in the resistivity data. The high temperature linear behavior in susceptibility can also be observed in this Ba(Fe<sub>1-x-y</sub>Co<sub>x</sub>Cu<sub>y</sub>)<sub>2</sub>As<sub>2</sub> ( $x \sim 0.047$ ) series.

Heat capacity data was collected for the first clearly overdoped member of this series: Ba(Fe<sub>0.934</sub>Co<sub>0.047</sub>Cu<sub>0.019</sub>)<sub>2</sub>As<sub>2</sub>. The heat capacity jump is consistent with the bulk superconductivity in the sample. The inset shows the the enlarged  $C_p/T$  vs.  $T$  data near  $T_c$ . The inferred  $\Delta C_p/T_c$  from "isoentropic" construction is 14 mJ/mole  $K^2$  with  $T_c$  equal to 14 K.

Table 6.4 summarizes these data and Fig. 6.21 is a temperature-Cu doping concentration ( $T - y$ ) phase diagram. It is worth noting from Fig. 6.21 that with the addition of Cu in Ba(Fe<sub>0.953</sub>Co<sub>0.047</sub>)<sub>2</sub>As<sub>2</sub>,  $T_c$  does not decrease but rather increasing to  $\sim 20K$  at  $y = 0.0045$ ,

dopant	$x$	$y$	$\rho$				$M$	$C$
			$T_s$	$T_m$	$T_c^{onset}$	$T_c^{offset}$	$T_c$	$T_c$
Cu / Co	0.047	0	64	48	17.8	16.5	15.9	13.5
	0.051	0.0045	40		21.5	20.4	20.1	
	0.047	0.019			15.9	15.2	14.8	
	0.047	0.034			6	4.6	5.7	
	0.045	0.046			0	0		

Table 6.4 Summary of  $T_s$ ,  $T_m$  and  $T_c$  from resistivity, magnetization and specific heat measurements for  $\text{Ba}(\text{Fe}_{1-x-y}\text{Co}_x\text{Cu}_y)_2\text{As}_2$  ( $x \sim 0.047$ ) series.

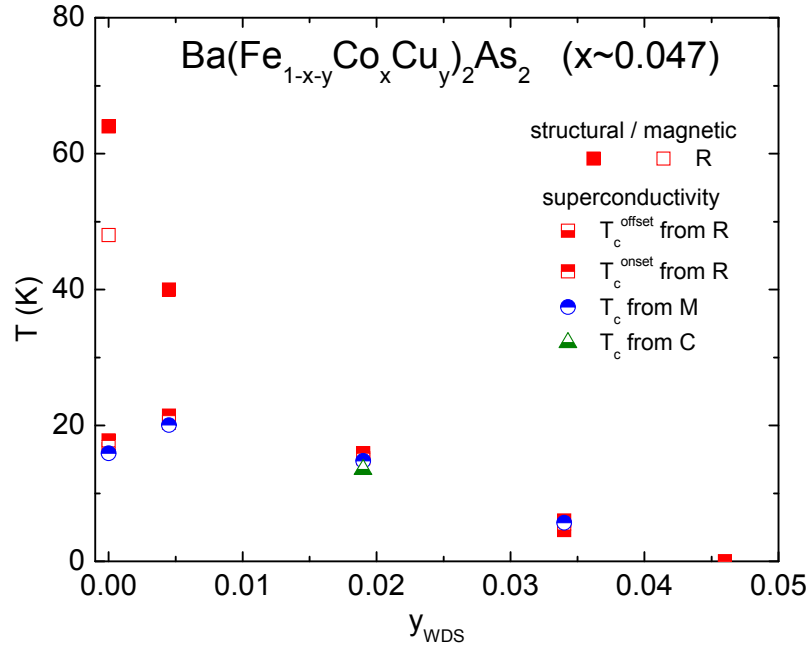


Figure 6.21  $T - y$  phase diagram of  $\text{Ba}(\text{Fe}_{1-x-y}\text{Co}_x\text{Cu}_y)_2\text{As}_2$  ( $x \sim 0.047$ ) single crystals.

and has a value  $\sim 15\text{K}$  at  $y = 0.019$  Cu. These data, along with the other Co / Cu doping series we discussed in the previous section, clearly indicate that superconductivity can be induced and stabilized to high  $T_c$  values of  $T_c$  by Cu doping under well defined circumstances.

### 6.2.5 $\text{Ba}(\text{Fe}_{1-x}\text{Rh}_x)_2\text{As}_2$

Fig. 6.22 shows the normalized lattice parameters  $a/a_0$ ,  $c/c_0$  and  $V/V_0$  of  $\text{Ba}(\text{Fe}_{1-x}\text{Rh}_x)_2\text{As}_2$  series, where  $a_0$ ,  $c_0$  and  $V_0$  are the ones of pure  $\text{BaFe}_2\text{As}_2$ . Lattice parameter  $a$  and unit volume  $V$  almost linearly increases by 0.7% and 0.28% respectively, while lattice parameter  $c$  linearly decreases by 1.15% at  $x=0.166$ . Comparing with 3d Co-doping, in which at  $x = 0.114$  the lattice parameter  $c$  linearly decreases by 0.5%, we found that although Co and Rh have the same valence electrons, the substitution of these atoms for Fe sites affects the lattice parameters very differently due to the larger atomic size of Rh: the changes of  $a$  and  $c$  with Rh-doping are almost 4 and 2 times of the ones in Co-doping respectively which results in an expansion of the unit cell volume in Rh-doping, but a compression, in Co-doping.

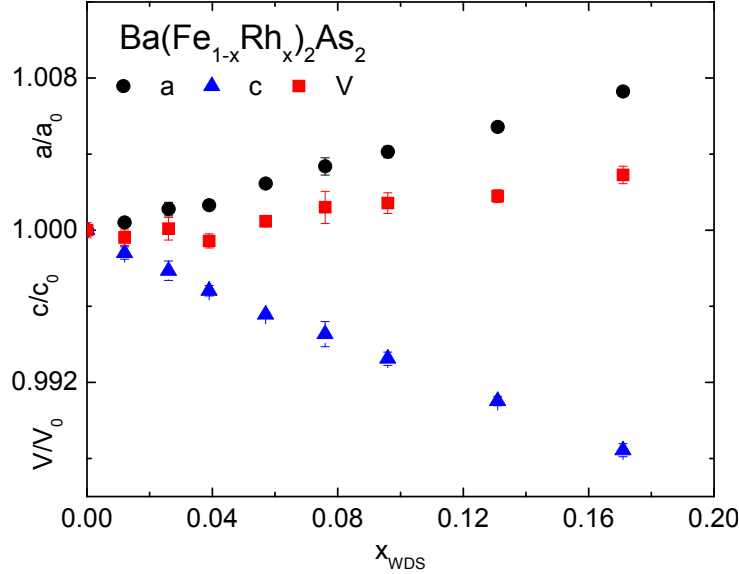


Figure 6.22 Lattice parameters of  $\text{Ba}(\text{Fe}_{1-x}\text{Rh}_x)_2\text{As}_2$  series,  $a$  and  $c$  as well as unit cell volume,  $V$ , normalized to the values of pure  $\text{BaFe}_2\text{As}_2$  as a function of measured Rh concentration,  $x_{\text{WDS}}$

Fig. 6.23 (a) presents the normalized electrical resistivity data of the  $\text{Ba}(\text{Fe}_{1-x}\text{Rh}_x)_2\text{As}_2$  series from 2 K to 300 K. As in the case of Co, Ni and Cu substitutions [33, 34], as  $x$  is increased the temperature of the resistive anomaly is suppressed monotonically and the shape of the feature changes from a sharp decrease in pure  $\text{BaFe}_2\text{As}_2$  to a broadened increase in

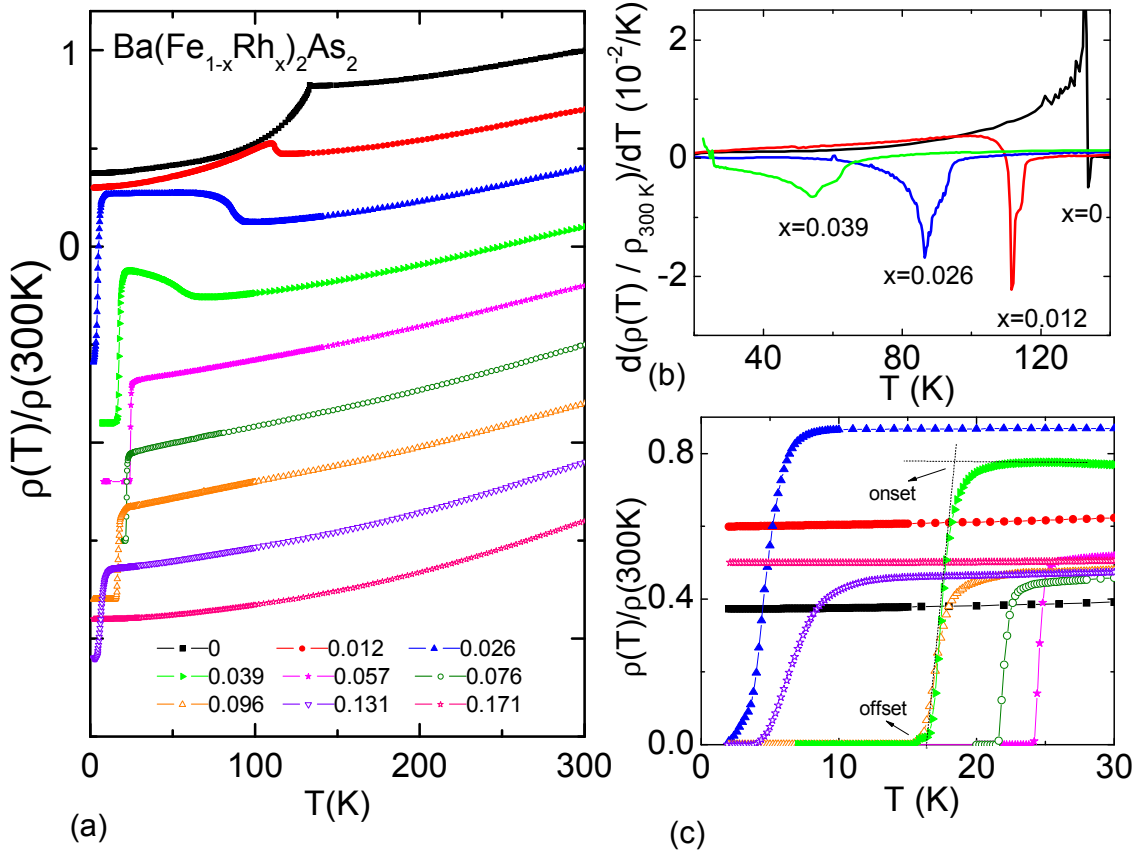


Figure 6.23  $\text{Ba}(\text{Fe}_{1-x}\text{Rh}_x)_2\text{As}_2$  series: (a) The temperature dependent resistivity, normalized to the room temperature value. Each subsequent data set is shifted downward by 0.3 for clarity. (b)  $d(\rho(T)/\rho_{300K})/dT$  for  $x \leq 0.039$ . (c) Enlarged low temperature  $\rho(T)/\rho_{300K}$ .

doped samples. It is no longer detectable for  $x \geq 0.057$ . For  $x = 0.026$ , superconductivity can be stabilized, with  $T_c \approx 3$  K inferred from the sharp drop in the resistivity data. For  $x = 0.057$ , superconducting temperature  $T_c$  has a maximum value of 24 K with a width  $\Delta T_c \approx 0.7$  K. With even higher  $x$ ,  $T_c$  is suppressed. The features of the structural / magnetic phase transitions manifest as two kinks in the  $d(\rho(T)/\rho_{300K})/dT$  plot shown in Fig. 6.23 (b). Fig. 6.23 (c) shows the enlarged low temperature  $\rho(T)/\rho_{300K}$  data for  $\text{Ba}(\text{Fe}_{1-x}\text{Rh}_x)_2\text{As}_2$  and we can clearly see the evolution of  $T_c$  with respect to the doping level.

Fig. 6.24 (a) shows the  $M(T)/H$  data for the  $\text{Ba}(\text{Fe}_{1-x}\text{Rh}_x)_2\text{As}_2$  series taken at 2.5 mT with  $H$  perpendicular to the crystallographic  $c$ -axis. A clear diamagnetic signal can be seen

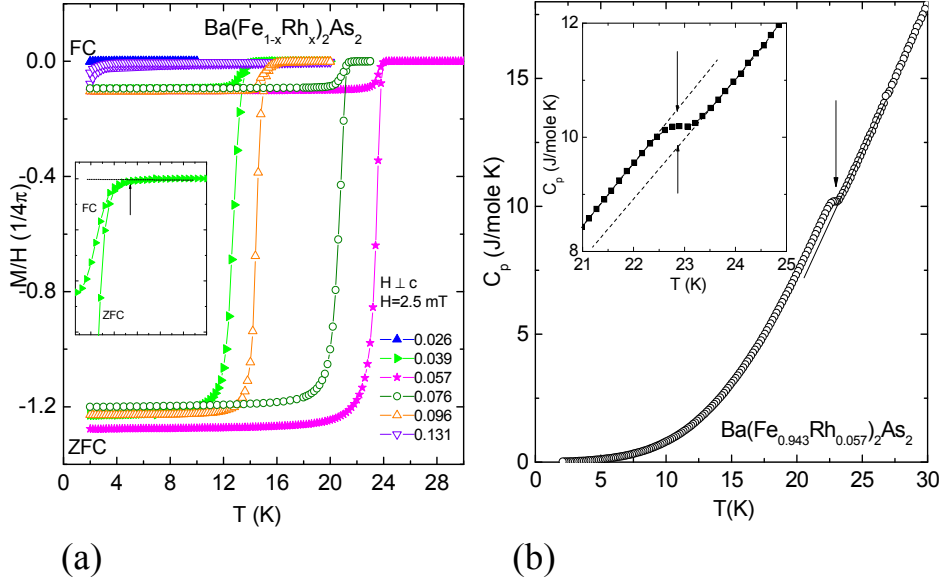


Figure 6.24 (a) Low magnetic field  $M(T)/H$  of  $\text{Ba}(\text{Fe}_{1-x}\text{Rh}_x)_2\text{As}_2$  series. Inset: the criterion used to infer  $T_c$  is shown for  $\text{Ba}(\text{Fe}_{0.961}\text{Rh}_{0.039})_2\text{As}_2$ . (b) Temperature dependent heat capacity of  $\text{Ba}(\text{Fe}_{0.943}\text{Rh}_{0.057})_2\text{As}_2$ . Inset:  $C_p$  vs.  $T$  near the superconducting transition with the estimated  $\Delta C_p$  shown.

in both field-cooled (FC) and zero-field-cooled (ZFC) data. Because of the low  $T_c$  values for  $x = 0.026$  and  $x = 0.131$ , which are on the low- and high-  $x$  extremes of the superconducting dome respectively, we only observe the onset of the diamagnetic signal and no large drop below the superconducting temperature is seen down to our base temperature of 2 K. However, for all the other concentrations, the large superconducting, shielding fraction and the sharp drop below  $T_c$  are consistent with the existence of bulk superconductivity. Compared to the low field  $M(T)/H$  data for  $\text{Ba}(\text{Fe}_{1-x}\text{Co}_x)_2\text{As}_2$  [34], the superconducting fraction associated with the  $\text{Ba}(\text{Fe}_{1-x}\text{Rh}_x)_2\text{As}_2$  series is very similar to that of the  $\text{Ba}(\text{Fe}_{1-x}\text{Co}_x)_2\text{As}_2$  series.

The temperature dependent heat capacity data of  $\text{Ba}(\text{Fe}_{0.943}\text{Rh}_{0.057})_2\text{As}_2$  is shown in Fig. 6.24 (b). This concentration has the maximum  $T_c$  value in this series. The heat capacity anomaly is relatively sharp and consistent with the superconducting phase transition we observed in both resistivity and low field magnetization data. The large arrow in the inset shows the onset of superconductivity and  $T_c = 22.9$  K. An estimate of  $\Delta C_p$  is shown in the inset;

$\Delta C_p \approx 660$  mJ/mole K.

dopant	$x$	$\rho$				$M$	$C$
		$T_s$	$T_m$	$T_c^{onset}$	$T_c^{offset}$	$T_c$	$T_c$
Rh	0.012	116	112				
	0.026	95	87	6	3	4.8	
	0.039	65	54	18.2	16.7	14.5	
	0.057			25	24.2	24.4	22.9
	0.076			22.5	21.6	21.8	
	0.096			18	16	17.2	
	0.131			8.8	4.6	4.8	
	0.171			0	0		

Table 6.5 Summary of  $T_s$ ,  $T_m$  and  $T_c$  from resistivity, magnetization and specific heat measurements for  $\text{Ba}(\text{Fe}_{1-x}\text{Rh}_x)_2\text{As}_2$  series.

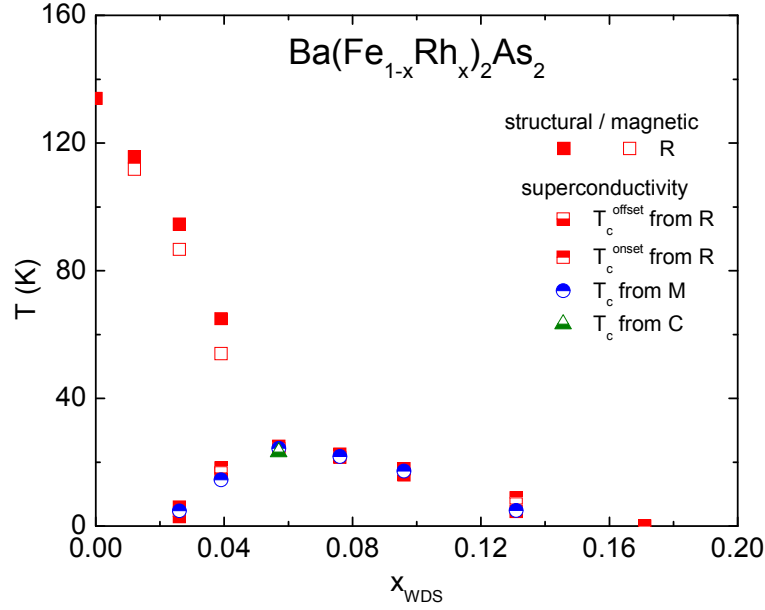


Figure 6.25  $T - x$  phase diagram of  $\text{Ba}(\text{Fe}_{1-x}\text{Rh}_x)_2\text{As}_2$  single crystals.

All  $T_s$ ,  $T_m$  and  $T_c$  for  $\text{Ba}(\text{Fe}_{1-x}\text{Rh}_x)_2\text{As}_2$  series inferred from Figs. 6.23 and 6.24 are listed in Table 6.5 and graphically shown as a  $T - x$  phase diagram in Fig. 6.25. As we can see, although isoelectronic 4d element Rh and 3d element Co affect the lattice parameters of the unit cell very differently, they have very similar effects on the rate of the suppression of the structural / magnetic phase transitions and the stabilization of the superconductivity. The

location and the extent of the superconducting domes of these two series are almost the same.

### 6.2.6 $\text{Ba}(\text{Fe}_{1-x}\text{Pd}_x)_2\text{As}_2$

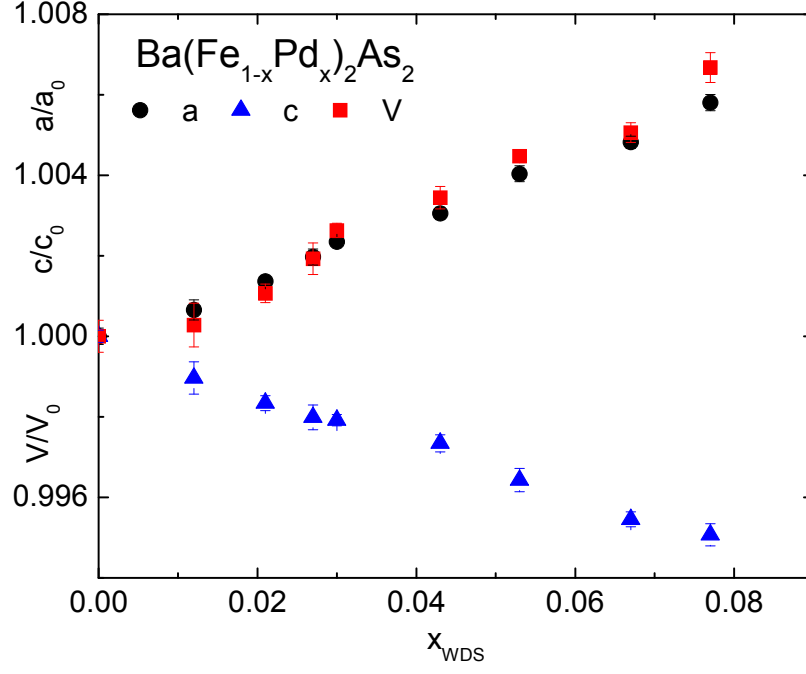


Figure 6.26 Lattice parameters of  $\text{Ba}(\text{Fe}_{1-x}\text{Pd}_x)_2\text{As}_2$  series,  $a$  and  $c$  as well as unit cell volume,  $V$ , normalized to the values of pure  $\text{BaFe}_2\text{As}_2$  as a function of measured Pd concentration,  $x_{\text{WDS}}$

The normalized lattice parameters of  $\text{Ba}(\text{Fe}_{1-x}\text{Pd}_x)_2\text{As}_2$  series are shown in Fig. 6.26. Lattice parameter  $a$  increases almost linearly by 0.6% while lattice parameter  $c$  decreases linearly by 0.5% at  $x=0.077$ . This behavior is quite different with the change in  $\text{Ba}(\text{Fe}_{1-x}\text{Ni}_x)_2\text{As}_2$  series, in which  $a$  increases by 0.04%,  $c$  decreases by 0.3% at  $x = 0.072$  Ni doping level. If we compare 4d Rh doping and Pd doping, it can be seen that although the addition of these atoms have quantitatively similar effect on  $c$ , the change in  $a$  due to additional Pd atoms is roughly twice of the one caused by Rh atoms.

Fig. 6.27 (a) shows the normalized electrical resistivity data for the  $\text{Ba}(\text{Fe}_{1-x}\text{Pd}_x)_2\text{As}_2$  series from 2 K to 300 K. A systematic behavior, similar to the  $\text{Ba}(\text{Fe}_{1-x}\text{Ni}_x)_2\text{As}_2$  series, is seen: the temperature of the resistive anomaly associated with the structural / antiferromagnetic

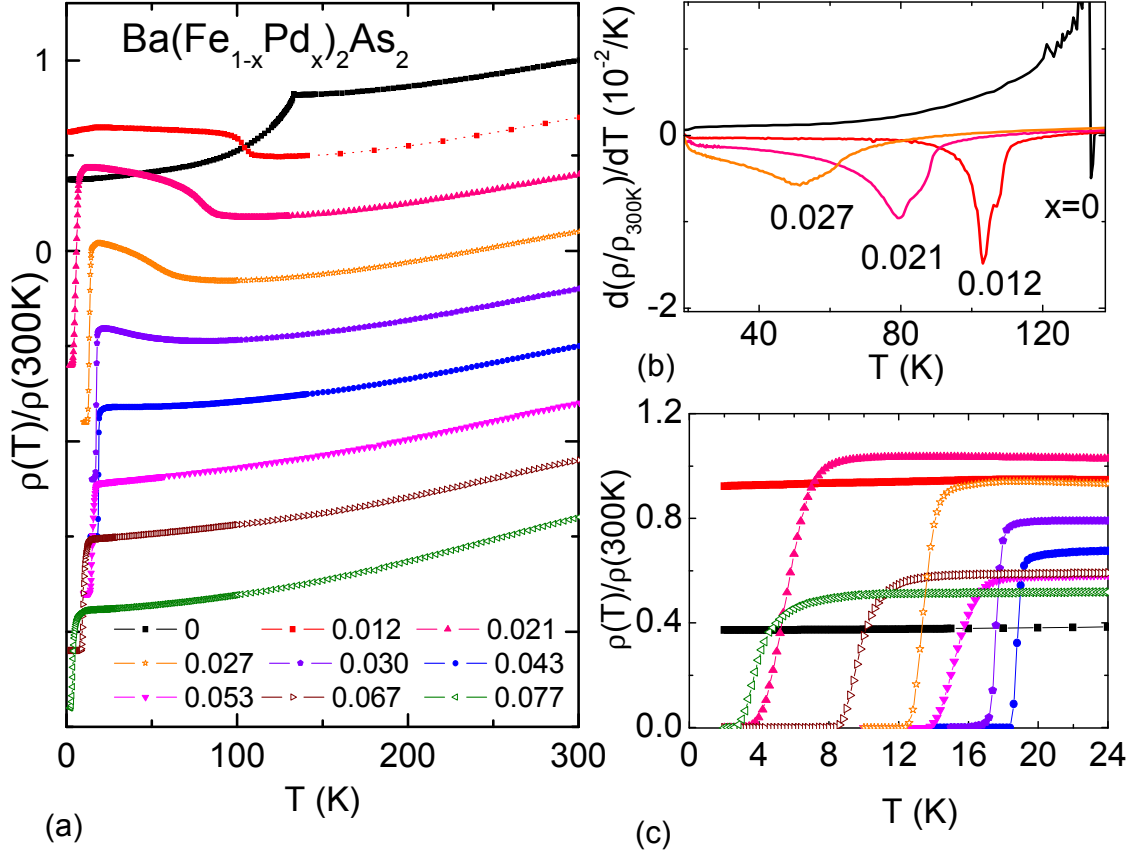


Figure 6.27  $\text{Ba}(\text{Fe}_{1-x}\text{Pd}_x)_2\text{As}_2$  series: (a) The temperature dependent resistivity, normalized to the room temperature value. Each subsequent data set is shifted downward by 0.3 for clarity. (b)  $d(\rho(T)/\rho_{300K})/dT$  for  $x \leq 0.027$ . (c) Enlarged low temperature  $\rho(T)/\rho_{300K}$ .

phase transitions is suppressed monotonically with Pd doping and the shape of the anomaly changes from a sharp decrease to a broadened increase in resistivity upon cooling. For  $x = 0.021$ , the resistive anomaly can still be clearly seen and superconductivity is detected with  $T_c \approx 5.7$  K. For  $x = 0.043$ , the temperature of the resistive anomaly is further reduced and it is only inferred from a minimum in the resistivity above the superconducting transition. For  $x = 0.053$ , the resistive anomaly is completely suppressed and  $T_c$  has its highest value of about 19 K and a width of  $\Delta T_c \approx 0.6$  K. With higher  $x$  values,  $T_c$  is reduced. Fig. 6.27 (b) presents the  $d(\rho(T)/\rho_{300K})/dT$  for  $0.027 \geq x$  which are used to infer  $T_c$ ; the superconducting feature



can be clearly seen in Fig. 6.27 (c).

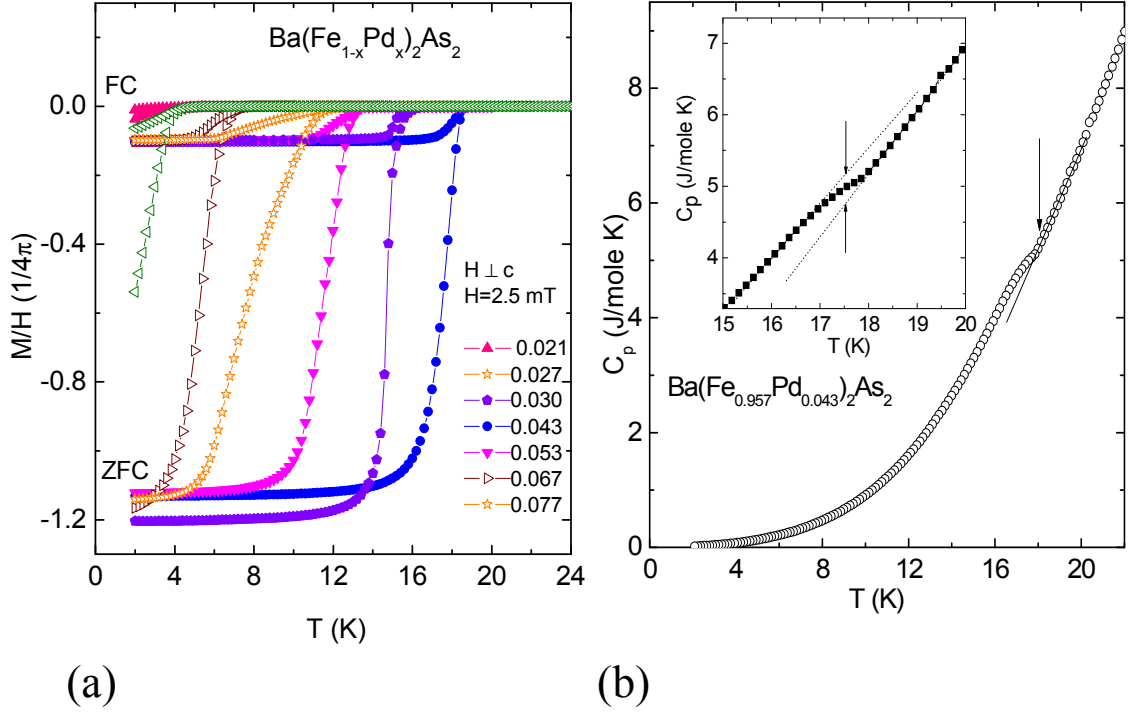


Figure 6.28 (a) Low magnetic field  $M(T)/H$  of  $\text{Ba}(\text{Fe}_{1-x}\text{Pd}_x)_2\text{As}_2$  series. (b) Temperature dependent heat capacity of  $\text{Ba}(\text{Fe}_{0.957}\text{Pd}_{0.043})_2\text{As}_2$ . Inset:  $C_p$  vs.  $T$  near the superconducting transition with the estimated  $\Delta C_p$  shown.

The low field  $M(T)/H$  data of the  $\text{Ba}(\text{Fe}_{1-x}\text{Pd}_x)_2\text{As}_2$  series (FC and ZFC) are shown in Fig. 6.28 (a). They were taken at 2.5 mT with  $H$  perpendicular to the crystallographic  $c$ -axis. The broader feature seen in the magnetization for  $x = 0.027$  implies a larger inhomogeneity associated with this sample. Indeed, the WDS data for  $x = 0.027$  does show local maximum in  $2\sigma$  values. Despite the broader drop of the magnetization, the large superconducting fraction is comparable to the rest of the Pd-doped series as well as to the Co-, Ni- and Rh-doped  $\text{BaFe}_2\text{As}_2$  results, all of which are consistent with bulk superconductivity. Again, only a small diamagnetic signal was observed at base temperature for  $x = 0.021$  due to the low  $T_c$  for this concentration.

Fig. 6.28 (b) shows the temperature dependent heat capacity data of  $\text{Ba}(\text{Fe}_{0.957}\text{Pd}_{0.043})_2\text{As}_2$ ,

dopant	$x$	$\rho$				$M$	$C$
		$T_s$	$T_m$	$T_c^{onset}$	$T_c^{offset}$	$T_c$	$T_c$
Pd	0.012	110	103				
	0.021	90	80	6.9	4	4.2	
	0.027	67	51	14.3	12.8	12.5	
	0.03	$45 \pm 25^*$		18	17.3	16.8	17.5
	0.043			19	18.4	18.8	
	0.053			16.5	14.1	13.6	
	0.067			10.8	8.8	8	
	0.077			5.2	2.8		

Table 6.6 Summary of  $T_s$ ,  $T_m$  and  $T_c$  from resistivity, magnetization and specific heat measurements for  $\text{Ba}(\text{Fe}_{1-x}\text{Pd}_x)_2\text{As}_2$  series.

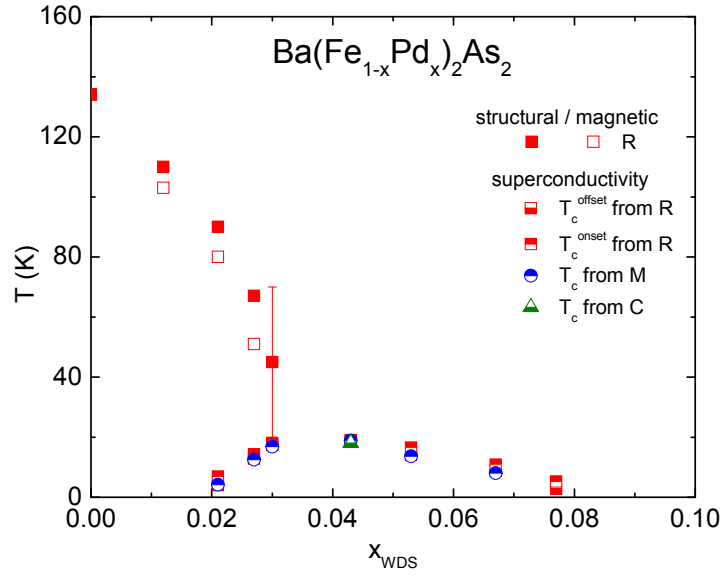


Figure 6.29  $T - x$  phase diagram of  $\text{Ba}(\text{Fe}_{1-x}\text{Pd}_x)_2\text{As}_2$  single crystals.

which manifests the highest  $T_c$  value in this series. The heat capacity anomaly at  $T_c$  can be clearly seen, although it is broader than the one found for  $\text{Ba}(\text{Fe}_{0.943}\text{Rh}_{0.057})_2\text{As}_2$  (Fig. 6.24). The arrows show the onset of superconductivity at  $T_c = 17.5$  K, and the estimated  $\Delta C_p$  is shown in the inset;  $\Delta C_p \approx 420$  mJ/mole K.

Table 6.6 summarized all  $T_s$ ,  $T_m$  and  $T_c$  for  $\text{Ba}(\text{Fe}_{1-x}\text{Pd}_x)_2\text{As}_2$  series inferred from Figs.

6.27 and 6.28. For the concentrations indexed by \*,  $T_s$  is determined by the same way explained in section 6.2.2. The  $T-x$  phase diagram of  $\text{Ba}(\text{Fe}_{1-x}\text{Pd}_x)_2\text{As}_2$  series is presented in Fig. 6.29. The appearance of the phase diagram is quite similar to the ones of Co-doping, Ni-doping, Co / Cu-doping and Rh-doping series. The superconducting dome shows very similar location and extent as Ni doped series.

### 6.3 Discussion

#### 6.3.1 Comparison of the phase diagrams of $\text{Ba}(\text{Fe}_{1-x}\text{TM}_x)_2\text{As}_2$ (TM=Co, Ni, Cu, Co / Cu, Rh and Pd) series

As we have seen, all the transport, magnetic and thermodynamic data presented so far are summarized in Tables 5.1, 6.1 to 6.6 and graphically presented in Figs. 6.5, 6.11, 6.16, 6.21, 6.25 and 6.29. Good agreements between resistivity, magnetization and heat capacity measurements for each series can be observed. The extensive measurement of over 60 samples spanning 7 different  $\text{Ba}(\text{Fe}_{1-x}\text{TM}_x)_2\text{As}_2$  series allows for the identification of some of the salient parameters controlling superconductivity in these materials. This comparison can start simply, with the isoelectronic Co / Rh doping and Ni / Pd doping. In Fig. 6.30, the upper panel presents the comparison of the  $T-x$  phase diagrams of 3d Co and isoelectronic 4d Rh doped  $\text{BaFe}_2\text{As}_2$ , the lower panel presents the comparison of 3d Ni and isoelectronic 4d Pd doped  $\text{BaFe}_2\text{As}_2$ . Despite the generic difference between 3d and 4d shells, the effects of Rh doping are exceptionally similar to the effects of Co doping and the effects of Pd doping are exceptionally similar to the effects of Ni doping. At the same time, there is a clear difference in the extent of the superconducting domes found for Co (Rh) doping as opposed to Ni (Pd) doping.

The composite  $T-x$  phase diagram, shown in Fig. 6.31 (a) highlights the similarities and differences between the various  $\text{Ba}(\text{Fe}_{1-x}\text{TM}_x)_2\text{As}_2$  series. Given that Fig. 6.30 shows that the  $T-x$  phase diagrams for the 4d dopings are virtually identical to those for the isoelectronic 3d dopings, only 3d doping is shown in Fig. 6.31 for clarity. The suppression rates of the upper phase transitions for all these different series appear to depend on  $x$  in a roughly similar

manner. Although there is some variation (that will be discussed below) the suppression and splitting of the structural and magnetic transitions essentially just depend on  $x$ , the number of TM substituted for Fe (note for double doping with both Co and Cu,  $x$  is the sum of Co and Cu doping levels). On the other hand, as pointed out above, the superconducting dome is not uniquely described by this parameterization. The  $\text{Ba}(\text{Fe}_{1-x}\text{Co}_x)_2\text{As}_2$  series has the widest superconducting dome, ranging from  $x \sim 0.03$  to  $0.166$ .  $\text{Ba}(\text{Fe}_{1-x-y}\text{Co}_x\text{Cu}_y)_2\text{As}_2$  ( $x \sim 0.047$ ) has a dome extending to  $x_{\text{total}} = x + y \sim 0.092$ .  $\text{Ba}(\text{Fe}_{1-x}\text{Ni}_x)_2\text{As}_2$  ranks third with the dome starting at  $x \sim 0.02$  and ending at  $x \sim 0.075$ . The  $\text{Ba}(\text{Fe}_{1-x-y}\text{Co}_x\text{Cu}_y)_2\text{As}_2$  ( $x \sim 0.022$ ) series has the narrowest superconducting dome ranging from  $x_{\text{total}} = x + y \sim 0.032$  to  $x_{\text{total}} = x + y \sim 0.065$ .  $\text{Ba}(\text{Fe}_{1-x}\text{Cu}_x)_2\text{As}_2$  series might have one superconducting point about  $x = 0.044$ .

Since the amount of TM doping is directly measured via WDS, a closely related parameter, the extra electrons added,  $e$ , can be inferred and the temperature-extra electrons phase diagram ( $T - e$ ) can be constructed. If we assume that all transition metals have the same valence electrons as Fe for these relatively small doping levels in this work, the electronic configuration of  $\text{Co}^{2+}$  is  $[\text{Ar}]3d^7$  and  $\text{Co}^{2+}$  introduces one extra electron, compared to  $\text{Fe}^{2+}$  for which the electron configuration is  $[\text{Ar}]3d^6$ . Following the same logic,  $\text{Ni}^{2+}$  has two extra electron comparing to  $\text{Fe}^{2+}$ ;  $\text{Cu}^{2+}$  has three extra electron comparing to  $\text{Fe}^{2+}$ . This leads to extra electron counts corresponding to  $x$  for Co doping,  $2x$  for Ni doping,  $3x$  for Cu doping,  $x + 3y$  for Co / Cu mixed doping. This assumption is consistent with our Hall resistivity and Seebeck coefficient measurements [55], and as shown below allows for simple parameterization of the superconducting dome. Based on this assumption, the  $T - e$  phase diagrams are presented in Fig. 6.31 (b). The  $T - e$  phase diagram reveals several points of note. The structural / magnetic phase transitions separate (especially Cu doping) but the superconducting domes form a much more revealing manifold, one that collapses onto a universal curve for the "overdoped" side of the domes. This can be seen more clearly in Fig. 6.32 which shows the superconducting domes for all series on an expanded scale. The  $T - e$  phase diagram makes clear that superconductivity seems to only exist over a limited, and well delineated, range of  $e$ -values.

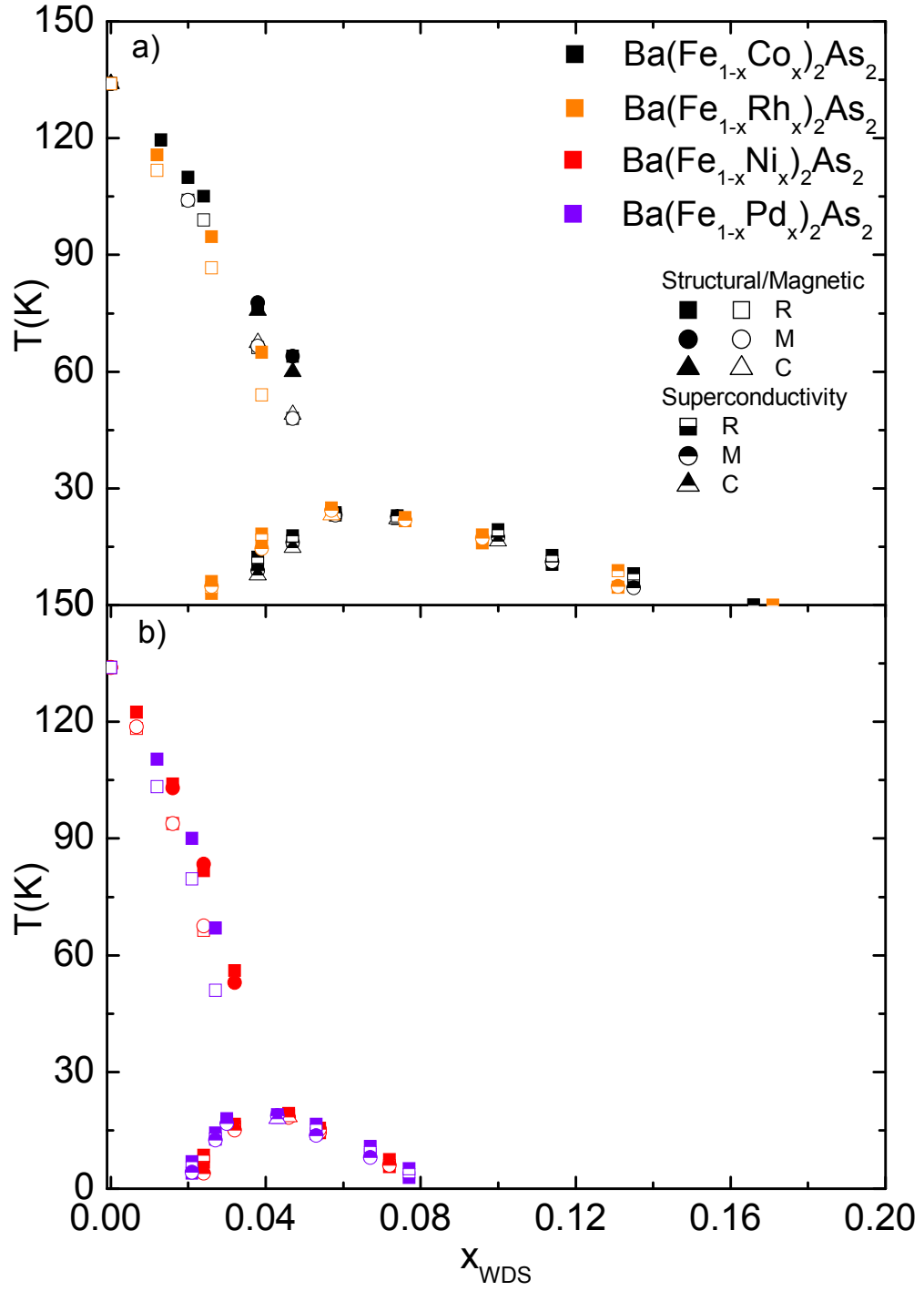


Figure 6.30 (a)  $T - x$  phase diagrams of  $\text{Ba}(\text{Fe}_{1-x}\text{Rh}_x)_2\text{As}_2$  and  $\text{Ba}(\text{Fe}_{1-x}\text{Co}_x)_2\text{As}_2$  series. (b)  $T - x$  phase diagrams of  $\text{Ba}(\text{Fe}_{1-x}\text{Pd}_x)_2\text{As}_2$  and  $\text{Ba}(\text{Fe}_{1-x}\text{Ni}_x)_2\text{As}_2$  series.

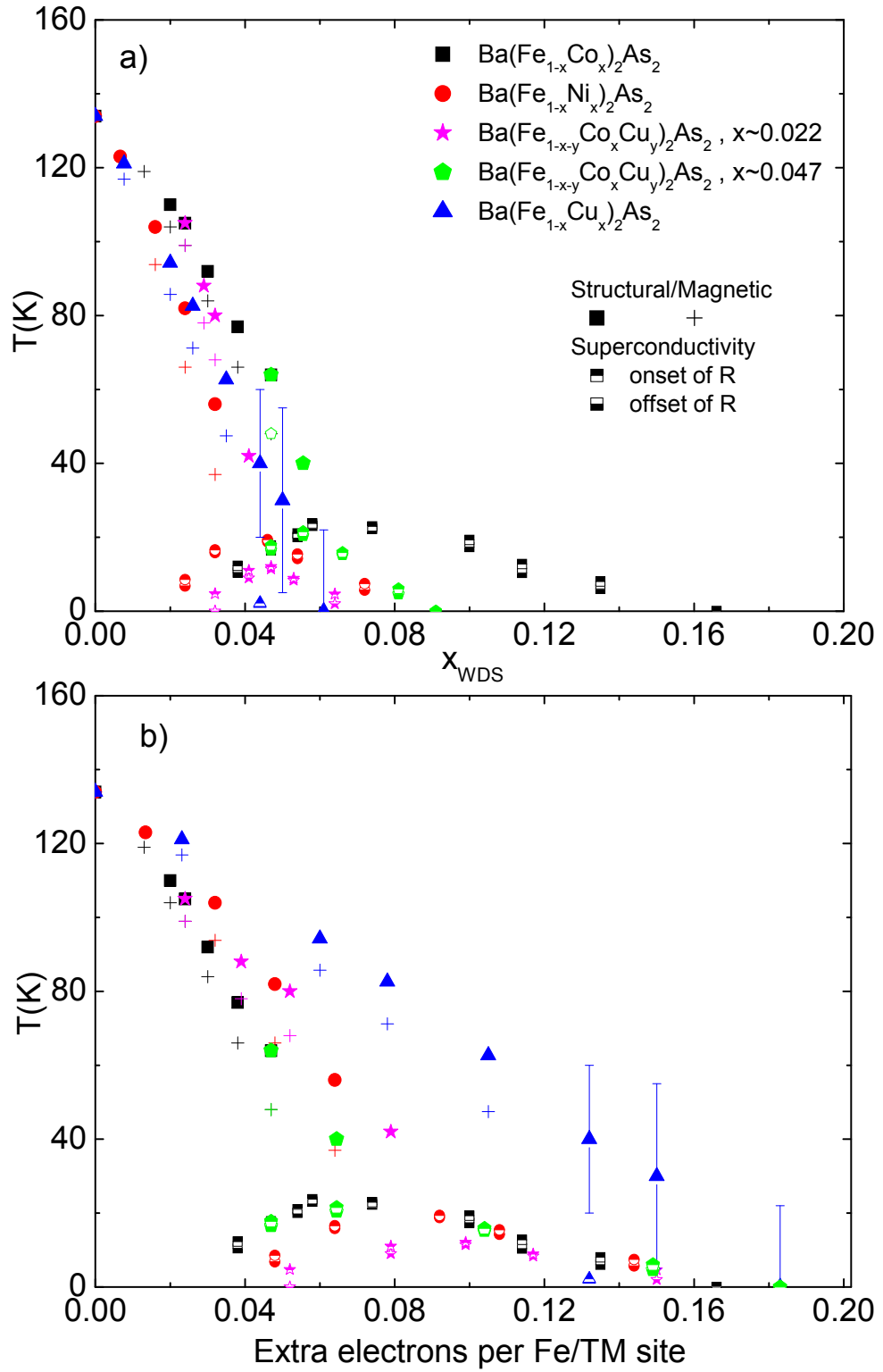


Figure 6.31 (a)  $T-x$  phase diagrams of  $\text{Ba}(\text{Fe}_{1-x}\text{TM}_x)_2\text{As}_2$  (TM=Co, Ni, Cu, Co / Cu). (Note: for Co / Cu doping,  $x_{WDS} = x + y$ ). (a)  $T-e$  phase diagrams of  $\text{Ba}(\text{Fe}_{1-x}\text{TM}_x)_2\text{As}_2$  (TM=Co, Ni, Cu, Co / Cu).

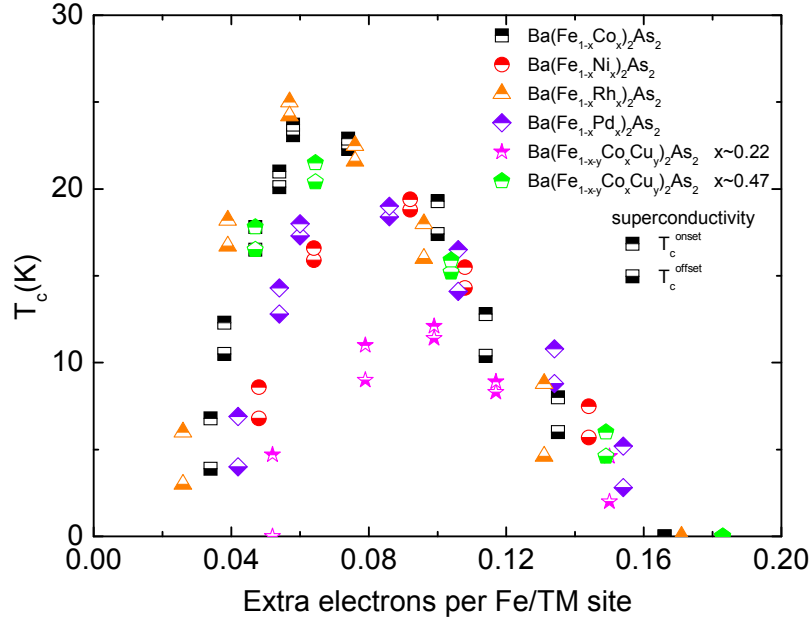


Figure 6.32  $T_c$  as a function of extra electrons,  $e$ , per Fe/TM site for all the series we grew.

The fact that whereas the suppressions of the structural / antiferromagnetic transitions are approximately parameterized by the number of TM dopant ions, the superconducting domes are parameterized by the number of electrons added by doping and exist over a limited range of  $e$ -values (band filling) allows for a decoupling of these transitions as well as the understanding that the suppression of the structural / antiferromagnetic phase transitions to low enough temperature is a necessary, but not sufficient, condition for superconductivity. For example, the data from the  $\text{Ba}(\text{Fe}_{1-x}\text{Cu}_x)_2\text{As}_2$  series clearly demonstrate that, if by the time the structural / antiferromagnetic phase transitions are suppressed enough, too many conduction electrons have been added, the  $e$ -filling window for superconductivity can be missed. On the other hand, if we adjust the position of the upper phase line in the  $T - e$  phase diagram by judicious doping, so that it does not miss the superconducting window, superconductivity can occur. This is demonstrated by the Co / Cu doped series: although  $\text{Ba}(\text{Fe}_{0.979}\text{Co}_{0.021})_2\text{As}_2$  and  $\text{Ba}(\text{Fe}_{0.974}\text{Cu}_{0.026})_2\text{As}_2$  are not superconducting, by tuning the extra electrons added and the position of the upper phase line, the mixed doped  $\text{Ba}(\text{Fe}_{0.953}\text{Co}_{0.021}\text{Cu}_{0.026})_2\text{As}_2$  is superconducting at 12 K.

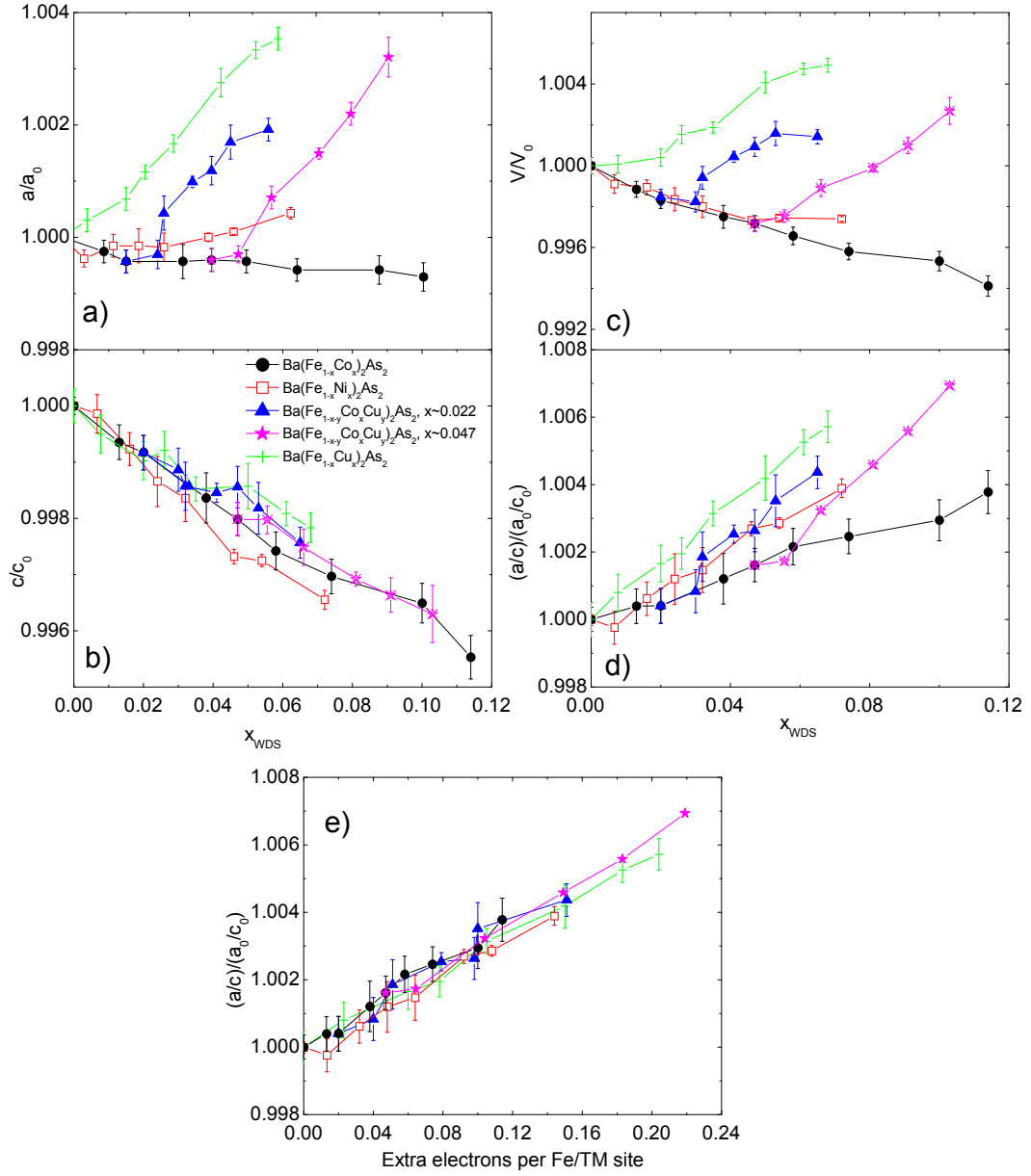


Figure 6.33 Comparison of the lattice parameters ( $T \sim 300$  K), normalized to the values of pure  $\text{BaFe}_2\text{As}_2$ , for all the 3d electron doped series: (a)  $a/a_0$ , (b)  $c/c_0$ , (c)  $V/V_0$ , (d)  $(a/c)/(a_0/c_0)$  as a function of transition metal doping,  $x$ ; and (e)  $(a/c)/(a_0/c_0)$  as a function of extra conduction electrons added,  $e$ .



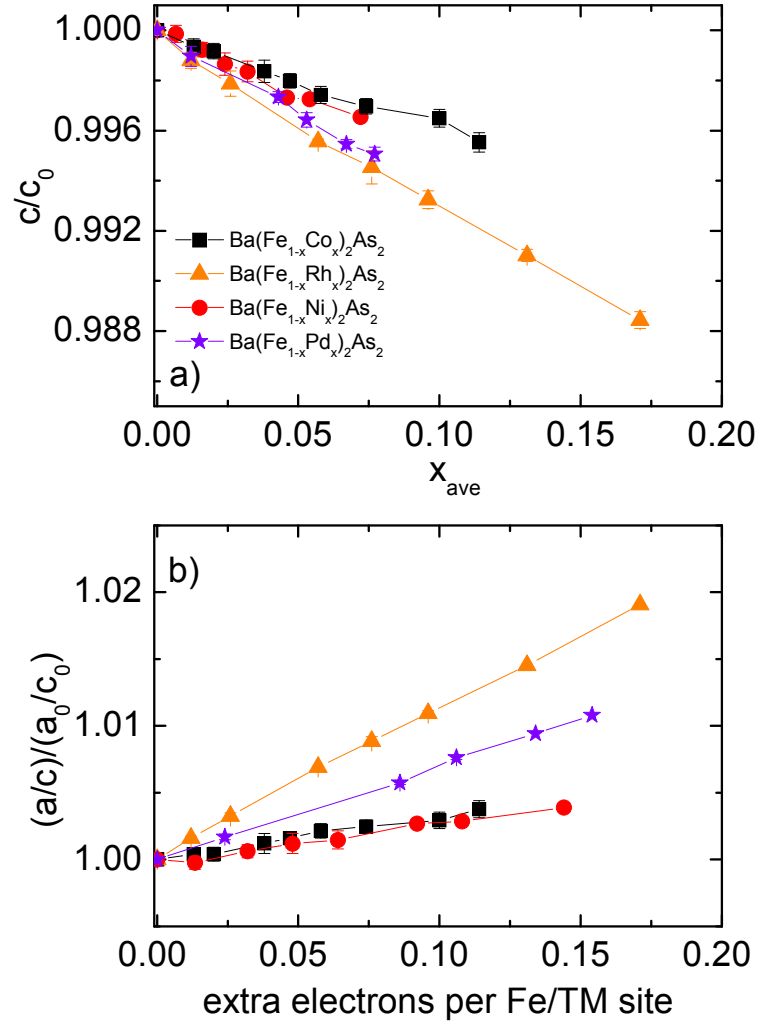


Figure 6.34 Comparison of the lattice parameters ( $T \sim 300$  K), normalized to the values of pure BaFe<sub>2</sub>As<sub>2</sub>, for Co-doped, Ni-doped, Rh-doped and Pd-doped BaFe<sub>2</sub>As<sub>2</sub> series: (a)  $a/a_0$  as a function of transition metal doping concentration  $x$ , (b)  $(a/c)/(a_0/c_0)$  as a function of extra electrons added,  $e$ .

Although  $x$  and  $e$  are intuitive parameters, there can be other ones. Lattice parameters obviously change with doping, so changes in  $a$ ,  $c$ ,  $V$  and  $a/c$  should be compared. To make the comparison as clear as possible, the lattice parameters are grouped into two graphs: Figs. 6.33 and 6.34. Fig. 6.33 presents the q33data for all the  $3d$  doped series and Fig. 6.34 compares the lattice parameters of the  $4d$  Rh and Pd doping with the isoelectronic,  $3d$  Co and Ni doping. Fig. 6.33 shows that whereas there is no simple (or universal) correlation between  $a$ ,  $V$  or  $a/c$  as a function of  $x$ , the  $c$ -lattice parameter collapses onto a universal curve with respect to  $x$ . It should be noted though, that whereas  $a$  and  $V$  vary with  $x$  in non-monotonic fashions (and show a range of behavior for different TM) and do not scale well with  $e$  (not shown), the  $a/c$  ratio does show a universal behavior when plotted as a function of  $e$  (Fig. 6.33 (e)). These results imply that we could not experimentally separate the effects of  $x$  from changes in  $c$ , or changes in  $e$  from changes in  $a/c$ . This dichotomy actually results in two differing scenarios: if  $x$  is the salient parameter, then the upper transitions are controlled by local physics such as TM disorder on the Fe sublattice or the disruption of very short range fluctuations; on the other hand, if the lattice parameter  $c$  is the salient variable, then details of band structure (nesting or not) or degree of As-As bonding across the Fe-plane would be more likely to control / affect the values of the upper transition temperatures.

Fortunately this ambiguity is resolved if we compare the lattice parameters of  $4d$  Rh and Pd doping samples with  $3d$  Co and Ni doping as shown in Fig. 6.34. Although the isoelectronic pairs have identical  $T - x$  (and also  $T - e$ ) phase diagrams, Rh and Pd change the  $\text{BaFe}_2\text{As}_2$  lattice parameters in distinctly different ways from Co and Ni. This is shown in Fig. 6.34; by tuning to  $4d$ -doping, we can actually distinguish between  $x$  and  $e$  on one hand and  $c$ ,  $a/c$  on the other. The lattice parameter  $c$  decreases with all dopings and the ratio of  $a/c$  increases with all dopings, but in both cases there is a clear difference between the  $3d$ - and  $4d$ - data sets. Changes in  $c$  and  $a/c$  no longer simply scale with  $x$  or  $e$  respectively. This decouples these two different parameterizations and leads to the statement that the upper, structural and magnetic phase transitions can be parameterized by  $x$  while the superconducting dome can be parameterized by  $e$ , they are no longer universally parameterized by either  $c$  or  $a/c$ . It

is still possible that some other structural parameter, such as bonding angles associated with the As position, offers better or alternate parameterization of these transition temperatures, but these data are not currently available.

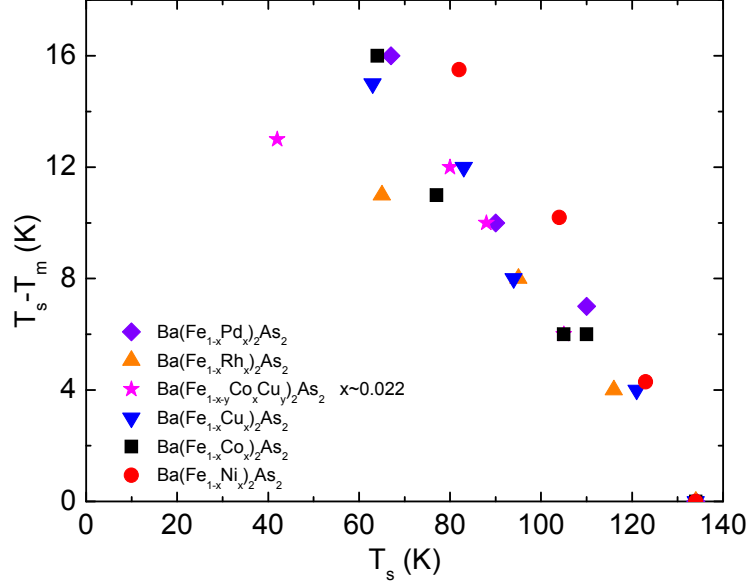


Figure 6.35  $T_s - T_m$  as a function of  $T_s$ . The data points from the samples indexed by "\*" and "\*\*" are not included.

Other trends and correlations can be found in the combined  $\text{Ba}(\text{Fe}_{1-x}\text{TM}_x)_2\text{As}_2$  phase diagram data. There is an increasing separation between  $T_s$  and  $T_m$  when these two transitions are suppressed to lower temperatures. It is worth seeing how the separation evolves quantitatively. Fig. 6.35 plots the separation,  $(T_s - T_m)$ , as a function of  $T_s$  for all the series, the data points indicated by \* and \*\* in Tables 5.1, 6.1-6.6, are not included. We can see that  $(T_s - T_m)$  for all the series evolves with  $T_s$  in similar fashion, but with some spread. At a gross level, it seems that Co and Rh split the transitions a little more slowly than Ni and Pd.

$T_s$  and  $T_m$  offer alternate variables for the parameterization of  $T_c$ , but only for underdoped samples. Such a parameterization is consistent with the idea that superconductivity is stabilized by suppressing these upper transitions. The potential appeal of this scheme can be

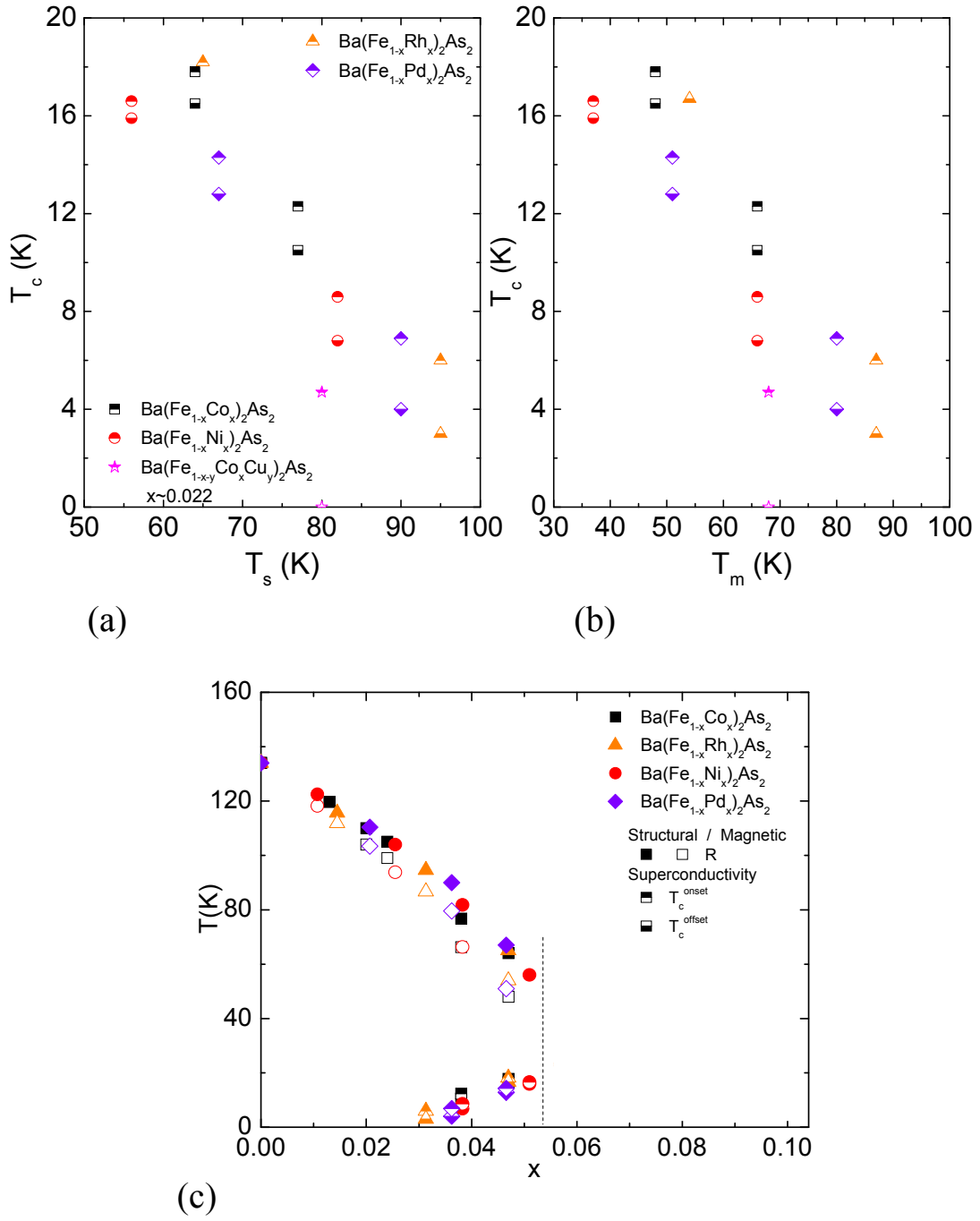


Figure 6.36 (a)  $T_c$  as a function of  $T_s$ . (b)  $T_c$  as a function of  $T_m$ . The data points from the samples indexed by "\*" and "\*\*" are not included. (c) Transition temperature as a function of adjusted  $x$ .  $x$  is normalized so as to bring the interpolated values of  $T_s$  onto the transition associated with  $\text{Ba}(\text{Fe}_{0.953}\text{Co}_{0.047})_2\text{As}_2$ : for Co doped  $\text{BaFe}_2\text{As}_2$ ,  $x = x_{WDS}$ ; for Rh doped  $\text{BaFe}_2\text{As}_2$ ,  $x = x_{WDS} \times 0.047/0.039$ ; for Pd doped  $\text{BaFe}_2\text{As}_2$ ,  $x = x_{WDS} \times 0.047/0.028$ ; for Ni doped  $\text{BaFe}_2\text{As}_2$ ,  $x = x_{WDS} \times 0.047/0.03$ .

seen in Fig. 6.32, where  $T_c$  is plotted as a function of  $e$  for comparison. As discussed above, there is excellent agreement of the  $T_c$  values when plotted as a function of  $e$  in the overdoped region but the data do not collapse onto a universal curve in the underdoped region. If as pointed out above, the behavior on the underdoped side of the superconducting dome is associated with the need to bring the upper transition to low enough temperature, so as to allow the superconductivity to turn on, it is worth examining the correlation between  $T_s$ ,  $T_m$  and  $T_c$  more directly. Fig. 6.36 (a) and (b) plot  $T_c$  as a function of  $T_s$  and  $T_m$  respectively. Both plots show a clear correlation. A more graphic way of examining the correlation between  $T_c$  and  $T_s$  ( $T_m$ ) is to create a composite diagram for the  $T_s$  ( $T_m$ )  $> T_c$  data by adjusting the  $x$  scales for the Ni, Rh, and Pd data so as to collapse the  $T_s$  and  $T_m$  phase lines onto the Co data set. This is plotted in Fig. 6.36 (c). As we can see, a clear consequence of this is to bring collapse the  $T_c$  data onto a single phase line as well.

### 6.3.2 Anisotropic upper critical field $H_{c2}$

As we have seen in the previous chapter, Co-doping and K-doping [144, 145] in  $\text{BaFe}_2\text{As}_2$  have quite similar  $H_{c2}$  curves. Both of them have a relatively small, anisotropic parameter  $\gamma$ . Given the similarities and differences between the Ni doped and Co doped  $\text{BaFe}_2\text{As}_2$  systems, a comparison of the  $H_{c2}(T)$  curves, which reflect the properties of the superconductivity in these two systems, is desirable. By comparing the  $T - x$  and  $T - e$  phase diagrams for Co and Ni doping, two Co dopings are logical comparably for optimally Ni doping,  $\text{Ba}(\text{Fe}_{0.954}\text{Ni}_{0.046})_2\text{As}_2$ : the comparably doped  $\text{Ba}(\text{Fe}_{0.953}\text{Co}_{0.047})_2\text{As}_2$  which has a similar  $T_c$ , and the near optimal doped  $\text{Ba}(\text{Fe}_{0.926}\text{Co}_{0.074})_2\text{As}_2$ .

High magnetic field anisotropic  $H_{c2}$  data taken for  $\text{Ba}(\text{Fe}_{0.954}\text{Ni}_{0.046})_2\text{As}_2$  in the magnetic field up to 33 T are summarized in Fig. 6.37. Two samples were measured. The upper panel of Fig. 6.37 presents the  $R(H)$  data taken from 11 K to 19 K with 1 K steps for  $H \perp c$ . The onset and offset criteria are shown. The lower panel presents the  $R(H)$  data taken from 5 K to 19 K with 1 K steps for  $H \parallel c$ . Temperature dependent  $H_{c2}$  curves for

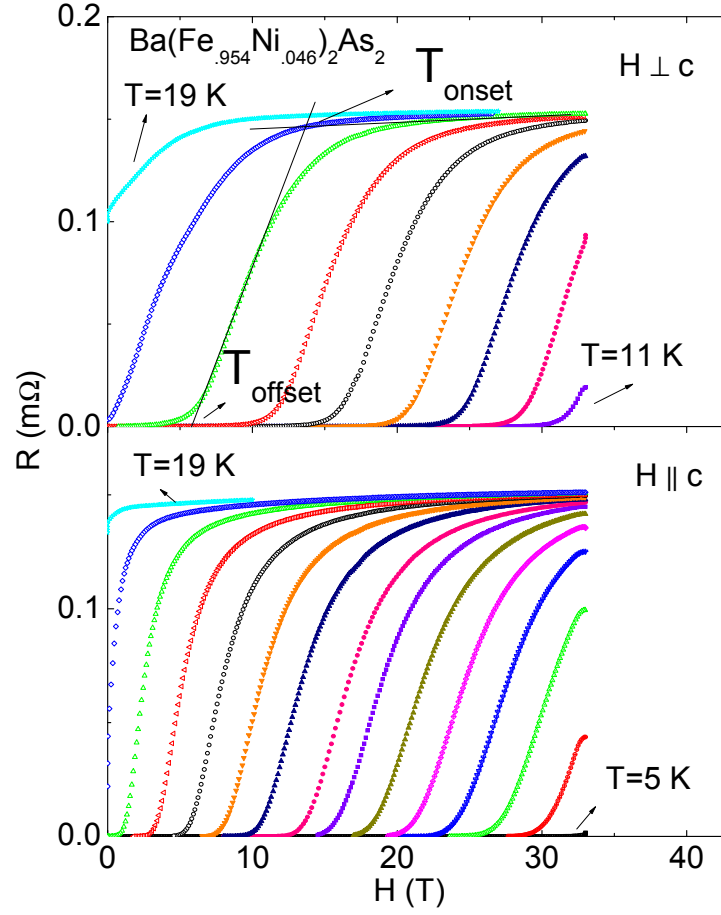


Figure 6.37  $R(H)$  data of  $\text{Ba}(\text{Fe}_{0.954}\text{Ni}_{0.046})_2\text{As}_2$  with  $H \perp c$  (upper panel) and  $H \parallel c$  (lower panel).

$\text{Ba}(\text{Fe}_{0.954}\text{Ni}_{0.046})_2\text{As}_2$  are presented in Fig. 6.38 in comparison to  $\text{Ba}(\text{Fe}_{0.953}\text{Co}_{0.047})_2\text{As}_2$  (Fig. 6.37 (a)) and  $\text{Ba}(\text{Fe}_{0.926}\text{Co}_{0.074})_2\text{As}_2$  (Fig. 6.37 (b)). A clear result of this comparison is that the anisotropy of the superconducting state is not defined by  $x$ , but rather by the low temperature structural / magnetic state of the system. Given that the addition of Ni suppresses  $T_s$  and  $T_m$  slightly faster than Co, anisotropy of near optimally doped  $\text{Ba}(\text{Fe}_{0.954}\text{Ni}_{0.046})_2\text{As}_2$  is virtually identical to near optimally doped  $\text{Ba}(\text{Fe}_{0.926}\text{Co}_{0.074})_2\text{As}_2$  as indicated from Fig. 6.37 (b) whereas it is almost 2 times larger than the underdoped  $\text{Ba}(\text{Fe}_{0.953}\text{Co}_{0.047})_2\text{As}_2$  as shown in Fig. 6.37 (a) despite they have similar doping level and  $T_c$ .

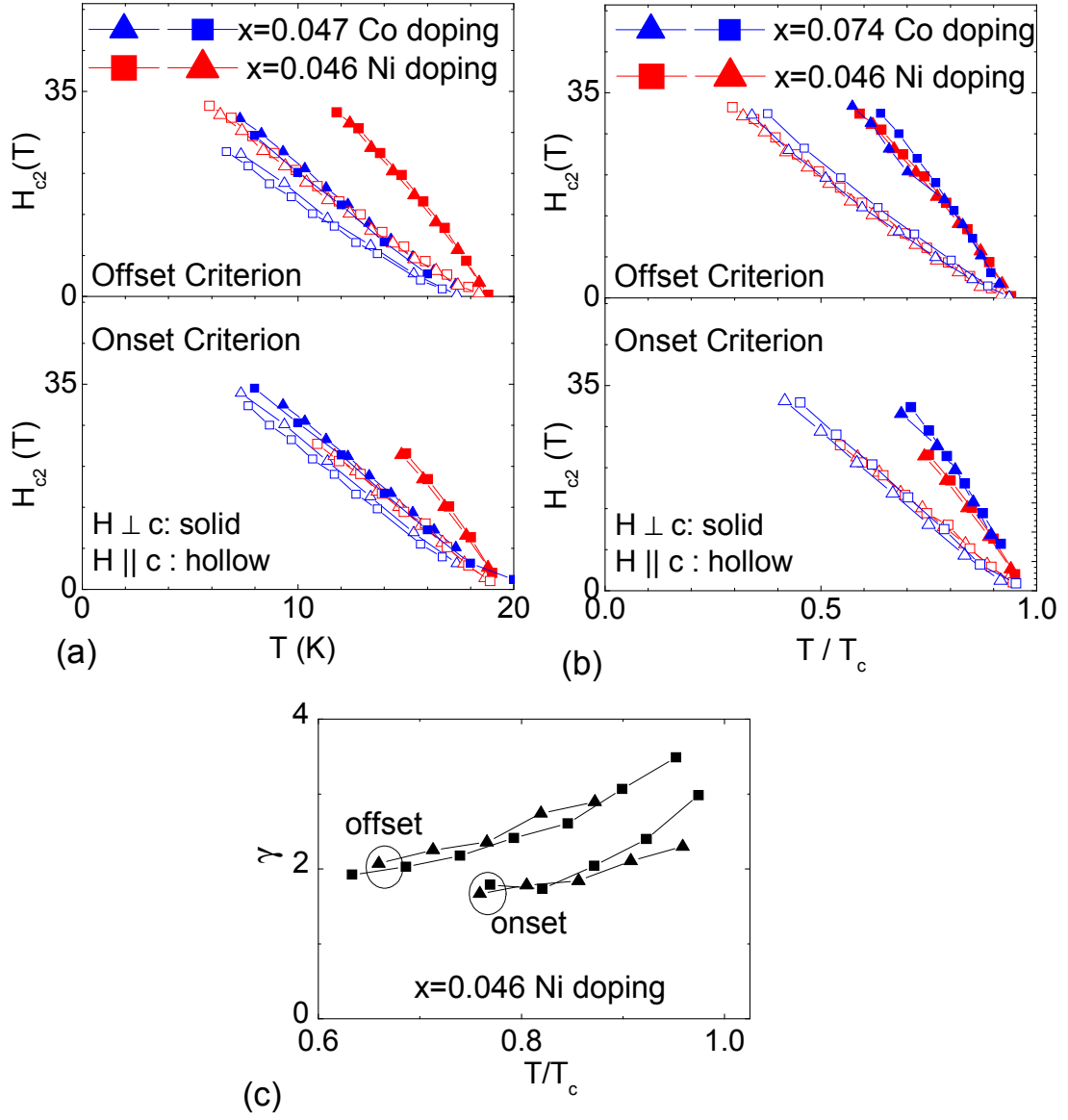


Figure 6.38 (a)  $H_{c2}$  vs.  $T$  from offset criterion (upper panel) and onset criterion (lower panel) of  $\text{Ba}(\text{Fe}_{0.954}\text{Ni}_{0.046})_2\text{As}_2$  and  $\text{Ba}(\text{Fe}_{0.953}\text{Co}_{0.047})_2\text{As}_2$ . (b)  $H_{c2}$  vs.  $T/T_c$  from offset criterion (upper panel) and onset criterion (lower panel) of  $\text{Ba}(\text{Fe}_{0.954}\text{Ni}_{0.046})_2\text{As}_2$  and  $\text{Ba}(\text{Fe}_{0.926}\text{Co}_{0.074})_2\text{As}_2$ . (c)  $\gamma = H_{c2}^{\perp c} / H_{c2}^{\parallel c}$  vs.  $T/T_c$  for  $\text{Ba}(\text{Fe}_{0.954}\text{Ni}_{0.046})_2\text{As}_2$ .

### 6.3.3 Universal scaling of $\Delta C_p/T$ at $T_c$ [54]

A final notable feature associated with superconducting dome is the observation that the specific heat jump,  $\Delta C_p/T_c$ , varies non-monotonically with  $x$ , but is roughly symmetric with  $T_c$  giving  $\Delta C_p/T_c \propto T_c^2$  [24, 25, 34, 35, 36, 54, 159, 160].

Fig. 6.39 (a) presents the values of  $\Delta C_p/T_c$  as a function of  $x$  of  $\text{Ba}(\text{Fe}_{1-x}\text{TM}_x)_2\text{As}_2$  (TM=Co and Ni) series.  $T_c$  as a function of the doping concentration is also presented in this figure for comparison.  $\Delta C_p/T_c$  rather than  $\Delta C_p/\gamma T_c$  is plotted because it is hard to make a reliable estimation of the normal state Sommerfeld constant  $\gamma$  due to the high upper critical field values in these samples. It can be seen that the  $\Delta C_p/T_c$  has a dome-like appearance as a function of  $x$ . The largest value of  $\Delta C_p/T_c$  is almost 10 times the smallest one. This feature is less likely due to the inhomogeneity of the samples since the WDS measurements summarized in Table 3.1 show the error bars including the instrument error is less than 5% of the  $x_{WDS}$  values for  $\text{Ba}(\text{Fe}_{1-x}\text{Co}_x)_2\text{As}_2$  series. On the other hand, this variation could come from the change of the density of states (DOS) at Fermi level. If we assume  $\Delta C_p/\gamma T_c$  is a constant, then the Sommerfeld constant  $\gamma$  in the normal state at  $x = 0.058$  should be 10 times smaller than the value at  $x = 0.038$ . Since  $\gamma$  can not be obtained reliably from experiment as we discussed above, it is hard to fully exclude this possibility, but this hypothesis is inconsistent with the band structure calculation for pure  $\text{BaFe}_2\text{As}_2$  [161], which does not support a dramatic change of DOS at Fermi level with small amount of doping.

$\Delta C_p$  as a function of  $T_c$  is plotted in Fig. 6.39 (b) for a wider selection of dopings.  $\Delta C_p$  data fall onto a universal curve, which monotonically, but not linearly, increases with  $T_c$  from 20 *mJ/moleK* around 10 K to 700 *mJ/moleK* around 24 K, no matter which dopant we used. This universal curve can be described as a  $T_c^3$  power law. This can be more clearly seen in a log-log plot as shown in Fig. 6.39 (c) where several more data points from K-doping [25] and other groups [24, 159, 160] are also added : a  $T_c^3$  relation is found over two decades in  $\Delta C_p/T_c$  and over one decade in  $T_c$ . These data are note worthy and are currently motivating several theoretical studies [162, 163]. These data have also been reproduced by other groups [164].



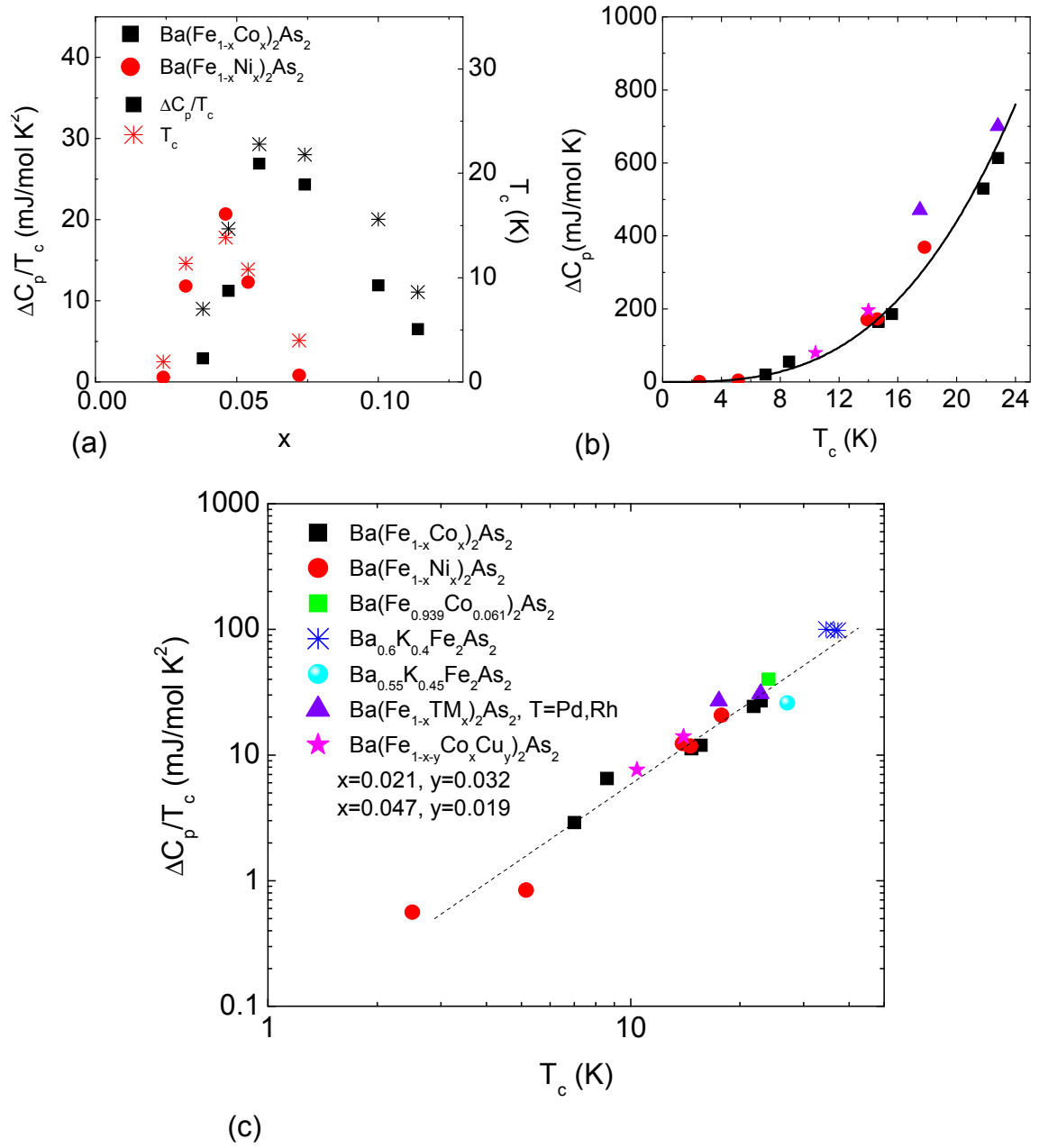


Figure 6.39 (a)  $\Delta C_p/T_c$  and  $T_c$  as functions of the doping level  $x$ . (b)  $\Delta C_p$  as a function of  $T_c$ . The solid line is the curve according to  $\Delta C_p = 0.055 T_c^3$ . (c) log-log plot of  $\Delta C_p/T_c$  vs.  $T_c$  [24, 25, 34, 35, 36, 54, 159, 160].

## CHAPTER 7. Summary and conclusions

Singlecrystalline  $\text{BaFe}_2\text{As}_2$  undergoes strongly coupled tetragonal to orthorhombic / paramagnetic to antiferromagnetic phase transitions at 134 K and can become superconducting under doping [23, 30, 31]. To study the correlations between the structural / magnetic phase transition and the superconductivity, seven series of  $\text{Ba}(\text{Fe}_{1-x}\text{TM}_x)_2\text{As}_2$  were grown and characterized by microscopic, transport and thermodynamic measurements.

From the study of  $\text{Ba}(\text{Fe}_{1-x}\text{Co}_x)_2\text{As}_2$  ( $x \leq 0.166$ ) series, we found that the substitution of Co for the Fe site monotonically suppresses the structural / antiferromagnetic phase transition at an initial rate of roughly 15 K per percent Co. As Co doping was increased, two features associated with the structural / magnetic phase transitions were found in the temperature derivatives of resistivity, magnetization and heat capacity data, indicating an increasingly separation of structural and magnetic phase transitions. It was later confirmed by neutron scattering measurements that the higher temperature feature is associated with the structural phase transition whereas the lower temperature one is associated with the magnetic phase transition. In addition, superconductivity can be stabilized in a dome-like area in the temperature-doping concentration ( $T - x$ ) phase diagram. It shows up at low temperature for  $x \geq 0.038$ , goes through a maximum and completely suppressed again by our highest doping level of  $x = 0.166$ . The maximum  $T_c$  values ( $\sim 23$  K) are found near  $x \sim 0.07$ , where the structural / magnetic phase transitions are completely suppressed. The  $T - x$  phase diagram of  $\text{Ba}(\text{Fe}_{1-x}\text{Co}_x)_2\text{As}_2$  clearly shows that superconductivity can occur in the orthorhombic / antiferromagnetic phase as well as the tetragonal / paramagnetic phases. This is indirectly confirmed by the high magnetic field anisotropic  $H_{c2}$  measurements which clearly manifests a  $\sim 50\%$  smaller anisotropy in the lower Co-doped samples, undergoing the structural / magnetic

phase transitions than the one in the higher Co-doped samples remaining in the tetragonal phase.

The  $T - x$  phase diagram of  $\text{Ba}(\text{Fe}_{1-x}\text{Co}_x)_2\text{As}_2$  reveals a clear correlation (and possible interaction) between the upper structural and magnetic phase transitions and the lower temperature superconducting phase. To understand these more fully and thus shed light on the occurrence of superconductivity in  $\text{BaFe}_2\text{As}_2$  systems, an extensive experimental effort was made on the other  $3d$ , and  $4d$  transition metal, electron doped,  $\text{BaFe}_2\text{As}_2$  series. Over 40 batches of  $\text{Ba}(\text{Fe}_{1-x}\text{TM}_x)_2\text{As}_2$  ( $\text{TM} = \text{Ni}, \text{Cu}, \text{Co} / \text{Cu mixtures}, \text{Rh}$  and  $\text{Pd}$ ) single crystals were grown and characterized. All the structural, compositional, transport and thermodynamic measurements enabled us to determine the temperature-doping concentration ( $T - x$ ) phase diagrams for all these  $3d$  and  $4d$ , electron doped  $\text{BaFe}_2\text{As}_2$  series. We found that whereas the structural and magnetic phase transitions in  $\text{BaFe}_2\text{As}_2$  were monotonically suppressed and increasingly separated in a grossly similar manner with increasing doping concentration for all these dopants, the superconducting domes act quite differently, scaling with  $e$ : the number of extra electrons added by the doping, at least on the overdoped side of the superconducting dome. The superconducting domes are almost identical for  $3d$  Co doping and  $4d$  Rh doping with the widest span of  $x$ , whereas for Ni doping and Pd doping, the spread of the domes is roughly half as large. When it comes to Cu doping, the superconducting dome, if there is one, shrink to the smallest one with only one concentration showing zero resistivity at 2.1 K.

The fact that the upper, structural / magnetic phase transitions, appear to be suppressed by the number of dopants while the location and extent of the superconducting dome scale with the number of additional electrons leads to the understanding that the suppression of the upper (structural / magnetic ) phase transitions is a necessary but not a sufficient condition for the occurrence of low temperature superconductivity. There exists a superconducting window (a limited range of the number of extra electrons added), inside which superconductivity can be stabilized if the structural and magnetic phase transitions are suppressed enough. Therefore, we can actually control the occurrence of superconductivity in electron doped  $\text{BaFe}_2\text{As}_2$  by changing the relative positions of the upper phase lines and the superconducting window with

different combination of dopants. In the case of Cu doping, too many extra electrons are added per Cu dopant, the upper phase line just overshoots the superconducting window, leading to an essentially non-existent superconducting dome with only one concentration showing zero resistivity at 2.1 K. If we dope Co into  $\text{Ba}(\text{Fe}_{1-x}\text{Cu}_x)_2\text{As}_2$  to adjust the upper phase line and the number of the extra electron added, the superconducting dome becomes wider with a higher  $T_c$ . Further examination of  $T_s$ ,  $T_m$  and  $T_c$  in the underdoped regime for these series reveals an essentially linear relation between  $T_s / T_m$  and  $T_c$ , which indicates a clear correlation between the suppression of structural / magnetic phase transitions and the stabilization of superconductivity. These observations all support the ideas that superconductivity exists over a limited  $e$ -value region if the upper phase transitions can be suppressed to low enough values.

However, at this moment "low enough" is only a qualitative concept rather than a quantitative one. It may be associated with reducing the size of the orthorhombic distortion and ordered moment "enough" or preserving enough of the magnetic fluctuations associated with the tetragonal phase to "low enough" temperatures. It is unclear if there are universal parameters to define "enough" at this moment. What's more, when we dope transition metal elements into  $\text{BaFe}_2\text{As}_2$ , we not only add extra electrons and change the DOS at Fermi level, we also introduce magnetic / nonmagnetic impurity scattering into this system. Since Fe pnictides have  $S_{\pm}$  order parameter proposed [82, 83, 84, 85, 86] and possibly have a multiple gap feature [51, 52, 165, 166, 167, 168, 169, 170, 171, 172, 173, 174, 175, 176], it is hard to estimate the effects of impurity scattering [177, 178, 179, 180, 181, 182]. However, we need to keep in mind that although the valence electron count picture is plausible as discussed above, the pair breaking effect due to magnetic / nonmagnetic impurity scattering is not excludable for explaining the difference in the maximum  $T_c$ . To answer these questions, further microscopic investigation of the magnetic moments associated with the dopant and the investigation of the density of states in these systems is required.

In the course of this work I have grown approximately 350 batches of samples and studied microscopic, structural, transport and thermodynamic properties of the majority of them. During the process, I have learned techniques of high temperature solution growth of single

crystals, solid state synthesis, wavelength dispersive spectroscopy, as well as electrical resistivity, magnetization and heat capacity measurements. In addition to the studies performed in this thesis, I have provided samples for approximately 20 different groups for scientific collaborations locally, nationally and internationally. These collaborations resulted in 57 papers submitted for publication outside the scope of this thesis, including 3 papers in the review process in Nature and Science, 8 published in Physical Review Letter, 35 published in Physical Review B [25, 34, 35, 47, 48, 49, 50, 52, 53, 54, 130].

## BIBLIOGRAPHY

- [1] H. K. Onnes, The resistance of pure mercury at helium temperatures, Commun. Phys. Lab. Univ. Leiden, 12, 120 (1911)
- [2] V. L. Ginzburg and D. A. Kirzhnits, Problema Vysokotemperaturnoi Sverkhprovodimosti, The Problem of High-Temperature Superconductivity, Moscow, Nauka (1977) [Translated into English: High-Temperature Superconductivity (NewYork: Consultants Bureau, 1982)]
- [3] J. G. Bednorz and K.A. Müller, Possible high  $T_c$  superconductivity in the Ba-La-Cu-O system, Z. Phys. B, 64 (2), 189 (1986)
- [4] M. K. Wu, J. R. Ashburn, and C. J. Torng, P. H. Hor, R. L. Meng, L. Gao, Z. J. Huang, Y. Q. Wang , and C. W. Chu, Superconductivity at 93 K in a new mixed-phase Yb-Ba-Cu-O compound system at ambient pressure, Phys. Rev. Lett., 58, 908 (1987)
- [5] R. J. Cava, B. Batlogg, R. B. van Dover, D. W. Murphy, S. Sunshine, T. Siegrist, J. P. Remeika, E. A. Rietman, S. Zahurak, and G. P. Espinosa, Bulk superconductivity at 91 K in single-phase oxygen-deficient perovskite  $\text{Ba}_2\text{YCu}_3\text{O}_{9-\delta}$ , Phys. Rev. Lett., 58, 1676 (1987)
- [6] Hiroshi Maeda, Yoshiaki Tanaka, Masao Fukutomi and Toshihisa Asano, A New High- $T_c$  Oxide Superconductor without a Rare Earth Element, Jpn. J. Appl. Phys., 27 L209 (1988)
- [7] Z. Z. Sheng, A. M. Hermann, Bulk superconductivity at 120 K in the Tl-Ca/Ba-Cu-O system, Nature, 332, 138 (1988)

- [8] A. Schilling, M. Cantoni, J.D. Guo and H. R. Ott, Superconductivity above 130 K in the Hg-Ba-Ca-C-O system, *Nature*, 363, 56 (1993).
- [9] P. Dai, B. C. Chakoumakos, G. F. Sun, K. W. Wong, Y. Xin and D. F. Lu, Synthesis and neutron powder diffraction study of the superconductor  $\text{HgBa}_2\text{Ca}_2\text{Cu}_3\text{O}_{8+\delta}$  by Tl substitution, *Physica C*, 243, 201 (1995)
- [10] L. Gao, Y. Y. Xue, F. Chen, Q. Xiong, R. L. Meng, D. Ramirez, C. W. Chu, J. H. Eggert, and H. K. Mao, Superconductivity up to 164 K in  $\text{HgBa}_2\text{Ca}_{m-1}\text{Cu}_m\text{O}_{2m+2\delta}$  ( $m=1, 2$ , and 3) under quasihydrostatic pressures, *Phys. Rev. B*, 50, 4260 (1994)
- [11] Yoichi Kamihara, Takumi Watanabe, Masahiro Hirano, and Hideo Hosono (2008), Iron-Based Layered Superconductor  $\text{LaO}_{1-x}\text{F}_x\text{FeAs}$  ( $x = 0.05-0.12$ ) with  $T_c = 26$  K, *J. Am. Chem. Soc.*, 130, 3296 (2008)
- [12] B. I. Zimmer, W. Jeitschko, J. H. Albering, R. Glaum and M. Reehuis, The rare earth transition metal phosphide oxides  $\text{LnFePO}$ ,  $\text{LnRuPO}$  and  $\text{LnCoPO}$  with  $\text{ZrCuSiAs}$  type structure, *J. Alloys Comp.*, 229, 238 (1995)
- [13] P. Quebe, L. J. Terbuchte, W. Jeitschko, Quaternary rare earth transition metal arsenide oxides  $\text{RTAsO}$  ( $T=\text{Fe, Ru, Co}$ ) with  $\text{ZrCuSiAs}$  type structure, *J. Alloys Comp.*, 302, 70 (2000)
- [14] Yoichi Kamihara, Hidenori Hiramatsu, Masahiro Hirano, Ryuto Kawamura, Hiroshi Yanagi, Toshio Kamiya, and Hideo Hosono, Iron-Based Layered Superconductor:  $\text{LaOFeP}$ , *J. Am. Chem. Soc.*, 128, 10012 (2006)
- [15] Takumi Watanabe, Hiroshi Yanagi, Toshio Kamiya, Yoichi Kamihara, Hidenori Hiramatsu, Masahiro Hirano, and Hideo Hosono, Nickel-Based Oxyphosphide Superconductor with a Layered Crystal Structure,  $\text{LaNiOP}$ , *Inorg. Chem.*, 46, 7719 (2007)
- [16] Hiroki Takahashi, Kazumi Igawa, Kazunobu Arii, Yoichi Kamihara, Masahiro Hirano, Hideo Hosono, Superconductivity at 43 K in an iron-based layered compound  $\text{LaO}_{1-x}\text{F}_x\text{FeAs}$ , *Nature*, 453, 376 (2008)

- [17] G. F. Chen, Z. Li, D. Wu, G. Li, W. Z. Hu, J. Dong, P. Zheng, J. L. Luo, and N. L. Wang, Superconductivity at 41 K and Its Competition with Spin-Density-Wave Instability in Layered  $\text{CeO}_{1-x}\text{F}_x\text{FeAs}$ , *Phys. Rev. Lett.*, 100, 247002 (2008)
- [18] Z. A. Ren, J. Yang, W. Lu, W. Yi, G. C. Che, X. L. Dong, L. L. Sun, Z. X. Zhao, Superconductivity at 52 K in iron based F doped layered quaternary compound  $\text{PrO}_{1-x}\text{F}_x\text{FeAs}$ , *Materials Research Innovations*, 12, 105 (2008)
- [19] Zhi-An Ren, Jie Yang, Wei Lu, Wei Yi, Xiao-Li Shen, Zheng-Cai Li, Guang-Can Che, Xiao-Li Dong, Li-Ling Sun, Fang Zhou and Zhong-Xian Zhao, Superconductivity in the iron-based F-doped layered quaternary compound  $\text{NdO}_{1-x}\text{F}_x\text{FeAs}$  *Europhys. Lett.*, 82, 57002 (2008)
- [20] X. H. Chen, T. Wu, G. Wu, R. H. Liu, H. Chen, and D. F. Fang, Superconductivity at 43 K in  $\text{SmFeAsO}_{1-x}\text{F}_x$ , *Nature*, 453, 761 (2008)
- [21] Takeshi Kondo, A. F. Santander-Syro, O. Copie, Chang Liu, M. E. Tillman, E. D. Mun, J. Schmalian, S. L. Bud'ko, M. A. Tanatar, P. C. Canfield, and A. Kaminski, Momentum Dependence of the Superconducting Gap in  $\text{NdFeAsO}_{0.9}\text{F}_{0.1}$  Single Crystals Measured by Angle Resolved Photoemission Spectroscopy, *Phys. Rev. Lett.*, 101, 147003 (2008)
- [22] J. Karpinski, N. D. Zhigadlo, S. Katrych, Z. Bukowski, P. Moll, S. Weyeneth, H. Keller, R. Puzniak, M. Tortello, D. Daghero, R. Gonnelli, I. Maggio-Aprile, Y. Fasano,  $\phi$ . Fischer, K. Rogacki and B. Batlogg, Single crystals of  $\text{LnFeAsO}_{1-x}\text{F}_x$  ( $\text{Ln} = \text{La}, \text{Pr}, \text{Nd}, \text{Sm}, \text{Gd}$ ) and  $(\text{Ba}_{1-x}\text{Rb}_x)\text{Fe}_2\text{As}_2$ : Growth, structure and superconducting properties, *Physica C*, 469, 370 (2009)
- [23] Marianne Rotter, Marcus Tegel, and Dirk Johrendt, Superconductivity at 38 K in the Iron Arsenide  $(\text{Ba}_{1-x}\text{K}_x)\text{Fe}_2\text{As}_2$ , *Phys. Rev. Lett.*, 101, 107006 (2008)
- [24] Marianne Rotter, Marcus Tegel, Inga Schellenberg, Falko M Schappacher, Rainer Pöttgen, Joachim Deisenhofer, Axel Günther, Florian Schrettle, Alois Loidl and



- Dirk Johrendt, Competition of magnetism and superconductivity in underdoped  $\text{Ba}_{1-x}\text{K}_x\text{Fe}_2\text{As}_2$ , *New J. Phys.*, 11, 025014 (2009)
- [25] N. Ni, S. L. Bud'ko, A. Kreyssig, S. Nandi, G. E. Rustan, A. I. Goldman, S. Gupta, J. D. Corbett, A. Kracher, and P. C. Canfield, Anisotropic thermodynamic and transport properties of single-crystalline  $(\text{Ba}_{1-x}\text{K}_x)\text{Fe}_2\text{As}_2$  ( $x=0$  and  $0.45$ ), *Phys. Rev. B*, 78, 014507 (2008)
- [26] X. F. Wang, T. Wu, G. Wu, H. Chen, Y. L. Xie, J. J. Ying, Y. J. Yan, R. H. Liu, and X. H. Chen, Anisotropy in the Electrical Resistivity and Susceptibility of Superconducting  $\text{BaFe}_2\text{As}_2$  Single Crystals, *Phys. Rev. Lett.*, 102, 117005(2009)
- [27] G. F. Chen, Z. Li, J. Dong, G. Li, W. Z. Hu, X. D. Zhang, X. H. Song, P. Zheng, N. L. Wang, and J. L. Lu, Transport and anisotropy in single-crystalline  $\text{SrFe}_2\text{As}_2$  and  $(\text{A}_{0.6}\text{K}_{0.4})\text{Fe}_2\text{As}_2$  ( $\text{A}=\text{Sr}, \text{Ba}$ ) superconductors, *Phys. Rev. B*, 78, 224512 (2008)
- [28] K. Hashimoto, T. Shibauchi, S. Kasahara, K. Ikada, S. Tonegawa, T. Kato, R. Okazaki, C. J. van der Beek, M. Konczykowski, H. Takeya, K. Hirata, T. Terashima, and Y. Matsuda, Microwave Surface-Impedance Measurements of the Magnetic Penetration Depth in Single Crystal  $(\text{Ba}_{1-x}\text{K}_x)\text{Fe}_2\text{As}_2$  Superconductors: Evidence for a Disorder-Dependent Superfluid Density, *Phys. Rev. Lett.*, 102, 207001(2009)
- [29] Athena S. Sefat, Ashfia Huq, Michael A. McGuire, Rongying Jin, Brian C. Sales, David Mandrus, Lachlan M. D. Cranswick, Peter W. Stephens, and Kevin H. Stone, Superconductivity in  $\text{LaFe}_{1-x}\text{Co}_x\text{AsO}$  *Phys. Rev. B*, 78, 104505 (2008)
- [30] A. S. Sefat, R. Jin, M. A. McGuire, B. C. Sales, D. J. Singh, and D. Mandrus, Superconductivity at 22 K in Co-Doped  $\text{BaFe}_2\text{As}_2$  Crystals, *Phys. Rev. Lett.*, 101, 117004 (2008)
- [31] L. J. Li, Y. K. Luo, Q. B. Wang, H. Chen, Z. Ren, Q. Tao, Y. K. Li, X. Lin, M. He, Z. W. Zhu, G. H. Cao and Z. A. Xu, Superconductivity induced by Ni doping in  $\text{BaFe}_2\text{As}_2$  single crystals, *New Journal of Physics*, 11, 025008 (2009)

- [32] S. Paulraj, Shilpam Sharma, A. Bharathi, A. T. Satya, Sharat Chandra, Y. Hariharan, C. S. Sundar, Superconductivity in Ru substituted  $\text{BaFe}_{2-x}\text{Ru}_x\text{As}_2$ , Unpublished, arxiv: 0902.2728
- [33] P. C. Canfield, S. L. Bud'ko, N. Ni, J. Q. Yan, and A. Kracher, Decoupling of the superconducting and magnetic/structural phase transitions in electron-doped  $\text{BaFe}_2\text{As}_2$ , Phys. Rev. B, 80, 060501 (2009)
- [34] N. Ni, M. E. Tillman, J.-Q. Yan, A. Kracher, S. T. Hannahs, S. L. Bud'ko, and P. C. Canfield, Effects of Co substitution on thermodynamic and transport properties and anisotropic  $H_{c2}$  in  $\text{Ba}(\text{Fe}_{1-x}\text{Co}_x)_2\text{As}_2$  single crystals, Phys. Rev. B, 78, 214515 (2008)
- [35] N. Ni, A. Thaler, A. Kracher, J. Q. Yan, S. L. Bud'ko, and P. C. Canfield, Phase diagrams of  $\text{Ba}(\text{Fe}_{1-x}\text{TM}_x)_2\text{As}_2$  single crystals ( $M=\text{Rh}$  and  $\text{Pd}$ ), Phys. Rev. B, 80, 024511 (2009)
- [36] Jiun-Haw Chu, James G. Analytis, Chris Kucharczyk, and Ian R. Fisher, Determination of the phase diagram of the electron-doped superconductor  $\text{Ba}(\text{Fe}_{1-x}\text{Co}_x)_2\text{As}_2$ , Phys. Rev. B, 79, 014506 (2009)
- [37] F. L. Ning, K. Ahilan, T. Imai, A. S. Sefat, R. Jin, M. A. McGuire, B. C. Sales, and D. Mandrus, Spin Susceptibility, Phase Diagram, and Quantum Criticality in the Electron-Doped High  $T_c$  Superconductor  $\text{Ba}(\text{Fe}_{1-x}\text{Co}_x)_2\text{As}_2$ , J. Phys. Soc. Jpn., 78, 013711 (2009)
- [38] X. F. Wang, T. Wu, G. Wu, R. H. Liu, H. Chen, Y. L. Xie, X. H. Chen, Abnormal T-linear susceptibility and Phase diagram of  $\text{Ba}(\text{Fe}_{1-x}\text{Co}_x)_2\text{As}_2$  single crystals, New J. Phys., 11, 045003 (2009)
- [39] L. Fang, H. Luo, P. Cheng, Z. Wang, Y. Jia, G. Mu, B. Shen, I. I. Mazin, L. Shan, C. Ren, H. Wen, Unpublished, Role of multiband effects and electron-hole asymmetry in the superconductivity and normal state properties of  $\text{Ba}(\text{Fe}_{1-x}\text{Co}_x)_2\text{As}_2$ , Phys. Rev. B, 80, 140508 (R) (2009)

- [40] Marianne Rotter, Marcus Tegel, and Dirk Johrendt, Inga Schellenberg, Wilfried Hermes, and Rainer Pöttgen, Spin-density-wave anomaly at 140 K in the ternary iron arsenide  $\text{BaFe}_2\text{As}_2$ , *Phys. Rev. B*, 78, 020503(R) (2008)
- [41] M. Pfisterer and G. Nagorsen, Zur struktur ternärer übergangsmetallarsenide, *Z. Naturforsch. B*, 35, 703 (1980).
- [42] Michael A. McGuire, Andrew D. Christianson, Athena S. Sefat, Brian C. Sales, Mark D. Lumsden, Rongying Jin, E. Andrew Payzant, David Mandrus, Yanbing Luan, Veerle Keppens, Vijayalaksmi Varadarajan, Joseph W. Brill, Raphaël P. Hermann, Moulay T. Sougrati, Fernande Grandjean and Gary J. Long, Phase transitions in  $\text{LaFeAsO}$ : Structural, magnetic, elastic, and transport properties, heat capacity and Mössbauer spectra, *Phys. Rev. B*, 78, 094517 (2008)
- [43] T. Nomura, S. W. Kim, Y. Kamihara, M. Hirano, P. V. Sushko, K. Kato, M. Takata, A. L. Shluger, and H. Hosono, Crystallographic phase transition and high-Tc superconductivity in  $\text{LaFeAsO:F}$ , *Supercond. Sci. Technol.*, 21, 125028(2008)
- [44] H.-H. Klauss, H. Luetkens, R. Klingeler, C. Hess, F. Litterst, M. Kraken, M. M. Korshunov, I. Eremin, S.-L. Drechsler, R. Khasanov, A. Amato, J. Hamannborreo, N. Leps, A. Kondrat, G. Behr, J. Werner, and B. Buchner, Commensurate Spin Density Wave in  $\text{LaFeAsO}$ : A Local Probe Study, *Phys. Rev. Lett.*, 101, 077005 (2008)
- [45] Clarina de la Cruz, Q. Huang, J. W. Lynn, Jiying Li, W. Ratcliff II, J. L. Zarestky, H. A. Mook, G. F. Chen, J. L. Luo, N. L. Wang, Pengcheng Dai, Magnetic order close to superconductivity in the iron-based layered  $\text{LaO}_{1-x}\text{F}_x\text{FeAs}$  systems, *Nature*, 453, 899(2008)
- [46] Q. Huang, Y. Qiu, Wei Bao, M. A. Green, J. W. Lynn, Y. C. Gasparovic, T. Wu, G. Wu, and X. H. Chen , Neutron-Diffraction Measurements of Magnetic Order and a Structural Transition in the Parent  $\text{BaFe}_2\text{As}_2$  Compound of FeAs-Based High-Temperature Superconductors, *Phys. Rev. Lett.*, 101, 257003 (2008).

- [47] R. Prozorov, N. Ni, M. A. Tanatar, V. G. Kogan, R. T. Gordon, C. Martin, E. C. Blomberg, P. Prommapan, J. Q. Yan, S. L. Bud'ko, and P. C. Canfield, Vortex phase diagram of  $\text{Ba}(\text{Fe}_{0.93}\text{Co}_{0.07})_2\text{As}_2$  single crystals, *Phys. Rev. B*, **78**, 224506 (2008)
- [48] S. L. Bud'ko, N. Ni, S. Nandi, G. M. Schmiedeshoff, and P. C. Canfield, Thermal expansion and anisotropic pressure derivatives of  $T_c$  in  $\text{Ba}(\text{Fe}_{1-x}\text{Co}_x)_2\text{As}_2$  single crystals, *Phys. Rev. B*, **79**, 054525 (2009)
- [49] M. R. Eskildsen, L. Ya. Vinnikov, T. D. Blasius, I. S. Veshchunov, T. M. Artemova, J. M. Densmore, C. D. Dewhurst, N. Ni, A. Kreyssig, S. L. Bud'ko, P. C. Canfield, and A. I. Goldman, Vortices in superconducting  $\text{Ba}(\text{Fe}_{1-x}\text{Co}_x)_2\text{As}_2$  studied via small-angle neutron scattering and Bitter decoration, *Phys. Rev. B*, **79**, 100501 (2009)
- [50] M. A. Tanatar, N. Ni, C. Martin, R. T. Gordon, H. Kim, V. G. Kogan, G. D. Samolyuk, S. L. Bud'ko, P. C. Canfield, and R. Prozorov, Anisotropy of the iron pnictide superconductor  $\text{Ba}(\text{Fe}_{1-x}\text{Co}_x)_2\text{As}_2$  ( $x=0.074, T_c=23$  K), *Phys. Rev. B*, **79**, 094507 (2009)
- [51] R. T. Gordon, N. Ni, C. Martin, M. A. Tanatar, M. D. Vannette, H. Kim, G. D. Samolyuk, J. Schmalian, S. Nandi, A. Kreyssig, A. I. Goldman, J. Q. Yan, S. L. Bud'ko, P. C. Canfield, and R. Prozorov, Unconventional London Penetration Depth in Single-Crystal  $\text{Ba}(\text{Fe}_{0.93}\text{Co}_{0.07})_2\text{As}_2$  Superconductors, *Phys. Rev. Lett.*, **102**, 127004 (2009)
- [52] R. T. Gordon, C. Martin, H. Kim, N. Ni, M. A. Tanatar, J. Schmalian, I. I. Mazin, S. L. Bud'ko, P. C. Canfield, and R. Prozorov, London penetration depth in single crystals of  $\text{BaFe}_{1-x}\text{Co}_x\text{As}_2$  spanning underdoped to overdoped compositions, *Phys. Rev. B*, **79**, 100506(R) (2009)
- [53] M. A. Tanatar, N. Ni, G. D. Samolyuk, S. L. Bud'ko, P. C. Canfield, and R. Prozorov, Resistivity anisotropy of  $\text{AFe}_2\text{As}_2$  ( $\text{A}=\text{Ca}, \text{Sr}, \text{Ba}$ ): Direct versus Montgomery technique measurements, *Phys. Rev. B*, **79**, 134528 (2009)

- [54] Sergey L. Bud'ko, Ni Ni, Paul C. Canfield, Jump in specific heat at the superconducting transition temperature in  $\text{Ba}(\text{Fe}_{1-x}\text{Co}_x)_2\text{As}_2$  and  $\text{Ba}(\text{Fe}_{1-x}\text{Ni}_x)_2\text{As}_2$  single crystals, Phys. Rev. B, 79, 220516 (2009)
- [55] Eun Deok Mun, Sergey L. Bud'ko, Ni Ni, Alex N. Thaler, and Paul C. Canfield, Thermoelectric power and Hall coefficient measurements on  $\text{Ba}(\text{Fe}_{1-x}\text{T}_x)_2\text{As}_2$  (T=Co and Cu), Phys. Rev. B, 80, 054517 (2009)
- [56] F. London, H. London, The Electromagnetic Equations of the Supraconductor, Proc. Roy. Soc. A, 149, 71, (1935)
- [57] W. Meissner and R. Ochsenfeld, Ein neuer effekt bei eintritt der supraleitfähigkeit, Naturwissenschaften., 21, 787 (1933)
- [58] V. L. Ginzburg and L. D. Landau, On the theory of superconductivity, Zh. Eksp. Teor. Fiz., 20, 1064 (1950)
- [59] A. A. Abrikosov, On the magnetic properties of superconductors of the second group, Zh. Eksp. Teor. Fiz., 32, 1442 (1957); Sov. Phys. JETP, 5, 1174 (1957)
- [60] L. N. Cooper, Bound Electron Pairs in a Degenerate Fermi Gas, Phys. Rev., 104, 1189 (1956)
- [61] J. Bardeen, L. N. Cooper, and J. R. Schrieffer, Microscopic Theory of Superconductivity, Phys. Rev., 106, 162 (1957)
- [62] J. Bardeen, L. N. Cooper, and J. R. Schrieffer, Theory of Superconductivity, Phys. Rev., 108, 1175 (1957)
- [63] J. Bardeen, Theory of the Meissner Effect in Superconductors, Phys. Rev., 97, 1724 (1955)
- [64] L. P. Gor'kov, Microscopic derivation of the Ginzburg-Landau equations in the theory of superconductivity, Zh. Eksp. Teor. Fiz., 36, 1918 (1959); Sov. Phys. JETP, 9, 1364 (1959)

- [65] G. M. Eliashberg, Interactions between electrons and lattice vibrations in a superconductor, *Zh. Eksp. Teor. Fiz.*, 38, 966 (1960); *Sov. Phys. JETP*, 11, 696 (1960)
- [66] J. P. Carbotte, Properties of boson-exchange superconductors, *Rev. Mod. Phys.*, 62, 1027 (1990)
- [67] A. A. Abrikosov and L. P. Gor'kov, On the theory of superconducting alloys I: The electrodynamics of alloy at absolute zero, *Zh. Eksp. Teor. Fiz.*, 35, 1558 (1958); *Sov. Phys. JETP*, 8, 1090 (1959)
- [68] P. W. Anderson, Theory of dirty superconductors, *J. Phys. Chem. solids.*, 11, 26 (1959)
- [69] A. A. Abrikosov and L. P. Gor'kov, Contribution to the theory of superconducting alloys with paramagnetic impurities, *Sov. Phys. JETP*, 12, 1243 (1961)
- [70] E. Helfand and N. R. Werthamer, Temperature and Purity Dependence of the Superconducting Critical Field,  $H_{c2}$ , *Phys. Rev. Lett.*, 13, 686 (1964)
- [71] E. Helfand and N. R. Werthamer, Temperature and Purity Dependence of the Superconducting Critical Field,  $H_{c2}$  II, *Phys. Rev.*, 147, 288 (1966)
- [72] N. R. Werthamer, E. Helfand, and P. C. Hohenberg, Temperature and Purity Dependence of the Superconducting Critical Field,  $H_{c2}$  III. Electron Spin and Spin-Orbit Effects, *Phys. Rev.*, 147, 295 (1966)
- [73] P. C. Hohenberg and N. R. Werthamer, Anisotropy and Temperature Dependence of the Upper Critical Field of Type-II Superconductors, *Phys. Rev.*, 153, 493 (1967)
- [74] N. R. Werthamer and W. L. McMillan, Temperature and Purity Dependence of the Superconducting Critical Field  $H_{c2}$  IV. Strong-Coupling Effects, *Phys. Rev.*, 158, 415 (1967)
- [75] L. Pitaevskii, *Superconductivity: Volume 1, Conventional and unconventional superconductors*, edited by K. H. Bennemann and J. B. Ketterson (Springer) (2008)

- [76] V. V. Schmidt, The physics of superconductors (Springer) (1997)
- [77] Emanuel Maxwell, Isotope Effect in the Superconductivity of Mercury, Phys. Rev., 78, 477 (1950)
- [78] C. A. Reynolds, B. Serin, W. H. Wright, and L. B. Nesbitt, Superconductivity of Isotopes of Mercury, Phys. Rev., 78, 487 (1950)
- [79] H. Frohlich, Interaction of Electrons with Lattice Vibrations, Proc. R. Soc. Lond. A, 215, 291 (1952)
- [80] K. H. Bennemann and J. B. Ketterson, Superconductivity: Volume 1, Conventional and unconventional superconductors, edited by K. H. Bennemann and J. B. Ketterson (Springer) (2008)
- [81] Charles Kittel, Introduction to solid state physics, (Wiley) (1996)
- [82] I. I. Mazin, D. J. Singh, M. D. Johannes, and M. H. Du, Unconventional superconductivity with a sign reversal in the order parameter of  $\text{LaFeAsO}_{1-x}\text{F}_x$ , Phys. Rev. Lett., 101, 057003 (2008)
- [83] Kazuhiko Kuroki, Seiichiro Onari, Ryotaro Arita, Hidetomo Usui, Yukio Tanaka, Hiroshi Kontani, and Hideo Aoki, Unconventional pairing originating from the disconnected Fermi surfaces of superconducting  $\text{LaFeAsO}_{1-x}\text{F}_x$ . Phys. Rev. Lett., 101, 087004 (2008).
- [84] S. Graser, T. A. Maier, P. J. Hirschfeld and D. J. Scalapino, Near-degeneracy of several pairing channels in multiorbital models for the Fe pnictides. New J. Phys., 11, 025016 (2009)
- [85] Fa Wang, Hui Zhai, Ying Ran, Ashvin Vishwanath, and Dung-Hai Lee, Functional renormalization-group study of the pairing symmetry and pairing mechanism of the FeAs-based high-temperature superconductor. Phys. Rev. Lett., 102, 047005 (2009).
- [86] C. T. Chen, C. C. Tsuei, M. B. Ketchen; Z. A. Ren, Z. X. Zhao, Integer and half-integer flux-quantum transitions in a niobium/iron-pnictide loop , Unpublished, arXiv:0905.3571

- [87] Charles P. Poole, Jr., Horacio A. Farach, Richard J. Creswick, Superconductivity (Elsevier) (2007)
- [88] F. Marsiglio and J. P. Carbotte, Superconductivity: Volume 1, Conventional and unconventional superconductors, edited by K. H. Bennemann and J. B. Ketterson (Springer) (2008)
- [89] P. G. Tomlinson, J. P. Carbotte, Multiple plane wave calculation of the resistivity of Pb and dilute Pb alloys, Can. J. Phys., 55, 751 (1977)
- [90] W. L. McMillan, Transition Temperature of Strong-Coupled Superconductors, Phys. Rev., 167, 331 (1968)
- [91] J. Frank, Physical properties of high temperature superconductors IV, edited by D. M. Ginzburg (World Scientific) (1994)
- [92] S. L. Bud'ko, G. Lapertot, C. Petrovic, C. E. Cunningham, N. Anderson, and P. C. Canfield, Boron Isotope Effect in Superconducting MgB<sub>2</sub>, Phys. Rev. Lett., 86, 1877 (2001)
- [93] B. Mitrovic, H. G. Zarate and J. P. Carbotte, The ratio  $2\Delta_0/k_B T_c$  within Eliashberg theory, Phys. Rev. B, 29, 184 (1984)
- [94] F. Marsiglio and J. P. Carbotte, Strong-coupling corrections to Bardeen-Cooper-Schrieffer ratios, Phys. Rev. B, 33, 6141 (1986)
- [95] M. Brian Maple, Eric. D. Bauer, Vivien. S. Zapf, Jochen Wosnitza, Superconductivity: Volume 1, Conventional and unconventional superconductors, edited by K. H. Bennemann and J. B. Ketterson (Springer) (2008)
- [96] L. P. Gor'kov, Superconductivity: Volume 1, Conventional and unconventional superconductors, edited by K. H. Bennemann and J. B. Ketterson (Springer) (2008)
- [97] David Markowitz and Leo P. Kadanoff, Effect of Impurities upon Critical Temperature of Anisotropic Superconductors, Phys. Rev., 131, 563 (1963)



- [98] P. Hohenberg, Anisotropic superconductors with nonmagnetic impurities, *Zh. Eksp. Teor. Fiz.*, 45, 1208 (1963); *Sov. Phys. JETP*, 18, 834 (1964)
- [99] V. G. Kogan, Macroscopic anisotropy in superconductors with anisotropic gaps, *Phys. Rev. B*, 66, 020509(R) (2002)
- [100] R. J. Radtke, K. Levin, H.-B. Schüttler and M. R. Norman, Predictions for impurity-induced  $T_c$  suppression in the high-temperature superconductors, *Phys. Rev. B*, 48, 653 (1993)
- [101] C. Petrovic, S. L. Bud'ko, V. G. Kogan, and P. C. Canfield, Effects of La substitution on the superconducting state of  $\text{CeCoIn}_5$ , *Phys. Rev. B*, 66, 054534 (2002)
- [102] M. F. Merriam, Electronic Structure and Superconductivity of Indium-Cadmium Alloys, *Phys. Rev.*, 144, 300 (1966)
- [103] G. Chanin, E. A. Lynton, and B. Serin, Impurity Effects on the Superconductive Critical Temperature of Indium and Aluminum, *Phys. Rev.*, 114, 719 (1959)
- [104] Y. Fukuzumi, K. Mizuhashi, K. Takenaka, and S. Uchida, Universal Superconductor-Insulator Transition and  $T_c$  Depression in Zn-Substituted High-  $T_c$  Cuprates in the Underdoped Regime, *Phys. Rev. Lett.*, 76, 684 (1996)
- [105] K. O. Cheon, I. R. Fisher, V. G. Kogan, and P. C. Canfield, P. Miranović, P. L. Gammel, Resistivity and magnetic susceptibility of single-crystal  $\text{Lu}(\text{Ni}_{1-x}\text{Co}_x)_2\text{B}_2\text{C}$  ( $x=0.0-0.09$ ), *Phys. Rev. B*, 58, 6463 (1998)
- [106] W. E. Pickett and D. J. Singh,  $\text{LuNi}_2\text{B}_2\text{C}$ : A novel Ni-based strong-coupling superconductor, *Phys. Rev. Lett.*, 72, 3702 (1994)
- [107] L. F. Mattheiss, Electronic properties of superconducting  $\text{LuNi}_2\text{B}_2\text{C}$  and related boride carbide phases, *Phys. Rev. B*, 49, 13279 (1994)

- [108] S. L. Bud'ko, M. Elmassalami, M. B. Fontes, J. Mondragon, W. Vanoni, B. Giordano and E. M. Baggio-Saitovitch, Effect of the Ni site substitution on superconducting properties of  $\text{YNi}_2\text{B}_2\text{C}$ , *Physica C*, 243, 183 (1994)
- [109] Sergey L. Bud'ko and Paul C. Canfield, Magnetism and superconductivity in rare earth-nickel-borocarbides, *Comptes Rendus Physique*, 7, 56 (2006)
- [110] P. C. Canfield, S. L. Bud'ko, B. K. Cho, W. P. Beyermann, A. Yatskar,  $\text{RNi}_2\text{B}_2\text{C}$  magnetic superconductors: An update from the front, *J. Alloys Comp.*, 250, 596 (1997)
- [111] S. Skalski, O. Betbeder-Matibet, and P. R. Weiss, Properties of Superconducting Alloys Containing Paramagnetic Impurities, *Phys. Rev.*, 136, A1500 (1964)
- [112] P. B. Allen, New method for solving Boltzmann's equation for electrons in metals, *Phys. Rev. B*, 17, 3725 (1978)
- [113] A. A. Golubov and I. I. Mazin, Effect of magnetic and nonmagnetic impurities on highly anisotropic superconductivity, *Phys. Rev. B*, 55, 15146 (1997)
- [114] A. V. Chubukov, D. V. Efremov, and I. Eremin, Magnetism, superconductivity, and pairing symmetry in iron-based superconductors, *Phys. Rev. B*, 78, 134512 (2008)
- [115] Yunkyu Bang, Han-Yong Choi and Hyekyung Won, Impurity effects on the  $\pm s$ -wave state of the iron-based superconductors, *Phys. Rev. B*, 79, 054529 (2009)
- [116] Rastko Sknepnek, German Samolyuk, Yong-bin Lee, and Jörg Schmalian, Anisotropy of the pairing gap of FeAs-based superconductors induced by spin fluctuations, *Phys. Rev. B*, 79, 054511 (2009)
- [117] L. P. Gor'kov, The critical supercooling field in superconductivity theory, *Zh. Eksp. Teor. Fiz.*, 37, 833 (1959); *Sov. Phys. JETP*, 10, 593 (1960)
- [118] A. M. Clogston, Upper Limit for the Critical Field in Hard Superconductors, *Phys. Rev. Lett.*, 9, 266 (1962)

- [119] R. A. Ferrell, Knight Shift in Superconductors, *Phys. Rev. Lett.*, 3, 262 (1959)
- [120] J. Appel, Spin-Orbit Coupling and the Knight Shift in Nontransition-Metal Superconductors, *Phys. Rev.*, 139, A1536 (1965)
- [121] J. C. Brice, *Crystal growth processes*, (Halsted Press), (1986)
- [122] J. C. Brice, *The growth of crystals from liquids*, (Elsevier), (1973)
- [123] B. R. Pamplin, *Crystal growth*, (Oxford), (1975)
- [124] P. C. Canfield, Z. Fisk, Growth of single crystals from metallic fluxes, *Phil. Mag.*, 65, 1117 (1992)
- [125] Z. Fisk, J. P. Remeika, *Handbook of the physics and chemistry of rare earth*, 12, 53 (1989)
- [126] P. C. Canfield and I. R. Fisher, High-temperature solution growth of intermetallic single crystals and quasicrystals, *J. Cryst. Growth.*, 225, 155 (2001)
- [127] V. D. Abulkhaev, Ce-Sb binary phase diagram, *Russ. J. Inorg. Chem.*, 42, 283 (1997)
- [128] T. A. Wiener, P. C. Canfield, Magnetic phase diagram of flux-grown single crystals of CeSb, *J. Alloys. Compounds.*, 303-304, 505 (2000)
- [129] J.-Q. Yan, A. Kreyssig, S. Nandi, N. Ni, S. L. Bud'ko, A. Kracher, R. J. McQueeney, R. W. McCallum, T. A. Lograsso, A. I. Goldman, and P. C. Canfield, Structural transition and anisotropic properties of single-crystalline  $\text{SrFe}_2\text{As}_2$ , *Phys. Rev. B*, 78, 024516 (2008)
- [130] N. Ni, S. Nandi, A. Kreyssig, A. I. Goldman, E. D. Mun, S. L. Bud'ko, and P. C. Canfield, First-order structural phase transition in  $\text{CaFe}_2\text{As}_2$ , *Phys. Rev. B*, 78, 014523 (2008)
- [131] N. A. Cokcen, *Bull. Alloy Phase Diagrams*, 11, 271 (1990)
- [132] T. B. Massalski, H. Okamoto, P. R. Subramanian and L. Kacprzak, *Binary Alloy Phase Diagrams*, 2nd ed, ASM Internatioanl, Materials Park, OH, 616, 618 (1990)

- [133] H. Okamoto, Phase Diagrams of Binary Iron Alloys, ASM Internatioanl, Materials Park, OH, 385 (1993)
- [134] H. Okamoto, J. Phase Equilibria, 12, 457 (1991)
- [135] M. E. Fisher, Relation between the specific heat and susceptibility of an antiferromagnet, Philos. Mag., 7, 1731 (1962).
- [136] M. E. Fisher, Resistive Anomalies at Magnetic Critical Points, Phys. Rev. Lett., 20, 665 (1968).
- [137] Z. Bukowski, S. Weyeneth, R. Puzniak, P. Moll, S. Katrych, N. D. Zhigadlo, and J. Karpinski, H. Keller, B. Batlogg, Superconductivity at 23 K and low anisotropy in Rb-substituted  $\text{BaFe}_2\text{As}_2$  single crystals, Phys. Rev. B, 79, 104521 (2009)
- [138] Josiah L. Mathieu and Susan E. Lattturner, Zintl phase as dopant source in the flux synthesis of  $\text{Ba}_{1-x}\text{K}_x\text{Fe}_2\text{As}_2$  type superconductors, Chem. Commun., 4965 (2009)
- [139] Y. Su, P. Link, A. Schneidewind, Th. Wolf, P. Adelmann, Y. Xiao, M. Meven, R. Mittal, M. Rotter, D. Johrendt, Th. Brueckel, and M. Loewenhaupt, Antiferromagnetic ordering and structural phase transition in  $\text{BaFe}_2\text{As}_2$  with Sn incorporated from the growth flux, Phys. Rev. B, 79, 064504 (2009)
- [140] S.-H. Baek, T. Klimczuk, F. Ronning, E. D. Bauer, J. D. Thompson, and N. J. Curro, Microscopic  $^{75}\text{As}$  NMR study of the effect of impurities on the first-order spin-density-wave transition in  $\text{BaFe}_2\text{As}_2$ , Phys. Rev. B, 78, 212509 (2008)
- [141] J. K. Dong, L. Ding, H. Wang, X. F. Wang, T. Wu, G. Wu, X. H. Chen and S. Y. Li, Thermodynamic properties of  $\text{Ba}_{1-x}\text{K}_x\text{Fe}_2\text{As}_2$  and  $\text{Ca}_{1-x}\text{Na}_x\text{Fe}_2\text{As}_2$ , New J. Phys., 10 123031 (2008)
- [142] Zhao-Sheng Wang, Hui-Qian Luo, Cong Ren, and Hai-Hu Wen, Upper critical field, anisotropy, and superconducting properties of  $\text{Ba}_{1-x}\text{K}_x\text{Fe}_2\text{As}_2$  single crystals, Phys. Rev. B, 78, 140501(R) (2008)

- [143] G. Li, W. Z. Hu, J. Dong, Z. Li, P. Zheng, G. F. Chen, J. L. Luo, and N. L. Wang, Probing the Superconducting Energy Gap from Infrared Spectroscopy on a  $\text{Ba}_{0.6}\text{K}_{0.4}\text{Fe}_2\text{As}_2$  Single Crystal with  $T_c=37\text{K}$ , Phys. Rev. Lett., 101, 107004 (2008)
- [144] M. M. Altarawneh, K. Collar, and C. H. Mielke N. Ni, S. L. Bud'ko, and P. C. Canfield, Determination of anisotropic  $H_{c2}$  up to 60 T in  $\text{Ba}_{0.55}\text{K}_{0.45}\text{Fe}_2\text{As}_2$  single crystals, Phys. Rev. B, 78, 220505(R) (2008)
- [145] H. Q. Yuan, J. Singleton, F. F. Balakirev, S. A. Baily, G. F. Chen, J. L. Luo and N. L. Wang, Nearly isotropic superconductivity in  $(\text{Ba,K})\text{Fe}_2\text{As}_2$ , Nature, 457, 565 (2009)
- [146] A. Yamamoto, J. Jaroszynski, C. Tarantini, L. Balicas, J. Jiang, A. Gurevich, D. C. Larbalestier, R. Jin, A.S. Sefat, M.A. McGuire, B.C. Sales, D.K. Christen, and D. Mandrus, Small anisotropy, weak thermal fluctuations, and high field superconductivity in Co-doped iron pnictide  $\text{Ba}(\text{Fe}_{1-x}\text{Co}_x)_2\text{As}_2$ , Appl. Phys. Lett., 94, 062511 (2009)
- [147] M. Kano, Y. Kohama, D. Graf, F. F. Balakirev, A. S. Sefat, M. A. McGuire, B. C. Sales, D. Mandrus, S. W. Tozer, Anisotropy of the Upper Critical Field in a Co-Doped  $\text{BaFe}_2\text{As}_2$  Single Crystal, J. Phys. Soc. Jpn., 78, 084719 (2009)
- [148] F. Ronning, T. Klimczuk, E.D. Bauer, H. Volz, J.D. Thompson, Synthesis and properties of  $\text{CaFe}_2\text{As}_2$  single crystals, J. Phys.: Condens. Matter, 20, 322201 (2008).
- [149] G Wu, H Chen, T Wu, Y L Xie, Y J Yan, R H Liu, X F Wang, J J Ying and X H Chen, Different resistivity response to spin-density wave and superconductivity at 20 K in  $\text{Ca}_{1-x}\text{Na}_x\text{Fe}_2\text{As}_2$ , J. Phys.: Condens. Matter, 20, 422201 (2008)
- [150] A. Leithe-Jasper, W. Schnelle, C. Geibel, and H. Rosner, Superconducting State in  $\text{Sr}(\text{Fe}_{1-x}\text{Co}_x)_2\text{As}_2$  by Internal Doping of the Iron Arsenide Layers, Phys. Rev. Lett., 101, 207004 (2008)
- [151] Milton S. Torikachvili, Sergey L. Bud'ko, Ni Ni, and Paul C. Canfield, Pressure Induced Superconductivity in  $\text{CaFe}_2\text{As}_2$  , Phys. Rev. Lett., 101, 057006 (2008)

- [152] D. K. Pratt, W. Tian, A. Kreyssig, J. L. Zarestky, S. Nandi, N. Ni, S. L. Bud'ko, P. C. Canfield, A. I. Goldman, R. J. McQueeney, Coexistence of Competing Antiferromagnetic and Superconducting Phases in the Underdoped  $\text{Ba}(\text{Fe}_{0.953}\text{Co}_{0.047})_2\text{As}_2$  Compound Using X-ray and Neutron Scattering Techniques, *Phys. Rev. Lett.*, 103 087001 (2009)
- [153] C. Lester, Jiun-Haw Chu, J. G. Analytis, S. Capelli, A. S. Erickson, C. L. Condon, M. F. Toney, I. R. Fisher, S.M. Hayden, A neutron scattering study of the interplay between structure and magnetism in  $\text{Ba}(\text{Fe}_{1-x}\text{Co}_x)_2\text{As}_2$ , *Phys. Rev. B*, 79, 144523 (2009)
- [154] A. Kreyssig, et al., private communication
- [155] U. Welp, R. Xie, A. E. Koshelev, W. K. Kwok, P. Cheng, L. Fang, and H. H. Wen, Calorimetric determination of the upper critical fields and anisotropy of  $\text{NdFeAsO}_{1-x}\text{F}_x$  single crystals, *Phys. Rev. B*, 78, 140510(R) (2008)
- [156] L. Balicas, A. Gurevich, Y. J. Jo, J. Jaroszynski, D. C. Larbalestier, R. H. Liu, H. Chen, X. H. Chen, N. D. Zhigadlo, S. Katrych, Z. Bukowski, and J. Karpinski, Probing Multi-band Superconductivity and Magnetism in  $\text{SmFeAsO}_{0.8}\text{F}_{0.2}$  Single Crystals by High-field Vortex Torque Magnetometry , Unpublished, arXiv:0809.4223.
- [157] J. Jaroszynski, F. Hunte, L. Balicas, Youn-jung Jo, I. Raicevic, A. Gurevich, D. C. Larbalestier, F. F. Balakirev, L. Fang, P. Cheng, Y. Jia, H. H. Wen, Upper critical fields and thermally-activated transport of  $\text{NdFeAsO}_{0.7}\text{F}_{0.3}$  single crystal, *Phys. Rev. B*, 78, 174523 (2008)
- [158] S. Weyeneth, R. Puzniak, N.D. Zhigadlo, S. Katrych, Z. Bukowski, J. Karpinski, H. Keller, Evidence for two distinct anisotropies in the oxypnictide superconductors  $\text{SmFeAsO}_{0.8}\text{F}_{0.2}$   $\text{NdFeAsO}_{0.8}\text{F}_{0.2}$ , *J. Supercond. Nov. Magn.*, 22, 347 (2009)
- [159] Gang Mu, Huiqian Luo, Zhaosheng Wang, Lei Shan, Cong Ren, and Hai-Hu Wen, Low temperature specific heat of the hole-doped  $\text{Ba}_{0.6}\text{K}_{0.4}\text{Fe}_2\text{As}_2$  single crystals, *Phys. Rev. B*, 79, 174501 (2009)

- [160] U. Welp, R. Xie, A. E. Koshelev, W. K. Kwok, H. Q. Luo, Z. S. Wang, G. Mu, and H. H. Wen, Anisotropic phase diagram and strong coupling effects in  $\text{Ba}_{0.6}\text{K}_{0.4}\text{Fe}_2\text{As}_2$  from specific-heat measurements, *Phys. Rev. B*, 79, 094505 (2009)
- [161] A. F. Kemper, C. Cao, P. J. Hirschfeld, and H.-P. Cheng, Effects of cobalt doping and three-dimensionality in  $\text{BaFe}_2\text{As}_2$ , *Phys. Rev. B*, 80, 104511 (2009)
- [162] J. Zaanen, The specific heat jump at the superconducting transition and the quantum critical nature of the normal state of Pnictide superconductors, Unpublished, arxiv: 0908.0033v1
- [163] V. G. Kogan, Pair-breaking in iron-pnictides, Unpublished, arxiv: 0910.4728v1
- [164] Gang Mu, Bin Zeng, Peng Cheng, Zhaosheng Wang, Lei Fang, Bing Shen, Lei Shan, Cong Ren, Hai-Hu Wen, Impurity Scattering Effect on Superconductivity and the Violation of Anderson Theorem in  $\text{BaFe}_{1-x}\text{Co}_x\text{As}_2$  Single Crystals, Unpublished, arxiv: 0906.4513
- [165] C. Liu, G.D. Samolyuk, Y. Lee, N. Ni, T. Kondo, A.F. Santander-Syro, S.L. Bud'ko, J.L. McChesney, E. Rotenberg, T. Valla, A.V. Fedorov, P.C. Canfield, B.N. Harmon and A. Kaminski, K-Doping Dependence of the Fermi Surface of the Iron-Arsenic  $\text{Ba}_{1-x}\text{K}_x\text{Fe}_2\text{As}_2$  Superconductor Using Angle-Resolved Photoemission Spectroscopy, *Phys. Rev. Lett.*, 101, 177005 (2008)
- [166] H. Ding, P. Richard, K. Nakayama, K. Sugawara, T. Arakane, Y. Sekiba, A. Takyama, S. Souma, T. Sato, T. Takahashi, Z. Wang, X. Dai, Z. Fang, G. F. Chen, J. L. Luo and N. L. Wang, Observation of Fermi-surface dependent nodeless superconducting gaps in  $\text{Ba}_{0.6}\text{K}_{0.4}\text{Fe}_2\text{As}_2$ , *Europhys. Lett.*, 83, 47001 (2008).
- [167] K. Nakayama, T. Sato, P. Richard, Y.-M. Xu, Y. Sekiba, S. Souma, G. F. Chen, J. L. Luo, N. L. Wang, H. Ding and T. Takahashi, Superconducting gap symmetry of  $\text{Ba}_{0.6}\text{K}_{0.4}\text{Fe}_2\text{As}_2$  studied by angle-resolved photoemission spectroscopy, *Europhys. Lett.*, 85, 67002 (2009)

- [168] H. Liu, W. Zhang, L. Zhao, X. Jia, J. Meng, G. Liu, X. Dong, G. F. Chen, J. L. Luo, N. L. Wang, W. Lu, G. Wang, Y. Zhou, Y. Zhu, X. Wang, Z. Zhao, Z. Xu, C. Chen and X. J. Zhou, Fermi surface and band renormalization of  $\text{Sr}_{1-x}\text{K}_x\text{Fe}_2\text{As}_2$  from angle-resolved photoemission spectroscopy, *Phys. Rev. B*, 78, 184514 (2008)
- [169] L. Wray, D. Qian, D. Hsieh, Y. Xia, L. Li, J. G. Checkelsky, A. Pasupathy, K. K. Gomes, A. V. Fedorov, G. F. Chen, J. L. Luo, A. Yazdani, N. P. Ong, N. L. Wang, M. Z. Hasan, Momentum dependence of superconducting gap, strong-coupling dispersion kink, and tightly bound Cooper pairs in the high- $T_c$   $(\text{Sr,Ba})_{1-x}(\text{K,Na})_x\text{Fe}_2\text{As}_2$  superconductors, *Phys. Rev. B*, 78, 184508 (2008)
- [170] D. V. Evtushinsky, D. S. Inosov, V. B. Zabolotnyy, A. Koitzsch, M. Knupfer, B. Buchner, G. L. Sun, V. Hinkov, A. V. Boris, C. T. Lin, B. Keimer, A. Varykhalov, A. A. Kordyuk, S.V. Borisenko, Momentum dependence of the superconducting gap in  $\text{Ba}_{1-x}\text{K}_x\text{Fe}_2\text{As}_2$ , *Phys. Rev. B*, 79, 054517 (2009)
- [171] G. Li, W. Z. Hu, J. Dong, Z. Li, P. Zheng, G. F. Chen, J. L. Luo, and N. L. Wang, Probing the Superconducting Energy Gap from Infrared Spectroscopy on a  $\text{Ba}_{0.6}\text{K}_{0.4}\text{Fe}_2\text{As}_2$  Single Crystal with  $T_c=37$  K, *Phys. Rev. Lett.*, 101, 107004 (2008)
- [172] K. Terashima, Y. Sekiba, J. H. Bowen, K. Nakayama, T. Kawahara, T. Sato, P. Richard, Y.-M. Xu, L. J. Li, G. H. Cao, Z. A. Xu, H. Ding and T. Takahashi, Fermi surface nesting induced strong pairing in iron-based superconductors, *PNAS*, 106, 7330 (2009)
- [173] Y. Sekiba, T. Sato, K. Nakayama, K. Terashima, P. Richard, J. H. Bowen, H. Ding, Y-M Xu, L. J. Li, G. H. Cao, Z-A Xu and T. Takahashi, Electronic structure of heavily electron-doped  $\text{BaFe}_{1.7}\text{Co}_{0.3}\text{As}_2$  studied by angle-resolved photoemission, *New J. Phys.* 11, 025020 (2009)
- [174] P. Samuely, Z. Pribulová, P. Szabó, G. Pristáš, S.L. Bud'ko and P.C. Canfield, Point contact Andreev reflection spectroscopy of superconducting energy gaps in 122-type family of iron pnictides, *Physica C*, 469, 507 (2009)



- [175] Yi Yin, M. Zech, T. L. Williams, X. F. Wang, G. Wu, X. H. Chen, and J. E. Hoffman, Scanning Tunneling Spectroscopy and Vortex Imaging in the Iron Pnictide Superconductor  $\text{BaFe}_{1.8}\text{Co}_{0.2}\text{As}_2$ , *Phys. Rev. Lett.*, 102, 097002 (2009)
- [176] L. Ding, J. K. Dong, S. Y. Zhou, T. Y. Guan, X. Qiu, C. Zhang, L. J. Li, X. Lin, G. H. Cao, Z. A. Xu and S. Y. Li, Nodeless superconducting gap in electron-doped  $\text{BaFe}_{1.9}\text{Ni}_{0.1}\text{As}_2$  probed by quasiparticle heat transport, *New J. Phys.*, 11, 093018 (2009)
- [177] I. I. Mazin, and J. Schmalian, Pairing symmetry and pairing state in ferropnictides: Theoretical overview, *Physica C*, 469, 614 (2009)
- [178] Yuko Senga and Hiroshi Kontani, Impurity Effects in Sign-Reversing Fully Gapped Superconductors: Analysis of FeAs Superconductors, *J. Phys. Soc. Jpn.*, 77, 113710 (2008)
- [179] Masashige Matsumoto, Mikito Koga, and Hiroaki Kusunose, Single Impurity Effects in Multiband Superconductors with Different Sign Order Parameters, *J. Phys. Soc. Jpn.*, 78, 084718 (2009)
- [180] Yunkyu Bang, Han-Yong Choi, Hyekyung Won, Impurity effects on the  $\pm s$ -wave state of the iron-based superconductors, *Phys. Rev. B*, 79, 054529 (2009)
- [181] Deepa Kasinathan, Alim Ormeci, Katrin Koch, Ulrich Burkhardt, Walter Schnelle, Andreas Leithe-Jasper and Helge Rosner,  $\text{AFe}_2\text{As}_2$  ( $\text{A} = \text{Ca}, \text{Sr}, \text{Ba}, \text{Eu}$ ) and  $\text{SrFe}_{2-x}\text{TM}_x\text{As}_2$  ( $\text{TM} = \text{Mn}, \text{Co}, \text{Ni}$ ): crystal structure, charge doping, magnetism and superconductivity, *New J. Phys.*, 11, 025023 (2009)
- [182] Masatoshi Sato, Yoshiaki Kobayashi, San Chul Lee, Hidefumi Takahashi, Yoko Miura, Studies of Impurity-Doping Effects and NMR Measurements of  $\text{La1111}$  and/or  $\text{Nd 1111}$  Fe-Pnictide Superconductors, Unpublished, arxiv:0907.3007 (2009)